2015

Ultrafine particle generation and measurement

Qiaoling Liu
liuq3@vcu.edu

School of Engineering
Virginia Commonwealth University

This is to certify that the dissertation prepared by Qiaoling Liu entitled "ULTRAFINE PARTICLE GENERATION AND MEASUREMENT" has been approved by her committee as satisfactory completion of the dissertation requirement for the degree of Doctor of Philosohpy

---

Dr. Da-Ren Chen, Committee Chair, Mechanical and Nuclear Engineering

---

Dr. Arunkumar Subramanian, Mechanical and Nuclear Engineering

---

Dr. Hooman V. Tafreshi, Mechanical and Nuclear Engineering

Dr. Meng-Dawn Cheng, Oak Ridge National Laboratory

Dr. Wei Zhang, Electrical and Computer Engineering

Dr. Gary C. Tepper, Chair of the Department of Mechanical and Nuclear Engineering

---

Dr. Barbara D. Boyan, Dean of the School of Engineering

Dr. F. Douglas Boudinot, Dean of the School of Graduate Studies

May 22, 2015

ULTRAFINE PARTICLE GENERATION AND MEANSUREMENT

A dissertation submitted in partial fulfillment of the requirements for the degree of Doctor of Philosophy
at Virginia Commonwealth University.

by

QIAOLING LIU
M.S., Environmental Science, Peking University, China, 2010
B.S., Environmental Science, Renmin University of China, China, 2007

Director: DR. DA-REN CHEN
PROFESSOR AND FLOYD D. GOTTWALD, SR. CHAIR IN MECHANICAL AND NUCLEAR ENGINEERING

Virginia Commonwealth University
Richmond, Virginia
August 2015

Acknowledgement

I wish to express my sincere appreciation to my advisor, Professor Da-Ren Chen, for his excellent guidance and never-ending support. His encouragement of independent thinking, his advice and patience were always invaluable and inspirational. I would like to acknowledge members of my committee, Dr. Arunkumar Subramanian, Dr. Meng-Dawn Cheng, Dr. Hooman V. Tafreshi and Dr. Wei Zhang for taking an interest in my work, examining my dissertation, and providing useful comments.

I would like to thank all members and alumni in the Particle Lab. In particular, I would like to thank Huijing Fu, Jingjie Zhang, Qisheng Ou, Siqin He, Li Huang, He Jing, Yaping Zhang, Qiang Wang, Di Liu, His-Wei Yeh and Nan Zhou for countless discussions and assistance. I would like to thank Graduate Program Director, Dr. Karla M. Mossi, for her kindness and sincere advice. I would also like to thank my colleagues in the Department of Energy, Environmental and Chemical Engineering in Washington University in St. Louis, and colleagues in the Department of Mechanical and Nuclear Engineering in Virginia Commonwealth University for their assistant. Many thanks also go to the department staff in both two universities, Rose Baxter, Trisha Sutton, Alison R. Bell, Lorita D. Mason for their kind assistance.

Funding support from USEPA are gratefully acknowledge. Also I would like to thank TSE Systms Inc. for providing test device.

Finally, my genuine gratitude goes to my parents and my boyfriend, Kai Ding, for their support during my study and research at Virginia Commonwealth University. Without their companionship, support and encouragement, this work could not be completed.

Qiaoling Liu

Virginia Commonwealth University

May, 2015

Dedicated to my parents, Qing Liu and Hui Zhou

and my boyfriend, Kai Ding

Table of Contents

List of Tables

Page

List of Figures

Page

Abstract

ULTRAFINE PARTICLE GENERATION AND MEASUREMENT

By Qiaoling Liu, M.S.

A dissertation submitted in partial fulfillment of the requirements for the degree of Doctor of Philosophy at Virginia Commonwealth University.

Virginia Commonwealth University, 2015

Major Director: Dr. Da-Ren Chen
Professor and Floyd D. Gottwald, Sr. Chair in Mechanical and Nuclear Engineering

Ultrafine particles (UFPs) with diameters smaller than 100 nm are omnipresent in ambient air. They are important sources for fine particles produced through the agglomeration and/or vapor condensation. With their unique properties, UFPs have also been manufactured for industrial applications. But, from the toxicological and health perspective, ultrafine particles with high surface-to-volume ratios often have high bio-availability and toxicity. Many recent epidemiologic studies have evidence UFPs are highly relevant to human health and disease. In order to better investigate UFPs, better instrumentation and measurement techniques for UFPs are thus in need. The overall objective of this dissertation is to advance out current knowledge on UFPs generation and measurement. Accordingly, it has two major parts: (1) ultrafine particle generation for laboratory aerosol research via electrospray (ES), and (2) ultrafine particle measurement for

ambient aerosol monitor and personal exposure study via the development of a cost-effective and compact electrical mobility particle sizer. In the first part, to provide monodisperse nanoparticles, a new single capillary electrospray with a soft X-ray photoionizer as a charge reduction scheme has been developed. The soft X-ray effects on electrospray operation, particle size distribution and particle charge reduction were evaluated. To generate ultrafine particles with sufficient mass concentration for exposure/toxicity study, a TSE twin-head electrospray (THES) was evaluated, as well. The configuration and operational variables of the studied THES has been optimized. Three different nanoparticle suspensions were sprayed to investigate material difference. In the second part, to develop a miniature electrical mobility based ultrafine particle sizer (mini e-UPS), a new mini-plate aerosol charger and a new mini-plate differential mobility analyzer (DMA) have been developed. The performances of mini-plate charger and mini-plate DMA were carefully evaluated for ultrafine particles, including intrinsic/extrinsic charging, extrinsic charge distribution, DMA sizing accuracy and DMA transfer function. A prototype mini e-UPS was then assembled and tested by laboratory generated aerosol. Also a constrained least square method was applied to recover the particle size distribution from the current measured by a mini Faraday Cage aerosol electrometer.

CHAPTER 1 Introduction and Overview

1.1 Introduction to Ultrafine Particle Generation and Measurement

Aerosol, defined as tiny solid/liquid particles suspended in gases, varies in size, surface area, number/volume/mass concentration, chemical composition, physical properties and sources. In aerosol research, particles are usually classified according to their aerodynamic diameters. Particles with diameters smaller than 10 μm are defined as PM_{10}, including "inhalable coarse particles" which are particles larger than 2.5 μm and smaller than 10 μm ($PM_{2.5-10}$), "fine particles" with diameters equal to and smaller than 2.5 μm ($PM_{2.5}$), and ultrafine particles (UFPs) with diameters smaller than 0.1 μm (USEPA, http://www.epa.gov/pm/). Ambient particles are generated from different sources via various mechanisms. UFPs either derive directly from fuel combustion and vehicle emission or are formed when compounds with lower vapor pressures spontaneously nucleate/condense on other small particles (Kulmala et al., 2004). UFPs are major sources for fine particles produced through the agglomeration and/or vapor condensation. In addition to their existence in ambient air, UFPs of various compositions have been manufactured for industrial applications (because of their unique mechanical, magnetic, optical, electrical and chemical properties), for example, applying silver nanoparticles in apparel for their antibacterial and anti-odor properties, titanium dioxide and zinc oxide nanoparticles in

cosmetics to effectively block the UV rays in the sunlight, and carbon nanoparticles to lengthen the lifetime of vehicle tires and as carriers for novel drug delivery systems (Somasundaran et al., 2010; Lee et al., 2007; Smijs & Pavel, 2011; Vassiliou et al., 2008; Madani et al., 2011).

With the National Nanotechnology Initiate, the concerns regarding to the environmental impact, toxicity and health effect of nanoparticles are emerging. From the toxicological and health perspective, nanoparticles with high surface-to-volume ratios often have high bio-availability and toxicity (Nel et al., 2006; Heinlaan et al., 2008; Park et al., 2011). Peer-reviewed literature reports that nanomaterials with the particle sizes between 10 to 50 nm could easily enter the human body and deposit in the alveolar region of a human lung, even entering in the blood stream and being transported to vital organs (Kreyling et al., 2002; Takenaka et al., 2001; Oberdörster et al., 2004; Paur et al., 2011). Recent epidemiologic studies have evidenced UFPs are particularly relevant to pulmonary diseases, cancer and mortality because of their higher diffusion coefficient and greater accumulation ability (Hoek et al, 2002; Peters et al. 2004; Delfino et al, 2005; Oberdörster et al, 2005; Bräuner et al, 2007; Shah et al, 2008; Li et al, 2010; Stewart et al, 2010). Moreover, the increased asthma prevalence has been found to often occur in the area with high UFP levels in ambient air or high motor vehicle traffic density and residence community in close proximity to freeways (Samet et al, 2000; Holguin, 2008; Salam et al, 2008; Patel and Miller, 2009). It has also been shown that the ultrafine particle induced health effects can be more resulted from the immediate exposure to particles than the exposure in the past 24 hours

(Gold et al. 2000; Li et al. 1999). In order to better investigate UFPs, better instrumentation and measurement techniques for UFPs are thus in need.

In laboratory aerosol research and aerosol instrumentation development, aerosol generators producing UFPs in stable concentration and size distribution, especially monodisperse distribution, play important roles in nanomaterial synthesis, nanoparticle toxicity studies, aerosol instrument calibration and many other areas. Aerosols can be generated by several approaches, such as mechanical atomization, nano-powder dispersion, ultrasonic nebulization, electrospray (ES), inkjet processes (IJAG), etc. Among the above techniques, ES, with unique advantage in producing monodisperse particles ranging from nanometers to micrometers, has been proposed in many nanoparticle applications. Because of the use of DC field in the ES processes, generated particles are electrically charged at high level. The charge reduction for electrosprayed particles is needed in order to keep them gas-borne. The limited mass throughout also prevents the use of ES from many research studies and practical applications. More effort should thus be paid in the aforementioned directions.

Instruments and techniques for aerosol characterization have been developed and applied for decades. Most of them are designed for scientific studies and laboratory usage. These aerosol instruments often have high resolution and sensitivity. However, they are expensive, heavy and large in size. Because of the tempo-spatial distribution of UFPs in the ambient, the demand for cost-effective aerosol sensors in much smaller packages for portability and ease of use is increasing.

Therefore, the overall objective of this dissertation is therefore to advance our current knowledge and techniques for the UFP generation via electrospray and for the UFP monitoring via the development of a cost-effective and compact electrical mobility particle sizer. The motivation for each part is explained in the following sections.

1.2 Part I: Ultrafine Particle Generation via Electrospray Technique

Electrospray is capable of generating highly charged monodisperse particles in a wide range of particle sizes. The highly charged particles are mostly like to deposit if the charge level is not reduced. The charges on particles could be balanced by bipolar ions via the diffusion charging mechanism. The common techniques to reduce the charges are radioactive materials, corona discharge and UV/soft X-ray irradiation (Chen et al. 1995; Ebeling et al. 2000; Hontanon and Kruis 2008; Modesto-Lopez et al. 2011). The increasing rigorous regulations for using radioactive materials make it difficult or even impossible to access them. Using Corona discharge approach requires complicate voltage control and ion monitoring system. And the ozone production issue accompanied with corona discharge also limits its application in *in-vivo* studies.

With higher intensity than UV light, soft X-ray becomes a preferred particle neutralizer or particle charge in some recent researches (Kulkarni et al., 2002; Shimada et al., 2002; Han et al., 2003; Lee et al., 2005; Jiang et al., 2007a; Kim et al., 2011). Because (1) without any decaying problem, the soft X-ray photoionizer can generate bipolar ions with a stable concentration during its entire lifetime; (2) photoionizers are easily purchased and operated compared with other approaches. The diffusion charging and photo charging take

place at the same time when particles are exposed to a soft X-ray. Previous applications of soft X-ray in minimizing electrical charges on particles occurred in completely separate units (Shimada et al. 2002; Han et al. 2003; Lee et al. 2005; Modesto-Lopez et al. 2011). No attempt has been devoted to integrate the electrospray and soft X-ray irradiation in close proximity, even to operate electrospray under direct soft X-ray irradiation.

Twin-head electrospray, in which one spray head produces positively charged droplets and the other produces negatively charged ones, is an alternative solution to overcome the aforementioned issues and limitation for charge reduction of electrosprayed particles. By operating two spray heads at the same time, the twin-head ES can produce particle with higher concentration than single head ES system. Due to the columbic repulsion among ES particles, the agglomeration effect of the ES particles could be minimized. The idea of using two sprays to generate countercharged droplets was first proposed in 1965 to study the collision of two charged droplets (Schneider et al., 1965). It was later applied to encapsulate solid particles with liquid droplets using electrostatic attractions (Langer and Yamate, 1969). Several studies using the twin-head electrospray had been carried out after that, such as twin-head ES for powder production (Borra et al., 1999; Camelot et al., 1999), Nanomats formation via twin-head electrospray (Morozov and Vsevolodov, 2007), and synthesis of controlled release drug particles (Fu et al.,2012). In order to generate un-agglomerated nanoparticles with a high mass concentration for *in-vivo* nanotoxicity studies, a new twin-head ES system was available from TSE Systems Inc. to be used with a 20-port nose-only animal exposure chamber.

The major objectives for the first half of the dissertation are:

1. To develop an electrospray ultrafine aerosol generator with a soft X-ray as a bipolar ion source for charge reduction.
2. To evaluate a twin-head electrospray system for the dispersion of ultrafine particles in concentrations high enough for animal testing.

1.3 Part II: Development of a New Electrical UPF Sizer (Mini-eUPS)

The concerns regarding to the environmental impact, toxicity and health effect of UFPs are emerging these days. Some epidemiologic studies have evidenced UFPs are particularly relevant to human health/diseases, such as pulmonary and cardiovascular diseases, cancer and asthma. Data on personal exposure to ultrafine particles and tempo-spatial distribution of UFPs in the ambient air however are very limit. In addition to the current implemented particulate matter standard monitor network, it is believe that the future air quality network for PM pollutant shall include the monitor of UFPs. Moreover, the area density of UFP monitor sites shall be higher than that of exist PM sites. It is because of the high diffusivity and high concentration of UFPs, resulting in their very dynamic transport behavior. Therefore, to meet the future demand in UFP monitor and to realize the aerosol sensing network for broader ground area coverage, cost-effective, compact aerosol sizers for UFPs are needed.

The instruments and technologies for UFP characterization have been developed and applied for decades. The comprehensive review can be found in the article given by Chen and Pui (2008). The instruments for integral measurement of physical parameters (i.e.

concentration, surface area and mass) involves condensation particle counter (CPC), electrical aerosol detector (EAD), nanoparticle surface area monitors, surface acoustic wave microbalance (SAWM), Quartz-crystal Microbalance (QCM) and Tapered-element Oscillating Microbalance (TEOM). To investigate one of the most important characteristic of particles, size distribution, electrical mobility based aerosol instruments (e.g. EAA, DMA and APM), inertia based aerosol instruments (e.g. impactor, nano-MOUDI, cyclone and virtual impactor) and light scattering based aerosol instruments (e.g. LPC, polarization intensity scattering and DLS) are widely used in aerosol or aerosol related researches. However, most of them are designed for scientific studies and laboratory usage, with high resolution and sensitivity. They are expensive in price and bulky in package. Even for some personal sensors, they are still expensive, heavy and large. That is, there are still no suitable aerosol instrument for future UFP monitoring. Furthermore, the demand for cost-effective aerosol sensors in much smaller packages for portability and ease of use is increasing.

With the capability to characterize particle sizes and to classify particles down to the nanometer range, electrical mobility based technique is preferred to be applied into the development of the next generation of UFP sizer. A typical electrical mobility based aerosol sizer consists of a particle charger which imposes a well-defined charge distribution on test aerosol, a differential mobility analyzer which separates/classifies particles based on their electrical mobility, and a particle detector which could be a condensation particle counter or a particle electrometer for number concentration measurement. Thus, we proposed to develop a cost-effective, more compact electrical ultrafine particle sizer (mini-eUPS), in

which a miniature corona based particle charger and a miniature differential mobility analyzer were needed to be developed.

The major objectives for the second half of the dissertation are:

1. To develop a miniature particle charger with high particle charging efficiency, low particle loss and fewer multiple charges on particles.

2. To develop a mini-plate DMA with high particle penetration efficiency and good sizing resolution.

3. To assemble and test a mini-eUPS with the capability of measuring and recording ultrafine particle size distribution, ambient temperature and humidity

1.4 Dissertation Structure

In addressing the two major components, the whole dissertation contains nine chapters. The first part, including chapters 2, 3 and 4, focuses on the design and evaluation of a single capillary electrospray with a soft X-ray charge reduction chamble and a TSE twin-head electrospray. The second part, including chapters 5, 6, 7 and 8, focuses on the development of a low-cost, miniature electrostatic ultrafine particle sizer, including mini-plate charger and mini-plate EAA/DMA development, device assembly and test. Brief descriptions of each chapter are as follows:

In Chapter 1, an overview of ultrafine particles, their sources, properties, applications, and challenges are presented. A general introduction, background information, and research objectives for the ultrafine particle generation and measurement are given.

Part I:

In Chapter 2, a general introduction on electrospray and its application are given. The charge reduction approaches for keeping electrosprayed aerosol airborne are summaried, including their pros and cons. The review leads to utilize and evaluate soft X-ray photoionizer in ES particle charge reduction. To generate a large amount of unagglomerated ultrafine particles, a twin-head electrospray technique is introduced. And previous studied regarding twin-head electrospray system are reviewed.

In Chapter 3, a prototype single-capillary electrospray (ES) aerosol generator having a soft X-ray photoionizer for charge reduction has been constructed and its performance under various configurations has been investigated in this study. Two soft X-ray irradiation directions (i.e., 90o and 180o relative to the spray direction) and two disk plates (with the orifice diameters of 0.25″ and 1.25″) were tested for the prototype configuration. In the investigation, the spray current as a function of ES voltage was recorded. The fluorescence analysis was applied in this study to quantify the transmission efficiency and the charge fractions of particles exiting from the prototype generator for particles with the sizes ranging from 30 to 300 nm. And a scanning mobility particle sizer (SMPS) was also utilized to measure the size measurement of ES particles when the prototype was operated at the cone-jet mode.

In Chapter 4, a twin-head electrospray (THES) nanoparticle disperser from TSE Systems Inc. for animal inhalation exposure studies has been studied. Different from the cone-jet electrospray method used in the majority of literature, we oeprated it at the multi-jet mode. The performance of the THES disperser was evaluated with respect to its mass

throughput and quality of size distribution of aerosol produced. Three different nanomaterials (TiO2, ZnO and NiO) were used in this study. The distance between two opposite spray capillary tips, the primary carrier to capillary sheath flow rates, liuqid feeding flow rate and concentration of nanomaterial suspension were investigated to find the optimal operation condition of the studied disperser. Finally, the spatial uniformity of nano-aerosol distribution in a TSE head-nose-only exposure chamber was investigated.

Part II:

Chapter 5 first introduces the electrical mobility based aerosol measurement technique. Some existing laboratory used nanoparticle sizers and portable nanoparticle sizers are summarized. The previous studies on the development of the corona chargers are overviewed. And the principle, design and development of the differential mobility analyzer are also reviewed in this chapter.

In Chapter 6, a new miniature DC-corona-based charger with a wire-to-plate design was developed for ultrafine particle charging. The charger performance is optimized under different operational conditions such as corona position (i.e. charger configuration), aerosol flowrate and corona current. Both intrinsic and extrinsic charging efficiencies are measured from monodisperse particles from 10 nm to 200 nm. A tandem-DMA technique was utilized to characterize extrinsic charge distributions of ultrafine particles with various sizes. Average charge of test particles were calculated. And a Gaussian distribution function with particle size as the only variable was proposed to predict the extrinsic charge distribution.

In Chapter 7, one miniature cost-effective mini-plate EAA, and two mini-plate DMAs had been designed. The prototypes all consist of two metal plates, installed in parallel to establish the particle classification region. To eliminate particle loss by wall effect in rectangular design, the aerosol entrance slit in length is less than the width of particle classification zone. The performance of prototypes had been experimentally calibrated using tandem DMA technique. The real transfer functions of prototypes at different particles sizes and under various conditions of aerosol and sheath flowrates were derived from the TDMA data. Based on the experimental data collected we proposed a modified equation for mini-plate DMAs to better calculate the voltage required to size particles with a given electrical mobility.

In Chapter 8, a mini Faraday cage electrometer as particle detector was calibrated and a prototype mini e-UPS was assembled, involving mini-plate charger, mini-plate DMA, mini Faraday cage, some control unit and circuit board. A user friendly software was developed based on Visual Basic programming to operate the entire system for ultrafine particle measurement. Also, a simple data inversion scheme was developed to recover the true particle size distribution from the raw data collected through electrometer. Laboratory generated NaCl aerosols were used to test the performance of the prototype mini e-UPS, compared to that of SMPS.

In Chapter 9, the accomplishments of this dissertation are summarized, and the issues and challenges that deserve future research efforts are addressed.

CHAPTER 2 Review of Ultrafine Particle Generation via Electrospray

2.1 Introduction

Electrospray or electrodydrodynamic atomization is a technique capable of converting liquids/solutions in the bulk phase into droplet phase with the droplet sizes ranging from nanometers to micrometers (Zeleny, 1914; Chen et al., 1995; Loscertales et al., 2002; Jaworek 2007; Morozov and Vsevolodov, 2007; Lee et al., 2011). The electrospray process had been applied to the surface coating (Hines, 1966; Paul, 1985; van Zomeren et al, 1994; Matsumoto et al., 2005; Fukuda et al., 2011), agricultural treatments (Coffee, 1964), emulsion (Nawab and Mason, 1958; Marín, et al., 2007; Lin et al., 2010) or super-micron aerosol production, fuel spraying (Jones and Thong, 1971; Deng et al., 2007; Yuliati et al., 2012), micro-encapsulation (Langer and Yamate, 1969; Xie et al., 2008), ink-jet printers (Tomita et al, 1986), and colloid micro-thrusters (Huberman et al, 1968; Si et al., 2007). More recently, new applications have been explored. Examples are (1) using the electrospray as ion sources for mass spectrometry (ES MS) for the macromolecular detection (Yamashita and Fenn, 1984; Thompson et al, 1985; Fenn et al., 1989; Cole, 1997; Smith et al., 1997; Dulcks and Juraschek, 1999; Loo, 2000; Hautreux et al., 2004; Sterling et al., 2010), (2) monodisperse nanoparticle generation (Chen et al, 1995; Suh et al., 2005; Kim et al., 2010), (3) biomolecule detection using gas-phase electrophoretic mobility molecular

analyzer (GEMMA) (Kaufman et al, 1996; Kaufman, 1998; Koropchak et al., 1999; Scalf et al., 1999; Bacher et al. 2001; Allmaier et al., 2008), (4) enhancement of droplet mixing by inter-electrospray (Dunn and Snarski, 1991; Snarski and Dunn, 1991; Dunn et al, 1994), (5) targeted drug delivery by inhalation (Tang and Gomez, 1994; Ijsebaert et al., 2001), (6) micro-mixing for drug power production (Borra et al, 1999), (7) ceramic nanoparticle preparation by electrospray pyrolysis (Lenggoro et al., 2000; Oh and Kim, 2007), (8) preparation of nano-structured ceramic thin films (Chen et al, 1999; Hosseinmardi et al., 2012), (9) electrospray gene transfection (Chen et al., 2000; Zeles-Hahn et al., 2011), and (10) dual-jet electrospray for the nano-encapsulation and enhancement of targeted lung delivery of nano-medicines (Chen and Pui, 2000). The general reviews of the electrostatic atomization processes and applications are covered in the books written by D. Michelson (1990) and by A. G. Bailey (1988) and paper of Oleg. V. Salata (2005). More advanced discussion on the spray modes in the process are presented in the works of Cloupeau and Prunet-Foch (1989, 1990, 1994), and Jaworek and Krupa (1999). Among all the operational modes, the cone-jet electrospray has been widely studied because of its production of monodisperse particles.

2.2 Review of Electrospray and Charge Reduction Scheme

A typical electrospray setup is in the point-to-plate configuration, i.e., a spray nozzle (i.e., single-, dual- or tri- capillary) facing a plate (with/without an orifice at the center). To operate the ES, a DC electrical field is established between the spray nozzle and the plate. Spray liquid is fed into the nozzle either by syringe pump or gravity force. Cone-jet meniscus

is then formed once the surface tension of liquid at the nozzle exit is balanced with the applied electrical force. The breakup of the liquid jet produces droplets.

Due to the operational principle of electrospray, generated particles carry high electrical charges in the same polarity as that of the voltage applied to the spray head. The columbic repulsion among generated particles thus prevents them from agglomeration. The degree of particle agglomeration could also be controlled by varying the liquid feeding rate of particle suspension, to simulate the realistic particle condition for exposure studies. Recently, Kim et al. (2010) proposed a nanoparticle dispersion system using the single capillary electrospray technique to deliver individual nanoparticles (PSL particles, TiO2, Au, Mn, quantum dots and carbon nanotubes) with controllable concentration for both in vitro and in vivo studies. His measurement evidenced that the system worked well for producing a stable nanoparticle size distribution. The charge level on electrosprayed particles depends on the particle size and the charge distribution is usually broader than the associated particle size distribution (de Juan and Fernández de la Mora 1997). The point-to-plate setup of ES systems makes it easy to place particles on surfaces since the collection surfaces can serve as one of the ES electrodes. For other aerosol applications which require keeping particles gas-borne, the reduction of electrical charges on electrosprayed particles is necessary in order to further transport them by carrier gas flow (because of particle loss by electrostatic and space charge effects).

Several charge reduction techniques have been applied to lower the charge level of ES-generated particles. They include the use of radioactive sources, corona discharge, and

UV/soft X-ray irradiation (Chen et al. 1995; Ebeling et al. 2000; Hontanon and Kruis 2008; Modesto-Lopez et al. 2011). Ions in both polarities (bipolar ions) are created in all the above-listed cases. Highly charged particles are mixed with bipolar ions in the cases, reducing their carried charges by the diffusion charging mechanism. Radiation sources such as $^{210}Po/^{241}Am$ of alpha sources have been effectively applied to produce bipolar ions. Unfortunately, the increasingly rigorous regulations in the use of radioactive material make it difficult for the future use of such sources. Even, in many countries, purchase or use of radioactive material is either under rigorous control or impossible. Corona discharge has been utilized as an alternative for bipolar ion generation. The complication in using such a technique involves the need of using high voltage power supplies with two polarities, the balance of ion concentration in both polarities (i.e., requiring the careful monitoring) and the potential of ozone production (i.e., undesirable due to its adverse heath effect). The effort in searching for alternative techniques to produce bipolar ions with symmetrical ion number concentration is thus continuous in the research community.

The modern advance in the development of UV and soft X-ray radiation sources has made them easily accessible to researchers. Photoionization by either a UV light or soft X-ray source thus provides other alternatives for bipolar ion generation. With the higher intensity than UV light and lower intensity than a hard X-ray, the soft X-ray photoionizer has been proposed as a particle neutralizer or particle charger in literatures (Kulkarni et al., 2002; Shimada et al., 2002; Han et al., 2003; Lee et al., 2005; Jiang et al., 2007a; Kim et al., 2011). When a particle-laden stream is irradiated by a soft X-ray, direct photoionization of

gas molecules and particles takes place at the same time (Shimada et al. 2002; Kulkarni et al. 2002; Jiang et al. 2007a, b), resulting in generating bipolar ions and effectively reducing the charges on particles. Compared with radioactive sources with a short lifetime (such as ^{210}Po) by which the concentration of bipolar ions produced decreases as they age, a soft X-ray source performs with a stable ion production rate during its entire lifetime and generates bipolar ions with nearly the same electrical mobility (Liu et al. 1986; Lee et al. 2005). More, commercialized soft X-ray sources can be easily purchased without any user license when compared with the order of radiation sources. Soft X-ray sources are also easily operated when compared with the requirement to operate the corona discharge. The compact sizes of these soft X-ray sources make them portable, easy for the safety protection and convenient to be included in various applications where the charge reduction is essential. Note that the irradiation intensity of soft X-ray can be readily varied by changing its distance from the irradiation zone or partially blocking of its light. Soft X-ray sources are thus considered in many recent studies as a good alternative candidate for particle charge reduction (in place of radiation sources).

Although photoionization with a soft X-ray has been applied to minimize electrical charges on particles (Shimada et al. 2002; Han et al. 2003; Lee et al. 2005; Modesto-Lopez et al. 2011), the particle generation and charge reduction in previous studies occurred in completely separate units/devices. Because of the presence of DC field in the electrospray process, significant particle loss is expected to occur in the electrospray unit if charges on generated particles were not reduced immediately. No previous attempt has been devoted to

investigate the performance of electrospray aerosol generator integrating the electrospray and soft X-ray irradiation in close proximity, even the electrospray under soft X-ray irradiation.

2.3 Particle Generation for Animal Exposure Study

An animal exposure system with an appropriate aerosol generator or disperser is thus needed for *in-vivo* investigations of the inhalation toxicity of nanoparticles. In principle, the aerosol generator or disperser for such applications shall provide airborne particles in (1) a steady mass concentration (at the desired level to perform the experiments); (2) controllable and stable size distribution; (3) homogeneous chemical composition without contaminants; and (4) reduced agglomeration (Yi et al., 2013). Recent inhalation/exposure studies however show that commonly-used particle dispersers, such as fluidized bed aerosol generators, nebulizers/atomizers, Wright dust feeders, turntable dispersers and Venture aspirators, cannot satisfy all the above requirements, especially particle agglomeration issue when dispersing nanopowders in air (William et al., 2009; Yi et al., 2013; Wong 2007).

With the advantages in generating monodisperse aerosol, electrospray technique has been applied into inhalation/exposure studied. An idea of using electrospray for target drug inhalation was first recognized by Tang and Gomez (1994). Battelle Memorial Institute developed a portable electrospray inhaler (Zimlich et al. 1999). A phase I clinical trial and in vitro studies showed that the dose efficiency was much higher than commercial inhalers (Gomez, 2002). Recently, Kim et al. (2010) proposed a nanoparticle dispersion system using the single capillary electrospray technique to deliver individual nanoparticles (PSL particles,

TiO_2, Au, Mn, quantum dots and carbon nanotubes) with controllable concentration for both *in vitro* and *in vivo* studies. His measurement evidenced that the system worked well for producing a stable nanoparticle size distribution. The degree of particle agglomeration could also be controlled by varying the liquid feeding rate of particle suspension, to simulate the realistic particle condition for exposure studies. In his study, the ^{210}Po radiation sources were used to generate bipolar ions for reducing the charge level on electrosprayed particles. Notice that the removal of all the charges on electrosprayed is not desirable.

As reviewed before, radioactive materials, corona discharge and UV irradiation are not very good charge reduction schemes for electrospray, especially for ES used in *in-vivo* studies. Because of producing relatively low concentrations of ions, soft X-ray sources are not good candidates for the charge reduction application when nanoparticles in high concentration are produced. Twin-head electrospray (THES) could be an alternative solution to overcome the aforementioned issues and limitation for charge reduction of electrosprayed particles.

Two spray heads are used in a twin-head electrospray system: one spray head producing positively charged droplets and the other producing negatively charged ones. Unique advantages can thus be gained by generating and mixing particles/droplets in both polarities. For examples, (1) the overall particle concentration can be increased by operating two spray heads instead of one, as used in a typical electrospray system; (2) the size distribution of droplets generated by electrospray is relatively narrow as compared to those produced by other mechanical spray techniques; (3) the size of generated particles can be

controlled by varying operational parameters (e.g., liquid feeding flow rate and concentration of spray solutions/particle suspensions); and (4) the charge levels on freshly generated particles can be significantly reduced by mixing particles of both polarities. Two spray heads could be aligned to face against each other or form an angle (e.g., 90° THES system) (Fu et al., 2012). The study of twin-head electrospray was first used in 1965 to generate counter-charged droplets with the diameter of about 180 μm (Schneider et al., 1965). Then the technique was further applied in powder production, in which super-micrometer sized droplets are favorable (Borra et al., 1999; Camelot et al., 1999). Morozov and Vsevolodov (2007) also applied the twin-head electrospray to the formation of nanomats. Fu et al. (2012) further investigated the performance of a twin head ES system for the generation of nanoparticles.

CHAPTER 3 Design and Evaluation of a Prototype ES Aerosol Generator with Photoionizer as charge reduction scheme

3.1 Introduction

In this study, a single-capillary ES aerosol generator having a soft X-ray charge reduction chamber in close proximity was designed and its performance was systematically investigated. To identify the best direction for X-ray irradiation, two positions were selected to install the source (one directly facing the ES capillary and the other irradiating particle stream at a 90^{o} angle). Two orifice plates with different orifice sizes of 0.25″and 1.25″ diameters (for separating the spray and charge reduction chambers) were also tested. The performance of the prototype in four configurations was thus investigated in this study. The final objective of this study is to optimize the performance of studied generator by varying its setup and operating conditions at the cone-jet mode for achieving high particle transmission efficiency and to characterize the final charge fractions for particles exiting the prototype. Further, the spray current as a function of applied voltage was characterized in both air and CO_2 environments to study the effect of X-ray irradiation on the ES operation.

3.2 Design of Prototype ES Aerosol Generator

A schematic diagram of the designed electrospray aerosol generator integrating a soft X-ray photoionizer in close proximity is shown in Figure 3.1. The generator consists of both

electrospray and charge reduction chambers, partitioned by an orifice disk plate. A typical configuration of point-to-plate was applied in the design of the electrospray chamber. A single capillary with the inner diameter (ID) of 0.008″ and outer diameter (OD) of 0.03125″ was used as the spray nozzle in the chamber. Positive high voltage was applied on the capillary and the orifice plate was electrically grounded. The distance between the capillary tip and the grounded orifice plate was kept at 0.25″. The cylindrical spray tube made of plexiglass serves as the electrical insulation between the capillary and orifice plate. A perforated Teflon disk was installed near the top of the spray chamber (between carrier gas flow inlet and orifice plate) to set up uniform flow for both sheathing the capillary tip and carrying droplets generated into the charge reduction chamber. Disk plates with the orifices of 0.25″ and 1.25″ in diameters (both having the same thickness of 0.125″) were tested in this work.

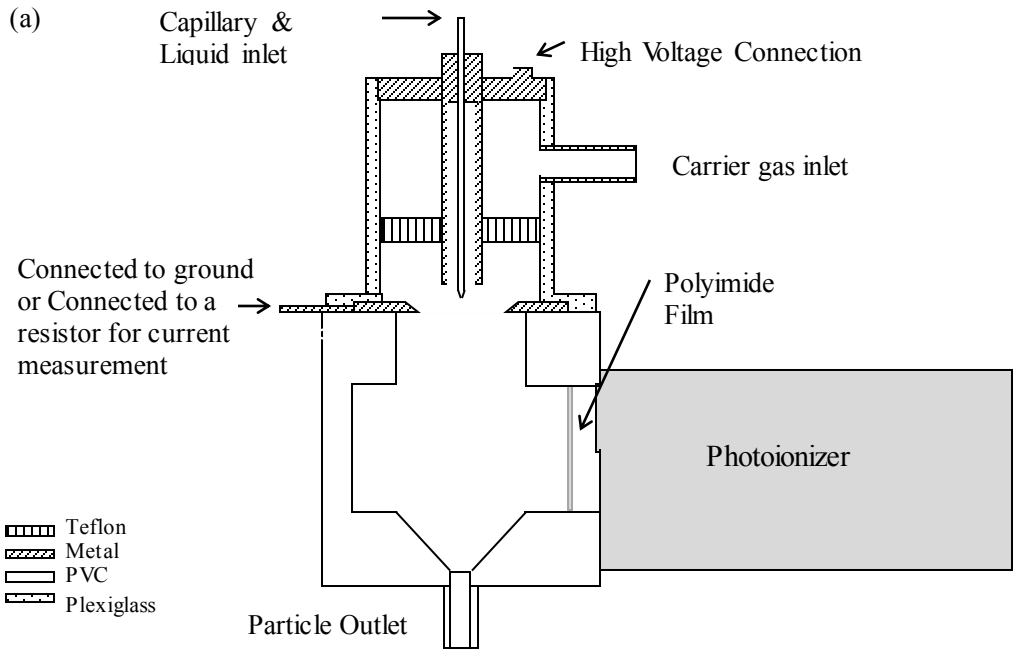
(a)
Capillary &
Liquid inlet
High Voltage Connection
Carrier gas inlet
Connected to ground
or Connected to a
resistor for current
measurement
Polyimide
Film
Photoionizer
Teflon
Metal
PVC
Plexiglass
Particle Outlet

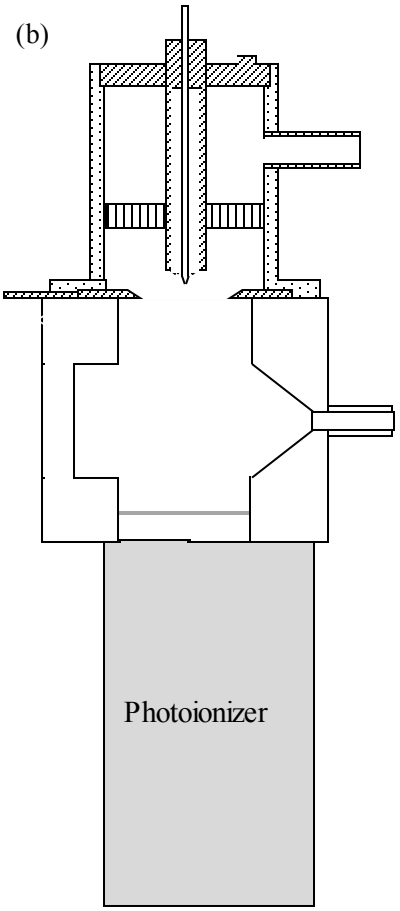

Figure 3.1: Design of the single capillary electrospray incorporated with a photoionizer installed at 90 °apart (a) and 180 °apart (b).

The charge reduction chamber was made in a cubic PVC block with the 2.5″ side, formed by the vertical crossing of two straight cylindrical channels of 1.25″ D. As shown in Figure 3.1(a), the top opening is for the entrance of sprayed particles. The bottom opening was for particle exit. One of side openings was used as a soft X-ray irradiation window while the other side opening was blocked by a PVC cap with the wall thickness of more than 0.5 cm. For the safety operation of X-ray, the photoionizer (Hamamatsu L9490 photo-ionizer,

Hamamatsu Photonics Corporation, Japan) was housed by a customer-made PVC case. The soft X-rays emitted by this photoionizer has the light ranging in wavelength from 0.13 to 0.41 nm (equivalent to the energy of 9.5 to 3 keV). In the above arrangement, particle stream was irradiated by the soft X-ray at 90°. We thus named this installation as "90° X-ray" for the future reference. Alternatively, as shown in Figure 3.1(b), the photoionizer (Hamamatsu L9490 photo-ionizer, Hamamatsu Photonics Corporation, Japan) was installed in the charge reduction chamber to face the electrospray tip. In this setup, one of the side openings was used for the particle outlet (while the other side opening was blocked). The above installation enables the particle stream to be irradiated by the soft X-ray in an opposite direction. It is labeled as "180° X-ray" for the later reference. A polyimide film (Kapton® Type HN, DuPont ™, 0.0003″ thickness) was used as the soft X-ray window between the charge reduction zone and ionizer. Note that the polyimide film was estimated to have the 90% transmission efficiency for soft X-ray (Kulkarni et al. 2002).

3.3 Experimental Setup and Characterization Method

3.3.1 Experimental Setup

Figure 3.2 is a schematic diagram of the experimental setup for the characterization of particles exiting the prototype. The aerosol generator in four configurations labeled as "90° X-ray & 0.25″D orifice", "90° X-ray & 1.25″D orifice", "180° X-ray & 0.25″D orifice" and "180° X-ray & 1.25″D orifice" were tested.

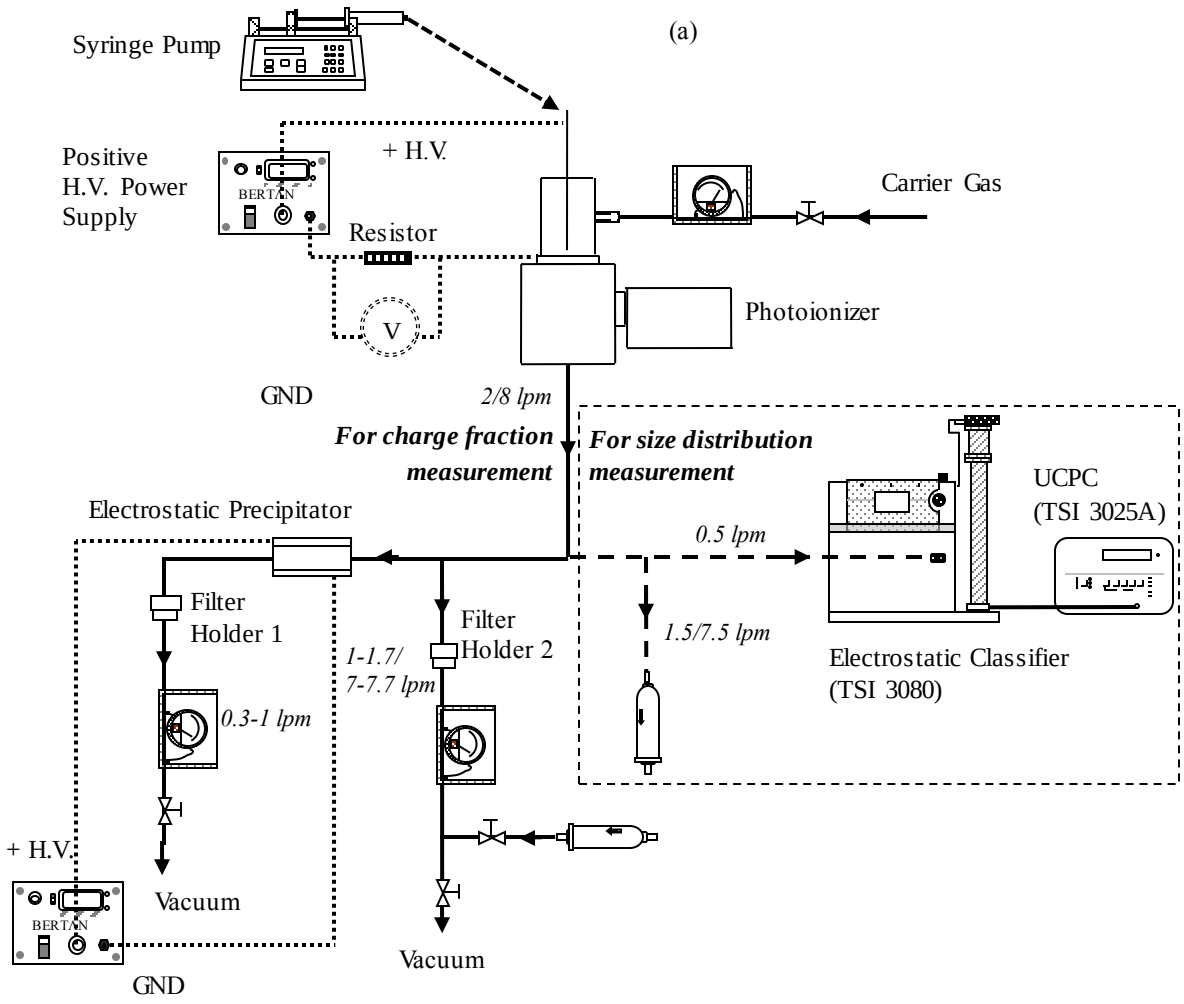
(a)
Syringe Pump
Positive
H.V. Power
Supply
+ H.V.
BERTAN
Resistor
V
Carrier Gas
Photoionizer
GND
2/8 lpm
For charge fraction
measurement
For size distribution
measurement
Electrostatic Precipitator
0.5 lpm
UCPC
(TSI 3025A)
Filter
Holder 1
Filter
Holder 2
1-1.7/
7-7.7 lpm
1.5/7.5 lpm
Electrostatic Classifier
(TSI 3080)
0.3-1 lpm
+ H.V.
Vacuum
BERTAN
Vacuum
GND

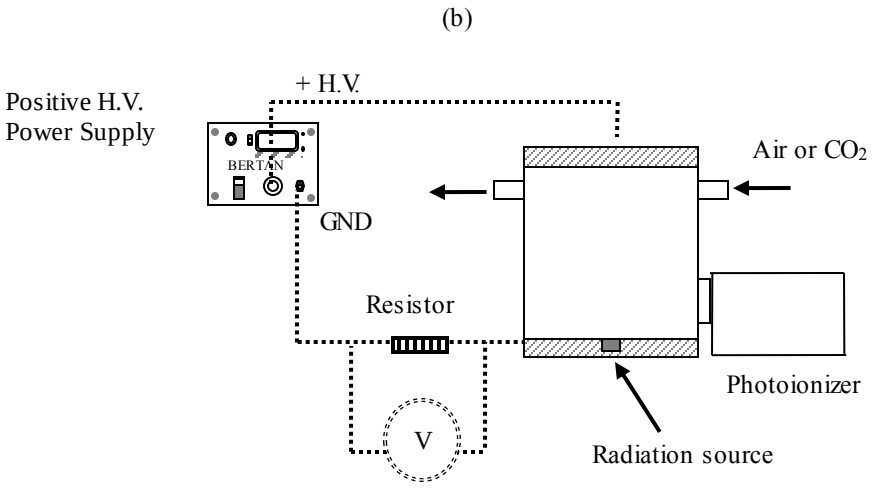

Figure 3.2: A schematic diagram of the experimental setup for system performance evaluation.

Spray solution was fed into the ES capillary at a controllable feeding rate by a syringe pump (Model PHD 2000, Harvard Apparatus, Holliston, MA). A positive voltage was applied on the capillary by a DC high voltage power supply (Bertan Series 230, Spellman High Voltage Electronics Corporation, Valhalla, NY). To characterize the operational modes observed in the ES process, the spray current as a function of applied voltage was recorded when step-ramping the ES voltage up and down. For the performance characterization, the prototype was operated at the cone-jet mode to produce monodisperse droplets. Either clean air or CO_2 was used in the generator as particle carrier flow. The volumetric flow rate of carrier gas was controlled by a needle valve and laminar flow meter. Two carry gas flow rates (i.e., 2.0 and 8.0 lpm) were chosen for testing, resulted in the estimated particle residence times of 1.28 s and 0.32 s in the charge reduction chamber.

To measure the size distribution of particles exiting the system, a scanning mobility particle sizer (SMPS) (TSI 3080 Electrostatic classifier, TSI 3025 UCPC, TSI, Shoreview, MN) was used in the downstream of the generation system and take a part of aerosol flow for detection (0.5 lpm). The rest of flow **(**1.5 lpm, 7.5 lpm**)** would exhaust through a HEPA filter. To measure the charge fraction of particles exiting the studied prototype, an electrostatic precipitator in the plate-to-plate configuration was used to collect positively and negatively charged particles (Fu et al. 2012). A separate high voltage power supply was utilized to operate the precipitator. When particle stream enters the precipitator, the charged fraction of particles would be deposited on either the top or bottom plate (depending on the polarity of charges on particles) when the high voltage is turn on. The precipitator voltage was set to establish an electrical field strong enough to collect singly charged particles of 300 nm at the designed gas flow rate of 1.0 lpm. A filter holder with a HEPA filter medium (Filter #1; Whatman 934-AHTM, 47 mm φ, GE Healthcare Bio-Sciences Corporation, Psicataway, NJ) was used at the downstream of the precipitator to collect all neutral particles exiting the precipitator. The aerosol flow rate passing the precipitator was again controlled by a needle valve and laminar flow meter at the precipitator downstream (0.3-1.0 lpm). The remaining aerosol flow (1.0-1.7 lpm at sheath flow rate of 2.0 lpm; 7.0 – 7.7 lpm at sheath flow rate of 8.0 lpm) was directed to the other filter holder having HEPA filter medium (Filter #2) for collecting the particles in the remaining stream. Two needle valves, a laminar flow meter and a HEPA filter were used after Filter #2 to ensure the flow balance in the experimental setups. Fluorescent salt particles of various sizes were generated in the

prototype generator in this part of the experiment for the measurement of transmission efficiency and final charge fractions for ES-generated particles.

3.3.2 Characterization Method

As mentioned above, positive high voltage was applied on the spray capillary via a power supply and sprayed current was measured by passing it through a resistor and measuring the resistor voltage via a sensitive electrometer (Keithley 2100 Multimeter, Keithley Instruments Inc. Cleveland, OH). For recording the spray current as a function of applied voltage, a simple Visual Basic program was coded to step the applied voltage (in either the increasing or decreasing ramping), record the resistor voltage (consequently deriving the spray current) and then plot the I-V curves. The spray solutions used in the spray current measurement were isopropanol (IPA) and water/IPA mixture. The electrical conductivity of spray solutions was controlled by adding a trace amount of nitric acid in the solutions. For this part of the experiment, the electrical conductivity of spray solutions was kept at 300 μS/cm. Both air and CO_2 gas were tested in order to explore the effect of carrier gas on the ES operation.

A fluorescence analysis method was used to quantify the mass throughput of the prototype and to characterize the fractions of charged and neutral particles exiting the prototype. Uranine was chosen as the fluorescent labeler for the quantitative analysis of collected particles (Fu, 2011). In this part of the experiment, electrospray solutions were prepared by dissolving 1.0 g/L uranine in sucrose/IPA/water mixture with the sucrose

volumetric concentration of 0%, 0.1%, 0.2%, 1.1 %, and 2.5% (for generating monodisperse particles of sizes at 30, 53, 109, 200 and 300nm, respectively). Each experimental run was performed for 6 hrs. After each run, cotton swabs wetted in aqueous solution of 0.001N ammonium hydroxide were used to recover the fluorescent particles deposited at various surfaces of the prototype. Recovered uranine on each wiped cotton swab was then dissolved in a wash solution of 25ml for two hrs. Particles deposited in the tubings in the downstream of prototype generator were also recovered via the above wiping method. The mass of fluorescent particles deposited in these places was then taken into the calculation of particle transmission efficiency and charge fraction. The filter media in the filter holders (collecting fluorescent particles) were separately immersed in different beakers having the same wash solutions of 25 ml for quantifying the mass of particles collected. The concentrations of uranine in all wash solutions were measured by a calibrated fluorometer (GloMax®-Multi Jr Single Tube Multimode Reader, Promega Corporation, CA). Note that, for each experimental case, an identical syringe having the spray solution the same as that in the run was installed on the syringe pump to inject the solution (at the same feeding flow rate as that in the case) into the wash solution of 25 ml. The uranine amount in the wash solution was characterized. The mass conservation can be checked by comparing the uranine data obtained above and the total amount of uranine recovered. In general, the recovered uranine from various surfaces of the prototype, downstream tubing and filters was within 95% of uranine amount injected.

The charge fractions of positive, negative and neutral particles ($\eta_{positive}$, $\eta_{negative}$ and $\eta_{neutral}$,

respectively) were calculated by Eq. (3-1):

$$\eta_i = \frac{m_i}{m_{positive} + m_{negative} + m_{neutral}} \quad (3\text{-}1)$$

where i indicates either positive, negative or neutral charge fractions of coagulated particles. The particle transmission efficiency of prototype was also calculated in the similar manner:

$$\eta_{transmission} = \frac{m_{positive} + m_{negative} + m_{neutral} + m_{filter2}}{m_{ground} + m_{chamber} + m_{filter2} + m_{positive} + m_{negative} + m_{neutral}} \quad (3\text{-}2)$$

Table 3.1 summarizes the solutions (solutes and solvents) and sheath gas used in each part of this experimental study. The electrical conductivities of spray solutions were also listed in the same table as the reference.

Table 3.1: Summary of solutions (solutes, solvents and electrical conductivities) and sheath gas used in each experiments.

		I-V curve Experiment	**Carrier Gas Experiment**	**Particle Transmission Efficiency Experiment**				
Solute	Uranine (g/L)			1	1	1	1	1
	Sucrose (v%)		0.1%	0%	0.1%	0.2%	1.1%	2.5%
Solvent	IPA	√						
	Water		√					
	Water/IPA			1:3	1:3	1:3	1:3	1:3
Conductivity (μS/cm)		300	320	50	46	60	56	46
Carrier Gas	Air	√	Air/CO_2 mixture	√	√	√	√	√
	CO_2							

3.4 Results and Discussion

3.4.1 On Spray Current vs. Applied Voltage (i.e. I-V curve) of Electrospray

(a) Soft X-ray ON/OFF Effect

Four operational modes (i.e., dripping, pulsating, cone-jet and multi-jet modes) have been observed in a single-capillary electrospray generator when spraying polar solutions (Chen et al., 1995). In this study, the same operation modes were also found in the studied prototype. Figure 3.3 shows the typical measurement of spray current as a function of applied voltage (i.e., I-V curve) for the studied generator in two different configurations (i.e., 90° X-ray & 0.25″ D, and 180° X-ray & 1.25″ D) and with/without X-ray irradiation. The spray liquid was IPA with the electrical conductivity of 300 μS/cm, and the liquid feed flow rate was set at 1.0 μl/min. In the case of 90° X-ray & 0.25″ D orifice plate (i.e., Figure 3.3a), the measured spray currents with and without X-ray irradiation were essentially the same when step-ramping the applied voltage up and down. The presence of soft X-ray radiation apparently had no effect on the spray in the above configuration. It is possible because the X-ray irradiation did not reach the spray capillary tip. However, for the case of 180° X-ray and 1.25″ D orifice plate (shown in Figure 3.3b), the overall I-V curve shifted to the higher voltage range (by approximately 0.9 kV) as compared to that under no X-ray irradiation. The above observed voltage shift likely happened because, in the above generator configuration, highly energetic photons emitted from the soft X-ray ionizer reached into the spray chamber and produced bipolar ions around the spray capillary tip, partially neutralizing the charges on liquid meniscus and lowering the electrical field strength. Consequently, a higher positive

voltage is required to maintain the sufficient electric field for the electrospray operation. Further, the spray currents at the cone-jet mode operation in both configurations were nearly at the same level and no noticeable difference in the characteristics of the two I-V curves was observed. It is interesting to notice that the hysteresis-like phenomenon observed in the case without soft X-ray on was not altered at all under the X-ray irradiation, indicating that X-ray irradiation with the energy smaller than 9.5 keV (the max. energy of photoionizer) will not change the electrical charge balance on the liquid meniscus at the capillary tip when the cone-jet mode can be established.

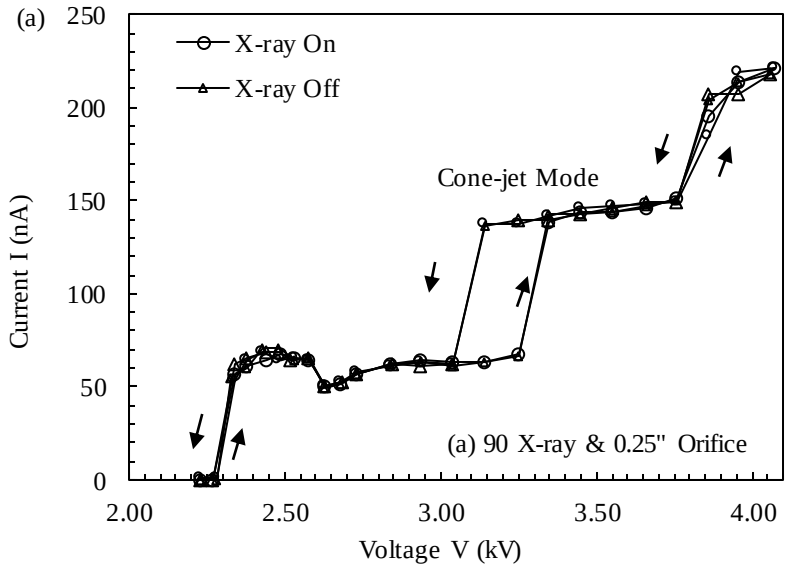

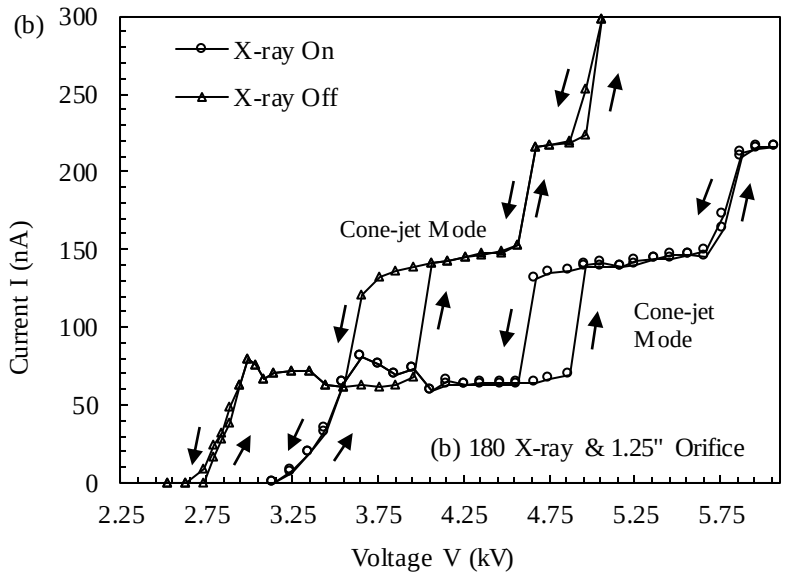

Figure 3.3: X-ray effect on the typical current vs. voltage curve within the overall operation range in air environment: (a) 90 ° X-ray and 0.25″ D orifice plate and case (b) 180° X-ray and 1.25″ D orifice plate.

(b) Effects of Generator Setup

Figure 3.4 gives four I-V curves measured under the soft X-ray ON condition for the prototype in four configurations (listed in the design section). From the leftmost curve in Figure 3.4 to the right, the I-V curves are for the cases of 90° X-ray & 0.25″ D orifice plate, 180° X-ray & 0.25″ D orifice plate, 90° X-ray & 1.25″ D orifice plate and 180° X-ray & 1.25″ D orifice plate. It is shown in Figure 3.3 that no effect on the I-V curve has been observed for the case with 90° X-ray and 0.25″ D orifice plate with/without the photoionizer turned on, thus serving as the reference in the following discussion. As shown in Figure 3.4, the I-V curves in the other three cases shifted to the higher voltage regime when compared with the reference.

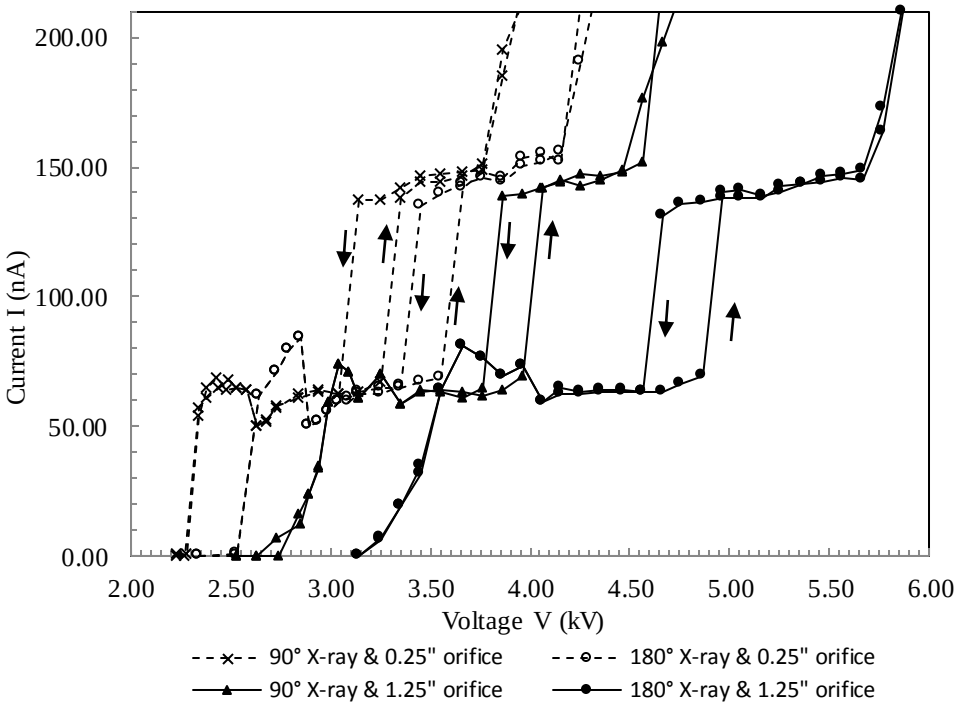

Figure 3.4: Effect of X-ray position and orifice plate on the typical current vs. voltage curve in air environment.

The effect of X-ray irradiation position on the electrospray process can be clearly identified by comparing the I-V curves for the cases having the same orifice diameter. To effectively operate the electrospray, the 180° X-ray setup needs to be operated at a voltage 0.3 kV higher than the 90° X-ray one for the cases with the 0.25″ D orifice plate. Similarly, for the cases with the 1.25″ D orifice plate, the increase of spray voltage for the 180° X-ray setup is approximately 0.9 kV higher than for the 90° X-ray setup. Further, when comparing cases with the same X-ray installation, we found that the larger the orifice opening, the larger the voltage shift. In the 90° X-ray configuration the spray voltage for the cone-jet mode operation with the 1.25″ D orifice plate is 0.7 kV larger than that with the 0.25″ D orifice

plate. Similarly, the cone-jet mode voltage shift of 1.3 kV was observed in the 180° X-ray configuration when comparing the cases with large and small orifice plates. However, the spray current at the cone-jet mode operation remained unchanged (at about 150 nA) in all four cases. The voltage shift observation can be explained by the fact that more X-ray photons can reach the spray chamber and produce more bipolar ions in the spray zone for the cases having larger orifice plate openings and more X-ray irradiation from the opposite position of the spray tip.

Finally, no measureable difference on the hysteresis-like phenomenon in measured I-V curves for these four cases were observed. The slight variation of hysteresis-like phenomenon among all four cases is in general under the variation of experimental measurement.

(c) Effect of Carrier Gas

The effect of X-ray irradiation on the I-V curve under the CO_2 gas flow was further investigated in this work. The CO_2 gas is often recommended in electrospray when spraying aqueous solutions. The configuration of the prototype generator was set at the 180° X-ray irradiation and with the 1.25″ D orifice plate. The spray solution was IPA with the electrical conductivity of 300 μS/cm. As shown in Figure 3.5, the studied system experienced the same spray modes in stepping the ES voltage up and down, and an additional 0.2 kV voltage shift to a higher voltage region was found in the CO_2 case when compared with that in the air case. Because of the lower ionization potential and higher proton affinity of CO_2 than those of air (i.e., N_2 and O_2), CO_2 molecules more easily lose electrons and become positive ions

when exposed to soft X-ray irradiation (Ito et al, 2004). In other words, more ions were generated in CO_2 gas when irradiated by the soft X-ray. Thus, even higher voltage was required to operate the electrospray. Furthermore, the hysteresis-like behavior of I-V curves (during the ramping up and down of the voltage) in the air case wasn't observed in the CO_2 case. This is probably because (1) the electrical permittivity of CO_2, serving as the insulator, has been altered under the soft X-ray irradiation; and (2) CO_2-generated ions are easier to be electrostatically separated than air ions are (Ito et al, 2004).

Because of its low surface tension, IPA can be easily electrosprayed in both air and CO_2 for the four generator setups studied above. For liquids with high surface tension, CO_2 is often used as a carrier gas in order to increase the voltage threshold for corona breakdown (Zeleny, 1915). Note that the corona breakdown usually kills the cone-jet mode operation. The capability of the prototype for spraying aqueous solution (0.1% sucrose in DI water) was thus investigated in this part of experiment. Figure 3.6 summarizes the observed cone-jet operation mode when the prototype in four configurations sprayed aqueous solutions under the carrier flow of the CO_2-air mixtures at various percentages. It was found that a weaker intensity of soft X-ray irradiation on the spray tip, achieved by changing configurations (i.e. for the case of 90° X-ray and 0.25″ D orifice plate), provided a wider workable range of CO_2-air ratio for cone-jet mode operation (i.e. $\geq$12.5% CO_2). A stable cone-jet mode was not achievable in the case of the 180° X-ray and with 1.25″ D orifice plate. In other words, the only way to effectively operate the cone-jet mode in the above case is to reduce the surface tension of aqueous solutions by doping them with additives such as IPA

or surfactants.

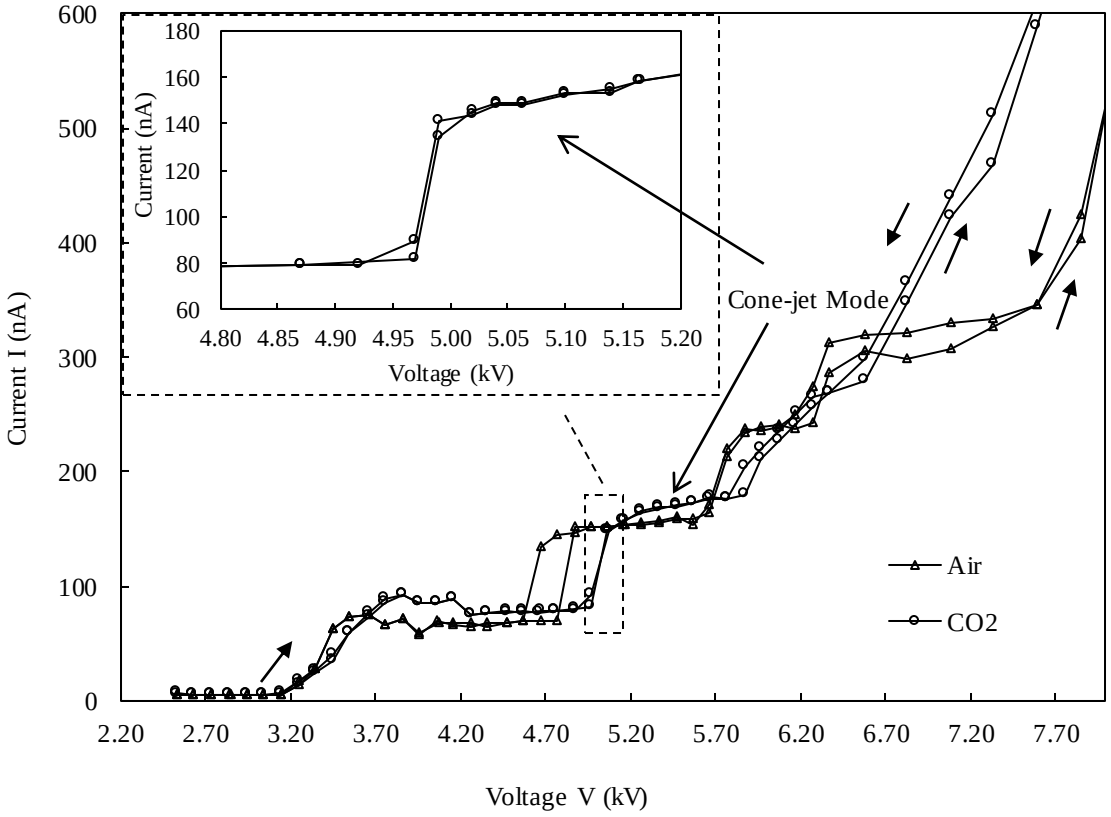

Figure 3.5: Sheath gas effect on the typical current vs. voltage curve when 1.25″ D orifice was used and photoionizer was installed 180 ° apart.

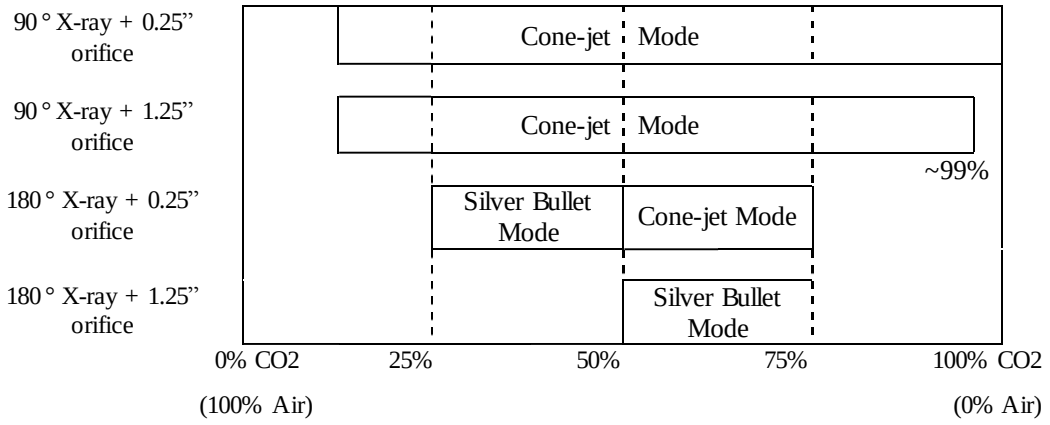

Figure 3.6: CO2 proportion range for operating electrospray for aqueous solution in 4 different configurations.

3.4.2 Monodispersity of Generated Particles

The monodispersity quality of particles generated by the prototype is further examined in this study. The sprayed solutions were 0.1% sucrose, 1g/L uranine in water/IPA(1:1) solution with 50 μs/cm electrical conductivity and 1.0% sucrose in a similar solution. SMPS was used for this measurement. Figure 3.7 shows a typical size distribution of particles produced by the prototype under the optimal setup and flow operation. The geometric mean diameter measured ware 53 nm and 109nm, respectively. And the geometrical standard deviations of measured particle size distributions shown in Figure 7 were in the range of 1.14-1.20. It is found that the monodispersity of produced particles remains in good quality when compared with those reported in the literature (Chen et al, 1995).

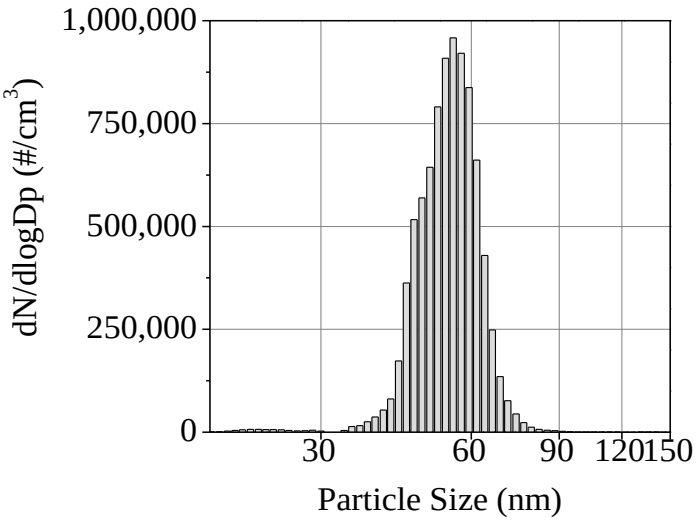

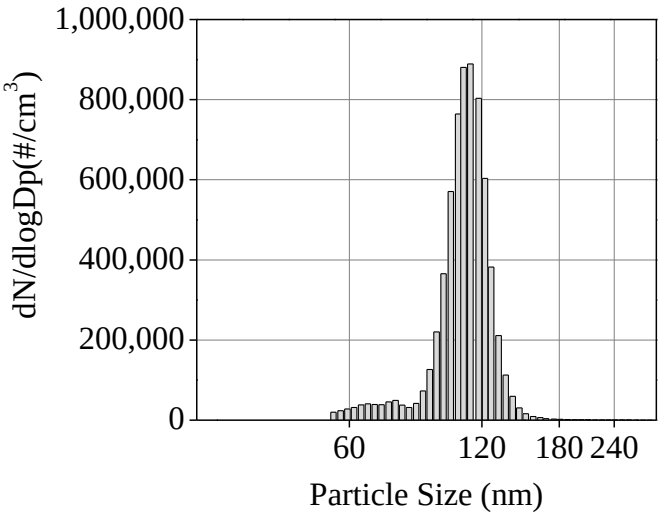

Figure 3.7: The size distributions of particles generated by the electrospray with 0.25″ D orifice plate and 180 °photoionizer.

3.4.3 Particle Transmission Efficiency at the Cone-jet Mode

In the studied electrospray generator, monodisperse particles with high electrical charges were carried to the charge reduction chamber via the carry gas flow. Because of the presence of an electrical field and columbic repulsion of charged particles in the same polarity, electrosprayed particles are easily deposited once generated. The transmission efficiency of the generator is thus a good indicator for the performance of an electrospray generator. It is expected that the transmission efficiency would be influenced by the system setup (i.e., photoionizer position & orifice size of the partition plate) and carrier gas flow rate. Thus, the effect of carrier gas flow rate and system setups on the particle transmission efficiency of the prototype was evaluated.

(a) Effect of Carrier Gas Flowrate

In this part of the experiment, two different flows of 2.0 and 8.0 lpm were used. Test uranine-tagged particles in the size of 109 nm were produced in the prototype generator. Figure 3.8 shows the particle transmission efficiencies measured when the system was set in two irradiation positions (i.e., 90° and 180° X-ray) and operated at two gas flow rates of 2.0 and 8.0 lpm. The 0.25″ D-orifice disk plate was used in both setups.

For the cases with 90 ° X-ray irradiation, the transmission efficiency of the studied aerosol generator at the carrier flow rate of 8 lpm was much higher than that at the 2 lpm flow rate (measured at 35% for the 8 lpm case and 5.78% for the 2 lpm case). A similar observation was obtained for the cases of 180° irradiation, in which approximately 46.2% of generated particles passed through the system at the flow rate of 8 lpm, while about 12.8% of particles passed through for the case of 2 lpm. For both studied setups, the disk plate with the 0.25″ D orifice was used to separate both spray and charge reduction chambers. Highly charged particles require overcoming the strong electrostatic attraction to the ground plate and the columbic repulsion force among them in order to enter the charge reduction chamber. Operating the generator at high flow rate increases the velocity of particles passing the orifice plate and reduces the residence time in the spray chamber, resulting in a better transmission efficiency.

In all the test cases, the measured percentage of particles deposited on the inner wall of the charge reduction chamber were all below 1%, indicating an effective charge reduction process at test gas flow rates, independent from the installation position of the photoionizer.

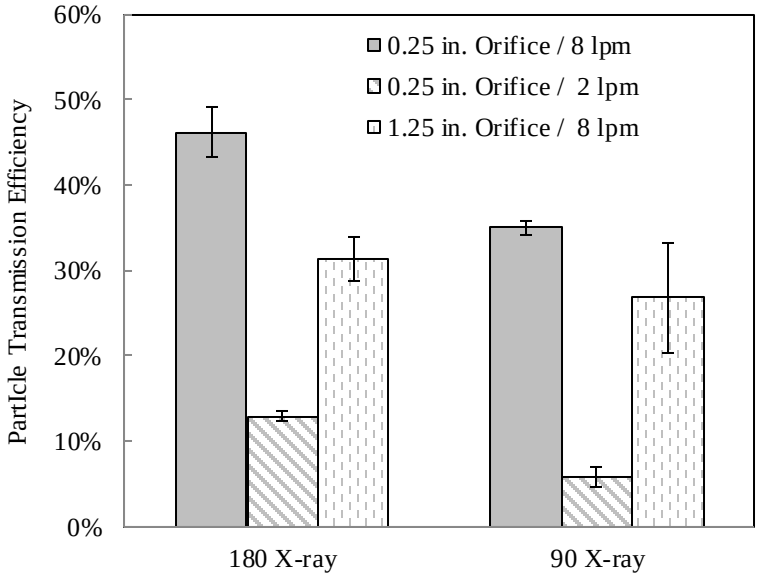

Figure 3.8: System configuration effects (sheath flow rate, X-ray position and orifice size) on transmission efficiency for 109 nm particles.

(b) Effect of System Setups

Also shown in Figure 3.8 is that measured particle transmission efficiencies in both 180 ° X-ray cases (measured at two different flow rates) are in general higher than those for two 90 ° X-ray cases. However, the efficiency improvement by increasing carrier flow in 180 ° X-ray cases is less than that in 90 ° X-ray cases. It is because the charge reduction for generated particles might easily occur in the spray chamber when the photonionizer was installed to directly irradiate it. Thus, the 180 ° X-ray installation in general has greater particle penetration than that of the 90 ° X-ray under the same carrier gas flow rate. Since electrical charges on particles could be reduced immediately after the particle production in the setup of the 180 ° X-ray, the efficiency improvement by increasing the carrier flow rate would not be greater than that in the cases of the 90 ° X-ray.

Figure 3.8 also shows the comparison of particle transmission efficiency when the generator was set up in four test configurations. In this comparison, the carrier air flow rate was kept at 8.0 lpm. Monodisperse particles in the size of 109 nm were also generated for this investigation. As evidenced in the figure, the setup with the 0.25″ D orifice plate offered the highest particle transmission efficiency (i.e., 46.2%) at the 180° irradiation. The 2nd highest transmission efficiency was obtained for the case with the 0.25″ D orifice plate at the 90° irradiation (i.e., 35%). The transmission efficiencies for the cases with the 1.25″ D orifice plate were less than those for the 0.25″ D orifice plate. In the experiments, we observed that the majority of particle loss were on the ground orifice plate in all four cases. The larger the orifice diameter the more particle loss (i.e., at the soft X-ray irradiation direction of 180°, the particle loss on the plates with orifice sizes of 1.25″ and 0.25″ D are 61.26% and 52.87%, respectively). High electric field strength used in operating electrospray thus remained as the primary force for the particle loss in this studied generator. When particles entered the charge reduction zone, their associated electrical charges were sufficiently reduced to much lower levels (as compared to that at the originally generated), enabling them to penetrate through the charge reduction zone. The above was evidenced by the more-than-99% particle penetration through the charge reduction zone in four studied configurations.

Under the similar system configuration and operational condition (i.e., 0.25″ D orifice plate, no spacer used, 8.0 lpm carrier gas flow rate for current study and 6.0 lpm carrier gas flow rate for Fu's study), the transmission efficiency of particles generated by

electrospray are 46.2% for the case with soft X-ray and 45.8% for the case with four Po^{210} radiative sources (Fu et al, 2011). It indicated that the charge reduction effect of soft X-ray is apparently comparable to four Po^{210} radiation sources. However, the above observation related to the effect of orifice opening is different from that obtained in the work of Fu et al (2011) in which the wider opening of the orifice plate improved the particle transmission efficiency (when the α-emitted radioactive sources were used). It is because (1) higher voltage is required to operate the electrospray in the cases of 180° X-ray irradiation, especially in 1.25″ D orifice plate case; (2) the particle velocity (passing through the orifice) reduction is much more than that of electrical potential gradient when using a larger orifice diameter, resulting in more particle loss in larger orifice; (3) α particles from α-emitted radioactive sources have a shorter travel distance, as compared with the long travel distance of X-ray photons in air.

(c) Transmission efficiency as a function of particle size

From the efficiency data collected above, we found that the optimal setup for the prototype is with the 0.25″ D orifice plate and 180° X-ray irradiation, operated at the carrier flow of 8.0 lpm. The transmission efficiencies of particles in various sizes were then characterized for the studied generator in the optimal configuration and operation. Prior to the transmission efficiency experiment, test particles with specific sizes were characterized by SMPS. The values of geometrical standard deviation of generated particles for each test size were in the narrow range from 1.14 to 1.20. The result of this characterization is shown in Figure 3.9, indicating the efficiency was around 45% for all of the studied particle sizes.

In general, the transmission efficiency achieved in this prototype is lower than that reported in the work of Fu et al (2011).

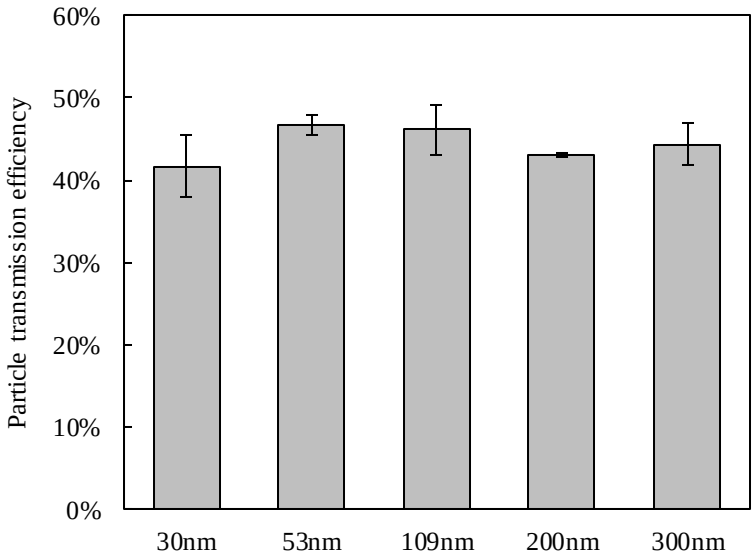

Figure 3.9: Transmission efficiency for electrosprayed particles at different sizes.

To explain the above observation, we set up a separate experiment to measure the ion concentration generated either by the soft X-ray source or fresh Po^{210} radiation source of 5 mCi (shown in Figure 3.2b). The apparatus used in this experiment is a cylindrical chamber made of PVC (~590 cm^3 inner volume) with two metal electrode plates capped the top and bottom of the chamber for the current measurement (via a Keithley 2100 multi-meter). On the side wall of the cylindrical chamber (closer to the bottom plate) an X-ray window was opened for soft X-ray irradiation. The radiation source was placed in the center cavity made in the bottom plate when measuring the ion concentration generated by the source. A high voltage power supply was used to establish an electric DC-field for separating bipolar ions

and driving them towards to the electrodes with the polarity in favor of ions' polarity. By measuring the saturation current (I_s) between these two electrode plates, ion concentrations in the chamber (N_{ion}) can be estimated by the following equation (Liu and Pui, 1974a):

$$N_{ion} = \sqrt{\frac{I_s}{1.6\times10^{-19}V\alpha}} \tag{3-3}$$

Where V is volume of ion detection chamber and α is the recombination coefficient of bipolar ions of 1.6×10^{-12} m^{-3}. The experimental result shows that bipolar ion concentration generated by a soft X-ray source was approximately 8.5×10^{12} ions/m^3, only 40% of that by a fresh ^{210}Po radiation source of 5 mCi. The less ion concentration generated by the soft X-ray could explain why the transmission efficiency of the studied prototype is generally lower than that in Fu's work (2011) using four ^{210}Po radioactive sources (7.1×10^{14} ions/ m^3) in maximum.

3.4.4 Charge Fraction Measurement on Generated Particles

It is known that particles generated from ES systems are highly charged. To keep particles airborne, the charge level on ES-generated particles should be reduced in order to minimize their transport loss due to the electrostatic and space charge effects. Soft X-ray photoionization was applied in this study for charge reduction. During the charge reduction, charged particles were exposed to the soft X-ray radiation. The mechanism for aerosol charging in soft X-ray radiation has been discussed in Jiang et al.'s work (2007a, b). Three main charging mechanisms are involved: photoemission effect of carrier gas molecules, photoemission effect of aerosol and diffusion charging effect by bipolar ions. However, none

of the previous studies on soft X-ray neutralization characterized the final charge status of ES-generated particles. The fractions of positively and negatively charged and neutral particles exiting from the studied ES prototype were thus measured in this part of the study to investigate the charge status of particles exiting the prototype.

The fluorescence analysis using uranine-labeled sucrose particles was applied to quantify the charge fractions of particles. Particles exiting the prototype ES generator were directed to a plate-to-plate precipitator operated at a high voltage of 12 kV to ensure that all of the charged particles up to 300 nm were collected in the device (Fu et al. 2011). The precipitator was operated at 1.0 lpm. The remaining flow was passed through a HEPA filter. In the precipitator, positively and negatively charged particles were deposited on the plates having the opposite polarity than that of charges on particles. Neutral particles were then collected by a different HEPA filter at the precipitator downstream.

Figure 3.10 shows the measured charge fractions of monodisperse particles in the sizes of 30, 53, 100, 200 and 300 nm. Also included in the figure are the fraction data calculated based on Fuchs bipolar charge distributions at the associated sizes (Fuchs, 1963 and Wiedensohler, 1988). The prototype was configured to have a 0.25″ D orifice plate and 180 ° radiation and operate at 8 lpm carrier flow. It is evidenced from the figure that the smaller the particle size, the closer its net charge to zero. For the sizes larger than 110 nm, positively charged particles become dominant, resulting in net positive charges (the same charge polarity for droplets freshly produced by electrospray). It is known that the larger the particle size generated by ES, the more electrical charge it has (Chen et al., 1995; Suh et al.

2005). As the particle size increases, a higher bipolar ion concentration is thus needed to reduce the charge level on ES particles.

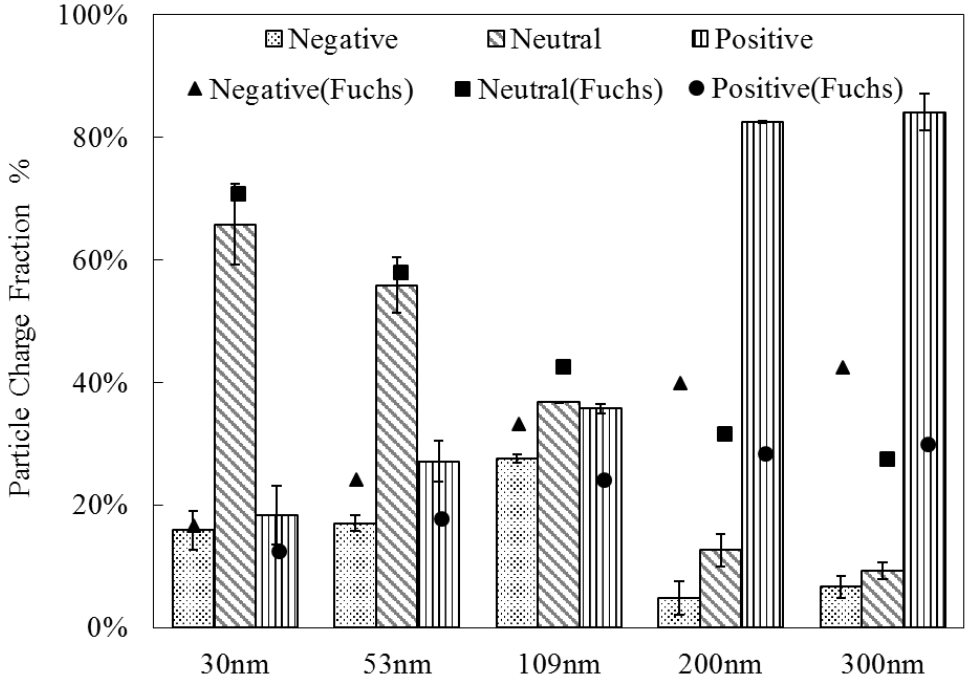

Figure 3.10: Charge Fraction for electrosprayed particles at different sizes, compared with ideal Fuchs charge distributions.

It is further observed from Figure 3.10 that the positive charge fraction of exiting particles increases as the particle size increases (i.e., from 18.3% for 30 nm particles to 84.1% for 300 nm particles). At the same time, the neutral fraction of particles decreases with the increase of particle size (i.e., from 65.8% for 30 nm particles to 9.2% for 300 nm particles). When compared with Fuchs bipolar charge distributions, excellent agreement has been obtained between the experimental and calculated data for the cases of particles with sizes smaller than 110 nm. However, for large particles (i.e., Dp > 110 nm), distinct

deviations from the Fuchs distributions were observed. Note that, in the aerosol practice, the charge levels on exiting particles however does not need to be in the bio-polar Fuchs charge distribution level.

As mentioned in previous sections, bipolar ion concentration generated from soft X-ray (8.5 × 1012 ions/m3), and the particle resident time (0.32s) were measured and calculated. So, the Nt value in the studied charge reduction zone was estimated about 2.8 × 1012 (ions/m3)(s). However, for particles smaller than 100 μm, the maximum Nt product needed for charge neutralization was found to be 6 × 1012 and 1 × 1011 (ions/m3)(s) respectively for the continuum regime and free molecular regimes (Liu and Pui, 1974a). The ineffective charge reduction for particles in the sizes larger than 110 nm, observed in this study, could be attributed to relatively insufficient bipolar ions in the charge reduction zone of the generator. Further, the non-uniformity of aerosol concentration (because of the flow 90° turning towards the outlet) and X-ray irradiation (because of a potential contamination of the polyimide X-ray window during long-time operation) in the charge reduction zone of the generator could locally result in ineffective charge reduction of particles. In addition, the large cross section area of large particles increases the collision with X-ray photons. High-energy photons absorption by particles could lead to electron emission from the particle surface, making particles more charged in positive polarity direction (Maisels et al., 2002). However, neighboring particles may become more charged in the negative polarity direction when capturing escaped electrons. It is very difficult to completely rule out the mechanism of direct photoionization of particles. Unfortunately, to quantify the percentage of observed

charge deviation attributed to the direct photo-charging is not possible because of no reported work functions of sucrose particles doped with various percentages of uranine.

3.5 Summary

A prototype single-capillary ES aerosol generator with a soft X-ray (photo-ionizer) for the charge reduction has been designed and experimentally investigated in the study. The prototype consists of two chambers: one for liquid spray and the other for charge reduction. A disk plate with an orifice at the center (having the thickness of 0.125″) was used to partition two chambers. With the prototype design, highly charged particles generated in the spray chamber were quickly carried by carrier flow through the orifice and entered the charge reduction chamber in which both the direct photo-charging and bipolar diffusion charging of particles took place at the same time. Bipolar ions were produced by photoemission of gas molecules when exposed to the soft X-ray. As a result, the charge level on ES-generated particles was reduced. To optimize the prototype performance for achieving high particle transmission efficiency, four generator configurations were tested in this study: two X-ray radiation directions (i.e., 90° and 180°), and two orifice plates (i.e., with 0.25″ and 1.25″ orifice diameters). In addition to the system setups, two carrier gases (i.e., air and CO_2) at two different flow rates (i.e., 2.0 and 8.0 lpm) were used in this investigation. To evaluate the soft X-ray's effect on electrospray operation, the spray current as a function of applied voltage was recorded.

Our study found that, by testing four configurations, the operation of a soft X-ray photoionizer does not affect the electrospray in the setup having 90 ° X-ray irradiation and

0.25″ D orifice plate, and the applied voltage needed to operate the electrospray was shifted towards the higher voltage region for the other setups. The largest shift of I-V curve was observed in the case with 180 ° X-ray irradiation and the 1.25″ D orifice plate. For the cases using CO_2 as the carrier gas flow, the similar trend of voltage shifting was also observed. The reason for the observed voltage shift is because of the X-ray exposure in the spray chamber. The higher the X-ray exposure chance in the spray chamber, the larger the ES voltage shift for ES operation. However, the spray current at the cone-jet mode operation in all of the test cases using the same spray solutions remained at the same value.

Fluorescence-labeled sucrose particles with sizes ranging from 30 to 300 nm were generated in the studied ES aerosol generator to evaluate the particle transmission efficiency of the prototype. Our study also evidenced that the particle transmission efficiency of the prototype could be improved by increasing the carrier gas flow rate. Our evaluation indicated that the highest particle transmission efficiency, 46%, was achieved for the prototype having the 180 ° X-ray irradiation and 0.25″ D orifice plate, operated at the carrier gas flow rate of 8.0 lpm (regarded as the optimal configuration and operation for the prototype). It is further shown that the transmission efficiency remained at the same level for the test particle size ranging from 50 to 300 nm.

The charge fractions (i.e., both positively and negatively charged, and neutral fractions) of particles exiting the prototype were finally characterized in this study to investigate the charge status of produced particles. Using the above measurement at various particle sizes and comparing them with the calculated Fuchs bipolar charge distribution of

test particles, it is concluded that the smaller the particles, the more effective the soft X-ray neutralization. For particles with the sizes less than 110 nm, the reasonable agreement between the measured fraction data and the calculated Fuchs data was obtained. The deviation from the Fuchs bipolar charge fraction was noted in the cases of particles with sizes larger than 110 nm. The reasons for the deviation could be attributed to (1) relatively insufficient ion concentration generated by the soft X-ray source; (2) spacial non-uniformity of ES generated aerosols and soft X-ray irradiation inside of generation chamber; (3) the potential of direct photoionization of particles under the X-ray irradiation.

CHAPTER 4 Evaluation of TSE Twin-head Electrospray Aerosol Generation System

4.1 Introduction

A twin-head electrospray system has been made available by TSE Systems Inc. to air-disperse nanopowders in reduced agglomeration form for *in vivo* nanotoxicity studies when combined with a 20-port nose-only animal exposure chamber (also available from TSE Systems Inc.). In This study, there were two objectives (1) to evaluate the performance of the twin-head electrospray system for nanopowder dispersion in regards to the output mass concentration and size distribution quality of nanoparticles for *in vivo* research, and (2) to investigate the uniformity of aerosol concentration at each port of the 20-port nose-only animal exposure chamber.

4.2 Experimental Setup and Evaluation Methods

4.2.1 THES Description and Its Performance Evaluation

The schematic diagram of experimental setup for evaluating the studied TSE Systems twin-head electrospray (THES) disperser of nanoparticles is shown in Figure 4.1. The THES case is a metal 6-way cross (i.e., formed by three straight cylindrical channels perpendicular to and intersecting with each other), thus having six openings. The top and the bottom openings are used as the inlet of primary particle-free carrier air flow and the outlet

of particle-laden flow, respectively. The volumetric flow rate of primary carrier air is variable by a needle valve and monitored by a flow meter. The front and the back openings are used as windows to illuminate the spray chamber by a light source and to observe the spray process by a microscopic lens and a CDD camera. The left- and right-hand side openings of the spray chamber are used to install two identical electrospray capillaries, aligned in the axial direction and faced against each other. The tested stainless steel capillaries have an inner diameter (ID) of 0.7 mm and an outside diameter (OD) of 1.0 mm. A sheath flow compartment is also included in the installation of each capillary to provide clean air flow sheathing the capillary. To operate the THES disperser, a positive DC high voltage was applied on one capillary and a negative voltage on the other (by the H.V. power supplies: Bertan Series 230, Spellman High Voltage Electronics Corporation, Valhalla, NY). The spray chamber was electrically grounded. The spray suspension was fed into two capillary needles by two identical syringe pumps (NE-300, New Era Pump System Inc. Farmingdale, NY). For simplicity in operation, the feeding flow rates of two capillaries were set the same. The flow rate of capillary sheath gases for two capillaries were also kept the same.

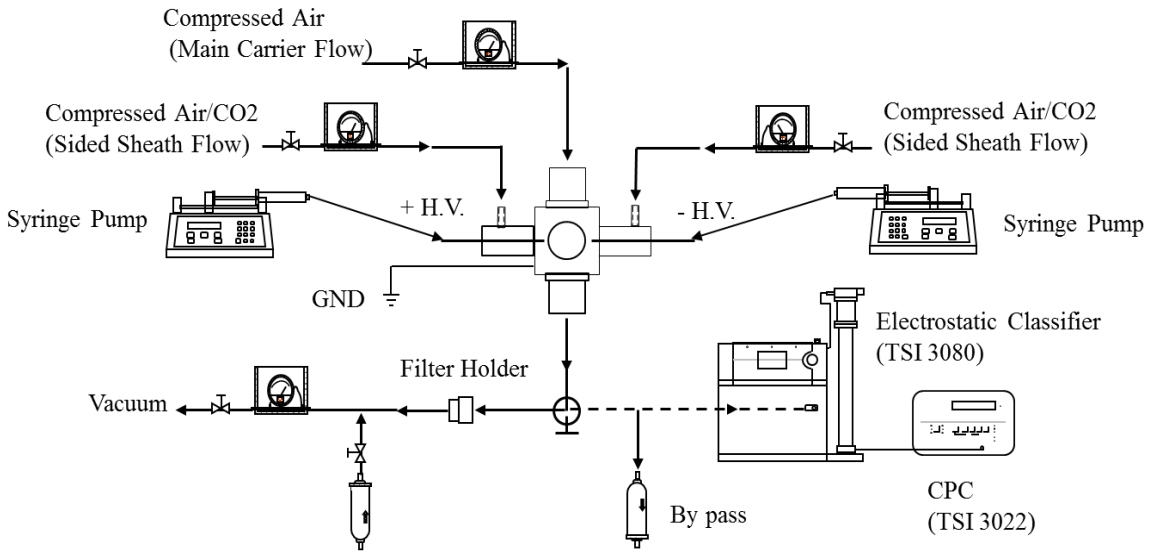

Figure 4.1: Schematic diagram of the studied twin-head electrospray disperser and its experimental setup for performance evaluation.

Distinguished from the typical cone-jet mode electrospray (applied in the majority of literature), the THES disperser operated the spray at the stable multiple-jet mode to produce a stream of particles in high aerosol concentration. The sizes of nanoparticles to be tested are pre-determined by their synthesis. There was no concern about altering the sizes of nanomaterials. The multiple-jet electrospray used in the disperser is just a means to disperse nanoparticles in air with the minimal agglomeration. Notice that the stable multi-jet electrospray described herein was operated at the mode when the maximal number of stable jets at the capillary tip was observed by a CCD camera with a microscopic lens.

To investigate the performance of the studied THES disperser, a Scanning Mobility Particle Sizer (SMPS) (including TSI 3080 electrostatic classifier and TSI 3025 UCPC, TSI incorporation, Shoreview, MN) was utilized to measure aerosol size distributions of

dispersed nanoparticles. During the operation, a camera with a microscopic lens was set up to observe and record the liquid meniscuses at the capillary tips.

To characterize the mass concentration of dispersed nanoparticles in the carrier gas stream output from the THES disperser, a stainless steel filter holder with a pre-weighted HEPA filter (Whatman 934-AH^{TM}, 47 mm φ, GE Healthcare Bio-Sciences Corporation, Psicataway, NJ) was installed at the downstream of the THES to collect all the particles in the gas stream exiting the system. The filter after collecting particles was kept in well-ventilated lab environment (usually kept at 30% RH) for more than three hours prior to its mass measurement to minimize the solvent contribution. The mass of particles collected on the HEPA filter was calculated as the filter mass difference before and after the collection. The total particle concentration in the exiting gas stream was derived as follows:

$$C\left(\frac{mg}{m^3}\right) = \frac{M_{load} - M_{clean}}{(Q_M + 2*Q_S)t} \quad (4\text{-}1)$$

where M_{clean} and M_{load} are the filter masses before and after particle collection, respectively; Q_M and Q_S are the flow rates of primary carrier and capillary sheath flows, respectively; t is the particle collection time in each run.

To achieve high mass concentration of particles in the gas stream, the following parameters were varied during the study: needle tip distance, main carrier flow rate, side sheath flow rate, liquid feeding rate and nanoparticle concentration in spray suspensions.

Three different nanomaterials, i.e., TiO_2 (99.7%, <25nm, Sigma-Aldrich Co.), ZnO (99.9+%, 20 nm, Nanostructured & Amorphous Materials Inc.) and NiO (20 nm, Nanostructured & Amorphous Materials Inc.) were chosen in this study because they are the

three most popular nanoparticles reported in toxicity studies and applications. Previous research showed that the breakage induced by nano TiO_2 and the oxidative stress under the exposure of nano TiO_2 could cause adverse effects on erythrocyte, implying a potential toxicity to human health (Li et al., 2008). Brunner et al. (2006) found that nano ZnO with the concentration above 15 ppm could kill almost all human or rodent cells. NiO was classified as a Class 1 carcinogenic material by the International Agency for Research on Cancer (IARC; IARC Monographs on the Evaluation of Carcinogenic Risk to Humans, Volume 49 Chromium, Nickel and Welding 1990; cited in Horie et al., 2012). In this study, spray liquids were prepared by dispersing nanoparticles (i.e., TiO_2, ZnO and NiO) in isopropanol (IPA)/aqueous (1:1 in v/v) mixtures at various concentrations ranging from 1.0 g/L to 10.0 g/L. A trace amount of nitric acid was added into the nanoparticle suspensions to control the electrical conductivity of spray suspensions at approximately 150 μS/cm. To keep the colloidal suspensions stable during the entire experimental run, the spray suspensions were sonicated by an ultrasonic processor (CPX 750, Cole-Parmer Instrument, IL).

4.2.2 Spatial Uniformity Evaluation for Nanoparticle Exposure Chamber

Shown in Figure 4.2 is the schematic diagram of the TSE direct-flow exposure chamber with 20 exposure ports for animal cages. The chamber essentially consists of two concentric cylinders (inner and outer ones). Upon the introduction into the inner cylinders of the chamber, test particle flow stream was radially directed into the animal cages through the port openings located on the wall of inner cylinder. After passing the nose area of each

cage, the excess particle stream was vented in the annular spacing between two cylinders for the discharge (directed-flow design). An additional port was also included in the exposure chamber to sample the test aerosol stream in the core region of the inner cylinder for the characterization when needed. The above directed-flow design ensures that each animal would breathe fresh aerosol and minimizes rebreathe of exhaled test aerosol. The studied chamber consists of two tiers with 10 animal cages per tier.

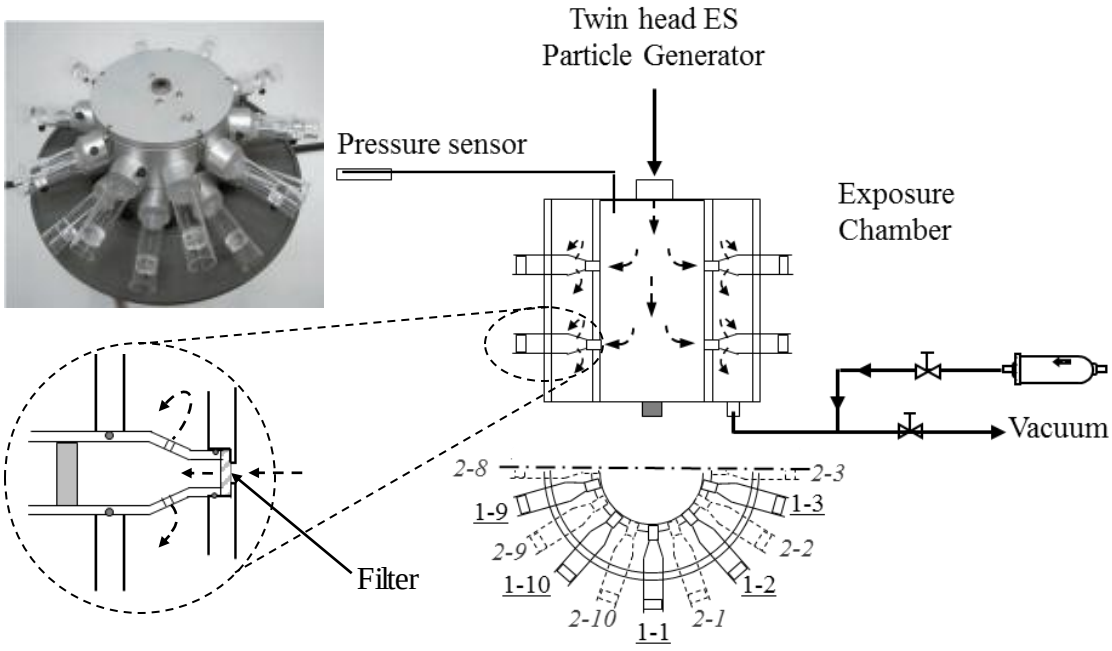

Figure 4.2: Schematic diagram of the animal inhalation exposure chamber as well as its experiment setup for performance evaluation.

The even distribution and directed-flow design of the studied animal exposure chamber has been investigated by Pauluhn (1994, 2007). However, no experiment was performed to verify the uniformity of nanoparticle distribution in each animal cage of the

exposure chamber. In this part of the experiment, the fluorescence analysis method was used to characterize the uniformity of nanoparticle mass concentration at each port of the exposure chamber. To perform the experiment, uranine was selected as the fluorescent labeler for the quantitative analysis of collected particles (Fu et al., 2011). In the experiment, electrospray solutions were prepared by dissolving 2.5 g/L uranine in IPA/water (1:1) mixture with the electrical conductivity of 200 μS/cm. Twenty animal cages were installed at the exposure ports and numbered (as shown in Figure 4.2). No animals were present in the cages. Twenty HEPA filters were separately placed at the entrance of exposure ports for collecting particles in the directed gas stream. The total particle flow rate was controlled at 10.0 lpm (i.e., capillary sheath flow of 3 lpm and primary carrier flow of 4 lpm). The temperature and relative humidity in the exposure chamber were also monitored during the experimental run. Each experimental run was conducted for 1.5 hours. The same experiment was repeated three times to get reliable data.

After each run, 20 filters were separately immersed in beakers having the same 25 ml aqueous solution of 0.001N ammonium hydroxide for two hours. The uraniune concentrations in all wash solutions were then measured by a calibrated fluorometer (GloMax®-Multi Jr Single Tube Multimode Reader, Promega Corporation, CA).

4.3 Results and Discussion

4.3.1 Effects of Operational Variables on Performance of TSE Twin-head Electrospray System

(1) Effect of capillary tip distance

The strength of electrical field in an electrospray system is the primary factor controlling the spray process. On the other hand, the particle loss because of the presence of an electrostatic field is also dependent on the field strength. It is because all the particles produced by electrospray are highly charged. The magnitude of applied voltages and the tip distance between two opposite spray capillaries are two variables for varying the field strength used in the THES disperser. In this part of the investigation, we varied the capillary tip distances of 1.5, 2.0, 3.0 and 4.0 cm. TiO_2 nanoparticle suspension was utilized as the spray liquid for all the cases. All the electrospray operations were under the stable multiple-jet mode. The total flow rate was controlled at 10 lpm with the flow rate ratio (Q_{main}: $Q_{capillary}$) of 4:3 and the feeding flow rate of particle suspensions was set at 20 μl/min. Figure 4.3 shows the measured nano TiO_2 mass concentrations in the cases of these four tip distances.

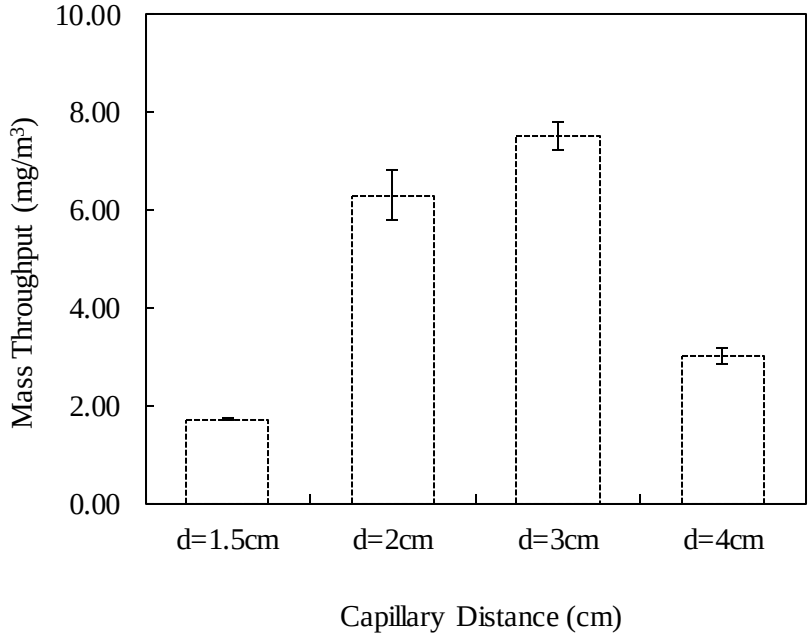

Figure 4.3: Effect of capillary tip distance on the particle mass throughput of studied disperser. (the standard deviations of measured data are included in the figure as the error bars)

It is found that the system configuration with the spray tip distance of 3.0 cm offered the highest TiO_2 mass concentration (i.e., 7.51 mg/m^3). The 2nd highest mass concentration (i.e., 6.3 mg/m^3) was observed in the case with the tip distance of 2.0 cm. The longer the tip distance, the higher the voltage required to operate the spray. The stronger field strength resulted in more particle loss. For cases with tip distances shorter than 2.0 cm, the collisions among particles of both polarities were less frequent because the spray plumes were not sufficiently fanned out. Charged particles thus tended to deposit on the capillary with the polarity opposite to that of particles. More particles were lost when the tip distance was reduced. Note that no capillary tip distance less than 1.5 cm was tested in the experiment because of the electrical arcing between two capillaries when applying high voltages on them for spraying.

(2) Effect of flow rates

The effect of primary carrier and capillary sheath flows on the mass throughput of the studied THES disperser was also investigated in this study. The parameters to be investigated include both the flowrate ratio (defined as the ratio of the primary carrier flowrate to the capillary sheath flowrate) and the total flowrate. Note that for simpilicity two capillary sheath flowrates were kept the same in this investigation. To obtain the optimal flowrate ratio, four flowrate ratio cases (i.e., $Q_{primary}$: $Q_{capillary}$ = 2:4, 4:3, 6:2 and 8:1) were studied while keeping the total flow rate at 10 lpm. The capillary distance was kept at 3.0

cm in this part of the experiment. Figure 4.4(a) shows the experimental result of this investigation. The measured data indicates the averaged nano TiO_2 mass concentration of 7.45 mg/m^3 was achieved. No noticeable difference of measured particle mass concentrations among four flowrate ratio cases was observed. However, the case with the flow rate ratio of 4:3 provided a slightly higher particle mass concentration of 7.74 mg/m^3 compared with others. It may be attributed to the relatively balanced flowrates of sheath and primary flows. The disperser was made of a metal 6-way cross (set up by perpendicularly welding three metal tubes of the same diameter). Sufficient sheath flow rates for both positive and negative spray chambers (i.e., sufficient flow velocity) were required to carry out produced droplets from their designated chambers with less particle loss. The mixing of the primary carry flow with two opposing streams is thus expected better at the flow rate close to that of sheath flow for the less particle mixing loss. The flow rate ratio of 4:3 was thus selected as the flow rate ratio setting in the part of the experiment investigating the effect of total flow rate on the mass throughput.

Figure 4.4(b) gives the measured mass concentrations of TiO_2 nanoparticles under the conditions of four different total flow rates (i.e., 5.0, 10.0, 15.0 and 20.0 lpm). The flow rate ratio was kept at 4:3 (Q_{main}: $Q_{capillary}$). It is evidenced that the highest mass concentration (i.e., 9.86 mg/m^3) was achieved under the total flow rate of 5.0 lpm. When the total flow rate was increased, the particle mass concentration at the system exit was decreased. It is because the residence time of nanoparticles in the spray system was decreased at high flow rate operation, resulting in less chance for charge reduction by collision of nanoparticles with

opposite polarities. Consequently, the charge level on particles remained high, leading to more particle loss during the transport (due to the electrostatic deposition). Further, the increase of the total flow rate resulted in the dilution of the final concentration of the particle stream exiting the THES disperser. Note that the operation of high carrier gas flow rate for the THES disperser also reduced the particle loss in the spray chamber although the particle residence time in the charge reduction chamber was reduced. It is the reason why the overall particle concentration reduction was less than 50% when the operational flow rate was increased from 5 to 10 lpm, and from 10 to 20 lpm.

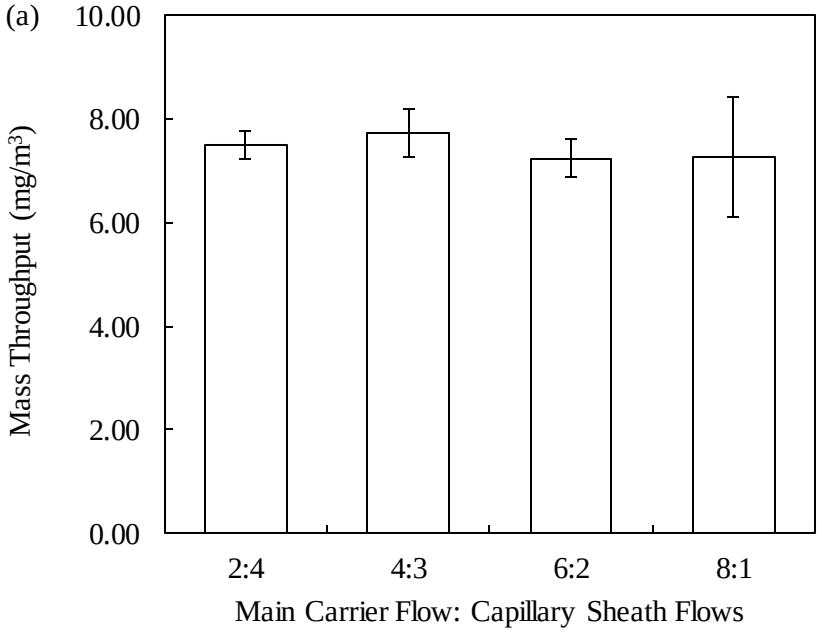

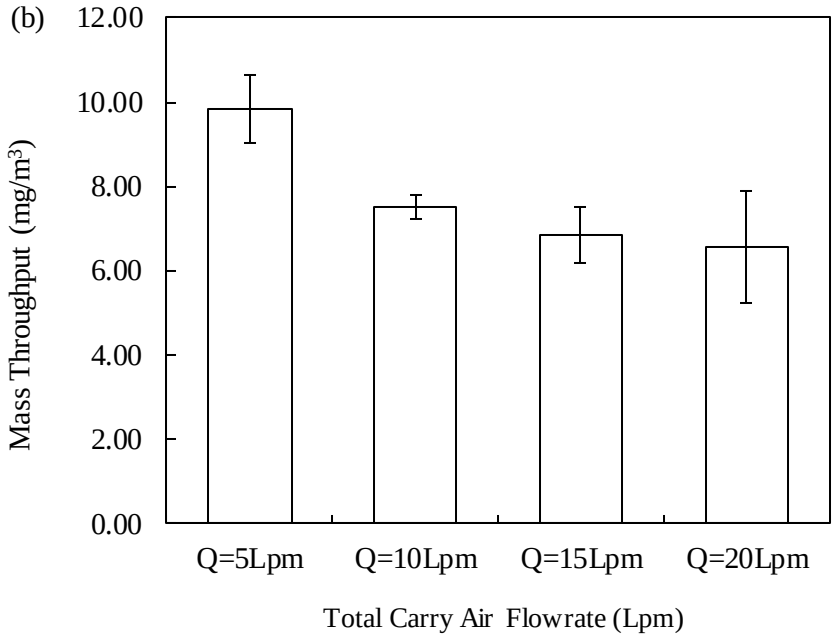

Figure 4.4: Effect of total carrier air flow rate on the particle mass throughput of studied disperser. (the standard deviations of measured data are included in the figure as the error bars).

(3) Effect of nanoparticle suspension feeding flow rate

In this part of the investigation, the THES disperser was operated at the total flow rate of 10.0 lpm with the flow rate ratio set at 4:3 and the capillary tip distance kept at 3.0 cm. The spray liquid was the nano TiO_2 suspension at the concentration of 10 g/L. The electrical conductivity of spray suspensions was kept at 150 μS/cm. The spray voltages (both negative and positive polarities) were varied in order to operate the spray at the multiple-jet mode. Figure 4.5 shows the comparison of nanoparticle mass concentrations at the exit of TSE System THES under three suspension feeding flow rates (i.e., 5, 10 and 20 μl/min). The higher the suspension flow rate fed, the more mass nanoparticle concentration produced. It

is also found that the increase factor in nanoparticle mass concentration (i.e., a factor of 2.41) is higher than that in feeding flow rate (i.e., a factor of 2.0). It is possibly because more particles were lost at a low feeding flow rate. Note that the feeding flow rate was limited to no more than 20 μl/min because of the small ID of capillaries used in this experiment. For feeding flow rates higher than 20 μl/min, the easy breakdown of carrier gas, resulted in the unstable multiple-jet operation, because of much higher electrical field required to operate the multi-jet spray.

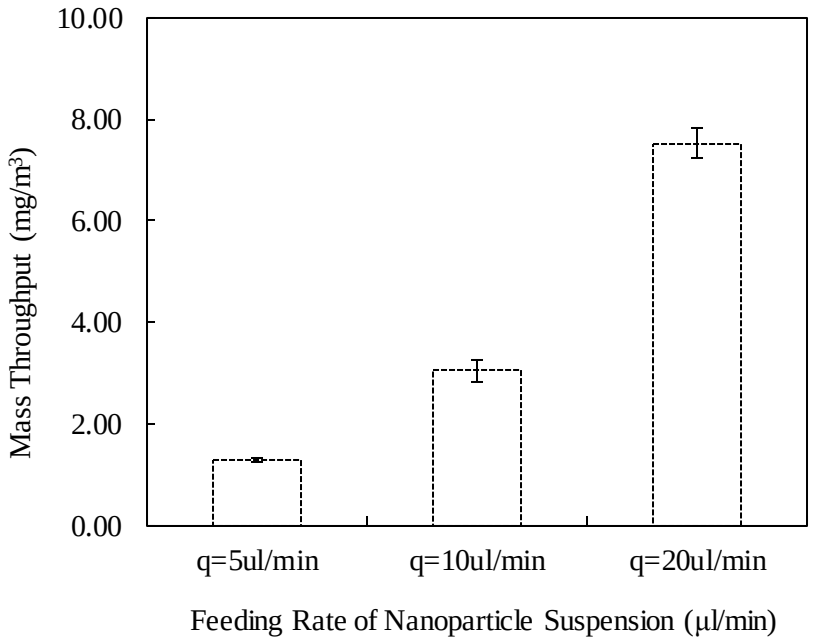

Figure 4.5: Effect of total carrier air flow rate on the particle mass throughput of studied disperser. (the standard deviations of measured data are included in the figure as the error bars).

(4) Effect of nanoparticle concentration and material

As the result of the above investigation, it is found that the studied THES disperser

can produce nanoparticles in high mass concentration when the system was set at the capillary tip distance of 3.0 cm and operated at the total flow rate of 5.0 lpm with the flow rate ratio of 4:3 and suspension feeding flow rate of 20.0 µl/min. Under this setting, both positive and negative spray voltages applied were within the range of 7.5 to 8 kV. To further study the mass concentration output from the THES when spraying different nanomaterial, we varied the concentration of nano TiO_2 suspensions (i.e., 1.0, 3.0, 5.0, 8.0, and 10.0 g/L). In addition to TiO_2 suspensions, nano ZnO and NiO suspensions at the same mass concentrations as those used in nano TiO_2 were also prepared to investigate the effect of particle materials on the mass throughput of the TSE System THES. Figure 4.6 shows the experimental result obtained in this part of study.

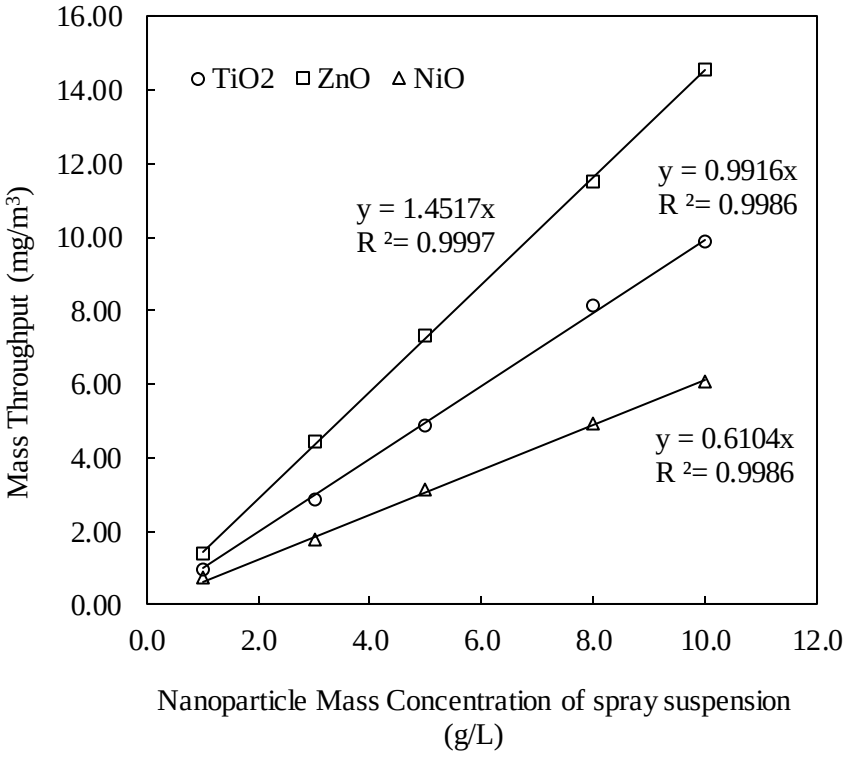

Figure 4.6: The linear relationship between particle mass throughputs of studied disperser and sprayed suspension concentrations for TiO_2, ZnO and NiO nano- materials.

The experimental data shown in Figure 4.6 evidence that for a specific nanomaterial, a linear relationship between the mass throughput of the TSE System THES and the concentration of nanoparticle suspension sprayed was obtained. Because of the differences in material density (i.e., 4.23, 5.61 and 6.67 g/cm^3 for TiO_2, ZnO and NiO particles, respectively), the line slopes for three test nanomaterials are different. It was expected that the heavier the nanoparticle density, the higher the line slope. For the cases of nano TiO_2 and ZnO, the ZnO line slope is higher than that for the TiO_2 case because the density ratio of nano ZnO to nano TiO_2 is larger than 1.0 (about 1.33). However, the slope for nano NiO (having the highest particle density) is the lowest among the three test nanomaterials. This may be caused by unstable nano NiO suspension when prepared as the same pH value (less than 7.0) as the other two nanoparticle suspensions. Note that in order to keep the properties of nanoparticle suspensions the same for all the test cases, nitric acid was used to control the electrical conductivity of all spray suspensions. This resulted in the pH value slightly less than 7.0 for all spray suspensions. A stable NiO-enriched suspension has been suggested to be prepared at the pH value greater than 9 (Hernández et al., 2005). Nano TiO_2 and ZnO were found to be stable at suspensions with a pH as low as 6.5 and 6, respectively (Shin et al., 2012; Habib et al., 2013). Nonetheless, the linear relationship between the mass concentration exiting from the studied THES disperser and the mass concentration of spray nanomaterial suspensions could be used to estimate the exit mass concentration of airborne

nanoparticles from the studied THES disperser (given the prepared mass concentration of nanomaterial suspension).

4.3.2 Measurement of Particle Size Distribution

The size distribution of particles generated by the studied THES disperser was further examined herein by a Scanning Mobility Particle Sizer (SMPS). A typical measured size distribution of nano TiO_2 particles, dispersed by the THES with the setting concluded in the section 3.1a, is shown in Figure 4.7(a). A majority of TiO_2 nanoparticles shown in the Figure 4.7(a) were smaller than 100nm in size and the peak particle size was 24 nm (the medium diameter of 26 nm), close to the nominal primary size (99.7%, <25nm) given in the original powder form. Compared to the work of Yi et al. (2013), in which airborne particles had a size distribution with the medium diameter of 157 nm when dispersing TiO_2 nanopowders with the primary size of 21 nm, the studied THES disperser had the much superior capability in dispersing nanoparticles in the un-agglomerated form.

In addition, PSL particles of 100 and 200 nm were also sprayed in the studied THES disperser to investigate the potential agglomerate issue resulted from the spray. Figure 4.7 (b, c) shows the measured size distributions of dispersed PSL particles of 100 and 200 nm in size. The peak sizes of measured PSL particles were consistent with the nominal sizes given by the vendor. The observed shoulder in the right-hand side of the measured size distributions is possible caused by either minor particle agglomeration or the coating of impurities (such as the surfactant in the original PSL suspensions or solvable in the solvents) on PSL particles. Particles of smaller sizes were also detected (in the left-hand side of the

measured size distributions). They were possibly attributed to satellite droplets produced in the ES process (with the presence of impurities such as surfactants). It is thus believed that the studied THES disperser can produce nanoparticles in good size distribution for animal exposure study.

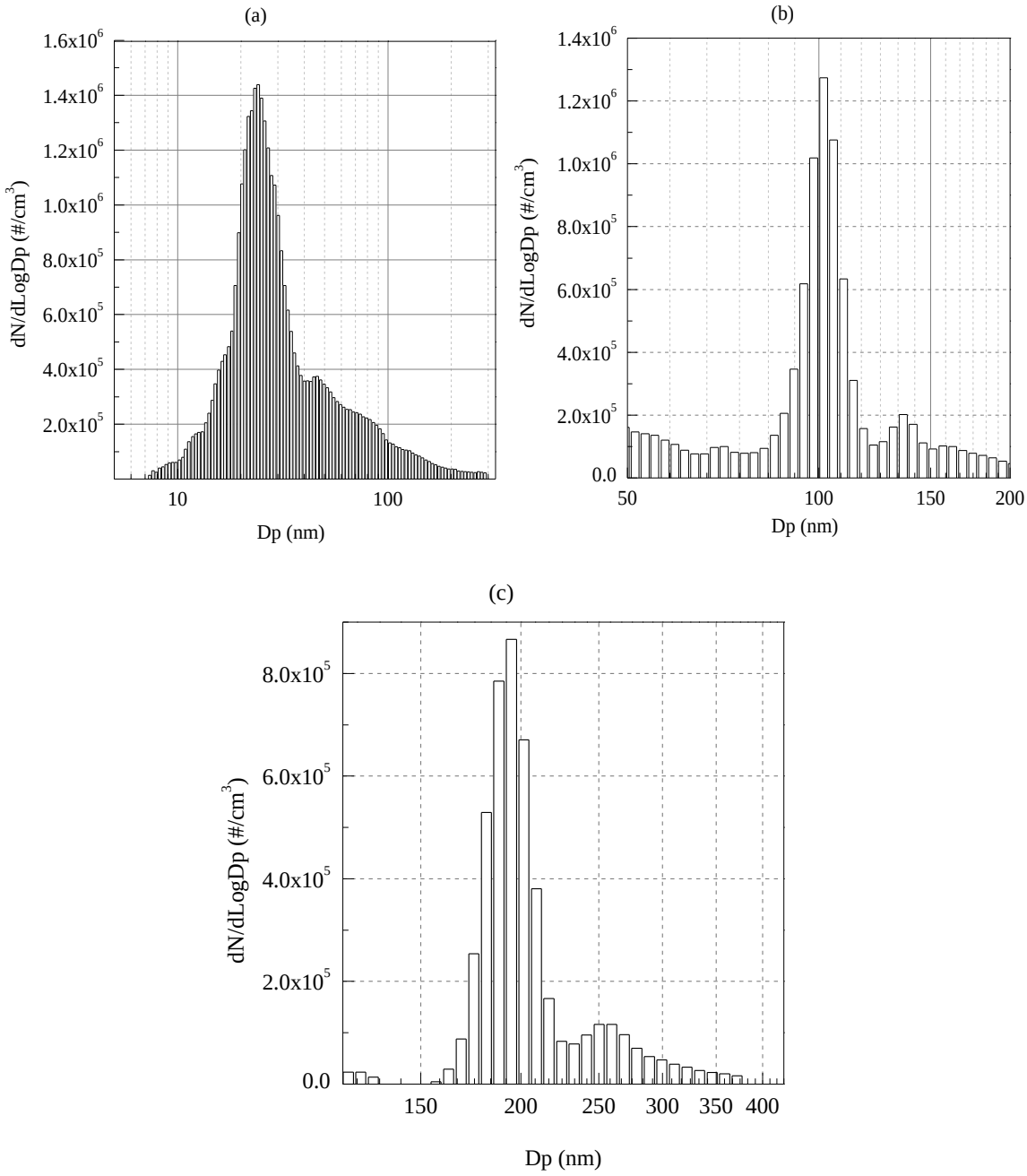

Figure 4.7: Measured size distributions dispersed by the studied THES disperser for (a) TiO_2 nanoparticles, (b) 100 nm PSL particles and (c) 200 nm PSL particles.

4.3.3 Uniformity Evaluation of Animal Exposure Chamber

In addition to the above study on the mass throughput of the studied THES disperser, fluorescent nanoparticles were used to examine the uniformity of the nano aerosol concentrations at all the nose ports of the animal cages in the TSE inhalation exposure chamber. The experimental procedure for the fluorescence analysis was given in Section 2.2. Figure 4.8 shows the percentage of concentration deviating from the mean mass concentration among all the evaluated nose ports. It is observed that deviations of aerosol concentration at the majority of the nose ports were within $\pm$13% of the mean value. Only one nose port located nearby the side exit port of the exposure chamber showed a slightly high value of deviation (i.e., ~27%). It is possibly because of the local variation of flow field near the side exit port. In reviews of aerosol exposure chambers (O'Shaughnessy et al., 2003; Dabish et al., 2010), the coefficient of variability (CV) of nose/head-only chamber (defined as the ratio of the standard deviation to the mean value) usually ranges from 4.8% to 16.3 %. Based on the above CV definition, the overall coefficient of variability for the studied exposure chamber was calculated as 11.4%, indicating a good spatial uniformity of the studied TSE inhalation exposure chamber for nanoparticles. The possible reason for slightly higher CV value in this study could be due to the fact that the studied flow rate of 10.0 lpm is lower than the optimal flow rate recommended for the 20-port nose-only animal exposure chamber (Oldham et al., 2009).

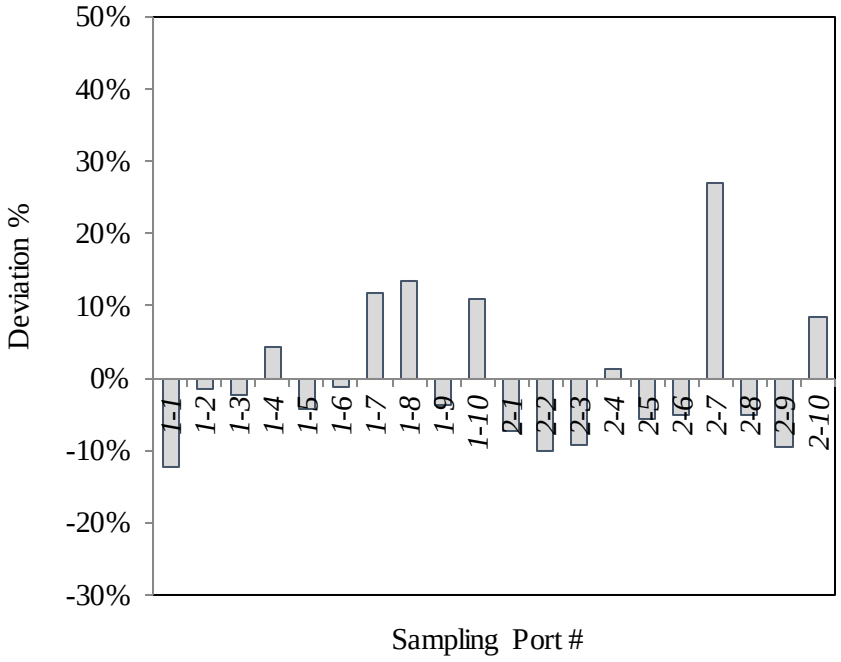

Figure 4.8: Deviation of the particle mass concentrations measured at 20 nose ports of inhalation exposure chamber, referenced to the mean of all measured mass concentrations.

4.4 Summary

As the recent development of nanotechnology, nanoparticles of various sizes and compositions have been synthesized and proposed for industrial applications. At the same time, the concern of adverse health effects due to the exposure of nanoparticles has been increasing. Tools are in demand to perform the toxicity studies of nanoparticles, particularly in its individual form (not in the agglomerate form). Unfortunately, such a tool for studying the toxicity of nanoparticles in their individual form has not been commercially available until now. In this study, the performance of a twin-head electrospray nanoparticle disperser developed by TSE Systems Inc. was evaluated. In addition, the spatial uniformity of nano

aerosol concentration in the 20-port nose-head-only animal exposure chamber was further evaluated when a nanoparticle stream was introduced in.

Electrospray technique has been recently proposed and applied in many applications involving particles, because of its capability of producing un-agglomerated droplets/particles with sizes ranging from nanometers to super-micrometers. With the presence of a DC electrical field for its operation, particles produced by electrospray are highly charged in the same polarity. Such charged particles are in general difficult to be kept airborne because of the electrostatic effects. The charge reduction is thus necessary for electrosprayed particles in order to minimize the loss during the particle transport. Without using radioactive materials or corona discharge as the bi-polar ion sources for reducing charges on electrosprayed particles, the twin-head electrospray technique was implemented in the studied disperser to achieve the same task. In the disperser, positive high voltage was applied to one spray head (i.e., capillary), producing positively charged particles, and negative high voltage applied to the other, generating negatively charged ones. The mixing and collision of particles in both polarities in general reduced the charge level on particles while increasing the mass concentration of particles exiting the studied disperser.

A systematic study has been performed on the studied electrospray disperser regarding to its mass throughput and quality of particle size distribution. The performance of the disperser was studied by varying the spray capillary tip distance, carrier-to-sheath flow rate ratio, total gas flow rate, liquid feeding rate, nanoparticle suspension concentration and particle material. In addition, the size distribution of dispersed nanoparticles and spatial

uniformity of particles in the inhalation exposure chamber was also investigated. It was found that the maximal mass concentration of nanoparticles exiting from the studied disperser was achieved by having a capillary tip distance of 3.0 cm, and operating it at the total flow rate of 10.0 lpm with the carrier-to-sheath flow rate ratio of 4:3 and the suspension feeding flow rate of 20 μl/min. The applied voltages on both spray capillaries ranged from 7.5 to 8 kV. Under this setting, nanoparticles in high mass concentrations (i.e., > 10 mg/m^3) could be produced when spraying a suspension of nanomaterial concentrations higher than 8.0 g/L. The linear relationship between the mass throughput and the mass concentration of sprayed nanoparticle suspensions was also observed in this study. Further, the mass throughput of the studied THES disperser depended on the nanoparticle composition. As a result, a mass concentration monitor is thus recommended to be included in the system for measuring the actual mass concentration of particles exiting from the disperser. Finally, the fluorescence study on the spatial uniformity gave a CV value within the range of uniformity susgested by previous research groups, indicating the acceptable particle uniformity in the studied exposure chamber.

CHAPTER 5 Review of Ultrafine Particle Measurement Techniques

5.1 Introduction

The comprehensive review of instruments and technologies for UFP characterization can be found in the article given by Chen and Pui (2008). Among these measurements, UFP size characterization is very important. Most of particle properties and effects, such as light extinction, electric mobility, diffusivity, inertia effect and health effect, are highly related to particle size. To characterize particle size distribution, a technique based on particle electrical mobility analysis is one of the most efficient, reliable methods and it is widely-used in many aerosol instruments. An electrical particle sizer consists of a particle charger which imposes a well-defined charge distribution on test aerosol, a differential mobility analyzer which separates/classifies particles based on their electrical mobility, and a particle detector which usually is a condensation particle counter or a particle electrometer for number concentration measurement.

However, current instruments to characterize UFPs are mostly expensive and bulky in package. For example, scanning mobility particle sizers (SMPSs) are capable of characterizing the size distribution of UFPs (Wang and Flagan, 1990). The ownership of an SMPS often costs from $60K to 100K. The big size and heavy weight of an SMPS prohibits them in in-situ sampling, occupational hygiene and other nanotechnologies which allows

greater flexibility of working arrangements. Fast Mobility Particle Spectrometer (FMPSTM, Mirme; 1994; Caldow et al, 2004) and Differential Mobility Spectrometer (DMS; Reavell, 2002) dynamically measure UFPs in the exhaust of combustion sources but they are limited for dry particle characterization. And their costs are at the level of ~ $80K.

Some portable nanoparticle sizers found in recent market include the Kanomax portable aerosol mobility spectrometer (PAMS), TSI Nanoscan 3910, Naneum Nano-ID PMC500 (Steer et al., 2014) and Grimm Mini wide range aerosol spectrometer (WARS). As shown in the Table 5.1, these instruments are still either big, heavy, low resolution or expensive. Current UFP studies (e.g. UFP effect on personal exposure, vertical distribution of UFP in ambient air, UFP monitor in aircraft and so on) all require devices to be much lighter, more compact, cost effective and of a good resolution. No aerosol size distribution instrument at low cost and in compact package is currently available to meet the demands of UFP measurement. Moreover, most of existing aerosol instruments were designed without the consideration of field deployment. Special care/modification or frequent maintenance is often required to deploy the instruments in the field. Existing aerosol instruments are also not easy to be networked, a much desired feature for modern ambient PM monitoring. This is because most of them were developed with the single-alone operation in mind.

Table 5.1: Some commercial portable particle sizers for UFP measurement

Instrument	Dimensions / Weight
TSI Nanoscan 3910	45 cm x 23 cm x 39 cm <8kg without batteries; <9kg with 2 batteries
Kanomax portable aerosol mobility spectrometer (PAMS)	23 cm x 23 cm x 15 cm 4.5 kg
Naneum Nano-ID PMC500	30 cm x 33 cm x 26 cm 6.25 kg
Grimm Mini wide range aerosol spectrometer (WARS)	34 cm x 31 cm x 12 cm 7.6 kg

We thus proposed to develop a cost-effective, compact electrical UPF sizer (eUPS) and wireless mesh network using proposed mini-eUPSs as the nodes for the future modern UFP monitor network. The designs of proposed eUPSs are also based on the particle electrical mobility technique.

5.2 Review of Particle Chargers

To classify UFPs by a differential mobility analyzer (DMA), they have to undergo a charging process at first. There are four main particle charging mechanisms developed in the past few decades: flame charging, static electrification, diffusion charging and field charging (Hinds, 1999). The ion-attachment method by using field or diffusion charging processes and the photo-ionization method are the two main approaches often used in particle charger development (Chen and Pui, 1999), and both charging processes can be modeled and predict (Jiang et al., 2007a,b). The ion-attachment method allows particles randomly collide with ions in an ion-rich environment, where field charging is the dominant mechanism for

particles larger than 1.0 μm and diffusion charging is the dominant mechanism for particles less than 0.1 μm even in the presence of an electric field (Hinds, 1999). Although photocharging has a higher charging efficiency than diffusion charging for particles smaller than 20nm, it highly depends on particle composition and particle size. Because the electron must have enough kinetic energy, larger than a given threshold, to escape from the particle surface. Usually, diffusion charging is accompanied in aerosol photocharging process (Schmidt-Ott and Siegmann, 1978).

When particles are exposed to bipolar environment, an equilibrium charge distribution of particles will achieve within sufficient residence time (Fuchs, 1963; Wiedensohler, 1988). Bipolar ions are usually produced by ionization of gas molecules by α-ray or β-ray emitted in the decay of radioactive material (e.g., ^{85}Kr, ^{210}Po, ^{241}Am), by AC corona discharge, by dual electrode corona discharge and by photoionization of gas molecules by soft X-ray (Fry, 1970; Adachi et al, 1985; Liu et al., 1986; Chen and Pui, 1999; Hewitt, 1957; Whitby, 1961; Liu and Pui, 1975; Stommel and Riebel, 2005; Qi et al., 2007; Li and Chen, 2011; Hontañón and Kruis, 2008; Romay et al., 1994; Shimada et al., 2002; Kim et al., 2011). It was demonstrated particles of submicron sizes can be effectively charged in bipolar ion neutralizers (Wang and Flagan, 1990). However, the charging efficiency of bipolar charger decreases with particle size, most notably in the nanometer range, which means most of valuable nanoparticles would be wasted during the following electrical classification process (Qi et al., 2008). High charging efficiency of aerosol of particles results in high sensitivity of measurement (Intra and Tippayawong, 2011). The

yield of singly charged particles by a unipolar corona charge conditioning process was found to be two to four times in concentration higher than those of bipolar charging units (Li and Chen, 2011). From this point of view, unipolar charger is better suited for nanoparticle applications.

In the past decades, a variety of unipolar aerosol chargers have been developed (Adachi et al., 1985; Romary and Pui, 1992; Chen and Pui, 1999; Kruis and Fissan, 2001; Qi et al., 2007; Li and Chen, 2011; Kim et al., 2011). These unipolar particle chargers does provide higher charging efficiency and can be classified into two types, based on their ion sources: unipolar ions (positive or negative) generated through the separation of bipolar ions coming from radioactive material or soft X-ray sources by using a DC electric field, and unipolar ions directly produced via corona discharge (Li and Chen, 2011). For personal monitoring or spatially distributed application, an aerosol charger without radioactive material is preferred because of safety perceptions and increasing license cost for its use. An expensive soft X-ray based particle chargers are also not impractical to implement in a small and low-cost package. Therefore, corona discharger is therefore recommended to provide unipolar ions for aerosol charging and is widely used.

In a corona discharge device, high voltage is often applied to a very thin wire or a needle (which has high curvature), while the other electrode (a plate or a tube) is typically grounded. Gases undergoes electrical breakdown in the corona region near the wire surface or needle tip, resulting in a large amount of positive ions and free electrons production. When an aerosol stream pass by, particles can be charged by random collision with ions due to

Brownian motion of ions. The amount of ion deposition on the particle surface depends on resident time, particle size and shape, electric field, etc. (Intra and Tippayawong, 2011). Hewitt (1957) developed a corona-wire diffusion charger to investigate the charging process in an electrostatic precipitator and conducted experiments for particles with size between 60 to 700 nm, showing nanoparticle loss due to the electric field strength. Later, several researchers continued working on similar design and investigating diffusion charging of particles. Whitby and Clark (1966) employed the corona-wire chargers based on Hewitt's design in an electrical aerosol analyzer (EAA) for measuring particle in 0.015 to 1 μm size range. Liu et al. (1967) explored the diffusion charging of particles under a low pressure condition, 0.0311 to 0.960 atm, and applied AC square-wave voltage to solve the aerosol loss problem. This charger was then improved and studied by Liu and Pui (1975) and Pui (1976). A sheath air flow to protect high intensity corona discharge region was added and significant charged particle loss was reduced to particles below 10 nm. To avoid particle losses due to insulator charging and to improve particle penetration efficiency, Buscher et al. (1980) modified the charger of Pui (1976) via making the charger surface conductive. Other efforts on minimizing charged particle loss due to wall deposition were done by some researchers. For example, Hutchins and Holm (1989) developed a charger using 3000 Hz AC voltage with maximum amplitude of 10 kV to generate sinusoidally driven ion current from a corona discharge for particle charging. Biskos (2004) designed another new Hewitt-type corona charger with an AC voltage applied on the outer electrode to drive charging ion without causing particle loss on the charger wall.

In a parallel but independent, the first corona-needle type charger was developed by Whitby (1961) to convert the corona current into positive, negative, or a mixing of positive and negative ions. Based on this, many research proposed unipolar chargers with different designs to improve particle charging performance. Medved et al. (2000) designed a corona jet charger which was later employed by the TSI 3070A electrical aerosol detector (TSI, 2004). Later, Marquard et al. (2006) proposed a twin corona-needle charger and reported high charging efficiencies for sub-100 nm partilces. At the same period, Hernandez-Sierra et al (2003), Aloson et al. (2006), Intra and Tippayawong (2006 a, b), Choi and Kim (2007), Park et al. (2007, 2010), and Qi et al. (2008) all developed different corona chargers with improved features. However, corona discharge has its own disadvantages, like ozone production problem, new particle formation, either from erosion and sputtering from the corona electrode itself or from gaseous contaminants in the charger (Han, 2003). The discharging wire or needle thus needs to be replaced after a certain time, or inert gas is used to protect corona discharge and extend the lifetime of electrode.

In an ideal particle charger, a high charging efficiency and reduced multiple charge effect are required, besides of stable ion concentration, low particle losses, no damage or contamination to aerosol, capability of working at low pressure or in different gases. Particles larger than 20 nm can easily get more than one charge in a unipolar charger (Alguacil and Alonso, 2006; Li and Chen, 2011). To separate particles based on electric mobility, the instrument performance would be influenced by multiple charge on particles. Multiple charging complicates the data reduction scheme used to recover size distribution.

Moreover, multiple charge caused server particle loss are often encountered in other process, like aerosol transport and electrospray aerosol generation. The reduction of charges on particles is often needed in these scenarios. Several attempts have been made to reduce the multiply charged fraction in aerosol or generate singly charged particles. Vivas, Hontañón and Schmidt-Ott (2008) studied multiple charge reduction in an existing corona diffusion charger (Büscher et al. 1994) by applying a positive-zero rectangular wave voltage to modify the ion trajectories in the charging region. Yli-Ojanpera et al. (2010) have described a method to produce singly charged di-octyl sebacate (DOS) particles from 10 nm to 500 nm by growing DOS on charge-confectioned NaCl seed particles. Li and Chen (2011) developed a prototype DC corona-based unipolar aerosol charger. The performance of the prototype was optimized by varying operational parameters (i.e., aerosol flow rate, corona current and ion-driving voltage) to achieve high extrinsic charging efficiency while minimizing the overcharge of large particles. Also, Qi and Kulkarni (2012) designed a unipolar corona charger and operated it at 1 μA corona current to minimize the $N_{ion} \cdot t$ product and reduce the multiple charging of particles. This level of corona current also resulted in an acceptable charging efficiency for measuring particle size distribution in a hand-held mobility spectrometer.

Therefore, in developing a mini-charger, ease of design, manufacture and maintenance (resulting in low cost), effective charging performance and reduced overcharging effect all should be taken into consideration.

5.3 Review of Electrical Mobility Based Aerosol Analyzers

The well-known DMA has been improved and used for many years to characterize particle sizes and to classify particles down to the nanometer range. The earliest studies on differential mobility analyzer can be traced back to the work of Zeleny (1898), McClelland (1898) and Langevin (1902, 1903) using coaxial cylindrical condensers to measure the mobility of air ions. Following them, many efforts have been made on DMA innovation, improvement of DMA performance and applications of DMA. Up to the present three types of DMA configurations has been designed, i.e., in cylindrical (Liu and Pui, 1974b, 1975; Knutson and Whitby, 1975; Winklmayr, et al., 1991; Chen et al., 1998), radial (Hurd and Mullins, 1962; Zhang et al., 1995; Rossell- Llompart et al., 1996) and planar (Erikson, 1921; Zhang and Wexler, 2006; Santos et al. 2009; Steer et al, 2014; Hontañón, et al., 2014) arrangement. The fundamental design concept however remains similar. A pair of electrodes used for establishing a stable DC electric field is set up in a DMA, called as particle classification region. Polydisperse aerosols, charged prior, are introduced into the DMA through the inlet designed on one electrode. A stream of particle-free sheath air comes from the same side of classification zone is usually used to keep the charged aerosol flow away from the other electrode. Under the fixed electric field, only particles with certain electric mobility can travel across the sheath flow, arrive at the aerosol outlet on the other electrode with the opposite electric polarity of particles and leave DMA as monodisperse aerosol. Particles with higher electric mobilities deposit at various positions on the other electrode,

while particles with lower electric mobilities exit the classification region with remaining flow from the other side of the flow channel.

The fundamentals of electric mobility and particle mobility diameter can be simply described through a force balance analysis on charged particles between drag force and electric force. For a spherical particle with n elementary units of charges and diameter d_p, moving in a steady electric field of intensity E, the drag force is given by Stokes Law:

$$F_d = \frac{3\pi\mu d_p}{C_c}(u - v)$$

where μ is the viscosity of the gas, C_c is the Cunningham slip correction coefficient which can be calculated by an empirical equation of the form

$$C_c = 1 + \frac{2\lambda}{d_p}(A_1 + A_2 e^{-\frac{A_3 d_p}{\lambda}})$$

where A_1=1.142, A_2=0.558, and A_3=0.500 (Allen and Raabe, 1985). Equating it to the electric force of particle, $F_e = neE$, the electrical mobility of the particle is then derived as

$$Z = \frac{neC_c}{3\pi\mu d_p}$$

By given the charges on the particle and DMA measured electrical mobility, the size determined by the above equation is often called particle electric mobility size. DMA can usually be operated either in a fixed voltage mode for particle classification or a scanning voltage mode for particle sizing.

Most popular and commercial DMAs are based upon a cylindrical geometry where two cylinders are coaxially aligned to create electric field. The famous Whitby aerosol

analyzer (WAA) was developed by Whitby and Clark (1966), which included all of the key features of later instruments, like a diffusion charger, a coaxial-cylinder mobility analyzer and an electrometer. This instrument was commercialized to TSI model 3000 WAA in 1967 (Flagan, 1998). Later, a second generation instrument, electrical aerosol analyzer (EAA, commercialized as TSI model 3030) was developed by Liu et al. (1974) with a reduced size for measuring size distribution of submicron aerosols. At the same period, with the need for a source of monodisperse particles for aerosol instrument calibration, Liu and Pui (1974b) improved the early differential mobility classifier developed by Hewitt (1957). Different from EAA, DMA has two inlets (for sheath air and polydisperse aerosol) and two outlets (for excess flow and monodisperse aerosol). Knutson and Whitby (1975) described the apparatus, theory and application of this instrument in detail. The value of their development later successfully enhanced by its commercialization as TSI 3071 DMA and world-wide application. After that, more and more researchers involved in DMA development and application. A great effort has been made to improve the performance of DMA, such as, reducing classification length (Kousaka et al. 1986; Rosell-Llompart et al. 1996) in order to shorten particle residence time for solving broadening problem of particle transfer function, modifying aerosol inlet for minimizing particle diffusional deposition losses (Winklmayr et al. 1991; Chen et al., 1999), modifying DMA geometry to lower DMA's sizing limit and achieve high sizing resolution (Reischl et al.1997; Chen et al. 1998; De Juan and Fernández de la Mora, 1998; Fernández de la Mora and Kozlowski, 2013), and enhancing aerosol flow rate for improvement of particle transmission efficiency (Hontañón and Kuris, 2009)

Significant progress on the DMA development has been made in past decades for nanoparticle characterization. Widely used mobility-based instruments that measure particle size distributions in the lower submicron and nanometer range, such as the scanning mobility particle sizer (SMPS; TSI model 3936), are more suitable for laboratory and scientific studies. Their size, weight, and cost are prohibitive for in situ sampling, occupational hygiene and other nanotechnologies allowing greater flexibility of working arrangements. In recent years, an increasing demand for smaller, portable, easy to use instruments has led to the research on developing miniature or size reduced aerosol devices. Ranjan and Dhaniyala (2007) designed a miniature electrical-moblity aerosol spectrometer (MEAS), which collects particles inside a rectangular region and does not provide a monodisperse aerosol outlet. The internal working principle of MEAS is similar as a DMA, however, the low resolution and difficulty in retrieving more precise particle size distribution limits its application in some cases. A similar work was done by Qi, Chen, and Greenberg (2008) in developing a miniature, low-cost disk-type electrostatic aerosol precipitator. No sheath flow was used in mini-disk precipitator, resulting in low sizing resolution. A mini-disk electrical aerosol classifier (mini-disk EAC) with the sheath flow was further developed by Li et al. (2009), providing the cumulative output for aerosol particles having the electrical mobility less than certain values defined by the unit. The sizing resolution of both mini-disk prototypes is not as good as that offered by DMAs. Martínez-Lozano and Labowsky (2009) studied the performance of a miniaturized version of the isopotential DMA developed by Labowsky and Fernández de la Mora (2006). A hand-held DMA was developed by

Fernández de la Mora and Labowski (2013) for measuring particles in the sizes ranging from 1 to 30 nm. Its high sheath flowrate operation limits its use for miniature particle sizers. Compact DMAs are also found in portable particle sizers in the market. Examples of portable units include portable aerosol mobility spectrometer (PAMS) by Kanomax, Nanoscan 3910 by TSI Inc., Naneum Nano-ID PMC500 (Steer et al., 2014) and Grimm Mini wide range aerosol spectrometer (WARS). However, these instruments are either large in its final package, heavy in weight, low resolution in particle sizing or expensive in cost. To address the needs of environmental or atmospheric sciences and occupational hygiene, a more cost effective, lighter, more compact and good resolution DMA is required.

Although rectangular channels appear in the early DMA development (Erikson, 1921), edge effects results in its poor function of particle sizing resolution. Nonetheless, from the view of device miniaturization and with the help of modeling study and advanced manufacturing technique, recent developments with this geometry showed more improvements (Zhang and Wexler, 2006; Kulkarni and Wang, 2006; Santos et al., 2009; Steer et al., 2014; Hontañón et al. 2014). DMA of rectangular geometry has inherent advantage rather than other designs. In traditional DMAs of cylindrical design, two electrodes should be aligned precisely to avoid losing desired sizing function and resolution. But in parallel-plate geometry, this is no longer an issue. The spreading of particles not only depends on the particle Brownian motion inside a DMA, but also depends on the change of electric field (Alonso, 2002; Song and Dhaniyala, 2007). Aloson (2002) showed that in a cylindrical DMA, the variance of particle distribution increases when particles move towards

the inner electrode, resulting in worse resolution. Thus, to eliminate effects of non-uniform electric field, a planar design is a better choose. Additionally, mechanical machining, simplicity on design and maintenance, and lower manufactory cost are also important. These are easier to be achieved in a DMA of parallel-plates than cylindrical DMA.

A similar DMA has been reported in the work of Steer et al. (2014), resulting in the commercial Nano-ID PMC500. However no Tandem DMA experiment was performed to calibrate the prototype performance (i.e., DMA transfer function). It remains at large regarding to the particle sizing and penetration of the above DMA. Therefore, in this work, a new cost-effective, more compact plate DMA was designed and its detail performance was evaluated via TDMA experiments. The effect of DMA geometry on the particle sizing performance of mini-plate DMAs was also investigated with two prototype mini-plate DMAs having different dimensions in the classification region.

CHAPTER 6 Development of a Prototype Miniature Plate Particle Charger

6.1 Introduction

In the study, a miniature DC-corona-based, plate-type particle charger has been designed and constructed. In order to charge particles for electrical mobility analyzing, it is necessary to optimize the charge efficiency for particles in the nanometer size range while minimizing the multiple charge effect of large particles. Experiments were conducted to investigate the performance of the prototype by varying the charger configurations and operational parameters such as the corona current and aerosol flowrate. Furthermore, the charging efficiencies and particle charge distributions for particles smaller than 200 nm were evaluated. Finally, a Gaussian distribution curve was used to predict the charge distribution for particles within desired size range.

6.2 Design of a New Mini-plate Corona Charger

The schematic diagram of the prototype DC-corona-based mini-plate charger is shown in Figure 6.1. The construction of the prototype consists of two brass blocks. Two stainless steel tubes designed to be hard pressed into the upper block were used as aerosol inlet and outlet, respectively. An aerosol charging channel was designed in the bottom block. Four identical corona channels (named as corona-A, -B, -C, and -D) were designed in both

upper and bottom blocks. Tungsten wires of 50 μm in diameter (Alfa Aesar, A Johnson Matthey Company, MA, USA) were welded to four metal pins and parallelly installed in the device. Different operational configurations can be set up in the prototype by applying positive/negative high voltage to one or two wires. Two grounded perforated plates with about 30% opening separated corona channels from the aerosol channel. When the electrical field strength at the surface of the wires is raised to a sufficiently high level, surrounding air undergoes an electrical breakdown process, resulting in a production of a large amount of ions. Ions produced in the corona zone will diffuse through the metal screen into the charging zone with a spacing of 0.125". The ion concentration in the charging zone can be controlled by varying the strength of the high voltage applied to the wires and number of the wire used. Note that, for simplicity, no sheath air and driving voltage were designed to be used in this prototype. Aerosol flow was injected into the charger from the left top tube, crossed the charging zone where particles could be charged by random collision with positive/negative ions, and finally existed the device through the right bottom tube. The prototype particle charger has an overall size of $2.2" \times 1.25" \times 0.69"$ in length $\times$ width $\times$ height.

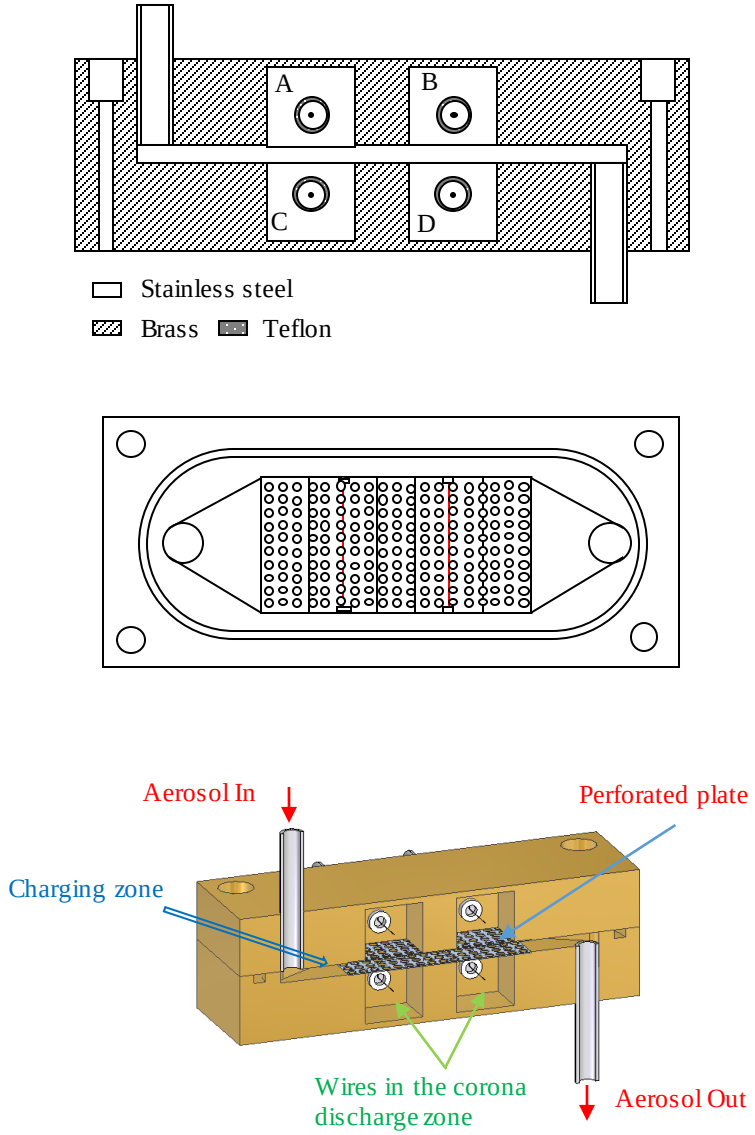

Figure 6.1: Schematic diagram of prototype DC-corona-based mini-plate charger

6.3 Experimental Setup for Evaluating the Mini-plate Particle Charger

The experimental setup as shown in Figure 6.2 to characterize the performance of the prototype mini plate charger includes measuring the charging efficiency and particle

charge distribution. Both intrinsic and extrinsic charging efficiencies were measured in this study. Different from intrinsic charging efficiency, extrinsic charging efficiency takes into account the loss of charged particle in the charger. The definition and measurement setups for evaluating charging efficiency was reviewed by Marquard, Meyer, and Kasper (2006). Two different aerosol techniques were used to produce test aerosols. A customer-made collision atomizer was used to produce NaCl particles with peak electrical mobility sizes from 30 nm to 120 nm. The operational flow rate of the atomizer was 4.0 lpm when the compressed air pressure was at 30 psig. Droplets produced by the atomizer were dried into solid particles by passing through a diffusion dryer with silicone gel as the desiccant right after the atomizer. To produce particles with electrical mobility sizes smaller than 30 nm, the evaporation-and-condensation method (Scheibel & Porstendörfer, 1983) was used. NaCl powders were placed in a ceramic boat, located in a high temperature tube inside a furnace (Lindberg/Blue M tube Furnace, HTF55322C, Thermo Scientific). The vapor carrier gas, Nitrogen or compressed air usually, was controlled and monitored by a needle valve and a laminar flowmeter prior the ceramic tube, at the flow rate of 1.5 lpm. The solid powder in the combustion boat was evaporated at high temperature, and its vapor was carried out. At the exit of the furnace, vapor-rich carrier gas mixes with particle free air at room temperature to produce nanoparticles by nucleation and condensation process.

At the downstream of the two polydisperse aerosol generation systems, a differential mobility analyzer (TSI model 3085) and TSI 3080 classifier was used to classify monodisperse particles with desired sizes. The DMA was operated at the aerosol-to-sheath

flowrate ratio of 1:10. A set of Po^{210} radioactive particle neutralizer and an electrostatic precipitator was used to obtain electrically neutral particles for evaluating mini plate charger. To measure the charged fraction of particles exiting the prototype charger, a 2nd electrostatic precipitator with capability of removing all charged particles and an ultrafine condensation particle counter (UCPC, TSI model 3776) to measure particle number concentration at upstream, downstream of prototype and downstream of precipitator were used. During the experiments, the aerosol flow rate through the prototype was controlled by both CPC pump operated at high flow mode (i.e., 1.5lpm) and low flow mode (i.e. 0.3lpm). The intrinsic charging efficiency (η_{in}) was then evaluated by the equation (Romay and Pui, 1992):

$$\eta_{in} = 1 - \frac{N_1}{N_2} \tag{6-1}$$

Where N_1 and N_2 are the particle number concentrations measured at the downstream of the 2nd electrostatic precipitator when simultaneously turning on and off the high voltage on the prototype and the 2nd precipitator, respectively. And the extrinsic charging efficiency (η_{ex}) was calculated as (Chen and Pui, 1999)

$$\eta_{ex} = \frac{N_3 - N_1/P_{ec}}{N_4} \tag{6-2}$$

where N_3 is the number concentration of particles exiting the prototype when it is turned on; N_4 is the number concentration of particles entering the prototype; and P_{ec} is the penetration efficiency of neutral particles through the 2nd electrostatic precipitator.

Particle charge distribution at the downstream of the prototype was further measured in this study. The tandem DMA technique (TDMA) was used to measure the particle charge

distribution of monodisperse test particles at different sizes. The particle generation systems for this part of the experiment were the same as those used in measurement of charge efficiency. Only one Kr^{85} particle neutralizer was used in front of the 1st DMA where fixed high voltages was applied to generate monodisperse particles at different sizes. The 2nd DMA without neutralized in front was operated under scanning mode to characterize charge distribution. Note that the charge distribution measured in this study is for particles at the exit of the prototype charger (defined as extrinsic charge distribution), not in the charging zone of the prototype (defined as intrinsic charge distribution) (Li and Chen, 2011).

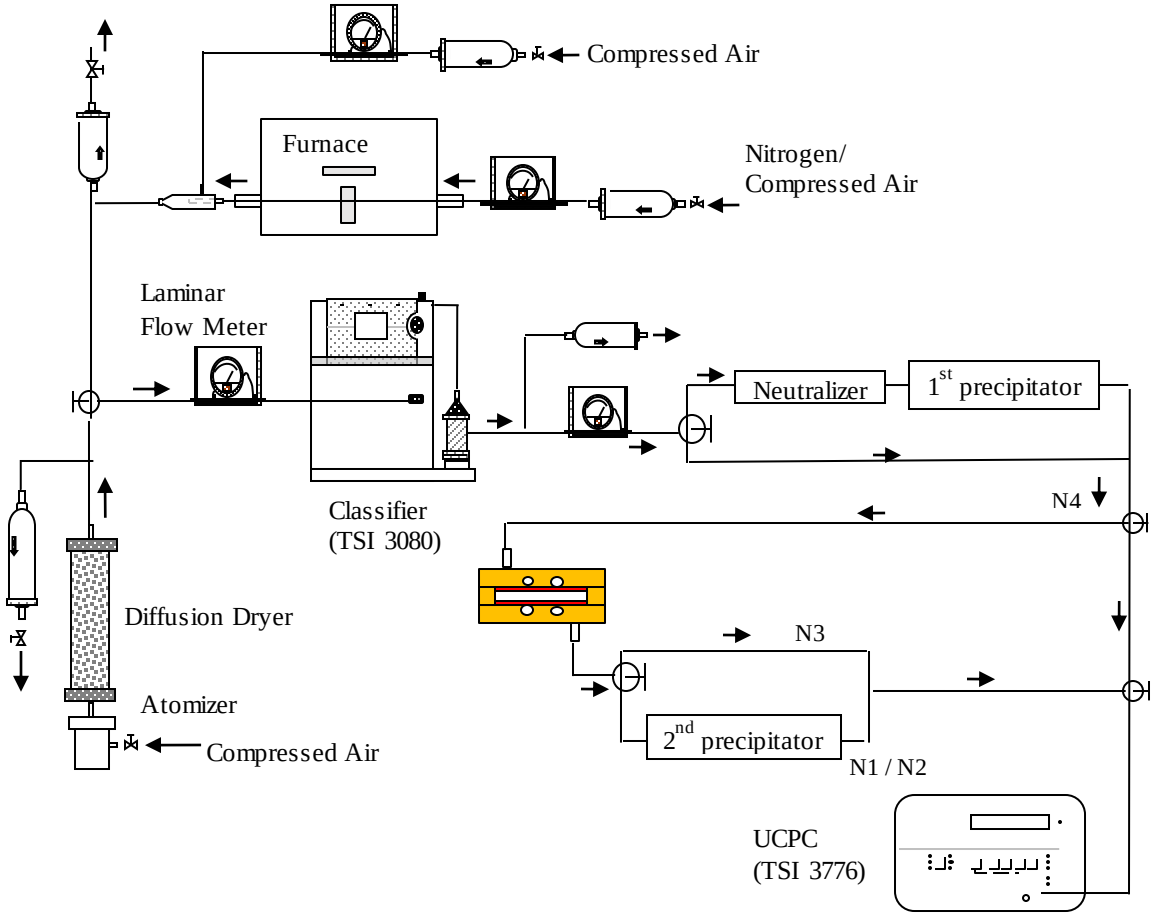

Figure 6.2: Experimental setup for the performance evaluation of the prototype

6.4 Results and Discussion

6.4.1 Optimization of the Prototype Configuration

The optimization of the prototype mini-plate charger is required to maximize the particle charging performance, especially to maximize the extrinsic charging efficiency. As shown in Figure 6.1, four corona channels locate at different positions (i.e., A,B C, and D) inside the mini-plate charger. For example, corona-A is most close to the aerosol inlet while

corona-D is most close to the aerosol outlet. To investigate the configuration effects on particle charging, the total corona current utilized for ion generation were firstly kept at a constant of 2 μA, no matter one or two wires were applied to high DC voltage. So, there are eight combinations for charger configuration and corona current, i.e., corona-A, -B, -C and –D operated at current of 2 μA individually; corona-A and –B, corona-A and –C, corona-C and –D, and corona-B and –D operated at current of 1 μA. Figure 6.3 shows the measured intrinsic and extrinsic charging efficiencies for these eight cases (labeled as 1, 2, 3, 4, 5, 7, 9 and 12) for 40 nm particles at aerosol flowrate of 0.3 lpm. It is found that the intrinsic charging efficiencies of 8 studied cases are all large than 90%, with no obvious difference among them, indicating the prototype charger performs as expected. Due to the different ion concentrations and distributions generated inside the charging channel of the prototype, the extrinsic charging efficiencies however are different. The maximum extrinsic charging efficiency (i.e. 63%) is found at the case with corona-D (i.e. case 4 in Figure 6.3) operated at current of 2 μA. Two wires operated at the same total corona current, even higher corona current (i.e. case 6, 8, 10, 11 in which two wires were both operated at 2 μA corona current) could not improve the extrinsic charging efficiency, implying more particle loss. It may be because of too much ions in the charging zone and low aerosol flowrate. Hence, the case #4 where corona discharge happened at the channel closed to the aerosol outlet gave the highest extrinsic charging efficiency and ratio of extrinsic-to-intrinsic charge efficiency. And the charger would be fixed at this operational configuration for the subsequent evaluation.

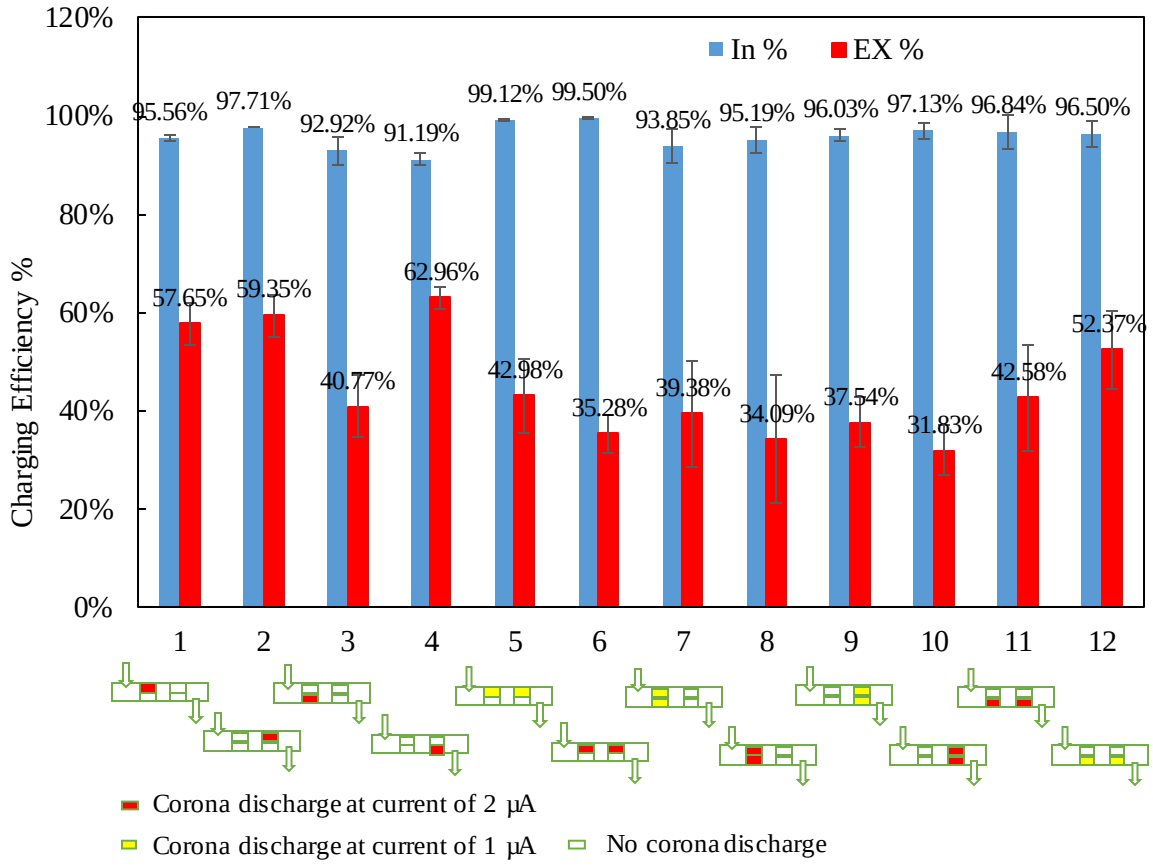

Figure 6.3: Comparison of intrinsic and extrinsic charging efficiencies among different charger configuration for 40 nm NaCl particle at aerosol flowrate of 0.3 lpm.

6.4.2 Effects of Operational Variables on Charging Efficiency of the Prototype

The particle residence time directly influence particle charging performance of the studied charger. Figure 6.4 shows the intrinsic and extrinsic charging efficiencies of 40 nm particles at three different aerosol flowrates, 0.3, 0.6 and 1.5 lpm, respectively. The corona discharge current was fixed at 2 μA on the corona channel D. As shown in Figure 6.4, both intrinsic and extrinsic charging efficiencies decrease with an increase of aerosol flowrate,

due to the decrease of the $N_i t$ value. Also, a decrease of the ratio of extrinsic and intrinsic charging efficiency was observed, indicating less particle loss in higher aerosol flowrate condition. Because the charged particles will be eventually measured by an aerosol electrometer, which is based on current measurement, more particles number is preferred. And by comparing the extrinsic charging efficiency (~63%) at 0.3 lpm aerosol flowrate with that (~60%) at 0.6 lpm aerosol flowrate, 0.6 lpm would be a better choice for aerosol flowrate control, because of no big reduced in aerosol charging efficiency in this case.

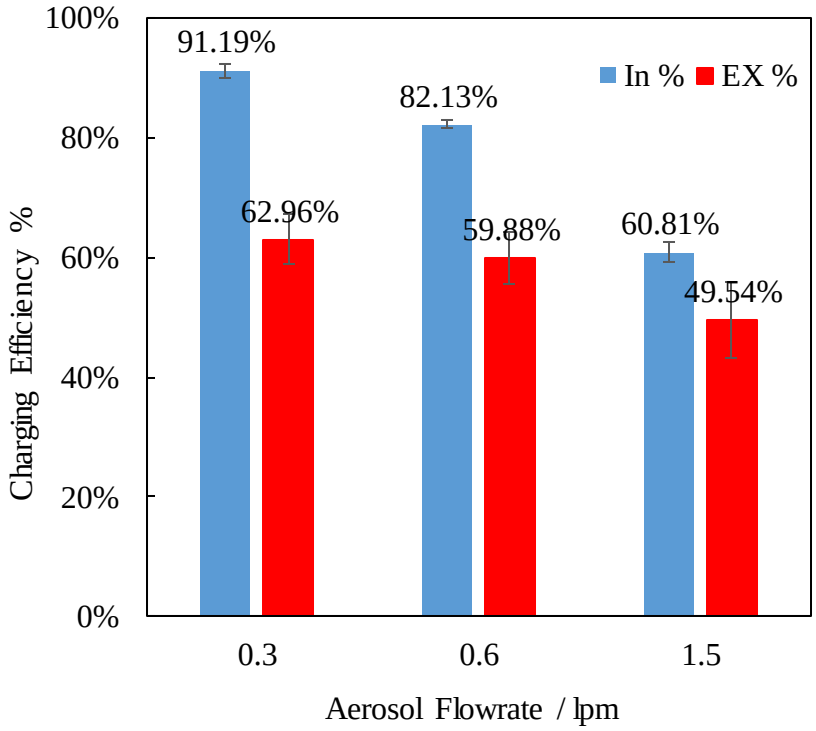

Figure 6.4: Aerosol flowrate effect on the charging efficiencies of the prototype mini-plate charger when operated at corona current of 2 μA.

The ion concentration in the prototype charger can be controlled by tuning the corona current. The higher the current is, the more ion could be generated form the DC corona, resulting in higher intrinsic charging efficiency. However, more charged particle loss could occur due to the space charging effect. That means, the extrinsic charging efficiency of the prototype would not be continuously increased if we simply increased the ion concentration. Three different corona currents, 1, 2 and 4 μA were applied into the prototype for evaluation. 40 nm NaCl particles were tested and the aerosol flowrate was kept at 0.6 lpm. Figure 6.5 shows the intrinsic and extrinsic charging efficiencies increase when corona current increases form 1 μA to 4 μA. But the increase of extrinsic charging efficiency is not so noticeable. That is, extrinsic charging efficiency of the studied charger is believed to stay at 60% no matter how much corona current increases. Therefore, from the view of energy saving, the optimal operational setting of the studied prototype was to operate one wire at corona channel D with 2 μA corona current.

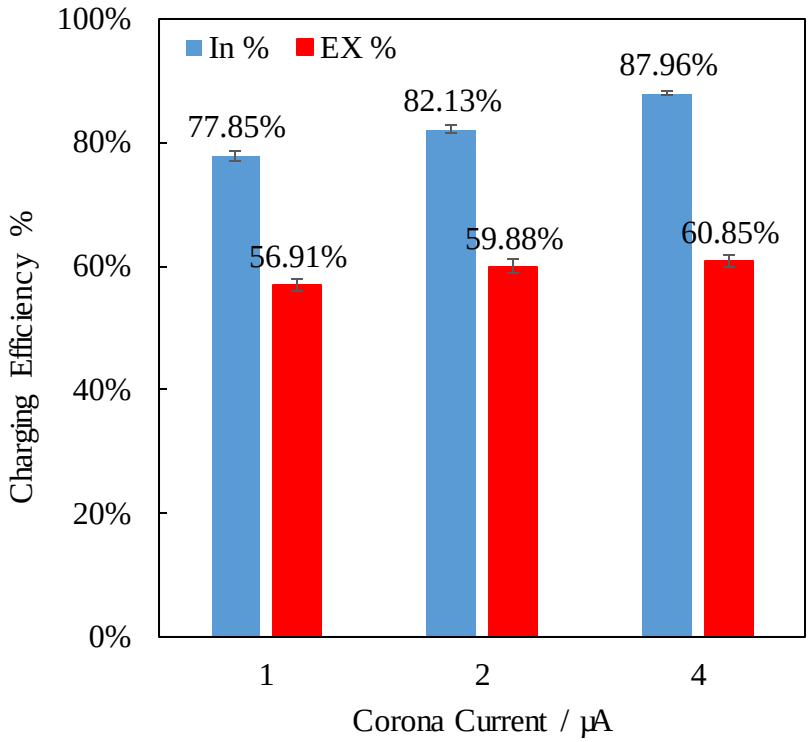

Figure 6.5: Corona current effect on the charging efficiencies of the prototype mini-plate charger when operated at aerosol flowrate of 0.6 lpm

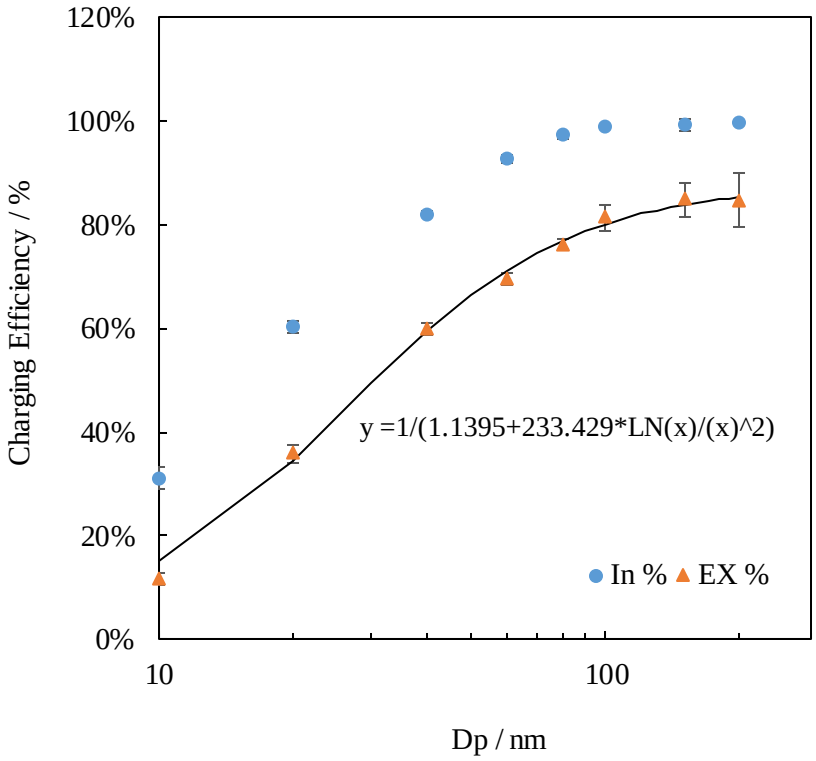

Figure 6.6: Charging efficiencies for particles from 10 nm to 200 nm when the prototype mini-plate charger was operated at aerosol flowrate of 0.6 lpm and corona current of 2 μA

Figure 6.6 shows the intrinsic positive charging efficiencies and extrinsic positive charging efficiencies for particles from 10 nm to 200 nm when operating the mini-plate charger at the optimal configuration. The charging efficiencies increase when particle size become larger. The extrinsic charging efficiency of 10 nm particles was about 12%, evidencing a good charging performance of the studied charger without any ion driving voltage/flow. For particles larger than 100 nm, the intrinsic charging efficiency reaches the maximum value of 100% while the extrinsic charging efficiency stays around 85%. Also, the ratio of extrinsic charging efficiency to intrinsic charging efficiency increased with the

increase of particle size, from 38% (for 20 nm particles) to 78% (for 60 nm particles), indicating that smaller particles were more likely lost inside the charger. More, a data-fitted equation in Figure 6.6 can be used in the data reduction scheme to recover the size distribution for particles smaller than 200 nm.

6.4.2 Charge Distributions for Ultrafine Particles

Extrinsic charging efficiency indicates only the percentage of particles that acquire electrical charges from the charging device. However, in many applications, including particle size distribution measurement based on electrical mobility, it is necessary to know the charge distribution of particles passing through a charger. The charge distribution data are required in the data inversion scheme of an aerosol electrical analyzer to recover the size distribution from measured electrical mobility distribution. Using the TDMA experimental setup described before, the charge distribution of monodisperse test particles of different size were measured when the prototype was operated at the optimized configuration. The experimental data for particles with mobility size of 10, 20, 40, 60, 80, and 100 nm are shown in Figure 6.7. Note that the experimental results are the extrinsic charging distributions of particles, no the intrinsic ones. For particles with sizes less than 20 nm, the charge distribution results indicate that almost all the charged particles were singly charged. As particle size increases, particle charge distributions move towards multiple charge status. Multiple charges of particles occurred for particles larger than 20 nm. For 100 nm particles, a small fraction of particles acquire 5 elementary charges while the dominant charge number

is 2 and 3. The average charge of the test particles can be calculated based on the charge distribution data and are shown in Figure 6.8. The average charge of particles increases from 1 for 10 nm particles to 2.69 for 100 nm particles.

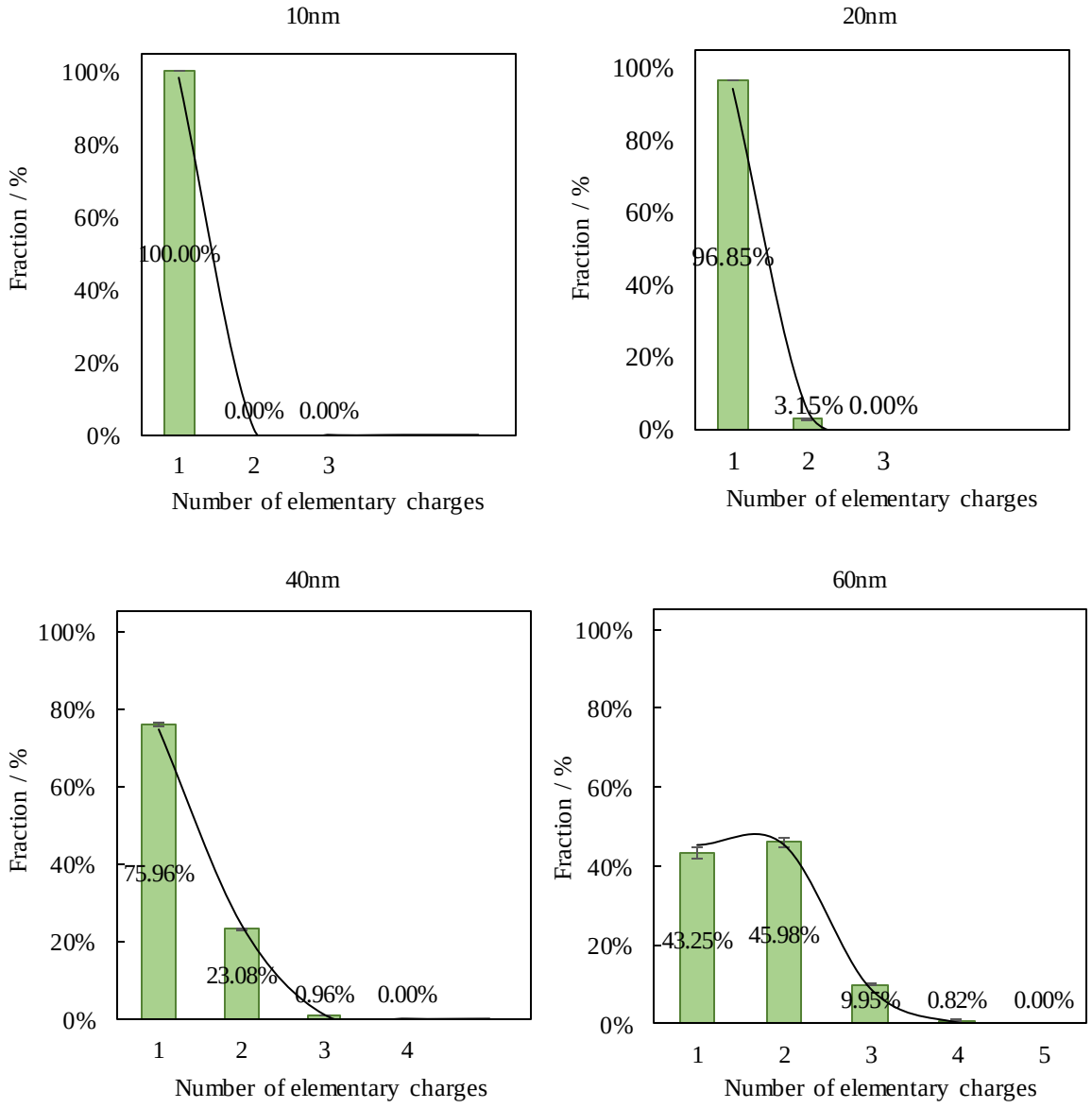

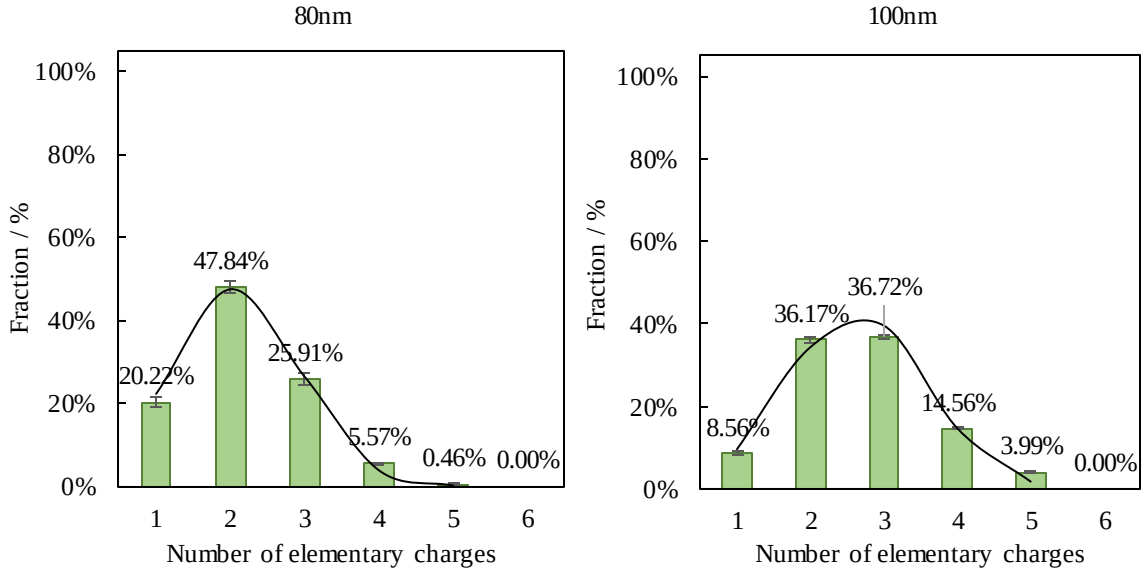

Figure 6.7: Measured positive charge distributions of monodisperse particles when the prototype was operated at 0.6 lpm aerosol flowrate and 2 μA corona current at channel D.

To well predict charge distribution for particles with different size, a Gaussian distribution function (i.e., $y = a \times \exp(\frac{(x-x_0)^2}{b^2})$) as was proposal to fit the charge distribution data for test particles. It is found that the three parameters in the Gaussian distribution equation are functions of average charge and particle size. By best fitting the experimental charge distributions, a data fitted Gaussian distribution equation for predicting the extrinsic charge distribution can be expressed as:

$$y = 8.3691 D_P^{-0.655} \times \exp\{\frac{[x-(0.0281\,D_p - 0.1847)]^2}{(0.0039 D_p + 0.5502)^2}\} \quad (6\text{-}3)$$

where D_p is particle size (unit: nm). As shown in Figure 6.7, the general trends of the experimental and fitted charge distribution agree very well. That is, the proposed equation (6-3) can be applied into the data inversion scheme for calculating particle size distribution.

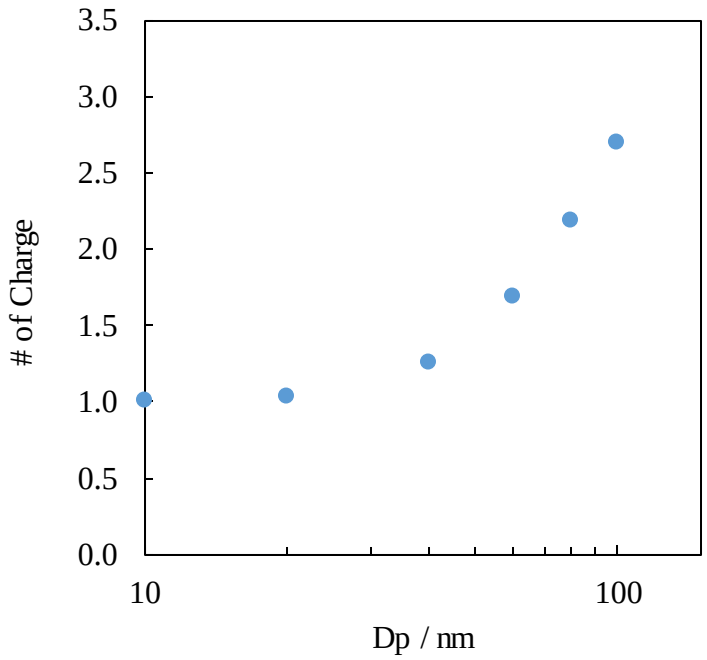

Figure 6.8: Average number of elementary charges as a function of particle size

6.5 Summary

The performance of a prototype DC corona-based, unipolar aerosol charger has been experimentally investigated in this study. The design of the prototype charger consists of two similar brass blocks, where four identical corona channels (two in each) were designed inside. 50 μm Tungsten wires were used to provide corona ions when high electric field was established between wires and the grounded perforated plates. An aerosol charging channel was designed in the bottom block, surrounding by corona channels. Aerosol flow was

injected into the charger through the top tube, passed through the charging zone and then exited from the bottom tube. The ion concentration in the charging zone depended on the strength of the high voltage applied to the wires, number of the wire used (or which corona channels were used). For simplifying the operation, no sheath air and ion driving voltage were designed to be used in this prototype.

The charger's performance was optimized by varying operational parameters (i.e., corona position, aerosol flowrate, corona current) to achieve high extrinsic charging efficiency as possible. The optimization experiment was done with DMA classified monodisperse NaCl particles of 40 nm mobility diameter. Based on the experimental results (i.e. intrinsic and extrinsic charging efficiencies), it is concluded that one wire corona condition is better for particle charging than two wire corona. The corona occurring at the channel closed to the aerosol outlet provides highest extrinsic charging efficiency, resulting in less particle loss. By investigating the charging performance at different corona currents, the corona current of 2 μA with good charging efficiency and low energy consumption was used in the rest of the study. It is also found that operating the prototype at a 0.6 lpm aerosol flow is a better choice when considering to use an electrical detector for aerosol measurement downstream.

Both intrinsic and extrinsic charging efficiencies of particles with mobility diameters ranging from 10 to 200 nm were measured at the optimal operation condition (i.e. 0.6 lpm aerosol flowrate and 2 μA corona current occurring at the channel D). As expected, the intrinsic and extrinsic charging efficiencies increase with the increase of particle size. The

highest extrinsic charging efficiency of the prototype was about 85%. The extrinsic charge distributions of monodisperse particles from 10 nm to 100 nm at the downstream of the prototype were measured by the tandem-DMA technique. Multiple charge effect could be found for particle larger than 20 nm. The average charge was calculated based on the experimental charge distribution data. A Gaussian distribution function with particle size as variable was used to fit particle charge distribution. And a reasonable agreement was achieved when the fitted charge distribution of particles were compared with the extrinsic charge distributions measured, indicating the fitted Gaussian function could be used into the data inversion scheme for retrieving particle size distribution from the measured mobility distribution in a particle mobility analyzer.

CHAPTER 7 Design and Evaluation of Miniature Plate EAA/DMAs (mini-plate EAA/DMAs) for Ultrafine Particle Sizing and Characterization

7.1 Introduction

A new miniature DMA in the parallel plate configuration were proposed in this study to classify ultrafine particles because of the simple design, easy maintenance as well as low manufacturing cost. A similar DMA, which was the particle sizer in the commercial Nano-ID PMC500, has been reported in the work of Steer et al. (2014). However, no Tandem DMA experiment was performed to calibrate the prototype performance (i.e., DMA transfer function). It remains at large regarding to the particle sizing and penetration of the above DMA.

Due to its simple operation, the first generation of plate aerosol electrical mobility analyzer, a cost-effective, mini-plate EAA was designed and constructed in this work. The detail performance of the prototype EAA was carefully evaluated via TDMA experiments, by measuring its penetration curves for DMA classified particles with different electrical mobilities at fixed flow condition. The flow condition was also needed to be optimized by varying aerosol and sheath flowrates. The transfer function of the prototype mini-plate EAA was retrieved from experimental data via a deconvolution scheme. And, a simple 2D model

to predict the performance of the prototype was also derived for comparison with experimental transfer function.

With the success in developing mini-plate EAA for ultrafine particle sizing and characterization, the advanced version of plate aerosol electrical mobility device, mini-plate DMA, was designed. Two prototype mini-plate DMAs with different geometric dimensions were manufactured and studied. The TDMA experiments were also conducted carefully for two DMAs by varying the voltage applied on the mini-plate DMA while the calibrated first DMA was operated at fixed voltage. The transfer function was obtained through a piecewise-linear function deconvolution method developed by Li et al. (2006). The sizing accuracy and transfer functions of the prototypes under different flow conditions were evaluated from their TDMA data. The effect of DMA geometry on the particle sizing performance of mini-plate DMAs was also investigated with two prototype mini-plate DMAs having different dimensions in the classification region.

7.2 Design of Studied Mini-plate EAA

The schematic diagram of mini plate EAA with critical dimensions is shown in Figure 7.1. The prototype mainly consists of two insulating blocks (made of Delrin), in which two identical stainless steel plates are parallelly installed to create the particle classification zone. The 1/16" spacing between these two electrodes is determined by the difference between the depths of two electrode plate grooves. The length of particle classification zone is 1 39/64" and the width is 1". Also, the aerosol flow entrance, sheath flow entrance and aerosol flow outlet were built in the delrin blocks. As shown in Figure

7.1, aerosol flow enters the device from the middle channel of the lower block, and then meets with the particle-free sheath flow from the right. Both of the aerosol entrance and exit slit were designed to be a narrower 1/2" in width compared with the full width (1") of the classification zone. After passing through the electric classification zone, the total flow goes out of the device through the outlet on the left. In order to provide laminar flow condition for well classifying ultrafine particles, a flow larminazer was installed at the beginning of classification zone. For creating electric field, negative high voltage was chosen to be connected to the upper plate and the ground was applied to the lower plate. Thus, positive charged particles can be selected through the device. The overall size of this prototype mini-plate EAA was 3 7/32" in length, 1 3/4" in width and 13/16" in height, which is comparable to the size of an iPhone 5s.

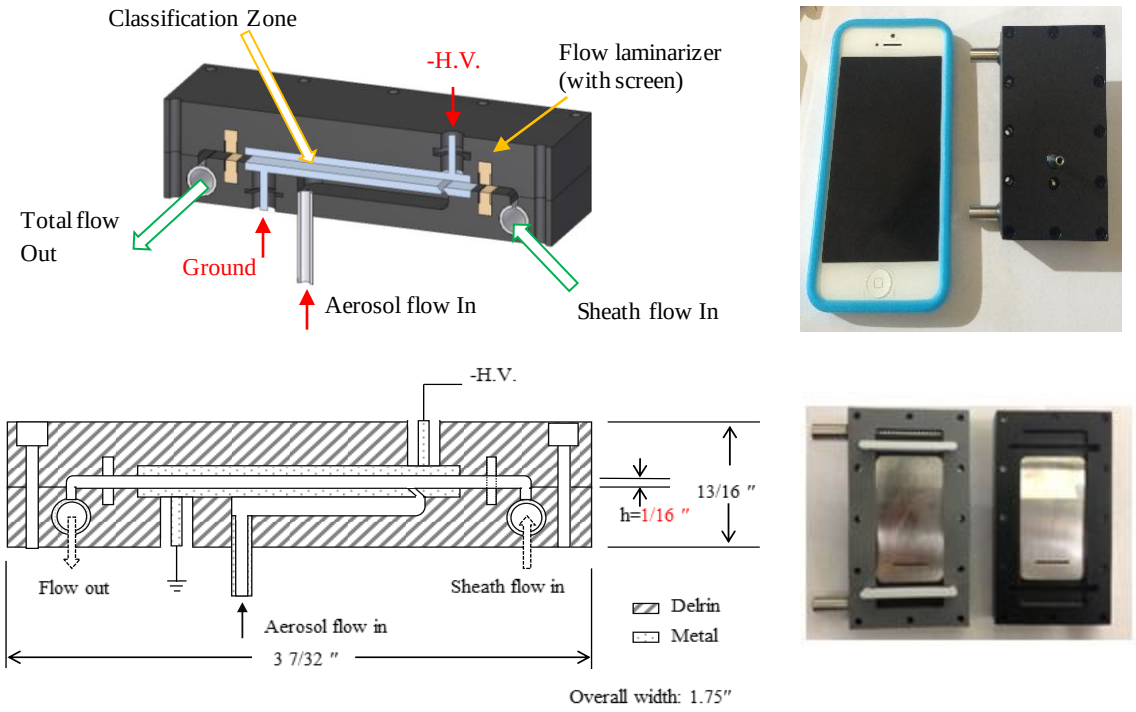

Figure 7.1: Schematic diagram of prototype mini plate EAA

7.3 Experimental Setup for Mini-plate EAA Evaluation

The experimental setup to evaluate the performance of prototype mini-plate EAA is shown in Figure 7.2. Test NaCl nanoparticles were generated by DMA-classifying polydisperse particles generated from either a custom-made Collison atomizer or evaporation-condensation technique (Scheibel and Porstendorfer, 1983; Li et al. 2009). Droplets produced by the atomizer were dried into solid particles by passing through a diffusion-type dryer with silicone gel as the desiccant. NaCl aerosol particles generated by the atomization technique had the peak electrical mobility sizes larger than 30 nm. The peak sizes of generated particles were varied by atomizing the NaCl solution at various

concentrations. To produce particles with electrical mobility sizes smaller than 30 nm, NaCl powder (ACS reagent, ≥ 99.0%, Sigma-Aldrich) was placed in a ceramic boat (Al_2O_3, Coors Ceramics Co), located in a high-temperature tube furnace (Lindberg/Blue M tube Furnace, HTF55322C, Thermo Scientific). The powder was evaporated when the furnace temperature was set in the range of 500-700 ℃. NaCl vapor was then carried by carrier gas (either nitrogen or compressed air) which flowrates were controlled by a needle valve and a laminar flowmeter. At the exit of the furnace, the vapor-rich carrier gas was mixed with particle free air (as the quenching flow) at the room temperature to produce nanoparticles by nucleation and condensation processes. The mean sizes and concentration of generated particles could be varied by the furnace temperature and the ratio of vapor-rich and quenching flow.

To evaluate the performance of mini-plate EAA, singly charged monodisperse aerosol were obtained by using a calibrated DMA (TSI Model 3081 and 3085) at the aerosol-to-sheath flowrate ratio of 1:10. Prior to the TSI DMAs, polydisperse aerosol was passed through a Kr^{85} radioactive bipolar charger to impart a steady-state charge distribution on them (Knutson & Whitby, 1975). A laminar flowmeter monitored the flowrate of polydisperse aerosol stream into the DMAs. Seven particle sizes were chosen for EAA calibration: 20, 40, 60, 80, 100, 120 and 150 nm.

The aerosol flowrate of mini-plate EAA was also monitored by a laminar flowmeter. An Ultrafine Condensation Particle Counter (UCPC, TSI model 3776) and a vacuum pump with a needle valve at the downstream of the studied EAA were used to measure the particle number concentration and the total flowrate at the downstream of the mini-plate EAA.

Another two laminar flowmeter and a needle valve were used to monitor flowrates and check flow balance. To investigate flow effects on the performance of mini-plate EAA (e.g., aerosol-to-sheath flowrate ratio, total flowrate), aerosol and sheath flows were varied at the rates less than 0.7 lpm and 3.2 lpm, respectively. And a high-voltage power supply (Bertan Model 205B-10R) was used to apply various high DC voltage to the mini-plate EAA.

By turning off the high voltage on studied EAA and measuring the particle concentrations at both upstream (N_p) and downstream ($N_d(0)$) of the prototype, the transmission efficiency of singly charged particles through the prototype was first investigated for different particle sizes, as the ratio of these two values:

$$Transmission = \frac{N_d(0)}{N_p} \tag{7-1}$$

To measure the particle penetration curves of the mini-plate EAA, a series of high voltages were applied onto the mini plate EAA and the downstream particle concentration at different voltage settings $N_d(V)$ were then measured. As applied voltage was gradually increased from zero, more number of particles precipitated on the bottom electrode. All charged particles eventually precipitated when sufficiently high voltage was applied. The particle penetration curve for a given DMA-classified aerosol was obtained by the measured particle penetration (P) as a function of applied voltage:

$$P(V) = \frac{N_d(V)}{N_d(0)} \tag{7-2}$$

Note that, the applied voltage when 50% particle penetration efficiency of mini-plate DMA was obtained was considered as the 50% voltage (V_{50}) for sizing particles of selected sizes.

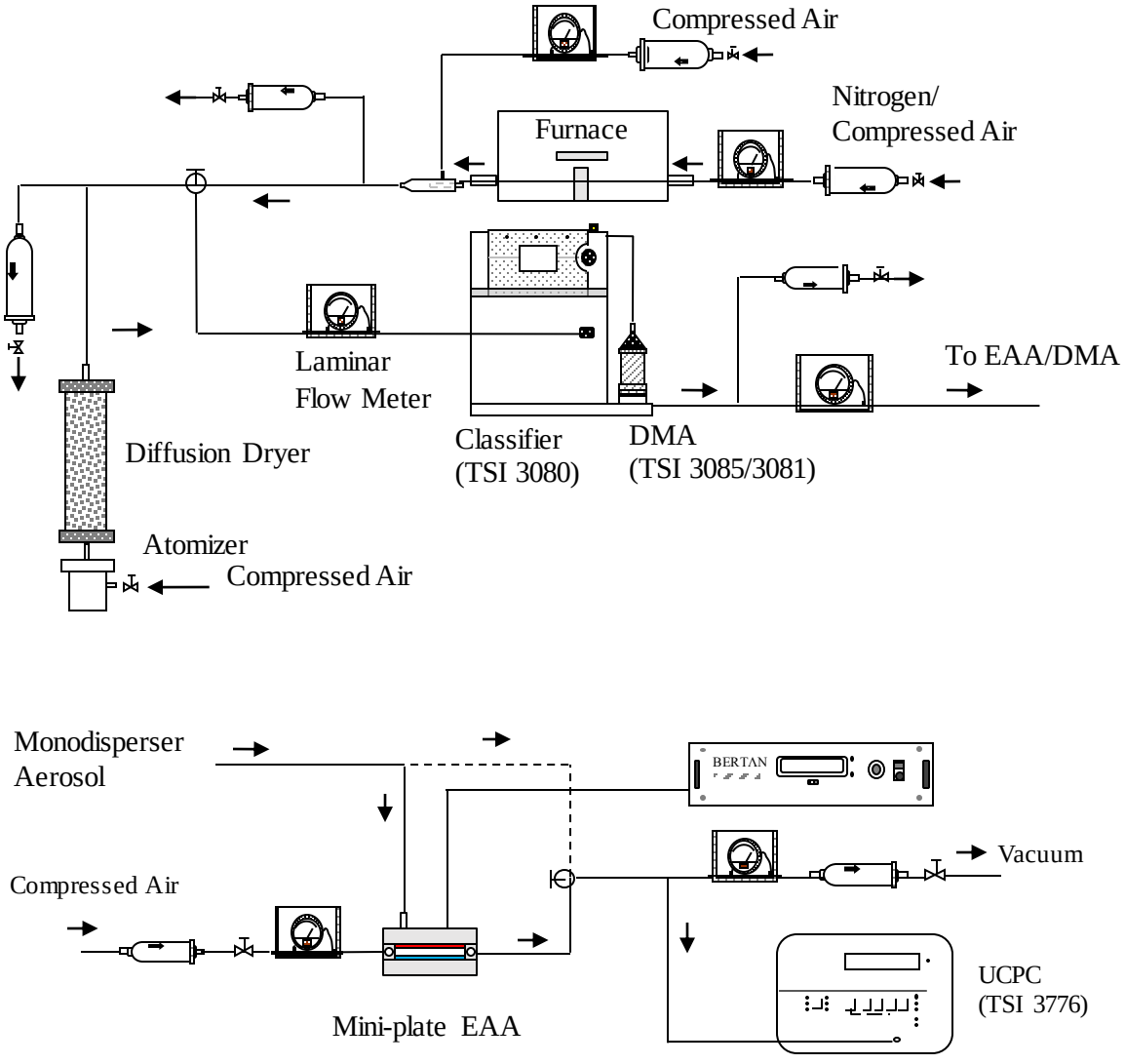

Figure 7.2: Experimental setup for the performance evaluation of mini-plate EAA

7.4 Result and Discussion for EAA

7.4.1 Particle Transmission Efficiency

Figure 7.3 shows the measured transmission efficiency of singly charged particles with size ranging from 25 nm to 150 nm through the mini plate EAA, when operated at total flow rate of 2 lpm. Aerosol-to-sheath flow rate ratio of 1:8 and 1:4 were both investigated in this experiment. As shown in Figure 3, there is no difference of particle transmission efficiencies between the two studied cases. Which means, aerosol-to-sheath flowrate ratio has no apparent effect on the transmission efficiencies of singly charged particle in the prototype mini plate EAA. The loss of particle increases as the particle size decreases. The transmission efficiency of singly charged particles reduced to 72% and 78% at 25 nm, for aerosol-to-sheath flow rate ratio of 1:8 and 1:4, respectively. For particles larger than 60 nm, the loss is believed to be negligible, indicating a good transmission performance of the mini plate EAA, despite its narrow spacing of the classification region. Also, a data-fitted equation shown in Figure 3 can be used in the data inversion scheme to recover the true size distribution for particles larger than 25 nm.

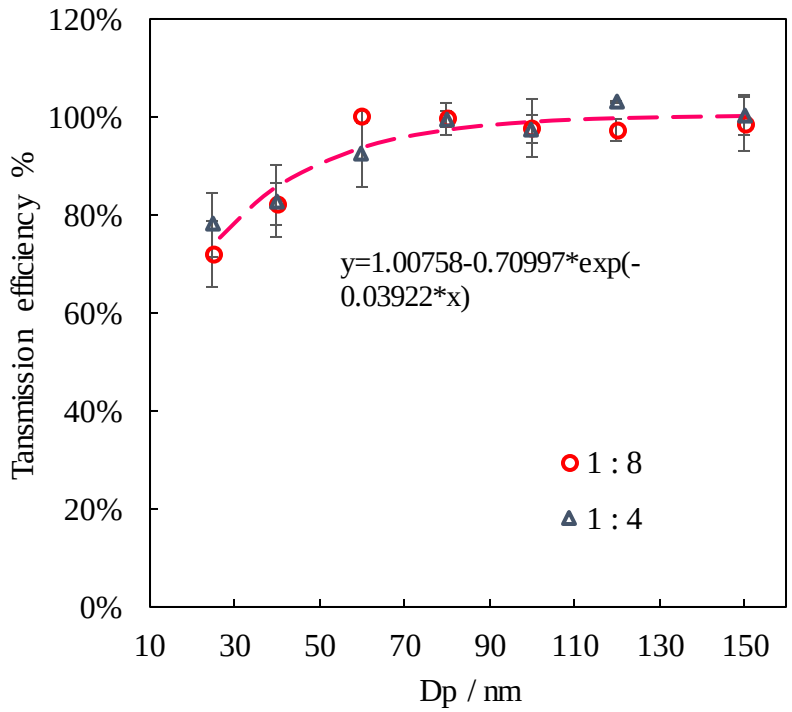

Figure 7.3: Transmission efficiency of singly charged particles in mini-plate EAA when the prototype was operate at aerosol-to-sheath flowrate ratio of 1:8 and 1:4, respectively

7.4.2 Penetration Curves of the Prototype Mini-plate EAA

(a) Effect of aerosol-to-sheath flow rate ratio

Given the geometry of EAA, at a fixed operational flowrate, the performance of a mini-plate EAA was characterized by its penetration curves or transfer function, which describes the particle penetration efficiency as a function of voltage applied to the device. Figure 7.4(a) shows the penetration curves of 100 nm particles, when the mini-plate EAA was operated at constant total flow rate of 2 lpm but with different aerosol-to-sheath flow rate ratio (i.e., 1:2, 1:4, 1:6, 1:8, 1:10, 1:12). The measured penetrations at voltage V was

normalized with transmission efficiency at V=0, while the corresponding voltage was normalized using V_{50}, the voltage at 50% particle penetration. As expected, the steepness of EAA penetration curves (i.e., the slope of lines tangential to the 50% normalized particle penetration) increases with the decrease of the aerosol-to-sheath flow rate ratio. The slope as a function of sheath-to-aerosol flowrate ratio is also evidenced in Figure 7.4(b). It is found that the sharpness of penetration curves could not be significantly improved by increasing sheath-to-aerosol flowrate ratio when it is larger than 8. Therefore, it is suggested to operate the prototype EAA at the aerosol-to-sheath flowrate ratio at 1:8 for the subsequent experiments. Because the lower aerosol-to-sheath flowrate ratio, the greater dilution of aerosol flow exiting the prototype mini-plate EAA. It is not worth to operate EAA with non-improved sizing resolution, while losing the aerosol detection accuracy if one is using Faraday cage as aerosol detector.

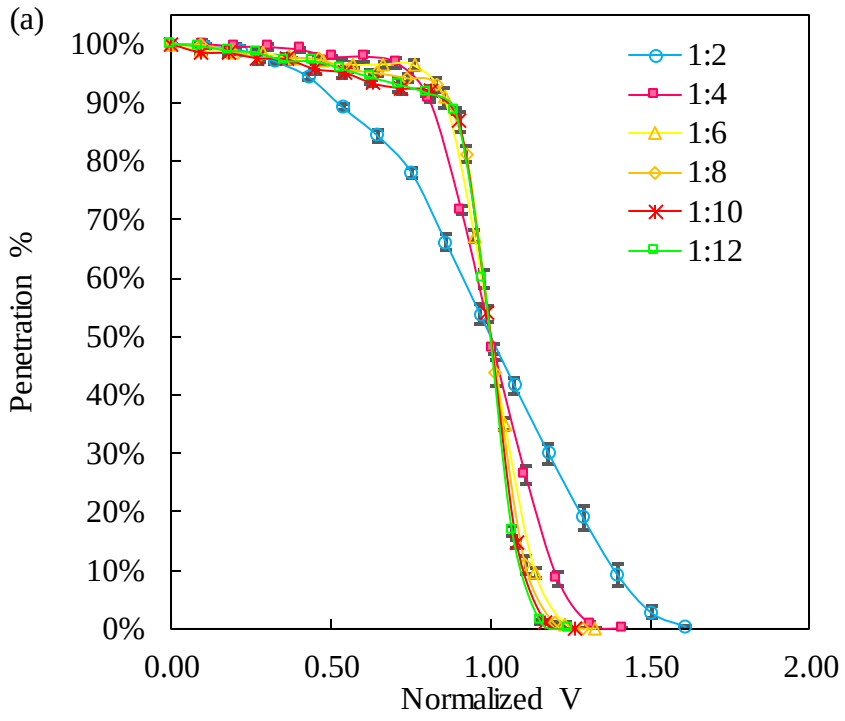
(a)
100%
90%
80%
70%
60%
50%
40%
30%
20%
10%
0%
Penetration %
0.00
0.50
1.00
1.50
2.00
Normalized V
1:2
1:4
1:6
1:8
1:10
1:12

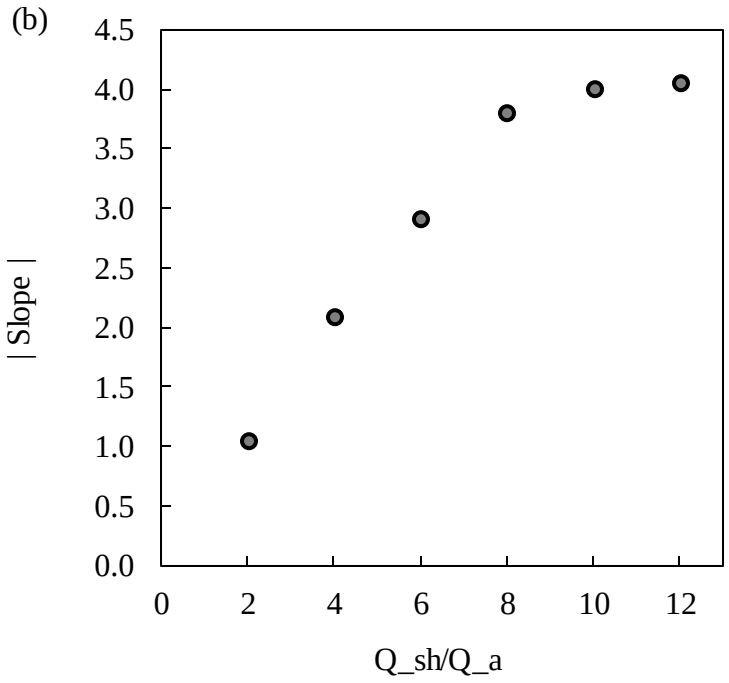
(b)
4.5
4.0
3.5
3.0
2.5
2.0
1.5
1.0
0.5
0.0
| Slope |
0
2
4
6
8
10
12
Q_sh/Q_a

Figure 7.4: (a) Particle cutoff curve of the mini-plate EAA for 100nm particles at different aerosol-to-sheath flowrate ratios when the total flowrate is 2 lpm; (b) The slope of the cutoff curve at 50% penetration as a function of sheath-to-aerosol ratio

(b) Effect of total flow rate

As shown in Figure 7.5 is the particle penetration curves of 100 nm particles when mini plate EAA was operated at different total flow rate (i.e., 1, 2, 2.5, 3 and 3.5 lpm) with a constant aerosol-to-sheath flow rate ratio of 1:8. By normalizing the penetration with respect to the transmission efficiency at V=0 and normalizing the applied voltage with V_{50}, all data collapse into one curve, indicating the effect of total flow rate on the characteristics of penetration curves of the mini-plate EAA is negligible when it is smaller than 3.5lpm. From the view of personal instrumentation, low voltages are preferable, resulting in low total flow rate requirement. Due to the optimal aerosol-to-sheath flowrate ratio of 1:8, aerosol flowrate is about 111 sccm when choosing total flowrate of 1 lpm. It is too low to be precisely controlled. In this study, it is thus desirable to operate the min plate EAA at total flow rate of 2 lpm for subsequent evaluation.

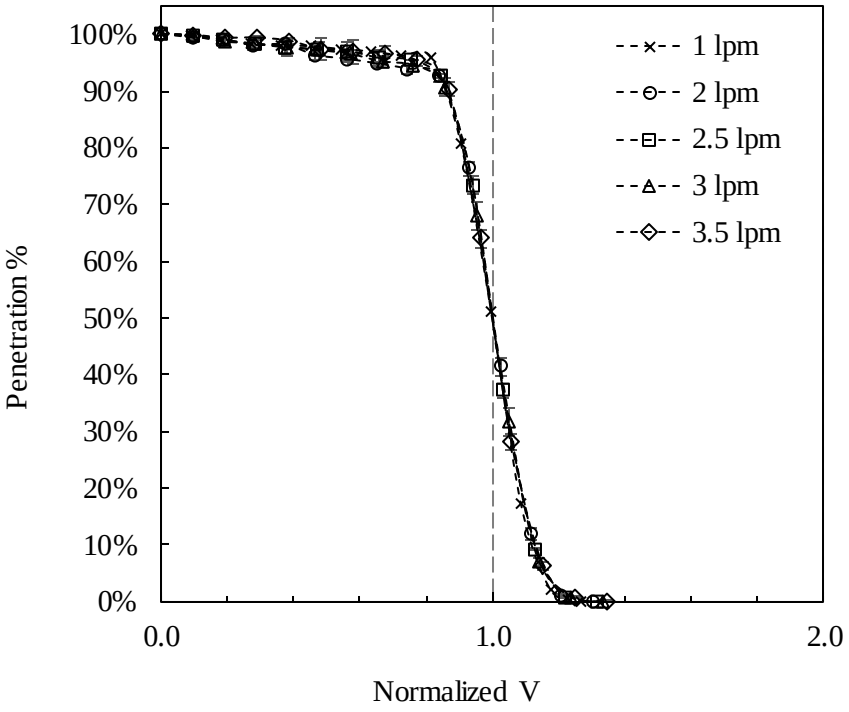

Figure 7.5: Particle cutoff curve of 100nm particles when the mini-plate EAA was operated at the aerosol-to-sheath flowrate ratio of 1:8 while varying the total flowrate

(c) Effect of particle size

Figure 7.6(a) are particle penetration curves for DMA-classified particles in different diameters when the prototype is operated at total flow rate of 2 lpm and aerosol to sheath ratio of 1:8, respectively. The measured penetrations for different particle size were also normalized with its transmission efficiency at zero voltage. As expected, the larger particle size is, the higher V_{50} is needed to reach 50% penetration efficiency. Moreover, from this curves, the critical electrical mobility Z_{pc}, defined as the electrical mobility of particles having 50% penetration as they pass through the prototype for any given voltage, can thus

be determined. After normalizing the applied voltages with V_{50}, all these curves merge into one, as shown in Figure 7.6(b). This indicates that the penetration characteristics, or the transfer function of the classifier, are size-independent over the measuring range at fixed flow condition.

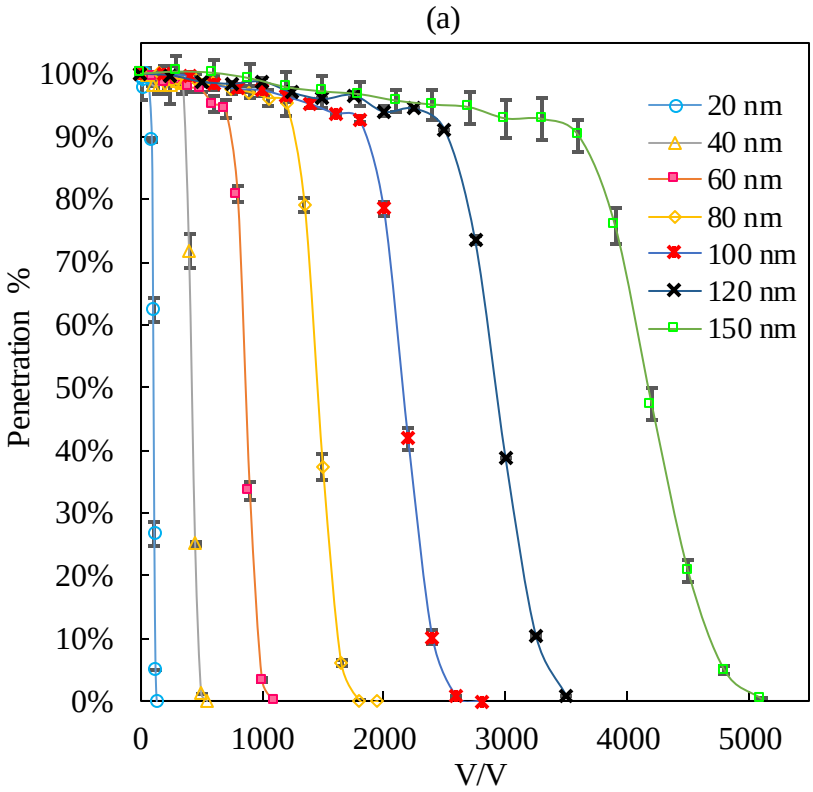

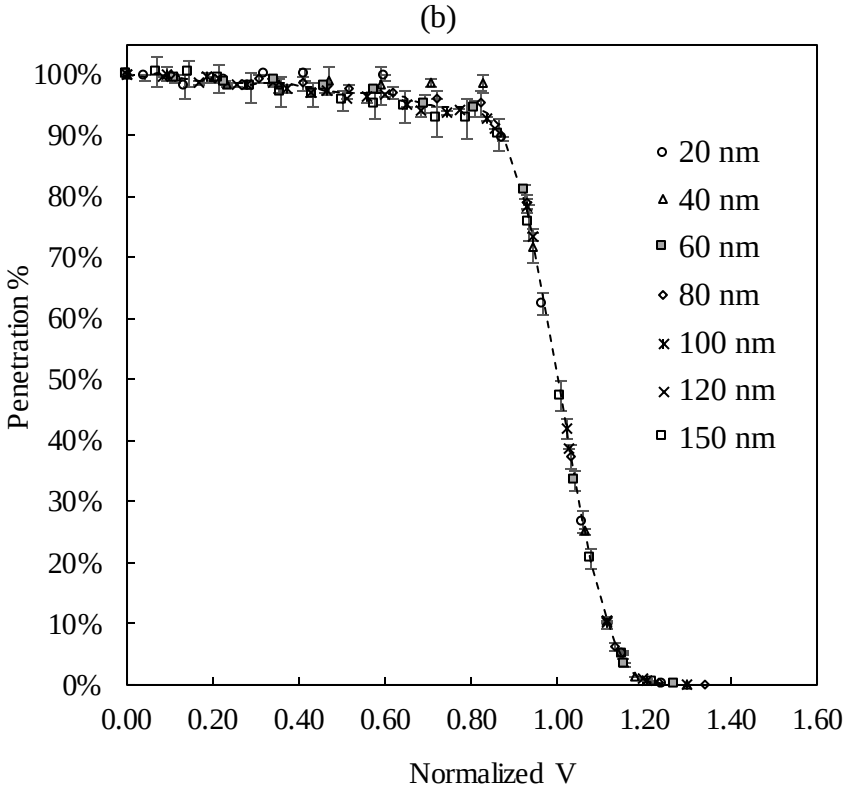

Figure 7.6: Particle cutoff curves of different particle sizes when the mini-plate EAA was operated at the total flowrate of 2lpm and aerosol-to-sheath flowrate ratio of 1:8: (a) Normalized penetration vs. applied voltage; (b) Normalized penetration vs. normalized voltage

7.4.3 2D Model and Transfer function of the Prototype Mini-plate EAA

The transfer function, which is defined as the probability that aerosol of mobility Z_p is classified through the EAA outlet when a voltage difference V is applied between the electrodes, is usually used to describe the characteristic of the mini-plate EAA. The measured penetration curve of the mini-plate EAA is actually the convolution of the transfer function of both the DMA and the mini-plate EAA. To characterize the performance of the

mini-plate EAA, a deconvolution scheme is used to recover the transfer function of the mini-plate EAA. A simple 2D model of plate EAA is also needed to be discussed to understand the classifying mechanism of EAA fundamentally. Once it is experimentally verified, the model can be applied to predict classifying voltage (V_{50}) and particle transfer function for recovering particle size distribution by a data inversion scheme.

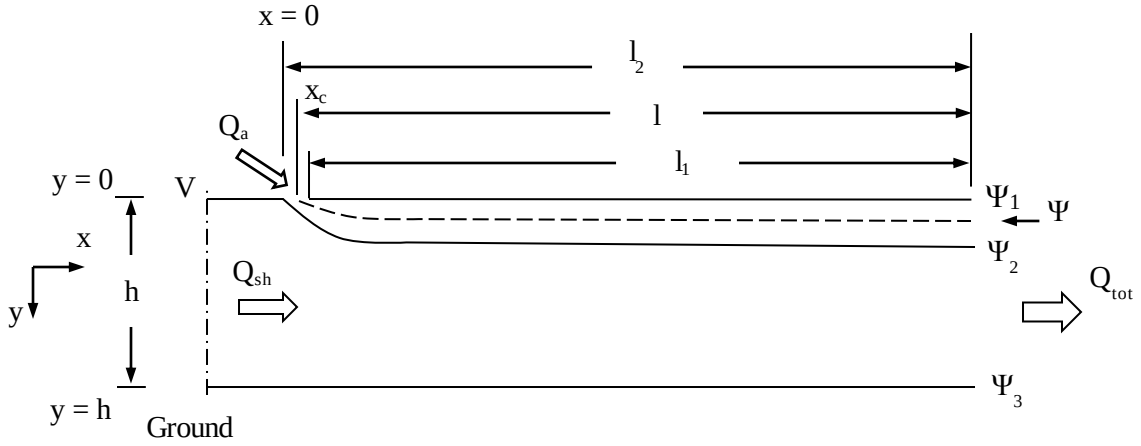

Figure 7.7: 2D illustration of the particle classification region in a plate EAA

Figure 7.7 shows the simplified classification region of the studied mini-plate EAA in 2D Cartesian coordinates, with x and y denoting the horizontal and vertical coordinates. As shown in Figure 7.7, sheath gas flows in horizontal direction, while aerosol flow is injected from a slit with y = 0. The electric field is directed along the y-coordinate, normal to the electrodes. Neglecting the particle inertial and diffusion effects, the trajectory of a charged particle is governed by the following equations:

$$\frac{dx}{dt} = u_x \tag{7-3}$$

$$\frac{dy}{dt} = Z_P E_y, \left(Z_P = \frac{q\, C_s}{3\pi\mu\, D_p}\right) \tag{7-4}$$

where u_x is the x-component of the flow velocity; E_y is the y-component of the electrical field; q is the charge level on test particle; C_s is the Cunningham correction factor; μ is the gas viscosity; and D_p is the test particle size. For simplification, it is also assume the electrical field distortion and flow distortion at both the aerosol entrance and outlet are negligible. The electric field is therefore constant in y-direction (i.e., $E_y = V/\, h$) and zero in x-direction. And the flow velocity in the classification region is thus to be considered in the x-direction only. Then, the stream function Γ formulation for non-diffusive particles can be expressed as

$$\Gamma(x,y) = \Psi(x,y) + Z_P \Phi(x,y) \tag{7-5}$$

in which, Ψ and Φ are the fluid stream function and electric flux function, respectively.

With the assumption of incompressible and laminar flow, the fluid stream function and electric flux function can be expressed as follows,

$$\Psi(x,y) = \int u_x\, dy \tag{7-6}$$

$$\Phi(x,y) = -\int E_y\, dx \tag{7-7}$$

Because particle stream function remains constant along the particle trajectory in an EAA, the following equation applies for the trajectory of particles with a given electrical mobility:

$$\Delta\, \Psi(x,y) = -Z_P \Delta\Phi(x,y) \tag{7-8}$$

Three limiting streamlines, Ψ_1 , Ψ_2 and Ψ_3 was schematically shown in Figure 7.7. The streamlines Ψ_1 and Ψ_2 are boundaries of the aerosol flow (Q_a) entering through the entrance

slit, while the streamlines Ψ_2 and Ψ_3 are boundaries of the sheath flow (Q_{sh}). Since both the aerosol flow and sheath flow leave the EAA from the same outlet, the streamlines Ψ_1 and Ψ_3 thus bound the total flow. The flowrates of aerosol flow and sheath flow can be described as

$$Q_a = w(\Psi_2 - \Psi_1) \tag{7-9}$$

$$Q_{sh} = w(\Psi_3 - \Psi_2) \tag{7-10}$$

where w is the width of the classification region of mini-plate EAA.

Prior to be classified in the classification region, a charged particle resides on some streamline Ψ_{in}, which is confined to the interval

$$\Psi_1 \leq \Psi_{in} \leq \Psi_2 \tag{7-11}$$

Similarly, the value of Φ for this particle prior to the aerosol entrance slit is described as Φ_{in}, which is deemed as a definite number. That is, the Φ value for the different inject points within the entrance slit is negligible. To simplify the calculate, the Φ value at the exit is defined as a common value of Φ_{out}. Thus, the equation (7-8) becomes:

$$\Psi_{out} = \Psi_{in} - Z_P \, \Delta\Phi \tag{7-12}$$

Here Ψ_{out} must be a number within the range $(\Psi_1 - Z_P \, \Delta\Phi, \; \Psi_2 - Z_P \, \Delta\Phi)$. Base on the equation (7-7), it is easy to obtain

$$\Delta\Phi = \int_{x_{in}}^{l_2} -E_y dx = -\frac{V}{h}(l_2 - x_{in}) \tag{7-13}$$

Due to the very narrow aerosol slit compared to the classification length of the mini-plate EAA, x_{in} can be approximately replaced by x_c (i.e., the center position of the slit in x-direction). So, equation (7-13) becomes:

$$\Delta\Phi = -\frac{Vl}{h} \tag{7-14}$$

where V is operation voltage, l is the classification length of mini-plate EAA and h the height of the classification region in the mini-plate EAA.

Let Ω be the probability that the particle will leave via the device outlet. This event occurs only if

$$\Psi_{out} \leq \Psi_3 \tag{7-15}$$

That is, the particles of Ψ_{out} larger than Ψ_3 will deposit on the bottom plate. Therefore, penetration probability Ω of a particle is equal to the fraction of the interval $(\Psi_1 - Z_P\,\Delta\Phi,\ \Psi_2 - Z_P\,\Delta\Phi)$, which is intercepted by the interval $(\Psi_1,\ \Psi_3)$. By drawing the intervals $(\Psi_1 - Z_P\,\Delta\Phi,\ \Psi_2 - Z_P\,\Delta\Phi)$and $(\Psi_1,\ \Psi_3)$ in juxtaposition, it is found that if $\Psi_2 - Z_P\Delta\Phi \leq \Psi_3$ (i.e., $Z_P \leq Q_{sh}h/(l_2 - x)wV$), all particles pass through the mini-plate EAA (i.e, Ω = 1). If $\Psi_1 - Z_P\,\Delta\Phi \geq \Psi_3$ (i.e., $Z_P \geq (Q_{sh} + Q_a)h/(l_2 - x)wV$), all particles are precipitated in the device (i.e, Ω = 0). And, if $Q_{sh}h/(l_2 - x)wV < Z_P < (Q_{sh} + Q_a)h/(l_2 - x)wV$, classified particles can partially pass through in the device with a penetration proability calculated as

$$\Omega = \frac{\Psi_3 - (\Psi_1 - Z_P\,\Delta\Phi)}{\Psi_2 - \Psi_1} \tag{7-16}$$

Therefore, with the help of (7-9), (7-10) and (7-14), the final result of transfer function of the mini-plate EAA is expressed in the form:

$$P = \max\left\{0, min\left[1{,}1 + \frac{Q_{sh}}{Q_a} - \frac{(Q_{sh}+Q_a/2)}{Q_a}\left(\frac{Z_P}{Z_{P,c}}\right)\right]\right\} \tag{7-17}$$

And the central mobility $Z_{P,c}$, with which particle has 50% penetration efficiency, can be calculated as following equation:

$$Z_{P,c} = \frac{(Q_{sh}+Q_a/2)h}{lwV_{50}} \tag{7-18}$$

(a)

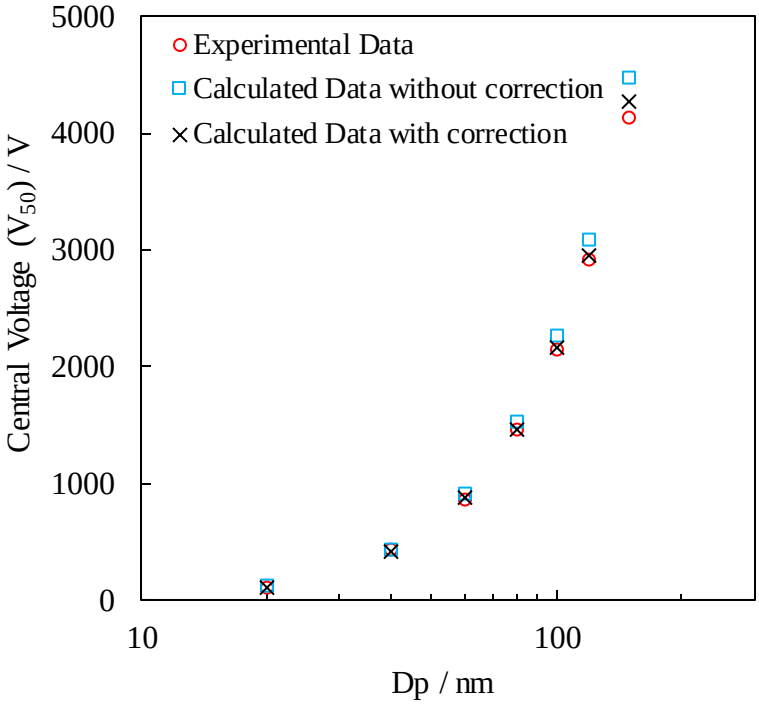
5000
4000
3000
2000
1000
0
Central Voltage (V_{50}) / V
Experimental Data
Calculated Data without correction
Calculated Data with correction
10
100
Dp / nm

(b)

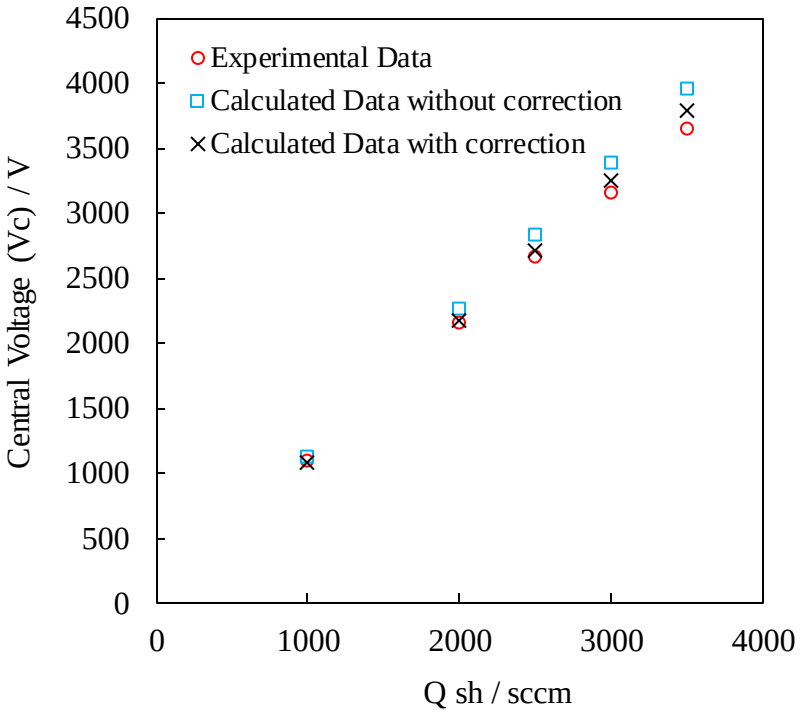
Experimental Data
Calculated Data without correction
Calculated Data with correction
Central Voltage (Vc) / V
Q sh / sccm
0
500
1000
1500
2000
2500
3000
3500
4000
4500
0
1000
2000
3000
4000

(c)

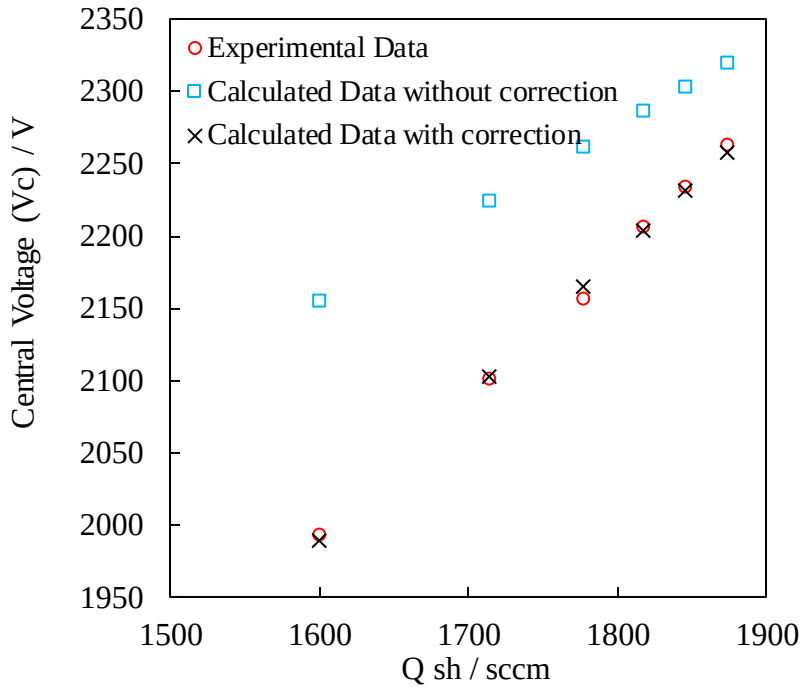

Figure 7.8: Comparison of V50 for particle sizing among experimental data, calculated date without correction and calculated data with correction for 3 different cases: (a) different particle sizing at total flowrate of 2 lpm and Qa/Qsh of 1:8; (b) 100 nm particle classified at Qa/Qsh of 1:8 and different total flowrate; (c) 100 nm particle classified at total flowrate of 2 lpm with different Qa/Qsh values

The experimental V_{50} and calculated V_{50} based on Eq. (7-18) for particles form 20 nm to 150 nm when the prototype mini-plate EAA was operated at total flowrate of 2 lpm and aerosol-to-sheath flowrate ratio of 1:8 are shown in Figure 7.8(a). The measured V_{50} has the same increasing trend as that of calculated V_{50}, indicating the prototype mini-plate EAA functions as expected. However, the measured V_{50} for classifying particles are all smaller than their calculated value. Then same observations were found in Figure 7.7(b) and (c),

when operating the EAA at different total flowrates but with constant aerosol-to-sheath flowrate ratio of 1:8 and at different aerosol-to-sheath flowrate ratios with 2 lpm total flowrate, respectively. These results evidenced that above 2D model cannot well predict V_{50} (or $Z_{P,c}$) for operating and characterizing the mini-plate EAA, resulting in underestimation of classified particle size. Hence, it is necessary to modify this model for further applying it in recovering particle size distribution by a data inversion scheme.

By taking ratios of the measured V_{50} to the calculated V_{50} (i.e. Vm/Vc), a linear relationship between voltage ratios and the aerosol-to-sheath flowrate ratios was found. Figure 9 shows that voltage ratio decreases as aerosol-to-sheath flowrate ratio increases. The result of linear curve fitting was also given in Figure 7.9. Here, the voltage ratio of measured V_{50} to calculated V_{50} based on classic 2D model is defined as an correction factor, η. The Eq. (16) is then rewritten as

$$Z_{P,c} = \frac{\eta(Q_{sh}+Q_a/2)h}{lwV_{50}} \tag{7-19}$$

where, $\eta(\beta) = -0.2761\beta + 0.9915$, β is the aerosol-to-sheath flowrate ratio. Three new sets value of calculated V_{50} with correction for mini-plate EAA operated under different conditions were plotted in the Figure 7.8 (a), (b) and (c), as well. Compared with previously calculated data and experimental data, it is found that Eq. (7-19) with the proposed correction is able to predict classifying voltage V_{50} more precisely than Eq. (7-18).

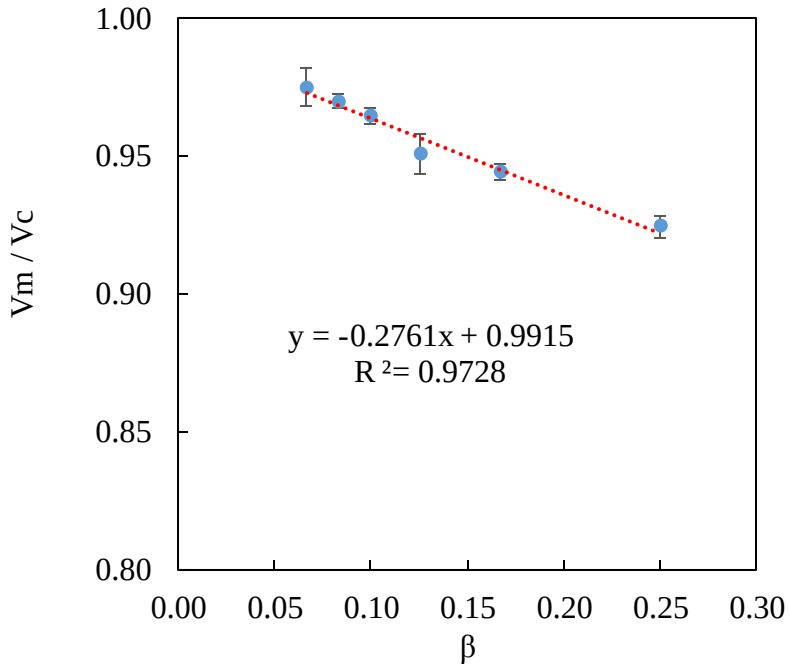

Figure 7.9: Correction factor as a function of aerosol-to-sheath flowrate ratio for two mini-plate EAA

7.4.4 Transfer function of the mini-plate EAA

As noted that the experimental penetration curve is the convolution result of transfer functions of DMA and mini-plate EAA, a predicted deconvolution curve for non-diffusive particles based on both DMA and EAA theory is also calculated and compared in Figure 7.10(a). For the prototype EAA operated at total flowrate of 2 lpm and aerosol-to-sheath flowrate ratio of 1:8, its sizing response is evidenced as a function of normalized voltage, with the same trend as the theoretical curve. For normalized voltage within a finite range, the normalized penetration decreases from 100% to 0% with voltage increase. The particle penetrations are 100% and 0%, when normalized voltage is smaller and larger than this

range, respectively. The slope of the theoretical non-diffusive curve is steeper than that obtained experimentally. The disagreement between theoretical and experimental values is possibly resulted from inaccuracy of corrected 2D model and experimental errors.

Based on previous derivation of EAA transfer function for non-diffusive particles, a theoretical transfer function as a function of normalized voltage for the studied mini-plate EAA operated at total flowrate of 2 lpm and aerosol-to-sheath flowrate ratio of 1:8 is shown in Figure 7.10(b). Also shown in Figure 7.10(b) is the experimental transfer function, which was retrieved by the piecewise linear deconvolution scheme (Li et al., 2006). Overall, the slope of the theoretical curve is also steeper than that obtained from experimental data. When considering maximum experimental error of 10% on flow controlling onto the theoretical curve, there still is an obvious difference between the experimental and predicted transfer functions, resulting in the disagreement between two convoluted curves in Figure 7.10(a). The simplified two dimensional flow model cannot well predict the true transfer function of mini-plate EAA. The most possible reason for its deviation could be the 3D effect inside the classification zone of the mini-plate EAA (e.g. the aerosol flow expansion). To well predict transfer function or convoluted penetration curve, a 3D modeling work may be required to investigate the above observation. However, the experimental transfer function of the mini-plate EAA can be used in the data inversion scheme to retrieve a more accurate particle size distribution from the raw data measured by the mini-plate EAA.

(a)

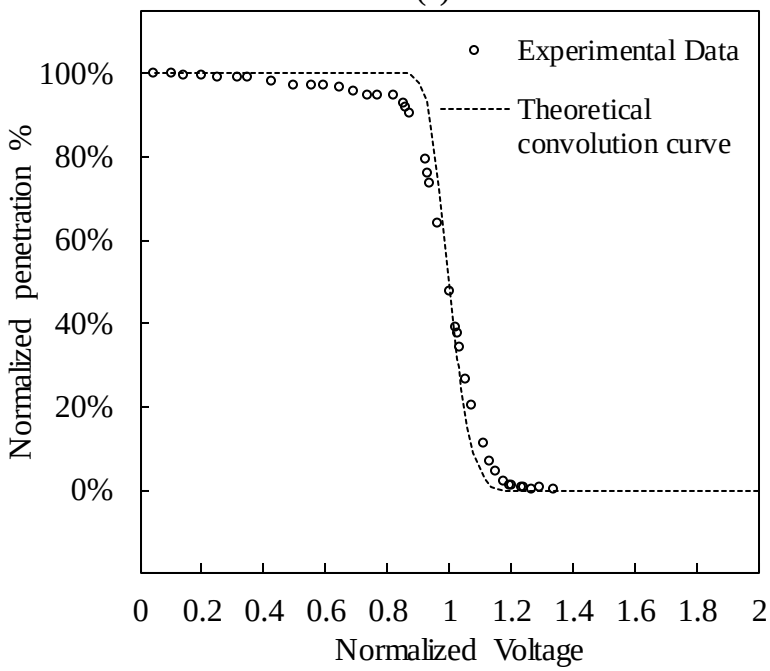
Experimental Data
Theoretical convolution curve
100%
80%
60%
40%
20%
0%
Normalized penetration %
0
0.2
0.4
0.6
0.8
1
1.2
1.4
1.6
1.8
2
Normalized Voltage

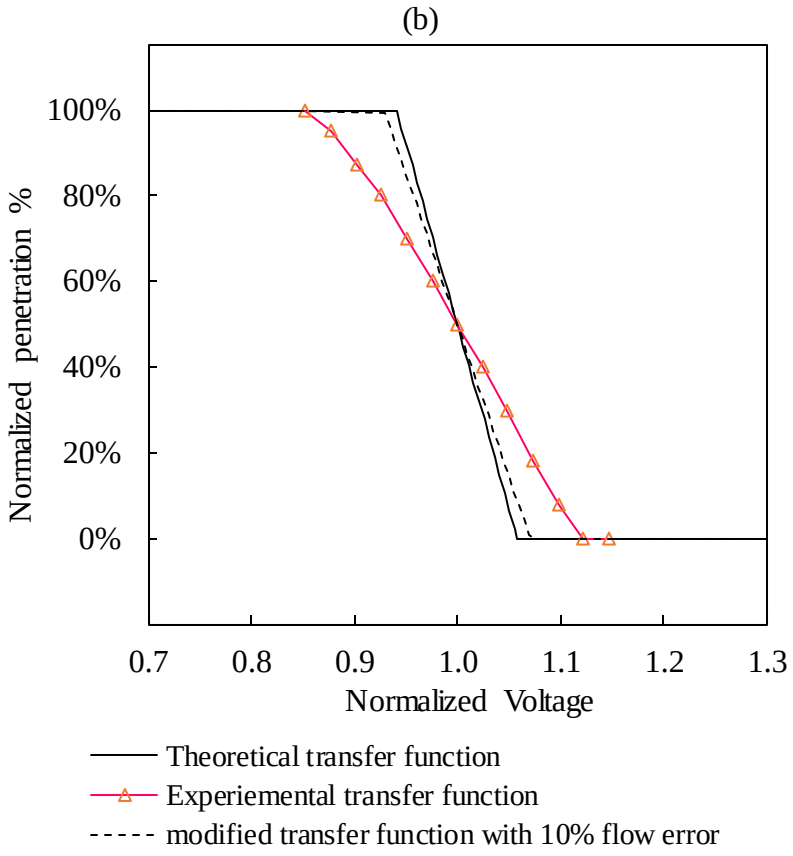

Figure 7.10: Comparison of experimental and predicted curves as a function of normalized voltage when the mini-plate EAA was operated at the total flowrate of 2 lpm and aerosol-to-sheath ratio of 1:8: (a) cutoff curves; (b) transfer functions

7.5 Design of Studied Mini-plate DMAs

Through developing and evaluating the first prototype of mini-plate EAA, we found there were some defects in its design although it functions as expected. For example, the aerosol inlet channel was formed by assembling the metal plate into the bottom Delrin block, indicating one of its walls is metal while the rest are Delrin. Charged particles were easily get lost during transport, whatever a DC voltage or ground was applied onto the metal plate.

And one-side injection and extraction of sheath flow may result in the flow non-uniformity. Hence, a second generation device, mini-plate DMA, was developed by modifying and improving the design of the prototype mini-plate EAA.

Figure 7.11 shows the schematic diagram of prototype mini-plate DMAs (i.e., DMA-1). The section view of the prototype is given in Figure 7.11a and the top view in Figure 7.11b. Prototype DMAs essentially consist of two metal plates installed in parallel and separated by the spacing of 1/16' (i.e., the height of particle classification zone). Both polydisperse and classified aerosol flow channels were designed in the metal plates to minimize the electrostatic particle loss during the transport. Polydisperse aerosol flow was injected at the DMA top plate, passed through a triangular-shaped flow channel and then entered the particle classification zone from the entrance slit. The dimensions of slits for aerosol entrance and exit of the classification zone are 1 1/8" (in length) × 1/32" (in opening) which is 75% of the width of particle classification zone (i.e., 1 1/2"). The reason for the shorter slit length as compared to the width of the classification zone is to keep the aerosol flow away from the side walls of DMAs for minimizing the wall effect. The classified aerosol channel built in the bottom metal plate was the same as that for the polydisperse aerosol flow. The distance between the aerosol entrance and exit slits was 2 1/16". A high DC voltage (positive/negative) was applied to the top electrode plate while the other on electrically grounded. A uniform electrical field was then established in the particle classification zone. For the safe operation, two metal plates were insulated in the Delrin enclosure. Particle-free sheath gas was directed into the DMAs from the left inlet, passed

through screen-type flow laminarizer prior to reaching the particle classification region. The excess flow exited the DMA from the outlet located at the right-hand side of the prototypes. This prototype DMA-1 was designed to size particles with the sizes up to 300 nm when operating at the sheath flow rate of 1.0 lpm. The overall size of this prototype mini-plate DMA was 4 7/8" in length, 2 7/16" in width and 21/32" in height, which is comparable to the size of an iPhone 6.

To further reduce the device size and to investigate the geometry effect on the mini-plate DMA performance, the other mini-plate DMA (DMA-2) was also made. The overall size of DMA-2 is similar to that of an iPhone 5. The detail of dimensions of two studied mini-plate DMAs are given in Table 7.1. The classification length and width of DMA-2 are less than those of DMA-1 while the spacing between two plates is higher in DMA-2. The length of aerosol slit opening in DMA-2 is 50% the width of its classification region. The prototype mini-plate DMA-2 measures particles with the sizes smaller than 200 nm at the sheath flow of 1.0 lpm.

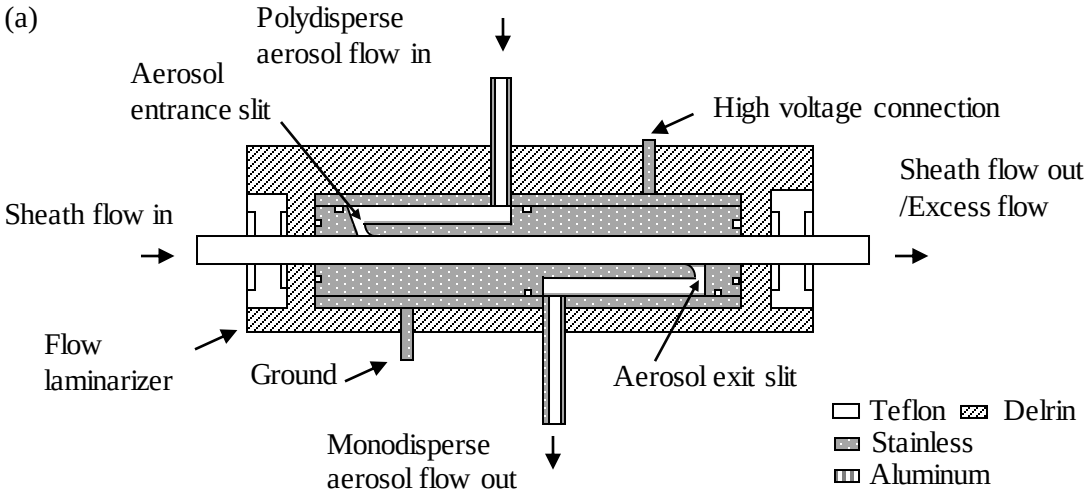
(a)
Polydisperse
aerosol flow in
Aerosol
entrance slit
High voltage connection
Sheath flow out
/Excess flow
Sheath flow in
Flow
laminarizer
Ground
Aerosol exit slit
Teflon
Delrin
Stainless
Aluminum
Monodisperse
aerosol flow out

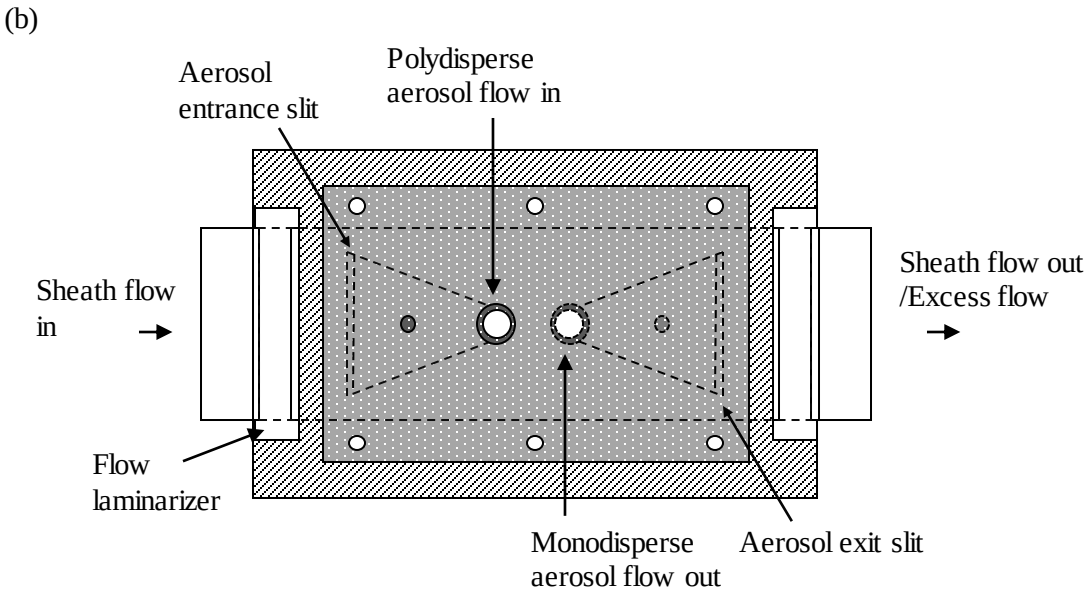
(b)
Aerosol
entrance slit
Polydisperse
aerosol flow in
Sheath flow
in
Sheath flow out
/Excess flow
Flow
laminarizer
Monodisperse
aerosol flow out
Aerosol exit slit

(c)

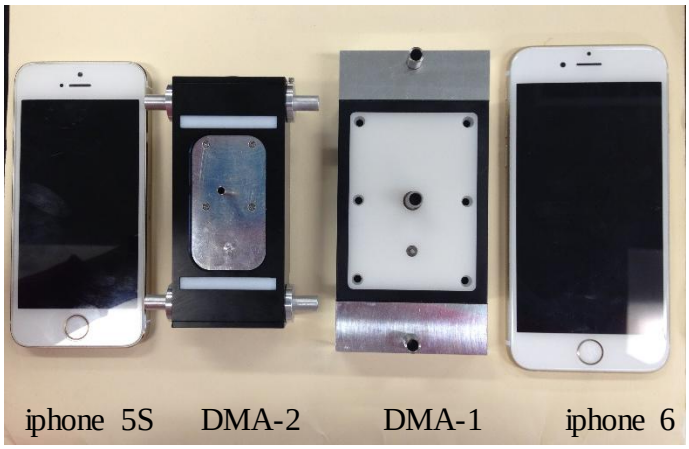

Figure 7.11: Schematic Diagram of core part of mini-plate DMA: (a) sectional view, (b) top view and (c) constructed mini-plate DMAs compared to iPhones

Table 7.1: Comparison of key dimensions in two mini-plate DMAs, units: in (mm)

	Classification Zone			**Aerosol slit opening**	**Overall Size**		
	Length	Width	Height		Length	Width	Height
DMA-1	2 1/16" (52.39)	1 1/2 " (3.81)	(2.11)	1 1/8" × 1/32" (28.58 × 0.79)	4 7/8" (123.83)	2 7/16" (61.91)	21/32" (16.67)
DMA-2	1 13/32" (35.72)	1" (25.4)	1/8" (3.18)	1/2" × 3/32" (12.7 × 2.38)	3 7/8" (98.43)	1 3/4" (44.45)	7/8" (22.23)

7.6 Experimental Setup and Data Reduction for Mini-plate EAA/DMAs

7.6.1 Experimental Setup

The experimental setup to generate singly charged monodisperse particles with desired electrical mobility for evaluating the performance of prototype mini-plate DMAs is the same as that used for mini-plate EAA evaluation, as shown in Figure 7.2. Also, the

tandem DMA (TDMA) technique, in which two DMAs are operated in series, was applied for this evaluation (Rader and McMurry 1986; Fissan et al, 1996; Hummes et al. 1996; Chen et al. 2007). One of calibrated DMAs (TSI Model 3081 and 3085) were used as the first DMA to classify monodisperse NaCl particles in selected sizes, operated at the aerosol-to-sheath flowrate ratio of 1:10. The classified aerosol particles were then directly delivered to the mini-plate DMA to be studied. For each mini-plate DMA under the study 5-6 particles sizes were selected for the evaluation.

As shown in Figure 7.12, the classified aerosol flowrate of mini-plate DMAs was also monitored by a laminar flowmeter. Two laminar flowmeters and needle valves were applied to control the sheath and excess flows of mini-plate DMAs. To investigate the performance of mini-plate DMAs under various flowrate conditions (i.e., different aerosol-to-sheath flowrate ratios, different aerosol and sheath flowrates), aerosol and sheath flows were varied at the rates less than 0.6 lpm and 6.0 lpm, respectively. A high-voltage power supply (Bertan Model 205B-10R) was used to apply a high DC voltage to the mini-plate DMA under investigation. The voltage on the 2^{nd} DMA (i.e., mini-plate DMA) was varied within its possible voltage range while the 1^{st} DMA was at a fixed voltage. The voltage needed to obtain the maximum downstream particle concentration of mini-plate DMA was considered as the central voltage for sizing particles of elected sizes. The particle number concentrations upstream (N_1) and downstream (N_2) the mini-plate DMA were measured by an Ultrafine Condensation Particle Counter (UCPC, TSI model 3776). The TDMA curve

was obtained by normalizing the above two concentration readings as a function of the voltage applied on the 2nd DMA.

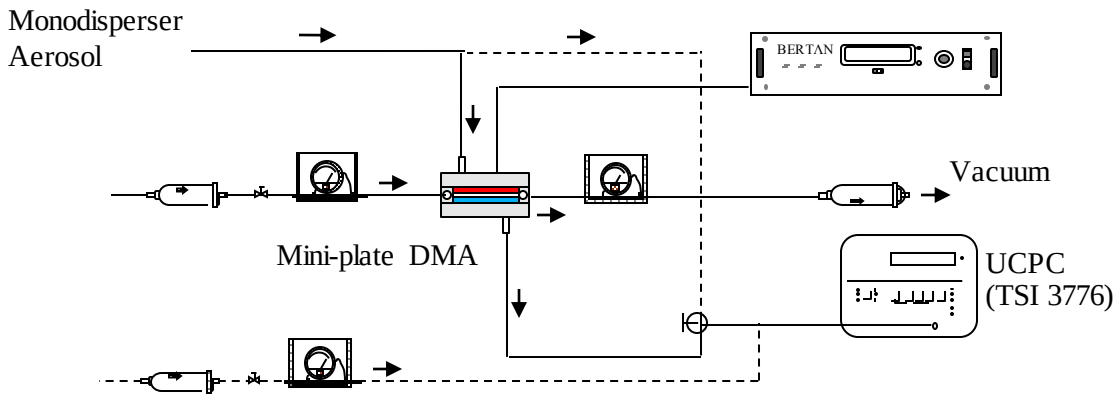

Figure 7.12: Experimental setup for the performance evaluation of mini-plate DMAs

7.6.2 Deconvolution Scheme for DMA Transfer Function

The experimental TDMA data are the result of convolution of the 1st and 2nd DMA transfer functions. A deconvolution scheme is required to obtain the real transfer function of mini plate DMAs. Since the 1st DMA (i.e., TSI DMAs) was different from the 2nd one (i.e., mini-plate DMAs) the prior knowledge is required for the transfer function of the 1st DMA. Such prior knowledge can be obtained by conducting the TDMA experiment with two identical TSI DMAs. A piecewise-linear function deconvolution scheme was then applied to recover the true transfer function of mini-plate DMAs (Li et al., 2006). In this scheme the transfer function curve is approximated by a series of linear functions in divided N subsections in the particle electrical mobility axis, resulting in (N+1) unknowns to be solved. The convoluted TDMA data can be calculated from two such representative transfer

functions of the 1st and 2nd DMA. A numerical optimization scheme was used to find best-fitted TDMA data to the experimental one in order to retrieve the unknowns. The same deconvolution scheme has been applied to obtain the real transfer function of Nano-DMA (Li et al., 2006), MDMA (Chen et al., 2007) and cDMA (Fan et al., 2011). The sizing accuracy and sizing resolution could thus be investigated once the real transfer function of mini-plate DMAs was recovered.

7.7 Result and Discussion for DMAs

7.7.1 Sizing Accuracy of Mini-plate DMAs

For a properly functioned DMA ones shall be able to calculate the central electrical mobility of classified particles from the applied voltage and operational flowrates (given the known DMA dimensions). Since mini-plate DMAs are in the parallel-plate configuration we assumed that the central electrical mobility of classified particles could be predicted by the classical 2-D model. Eq. (7-20) is derived from the model under the ideal condition in which the particle diffusion, flow expansion, wall effect and particle loss are negligible.

$$Z_{p,c} = \frac{Q_{sh}\, h}{L\, W\, V} \tag{7-20}$$

where $Z_{p,c}$ is central electrical mobility of classified particles; Q_{sh} : the sheath flowrate; V : the voltage applied on the DMA; L: the effective particle classification length; W: the width of classification region; and h: the effective height of classification zone. The comparison of the experimental and calculated voltage for a given particle electrical mobility is shown in Figure 7.13. The deviation between the experimental and calculated voltages at the given particle sizes is not negligible. It is further found that the voltage needed for classifying

particles with a given electrical mobility varied when varying the aerosol and sheath flowrates. To more precisely calculate the voltage applied for sizing particles with the desired electrical mobility, we also proposed to include the correction factor (η) in Eq. (7-20) to take into the consideration of the above observation:

$$Z_{p,c} = \frac{\eta\, Q_{sh}\, h}{L\, W\, V} \tag{7-21}$$

Figure 7.14 shows the correction factor, η, as a function of aerosol-to-sheath flowrate ratio (β). It is interesting to note that the relationship between η and β is quite linear. For both DMA-1 and DMA-2, the correction factor decreases with the increase of aerosol-to-sheath flowrate ratio. Because of the narrow space between two parallel plates, high sheath flow is likely to confine the aerosol stream in the regime closer to the inlet top plate when the aerosol flow remained constant. Higher voltage is thus required to classify particles when operated at a lower aerosol-to-sheath flowrate ratio. Due to the dimensional difference for both studied DMAs, the correction factor, $\eta(\beta)$, for DMA-1 is different from that for DMA-2. Note that the η value for DMA-1 is higher than that for DMA-2. The slope of $\eta(\beta)$ for DMA-2 is about twice the slope of $\eta(\beta)$ for DMA-1. A 3D modeling work may be required to investigate the above observation.

As evidenced in Figure 7.13 the reasonably good agreement between the calculated voltages based on the proposed Eq. (7-21) and the experimental data are achieved for both DMA-1 and DMA-2 operated at various aerosol and sheath flowrates. The ±2.5% for the voltage deviation for cases with DMA-1 and DMA-2 in Figure 7.13 might be attributed to

the accuracy in the flowrate control and measurement as well as the possible 3D flow effect (e.g. the aerosol flow expansion in the classification zone).

(a) DMA-1

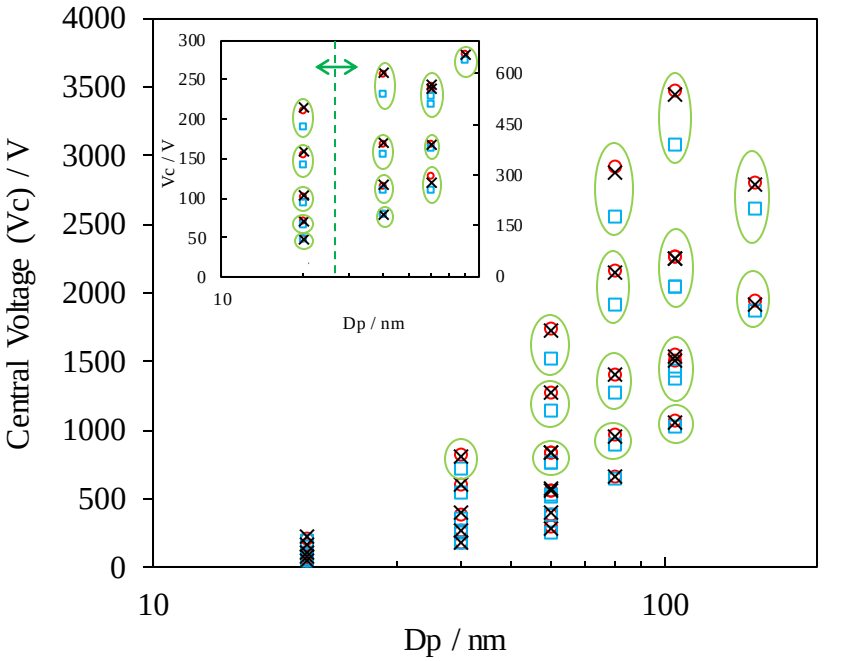
Central Voltage (Vc) / V
4000
3500
3000
2500
2000
1500
1000
500
0
10
100
Dp / nm
Vc / V
300
250
200
150
100
50
0
600
450
300
150
0
10
Dp / nm
Experimental Vc
Calculated Vc without correction
Calculated Vc with correction

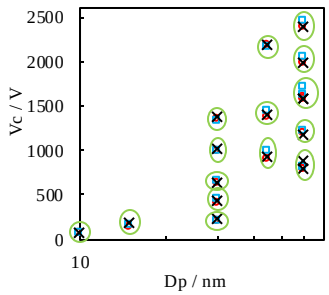
Vc / V
2500
2000
1500
1000
500
0
10
Dp / nm

(b) DMA-2

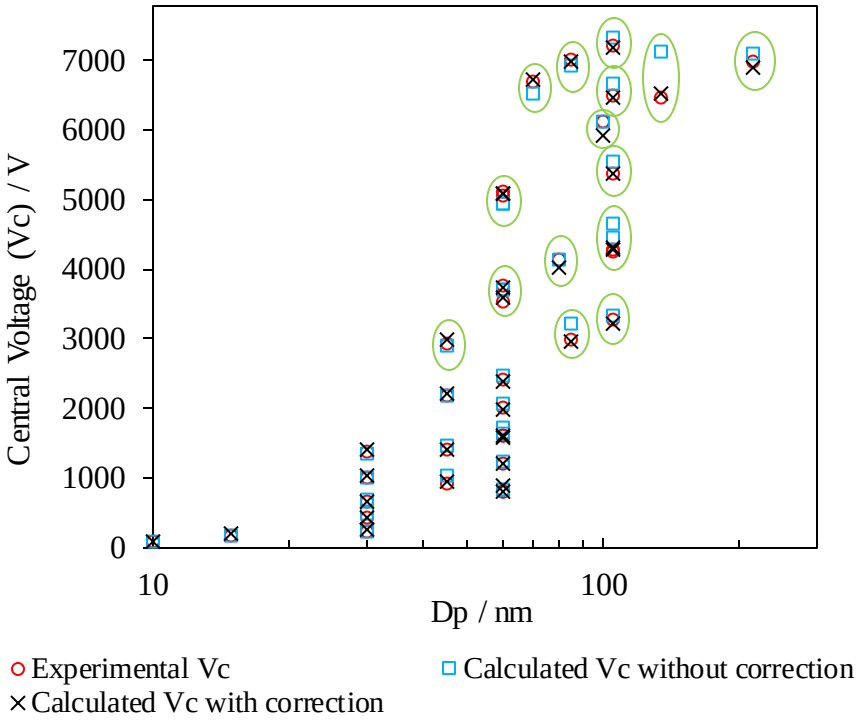

Figure 7.13: Comparison of central voltage for particle sizing among experimental data, calculated date without correction and calculated data with correction: (a) for DMA-1 and (b) for DMA-2

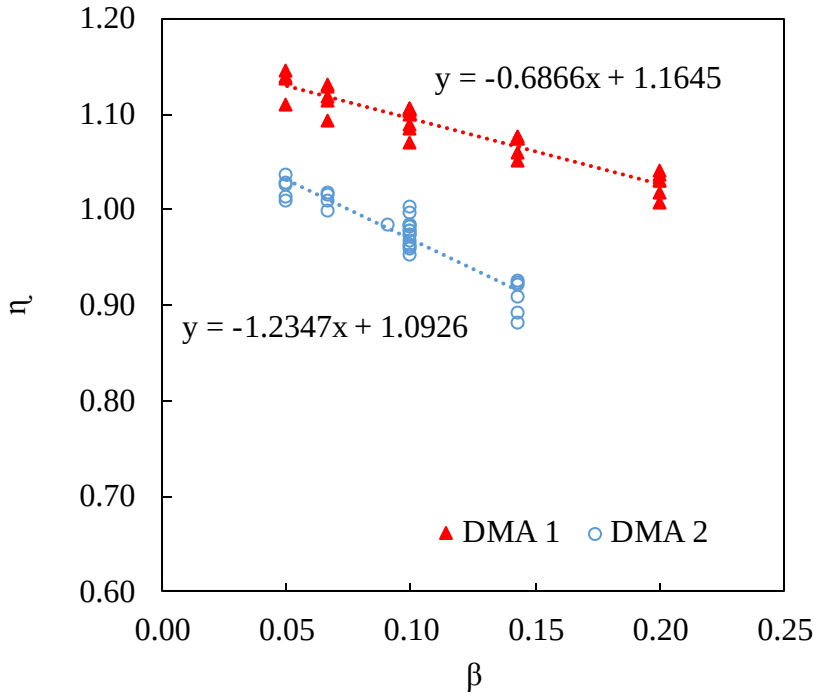

Figure 7.14: Correction factor as a function of aerosol-to-sheath flowrate ratio for two mini-plate DMAs

7.7.2 Transfer Function of Mini-plate DMAs

The performance of a DMA is characterized by its transfer function which can be de-convoluted from the TDMA data. Figure 7.15 (a) shows the typical comparison between the experimental TDMA data and calculated curves via the piecewise linear deconvolution scheme for the cases of 100 nm particles and operating mini-plate DMAs at the aerosol and sheath flowrates of 0.3 and 3.0 lpm, respectively. The good agreement between two sets of data for each mini-plate DMA was obtained. Figure 7.15(b) shows the de-convoluted transfer functions of DMA-1 and -2. The shape of two de-convoluted transfer functions are nearly triangular (using the normalized electrical mobility as the abscissa) when operating a

DMA at the polydisperse aerosol flowrate is the same as the classified aerosol flowrate. It is because the particle diffusion effect can be neglected for the particles with 100 nm in size and under the operational flow condition. Minor difference in the maximal transmission probability of the transfer functions for both prototype mini-plate DMAs was observed. The maximal probability values for the transfer function are 0.94 and 0.99 for DMA-1 and DMA-2, respectively. Both values are close to 1.0 for non-diffusive particles when the DMAs were properly designed. The full widths at half the maximum (FWHM) are approximately 0.13 and 0.17 for DMAs-1 and -2, respectively. It indicates that DMA-1 has a better sizing resolution than DMA-2. It may be due to the fact that less percentage in length of aerosol entrance slit relative to the width of DMA particle classification zone in DMA-2 (50%) than that in DMA-1 (i.e., 75%).

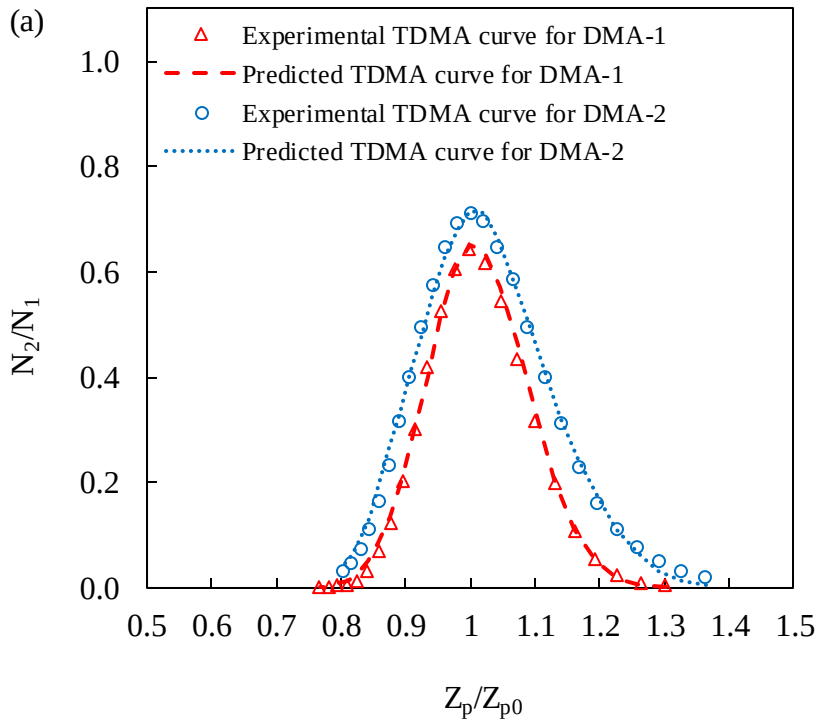

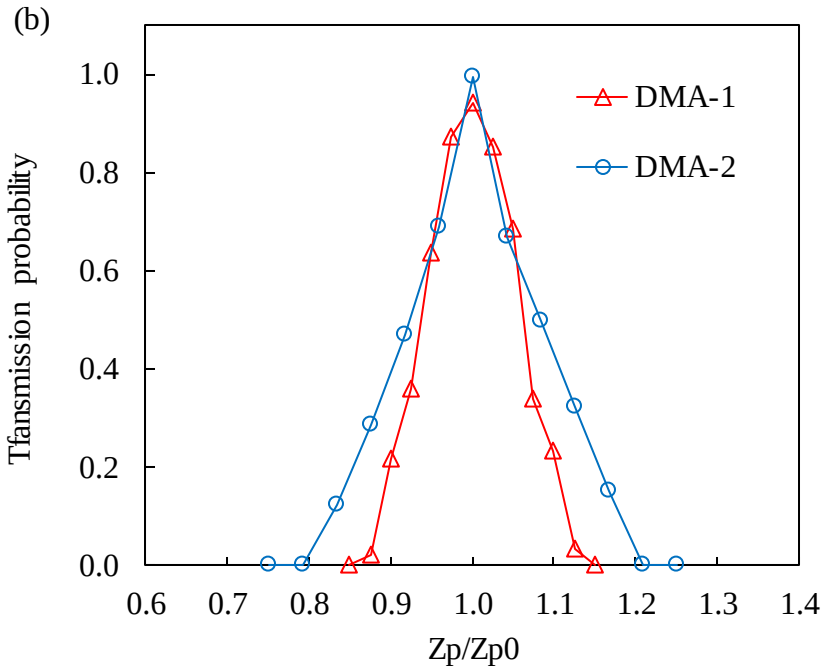

Figure 7.15: (a) Comparison of experimental and calculated TDMA curves for DMA-1and DMA-2; (b) Typical transfer function of DMA-1 and DMA-2 for 100 nm particle size, obtained via the linear-piecewise function deconvolution scheme, operated at the aerosol-to-sheath flowrate ratio of 0.1

7.7.3 Performance of Mini-plate DMA in Various Flow Conditions

The area and full width at half maximum (FWHM) of the transfer function are two important parameters for characterizing the performance of a DMA. The former indicates the particle penetration in the DMA at a fixed voltage and the later implies the sizing resolution. More, the effect of particle diffusion can be easily observed via the maximal height of the DMA transfer function (i.e., the maximal probability for particles with the central electrical mobility to pass through the DMA). The transfer function of DMAs is also required in the data reduction scheme to better recover the size distribution of particles. To evaluate the performance of mini-plate DMAs the TDMA experiment was conducted for the

cases of particles with the sizes varied from 20 to 180 nm and operating DMAs at the aerosol flowrate of 0.3 lpm and sheath flowrates of 1.5, 3.0 and 6.0 lpm.

Figure 7.16 shows the area (a), height (b) and FWHM (c) of mini-plate DMA-1 transfer function as a function of particle size at three different sheath flowrates while keeping constant aerosol flowrate of 0.3 lpm. The area of the DMA transfer function is slightly reduced as the particle size decreases. It is concluded that the particle loss in DMA-1 was negligible for particles in sizes larger than 20 nm. For particles larger than 40 nm in size the area under the transfer function curves approaches to constant values of 0.278, 0.1348 and 0.661 for the aerosol-to-sheath flowrate ratio of 0.2, 0.1, and 0.05, respectively. However, the particle diffusion effect in the DMA classification zone can be observed in Figure 7.16(b). The height of transfer function (i.e., the maximal probability for particles having central electrical mobility to pass through a DMA) decreases with the particle size decreases. The transfer function height was also decreased when the aerosol-to-sheath flowrate ratio was decreased.

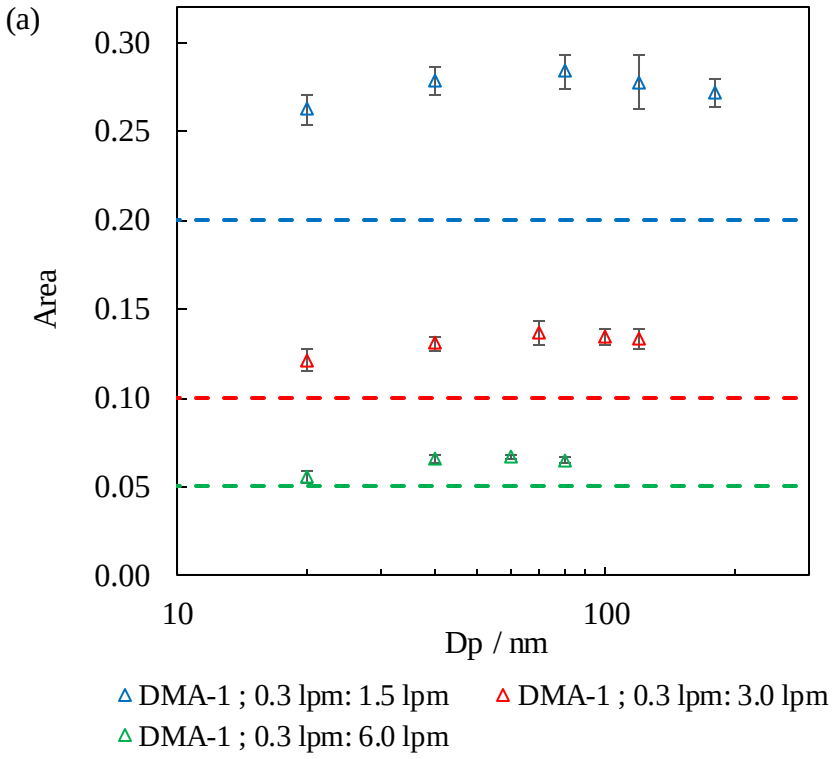
(a)
0.30
0.25
0.20
0.15
0.10
0.05
0.00
Area
10
100
Dp / nm
DMA-1 ; 0.3 lpm: 1.5 lpm
DMA-1 ; 0.3 lpm: 3.0 lpm
DMA-1 ; 0.3 lpm: 6.0 lpm

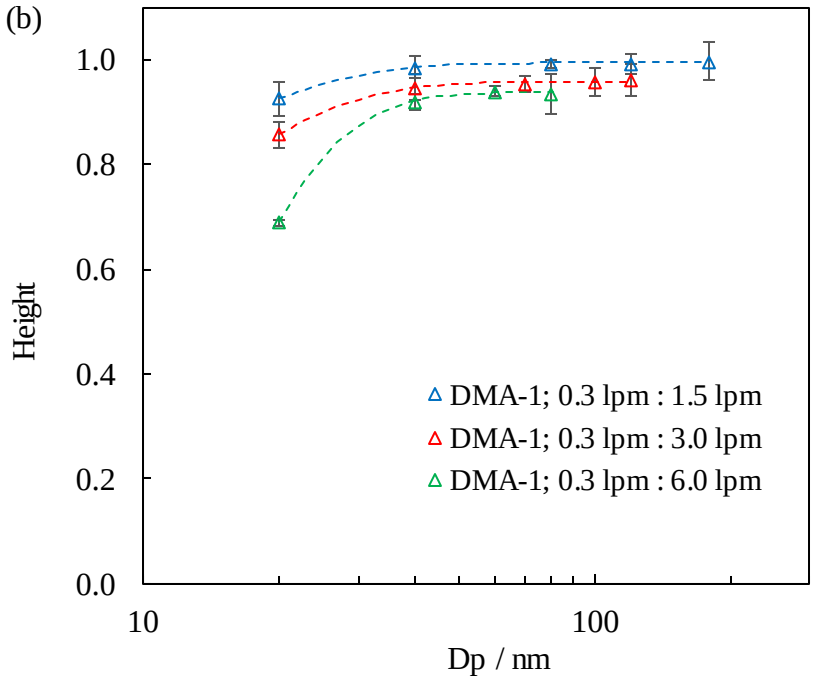
(b)
1.0
0.8
0.6
0.4
0.2
0.0
Height
10
100
Dp / nm
DMA-1; 0.3 lpm : 1.5 lpm
DMA-1; 0.3 lpm : 3.0 lpm
DMA-1; 0.3 lpm : 6.0 lpm

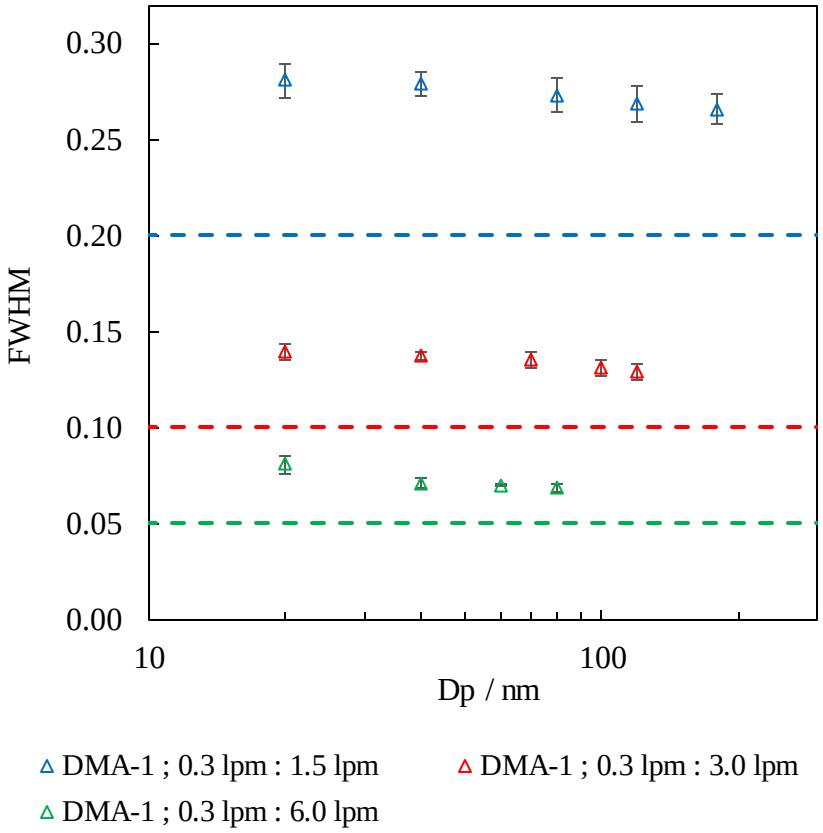

Figure 7.16: Comparison of the area (a), the height (b) and sizing resolution (c) of the transfer function of mini-plate DMA-1 at different flow condition.

The sizing resolution of a DMA for a given particle size can be found from the FWHM of the DMA transfer function. Figure 7.16(c) gives the FWHM of transfer function of mini-plate DMA-1 as a function of particle size. The FWHMs at three tested sheath flowrates follows the general trend that the FWHM value decreased and reached constants as the particle size increased. By the DMA theory (Knutson and Whitby, 1975a), the FWHM of a DMA transfer function for non-diffusive particles (in deal 2-D case) can be predicted by

$$FWHM = \alpha \times (1 + |\delta|) \quad (7\text{-}22)$$

where $\alpha = (Q_a + Q_s)/(Q_{sh} + Q_m)$, $\delta = (Q_s - Q_a)/(Q_{sh} + Q_a)$ and Q_a, Q_s, Q_{sh}, Q_m are the flowrates of polydisperse aerosol, classified aerosol, sheath and excess flowrates, respectively. Based on the operational flow conditions the FWHM of a plate DMA under the ideal 2-D assumption shall be 0.05, 0.1, and 0.2 for the cases of sheath flowrate at 6.0, 3.0 and 1.5 lpm, respectively. As shown in Figure 7.16(c) the experimental FWHMs of mini-plate DMA-1 are in general larger than the values calculated with the ideal 2-D model, even for large particles. The same observation is shown in Figure 7.16(a) for the area of mini-plate DMA transfer function.

Note that the aerosol slits in the classification region of prototype mini-plate DMAs were not fully opened across the entire width of the flow channel (i.e., 75% for DMA-1 and 50% for DMA-2). The reason for such aerosol slit design is to eliminate the wall effect. In such slit design, certain percentage of sheath flow was used to keep the aerosol flow away from the side walls of DMAs. Eq. (7-22) thus overestimates the sheath flowrate actually used for sheathing aerosol from the aerosol exit slit, resulting in lower value of FWHM for mini-plate DMAs. Via the experimental data for sizing resolution, the FWHMs based on the ideal 2-D case are approximately 72% - 77% of the experimental data. A detail modeling may be also required to investigate the 3-D flow effect on the sizing resolution of mini-plate DMAs.

7.7.4 Geometry Effect on Performance of Mini-plate DMAs

To investigate the effect of aerosol slit and plate-to-plate spacing on the particle sizing performance of mini-plate DMAs TDMA experiment was also conducted on DMA-2

for particles with the sizes varied from 10 to 100 nm. Figure 7.17 gives the comparison of area (a), height (b) and FWHM (c) of the transfer functions of DMA-1 and DMA-2 when operated at the aerosol and sheath flowrates of 0.3 and 3.0 lpm, respectively. The increasing trend on the height of mini-plate DMA the transfer function and the decreasing trend of FWHM with the increase of particle size are also observed herein.

In Figure 7.17(a) the area of transfer function for DMA-2 is close to 0.1782 for particles larger than 60 nm. The area of DMA transfer function is noticeably decreased as the particle size decreases. More, the area of transfer functions of DMA-2 is slightly larger than that of DMA-1 for all test particle sizes. It indicates a slightly better transmission efficiency of DMA-2 as compared to that of DMA-1. The larger area of the DMA-2 transfer function seems to imply that the shorter aerosol slit opening and larger plate-to-plate spacing of DMA-2 did minimize the particle loss due to the flow expansion and wall effect. In the meantime, the particle diffusion effect was more obviously observed in DMA-2 than that in DMA-1, evidenced by the height of DMA transfer function given in Figure 7.17(b).

Figure 7.17(c) further evidences the observation on the particle diffusion effect. The sizing resolution of mini-plate DMA-2 is worse than DMA-1. The FWHM of mini-plate DMA-2 transfer function noticeably increases with the decrease of particle size as compared to that for the cases with DMA-1. It is possibly because of the higher plate-to-plate spacing and shorter aerosol slit in DMA-2, resulting in flow mismatching in the neighborhood of the aerosol entrance slit. The flow disturbance may enhance the particle diffusion in the DMA classification zone. For both mini-plate DMAs, the FWHM of transfer functions deviate

much from the value of 0.1 estimated by the ideal 2D model. The FWHM of DMA-2 is in fact larger than that of DMA-1. It is probably because of the less opening in length of aerosol slit opening relative to the width of the classification zone.

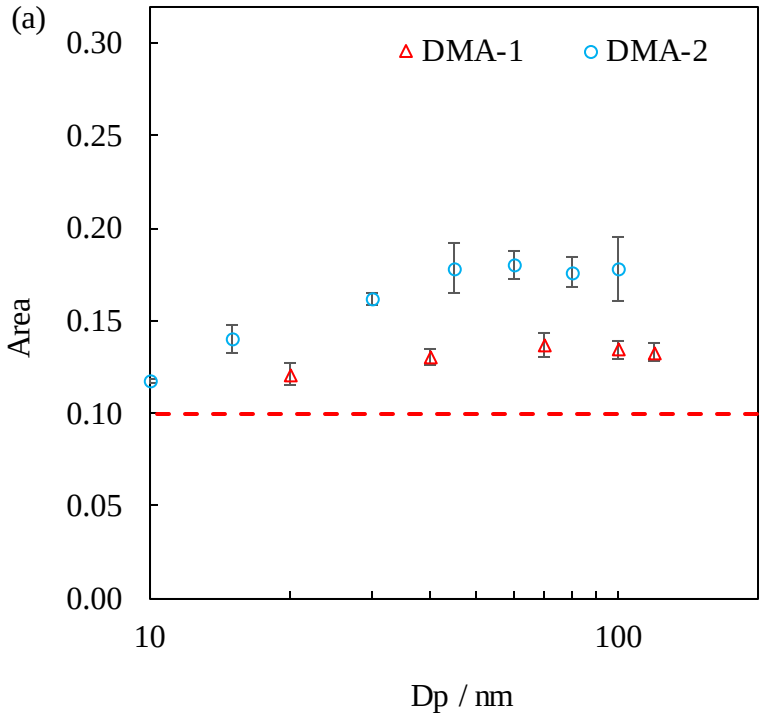

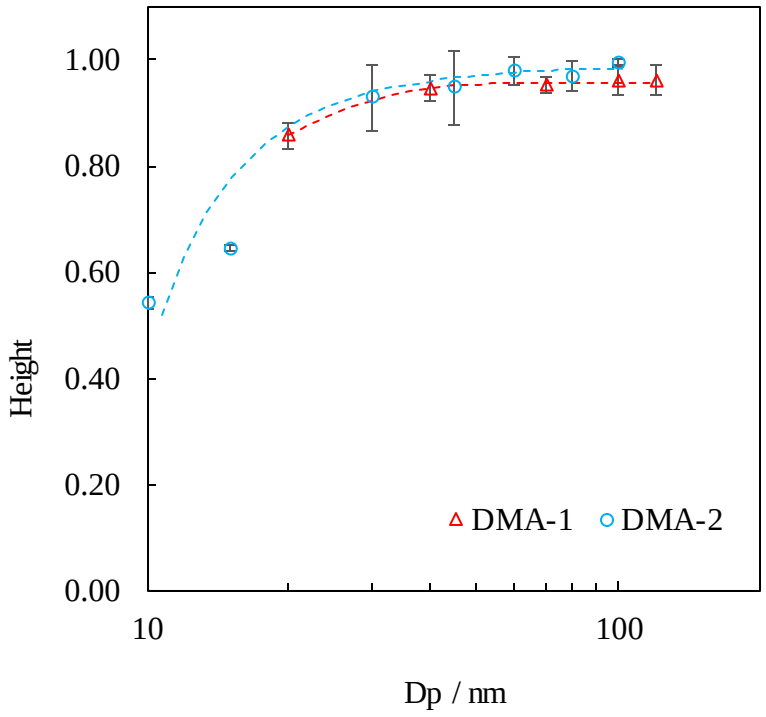
1.00
0.80
0.60
0.40
0.20
0.00
Height
DMA-1
DMA-2
10
100
Dp / nm

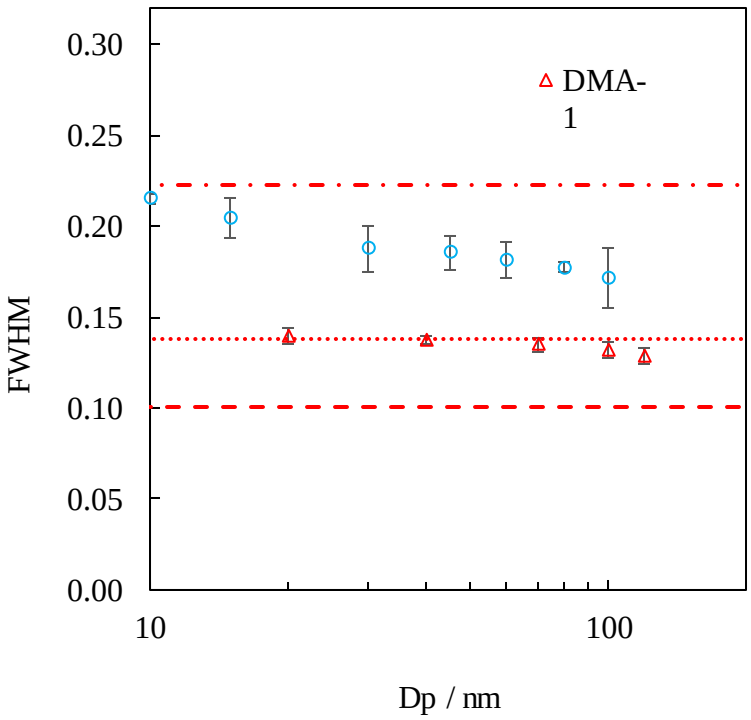
0.30
0.25
0.20
0.15
0.10
0.05
0.00
FWHM
DMA-
1
10
100
Dp / nm

Figure 7.17: Comparison of height (a) and FWHM (b) of mini-plate DMA-1and mini-plate DMA-2 at the aerosol and sheath flowrate of 0.3 and 3.0 lpm, respectively

7.8 Summary

A miniature plate EAA and two mini-plate DMAs have been developed and characterized for ultrafine particle measurement/monitoring. The tandem DMA technique was applied to evaluate the performance of mini-plate EAA and DMAs. The mini-plate EAA has a particle classification zone with 44.85 mm in length, 25.4 mm in width and 3.18 mm in height. To avoid particle loss from wall effect, the aerosol entrance slit was opened to be as 50% long as the width of its classification region. Mini-plate DMA-1 has the classification length of 52.4 mm, 75% aerosol slit opening in length (related to the width of the classification zone) and 2.11 mm in the plate-to-plate spacing, while mini-plate DMA-2 has 35.7 mm in length, 50% aerosol slit opening and 3.2 mm in height. By design, the particle sizing range of DMA-2 is less than that of DMA-1 under the same sheath flowrate operation. Compared with cylindrical DMAs, mini-plate DMAs are cost effective and easy to make and maintain. They however require detail experimental calibration for their performance. The compact size of mini-plate EAA/DMA make it suitable to incorporate in low-cost and compact ultrafine particle sizers.

DMA-classified NaCl nanoparticles were used to evaluate the performance of the prototype mini-plate EAA/DMAs. Despite its compact size, the prototype EAA/DMA was experimentally evidenced to have a satisfactory particle classifying performance.

The transmission efficiency of singly charged particles in mini-plate EAA were measured at constant total flowrate of 2 lpm, and the aerosol-to-sheath flowrate ratio of 1:4

and 1:8, respectively. For particles larger than 60 nm, the transmission efficiency was close to 100%. The smaller particle size is, lower transmission efficiency was obtained (e.g. 74% for 25 nm). The particle penetration curves (i.e., the normalized penetration vs. the normalized voltage) were carefully measured to investigate the performance of the prototype EAA, under different aerosol and sheath flow conditions. Form the experimental data, the optimal operation condition for the prototype was determined to be total flowrate of 2 lpm and aerosol-to-sheath flowrate ratio of 1:8. Because (1) the steepness of penetration curves was improved by increasing sheath-to-aerosol flowrate ratio until value of 8; and (2) while more flow distortion likely occurs in controlling low flowrate, too high flow operation in mini-plate EAA would also result in measuring difficulty of diluted downstream aerosol concentration by using electrical detectors. Nanoparticles with different sizes were tested to demonstrate a good and stable particle sizing performance of the prototype mini-plate EAA within the desired particle size range (< 150 nm). A simple model derived from the assumption of two dimensional flow field was developed and discussed in EAA study, to describe the central mobility, penetration curve and transfer function of the prototype. By comparison between experimental and predicted data, a correction factor (η) was successfully introduced into the classic 2D model to well predict the V_{50} for particles with different electrical mobility. It is interesting to observe that the factor is a linear function of aerosol-to-sheath flowrate ratio (β). The slopes of the experimental transfer function and the penetration curve are much smaller than the theoretic ones. This discrepancy may be attributed to flow distortion and 3D effect in the classification region of the device. However,

the experimental transfer function of EAA is still helpful in the data reduction schemes for recovering the more true size distribution of particles, by using it as a particle sizing component in miniature nanoparticle sizer.

Similarly in the DMA evaluation, the correction factor (η) was proposed to modify the equation derived from the 2-D assumption in order to better determine the applied voltage for sizing particles with the selected electrical mobility. Because of the difference in the DMA dimensions, the correction factors for DMA-1 and DMA-2 are different. To investigate the performance of mini-plate DMAs a piecewise linear deconvolution scheme was applied in our study to recover the real transfer function of DMAs from the collected TDMA data. For both DMA-1 and DMA-2 the typical transfer functions are in the triangular shape for non-diffusive particles (i.e., particles in large sizes). The maximal height, area and FWHM of DMA transfer function indicate the maximal transmission efficiency of particles with the central electrical mobility, transmission efficiency of DMA at a fixed DMA voltage and the sizing resolution, respectively. More, the experimental transfer function of DMAs is required in the data reduction schemes used to better recover the size distribution of particles.

In three studied cases (i.e., aerosol flowrate of 0.3 lpm; sheath flowrates of 1.5, 3.0 and 6.0 lpm) the height of transfer function of mini-plate DMAs increases as the particle size increases while the FWHM decreases. The better height of transfer function was found when DMAs were operated at a high aerosol-to-sheath flowrate ratio. The discrepancies between the FWHMs obtained in experiments and calculated by the 2-D modeling were obvious for all studied flow cases. It is possibly because the aerosol slits were not fully opened along

the entire width of classification zone. The higher percentage of opening in length (i.e., DMA-1) has the FWHM values closer to those calculated by the 2-D model when compared to those with DMA-2. It shall be noted that part of sheath flow was applied to keep the aerosol flow away from the side walls of DMAs, not for sheathing it from the aerosol exit slit. The effective sheath flowrate should be less than the total sheath flowrate used under the studied mini-plate DMA design. For plate DMAs having such aerosol slit design, the sizing resolution (i.e., FWHM) and accuracy cannot be simply estimated by the equations derived based on the ideal 2-D assumption. The less the percentage of slit opening in length (relative to the width of classification zone) the worse the particle sizing resolution.

CHAPTER 8 Development of a Prototype Mini-eUPS

8.1 Introduction

In this study, a prototype mini e-UPS has been developed by assembling a mini-plate charger, a mini-plate DMA and a calibrated mini Faraday cage aerosol electrometer. The voltage and flow control/monitor unit with circuit board was also developed into the sizer. A software was developed by Visual Basic programming. To recover the particle size distribution from measured current data, a constrained least square data inversion scheme was proposed and preliminarily test in this study. Last, we applied this data inversion scheme when measuring laboratory generated particles.

8.2 Calibration of a Miniature Faraday Cage for Particle Measurement

In order to measure particle size distribution by DMA technique, the classifier must be coupled to a particle detector. A condensation particle counter (CPC) and an aerosol electrometer (AE) are two typical aerosol detectors used to detect mobility classified particles. In a condensation particle counter, a vapor, typically butanol or water is mixed with the aerosol under a supersaturation condition to grow the particles to sufficiently large ones for optical detection. There is a minimum size requirement for particle growing in the CPC, called as Kelvin equivalent size. Vapor condensation helps particles growing to

supermicron sizes. Generally, the performance of a CPC is characterized in terms of the minimum size that is counted with 50% efficiency (Flagan, 1998). Particles with low number concentration detected by a CPC needs a longer counting time to guarantee counting accuracy. However, on the other hand, CPC cannot count too many particles. The current widely used TSI model 3775 CPC has a maximum particle counting of 10^7 particles/cm^3 by a mode transition from single particle counting to photometric counting. Although CPCs may continuously count particles with a high counting efficiency and has been used as particle detector for several decades, it is not a good candidate of particle detector in a portable, personal device because working fluids has to be used for detection. Also, the optical part of a CPC often suffers from contamination from both the presence of large particles and working fluids.

An aerosol electrometer, however, is more proper to conduct the monitoring task in a miniature device. A typical aerosol electrometer consists of an aerosol Faraday cage and an electrometer. When charged particles face a housing containing a filter surrounded by a conducting enclosure, a charge equal to that carried by the entering aerosol stream is induced. An electrometer connected to the cage measures the resultant current which is related to the number concentration and flow rate of aerosol stream. The sensitivity and accuracy of aerosol electrical detection are highly determined by the characteristics of electrometer. Moreover, due to the low charging efficiency of small particles, the sensitivity of aerosol electrometer decreases as well when particles size decreases. Nonetheless, aerosol electrometers have proven very useful in measurement of fine particles emitted by engines

and other sources, and for characterizing particles produced by aerosol synthesis reactors (Flagan, 1998). With the assumption of singly charged particles, aerosol electrometer is used in the calibration of CPC and other particle detectors.

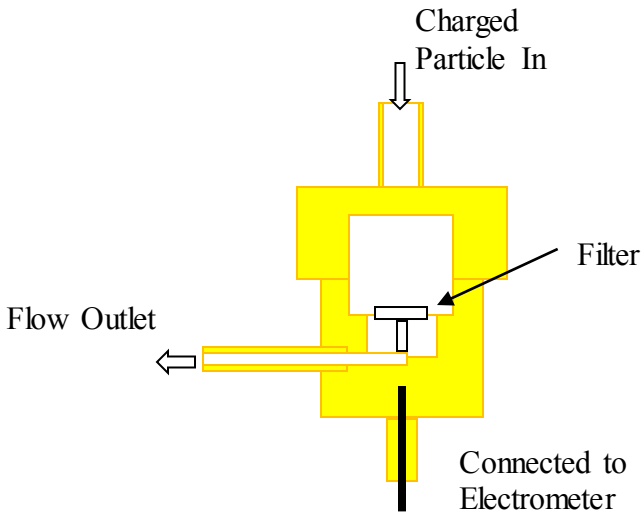

Figure 8.1: Schematic diagram of mini Faraday cage.

Figure 8.1 shows the design of the mini Faraday cage developed by Huang and Chen (2010) was used in mini e-UPS development. A miniature filter located inside the cage was used to collect DMA classified particles. The induced current in the Faraday cage can be measured when connected to an electrometer. The calibration results of the studied mini Faraday cage, for 80 nm particles, are shown in Figure 8.2. The current (I) measured by electrometer could be presented as a function of particle charge (ne), aerosol flow rate (Q_a) and the particle number concentrations (N) measured by UCPC:

$$I = n\ e\ (NQ_a) \tag{8-1}$$

By plotting the current I with the NQ_a product used as abscissa, the slope of linearly fitted curve would represent the charges on the particle tested. The cases of 0.3 lpm aerosol flow rate and 1.5 lpm aerosol flow rate were investigated in this study. Good linear relationships between two sets of data are shown in Figure 8.2 (a) and (b). The current induced in the Faraday cage goes rising with increase of particle number concentrations. The both values of two slopes are much closed to the value of elementary charge, indicating a good counting performance of mini Faraday cage. When integrated with a mini electrometer, the current measured by Faraday cage linearly increases with the increase of voltage signal from the electrometer, as shown in Figure 8.2(c). A fitted equation shown in the figure was later used for signal process when a data acquisition card was utilized in the mini e-UPS.

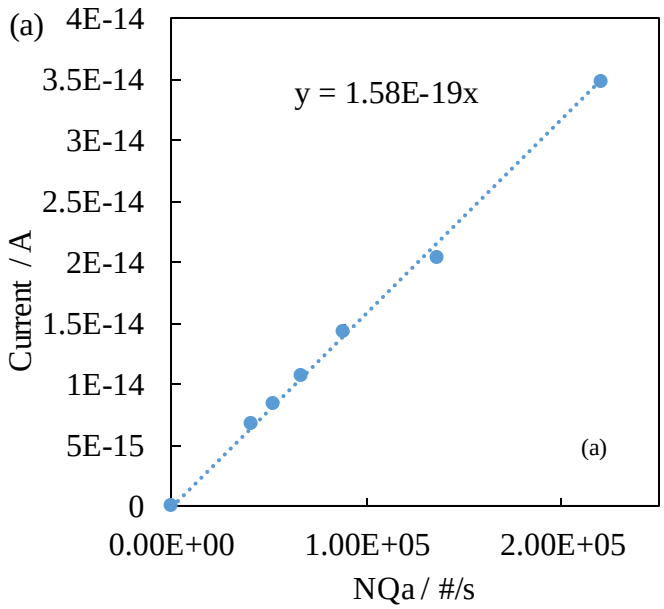

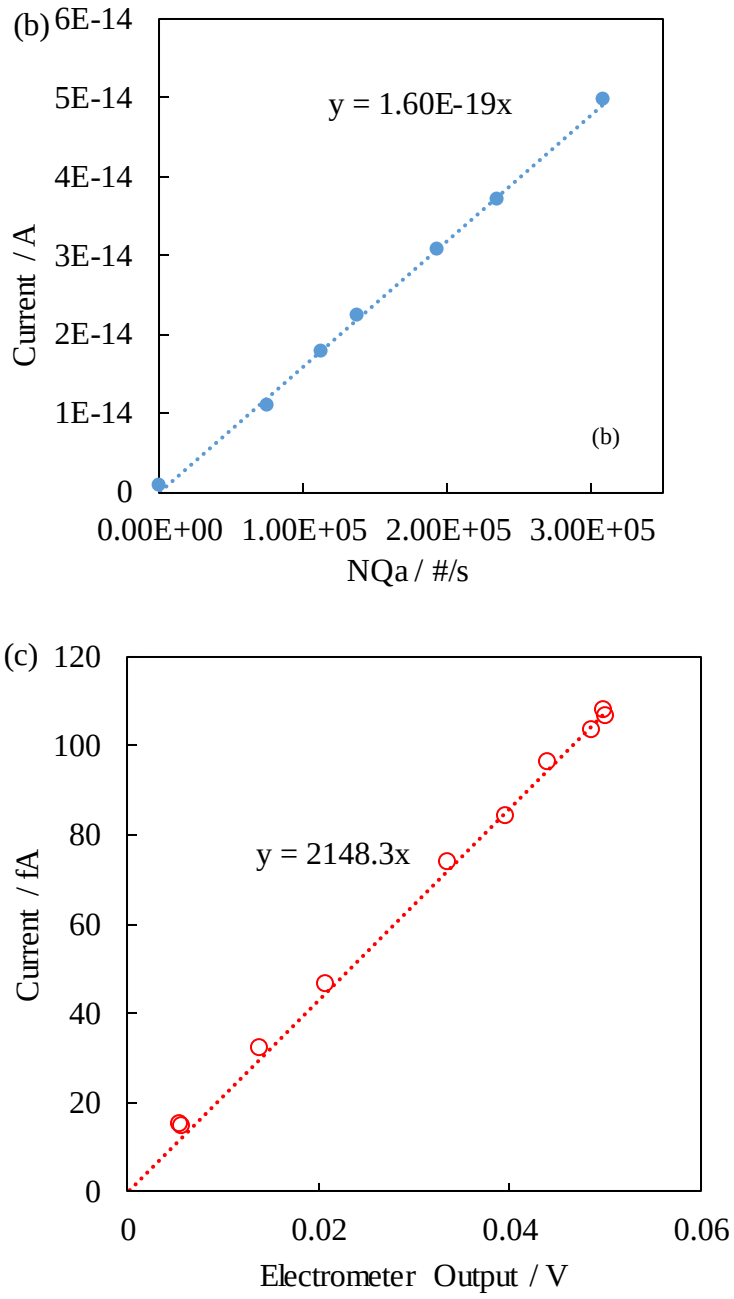

Figure 8.2: The calibration curves of mini Faraday Cage at (a) electrometer current as a function of collected particle number at aerosol flow rate of 0.3 lpm; (b) electrometer current as a function of collected particle number at aerosol flow rate of 1.5 lpm; and (c) electrometer current as a function of its voltage output.

8.3 Assembly of Prototype Mini-eUPS

With the three developed key components of a particle sizer, a prototype mini e-UPS could be developed by assembling all the components and control units together. As shown in Figure 8.3, in a mini e-UPS, aerosol will go into the device through the aerosol inlet which is a small Tee with a temperature sensor and a humidity sensor embedded. After passing the inlet, aerosol will go through mini-plate charger to get charged, mini-plate DMA to be classified according to their electrical mobility, mini Faraday cage to be measured and finally exhaust through a miniature air pump. The other air pump with two miniature HEPA filters in its upstream and downstream were used to provide particle-free sheath gas for DMA operation. Two miniature mass flow meters was used to monitor the sheath flowrate and aerosol flowrate. Three miniature high voltage power supplies were utilized to provide high DC voltage for DMA and charger, respectively. All of electronic components used to control/monitor the developed hardware for operating prototype mini e-UPS were shown in Table 8.1. The voltage and current to drive these electronic components are summarized, and the maximum power consumed for running the device is estimated also. Furthermore, the details about circuit board designed to support these electronic components is shown in Figure 8.4.

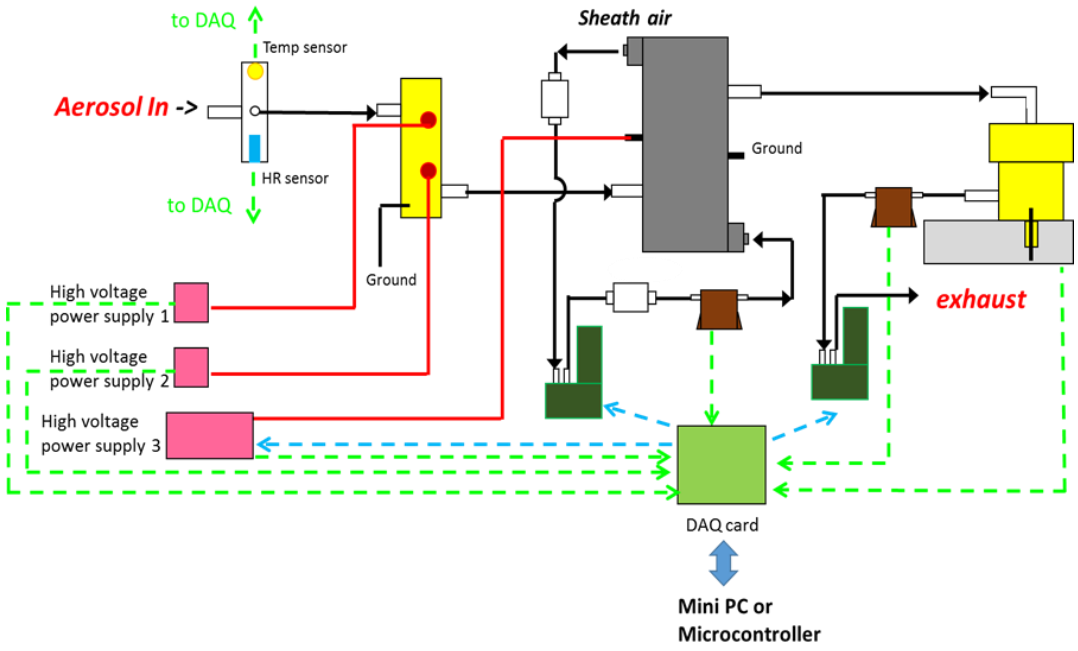

Figure 8.3: The schematic diagram of mini e-UPS.

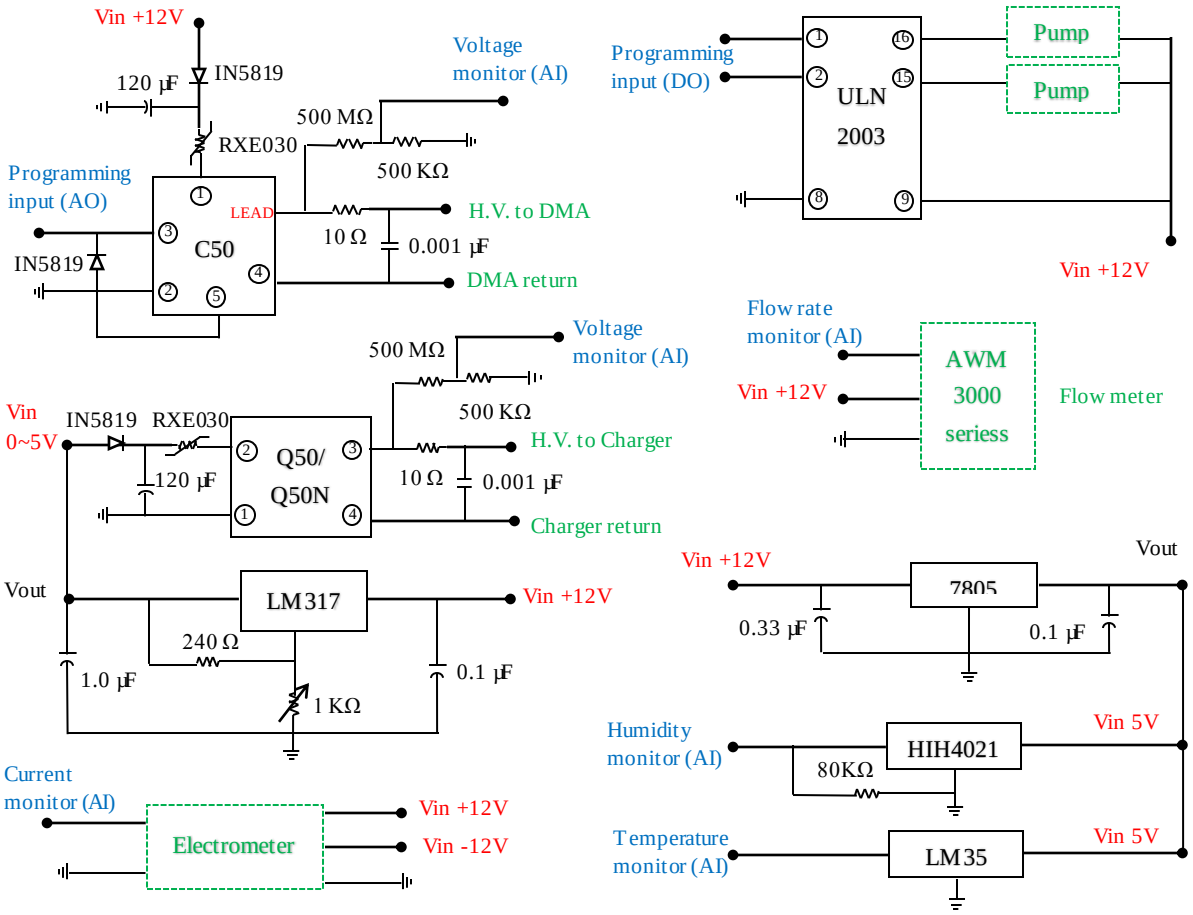

Figure 8.4: The diagram of the circuit for voltage control and signal acquisition.

Table 8.1: Summary of power consumption of mini E-sizer

Components	Input Voltage	Input Current	Power	Vendor, Model
Positive high voltage power supply for mini plate charger	0-5 V	< 250 mA	< 1.25 W	EMCO, Q50
Negative high voltage power supply for mini plate charger (optional)	0-5 V	< 250 mA	< 1.25 W	EMCO, Q50N
Positive high voltage power supply for mini plate DMA	12 V	< 250 mA	< 3 W	EMCO, C50

Aerosol flow pump	12 V	< 120 mA	< 1.44 W	Sensidyne, AA120CNSN50VC1
Sheath flow pump	12 V	< 120 mA	< 1.44 W	Sensidyne, 3A120CNSN30VC1
Aerosol flow meter	12 V		< 60 mW	Honeywell, AWM3100V
Sheath flow meter	12 V		< 60 mW	Honeywell, AWM3300V
Electrometer	±12 V			
Temperature sensor	5 V	60 μA	< 0.3 mW	LM35
Humidity sensor	5 V	< 500 μA	< 2.5 mW	HIH4021
Sum			**< 8.4 W**	

As shown in Figure 8.5, a prototype mini e-UPS has been developed with all components integrated into a box with the size of 6" (L) × 5" (W) × 4" (H). The total weight of prototype mini E-sizer is about 1.3 kg. The only two connections to the sizer are an AC to DC adapter and a USB cable for signal transmission between the sizer and computer. The voltage input for the prototype is 24 V. Such a compact, portable and simple design makes the mini e-UPS more easily to be carried, stored or moved between laboratories or test locations, and to be applied in various aerosol applications.

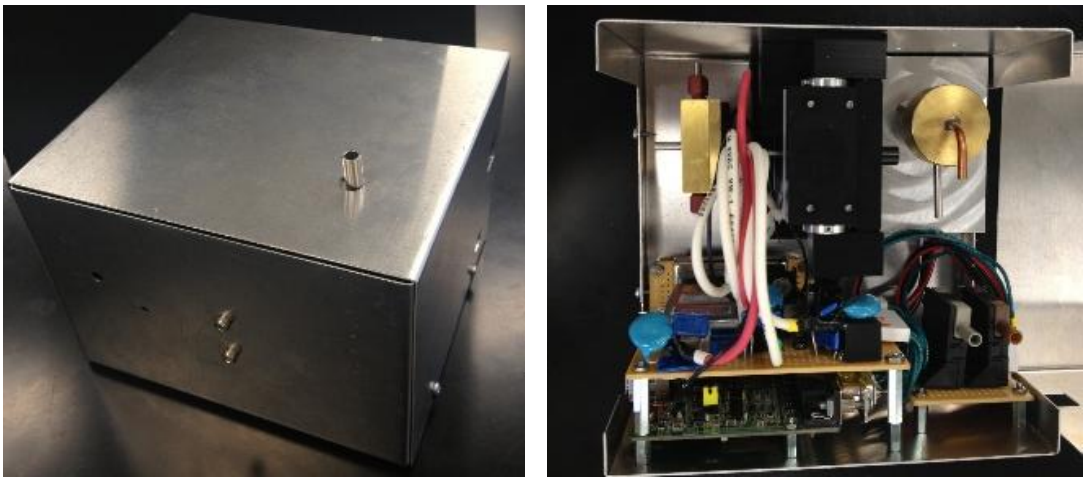

Figure 8.5: The overview of the prototype mini E-sizer.

8.4 Software Development for the Prototype

To control and monitor the prototype mini e-UPS, a software is necessary to be developed for the communication between a data acquisition card and a computer. Data acquisition is the process of sampling signals and converting the resulting samples into digital numeric values which can be manipulated by a computer. A data acquisition system typically converts analog waveforms into digital values for processing, or inversely. Software can be developed to control the data acquisition applications, by using various programming languages such as BASIC, C, FORTRAN, Java, Pascal, etc. I

In this study, a low-cost 12 bits USB data acquisition card (Advantech, Model USB-4702) was used. It is easy, efficient, reliable and rugged enough for many measurement applications. Table 8.2 lists the usage of each channel of the DAQ card, including eight analog to digital conversion channels, one digital to analog conversion channel and two digital signal output channels. With the help of DAQ card, a software was thus developed

based on Visual Basic language. Figure 8.6 shows the main software interface and the setting window of the developed software. Menu bar, tool bar, test information, real-time data table and graphs are all included. It is easy for users to create a new sample sequence, to run or stop measurement, to monitor the device and to save data. In the test information area, a user (users) can input sample name, set storage address for data file and see the current status of the mini sizer (e.g. running time, voltage range and size range of each sample). In the real-time data area, sample temperature, sample humidity, charger voltage and information about each particle size bin are all displayed and updated in time. The graphs for particle size distribution, DMA voltage and sheath flow rate are shown in the main interface as well. As shown in Figure 8.6 (b), a properties window was built to set the operational condition of DMA, to input some physical properties of air and aerosol (i.e. gas viscosity, gas mean free path, particle density) and to choose correction method if needed. Two DMA operational modes can be applied, stepping mode and scanning mode, for selecting particles with interested mobility size and measuring particle size distribution, respectively. To set sample sequence, the device can be used at continuous or semi continuous measurement, automatically. The raw data collected through the software will be saved for data inversion and the future analysis.

Table 8.2: DAQ Card channels and applications

DAQ Channel	Channel No	Application
AD	0	Aerosol flow rate monitor
	1	Sheath flow rate monitor
	2	DMA HV monitor

	3	Charger positive HV monitor
	4 (optional)	Charger negative HV monitor
	5	Humidity sensor
	6	Temperature sensor
	7	Electrometer current monitor
DA	0	DMA voltage control
Digital Out	0	Aerosol flow pump control
	1	Sheath flow pump control

(a)

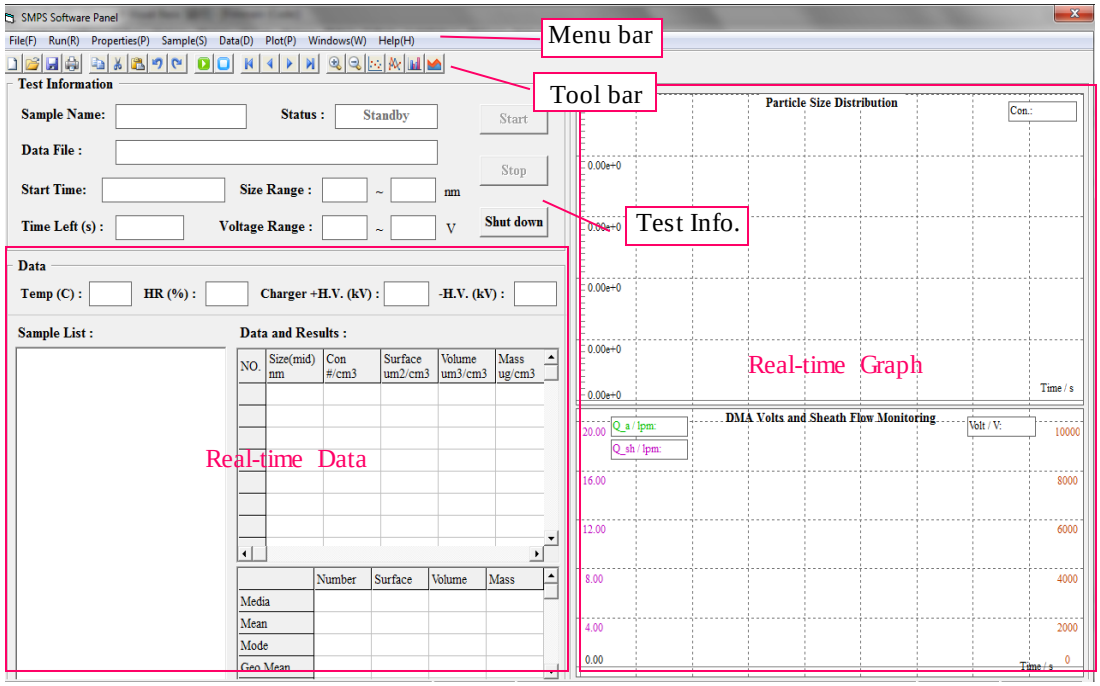

(b)

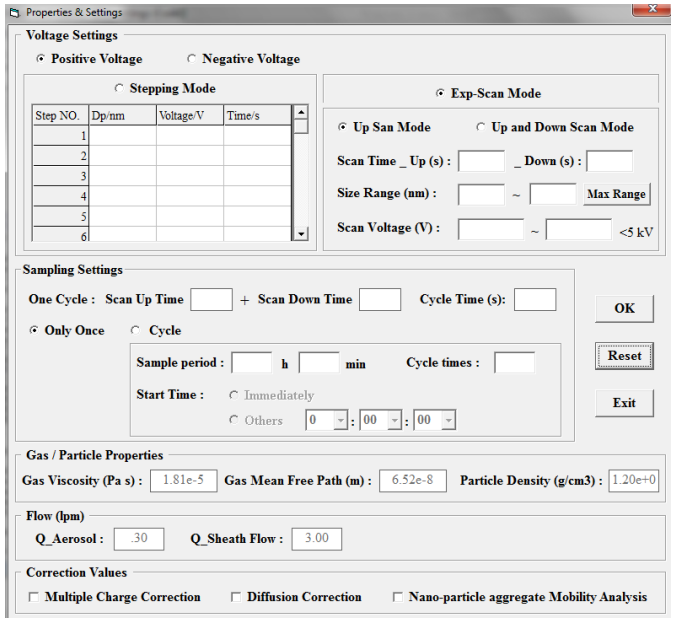

Figure 8.6: The software developed for mini E-sizer operation.

8.5 Date Inversion Scheme for Retrieving Particles Size Distribution

The size distribution of ultrafine particles is a fundamental property of an ultrafine aerosol stream, and is one of the most essential parameters for ambient/personal ultrafine particle assessment. The raw instrument data obtained from any electrical mobility based aerosol sizer is not straightforward, because it is not an ideal one to one correspondence between the measured channels and actual size bins (Kandlikar and Ramachandran, 1999). In most cases, the particles in measured size channel are not entirely the particles in corresponding size range, but might include particles from neighboring size bins due to the multiple charge effect on large particles. Thus, a degree of indeterminacy could be introduced into the size distribution retrieval process because of this non-ideal overlapping.

The retrieval process is called data inversion. Several mathematical techniques have been developed for data inversion, including linear inversion approach, nonlinear inversion approach, extreme value estimation method and Bayesian Method. A detailed review on inversion methods for analyzing aerosol measurement can be found in the article by Kandlikar and Ramachandran (1999). From these methods, to choose the most suitable algorithm for a size distribution measurement study, there is always a trade-off between algorithmic complexity, calculation speed, and the accuracy of reconstruction (Voutilainen et al., 2000). Especially for a miniaturized aerosol device, which has a limit CPU and memory, the computational effort in data inversion must be taken into consideration while the accuracy of solution cannot be negligible.

In this study, the constrained least square method was chosen to be applied for quickly recover the ultrafine particle size distribution during measurement. It was first developed by Philips in 1962, and later introduced into the aerosol measurement field by Twomey in 1965. To retrieve agreeable size distribution, the constrained method with a maximum error tolerance of 5% in the measurements was reported by Rizzi et al. (1982). For the developed mini e-UPS, the measured current I as a function of voltage V applied onto the differential mobility analyzer can be expressed as

$$I(V) = Q_a e \int_0^\infty f(D_p) \sum_n n \, \eta_{ex}(D_p) P(D_p, n) \, \Omega \left(Z_p, Z_p^*\right) dD_p \qquad (8\text{-}2)$$

where Q_a is the aerosol flowrate through mini Faraday cage, e is elementary charge, $f(D_p)$ is particle size distribution function, n is the number of charge on particles, $\eta_{ex}(D_p)$ is particle extrinsic charging efficiency, $P(D_p, n)$ is particle extrinsic charge distribution

and $\Omega\left(Z_p, Z_p^*\right)$ is the transfer function of mini-plate DMA. In reality, the prototype mini e-UPS was operated at stepping mode, which means the above equation could be simplified into discrete form as

$$I_m = Q_a e \sum_{j=1}^{J} \eta_{ex}(D_{p,j}) \sum_{n=1}^{N} nP\left(D_p, n\right) \Omega\left(Z_p, Z_{p,m}^*\right) \Delta D_{p,j} f\left(D_{p,j}\right) \quad (8\text{-}3)$$

and $$I_{M\times 1}/_{(Q_a e)} = \boldsymbol{A}_{\boldsymbol{M}\times \boldsymbol{J}}\, dN_{J\times 1} \quad (8\text{-}4)$$

where I is a $M \times 1$ vector, M represents the number of voltage steps applied on the mini-plate DMA, J is the number of size bins for the whole size distribution profile in the final output, A is $M \times J$ overall penetration matrix, dN is the number count for each size bin and is a $J \times 1$ vector. To solve the linear equation 8-4, Twomey-Philips solution was deducted to be

$$dN = \Delta D_{p,j} f\left(D_{p,j}\right) = (A^T A + \lambda H)^{-1} A^T (I/Q_a e) \quad (8\text{-}5)$$

Where H matrix is nearly diagonal and depends on the smoothing constraint of choice. Twomey (1977) gives the H matrix for a number of different constraints. λ is the smoothness conditioning parameter. Rizzi et al (1982) gave the range of λ to be between 10^{-4} and 0.05 for providing best solution when using this approach to retrieve aerosol size spectra from simulated spectral optical depths in the wavelength range from 0.37 to 2.2 μm. However, it might not be a range for mini e-UPS, because of different measuring technique and A matrix.

In order to applied constrained least square method into the prototype mini e-UPS, three simulated aerosol size distributions with corresponding currents were used as examples to test this inversion method first. They are monodisperse aerosol with geometric mean

diameter of 60 nm and geometric standard deviation of 1.15, polydisperse aerosol with geometric mean diameter of 40 nm and geometric standard deviation of 1.5, and aerosol with bi-modal size distribution of two peak sizes of 20 nm and 60 nm, respectively. As shown in Figure 8.7, for all three test cases, the particle size distributions calculated via inversion scheme agree with their reference distribution very well. This excellent agreement proved the constrained least square inversion method for recovering the particle size distribution for the developed mini e-UPS.

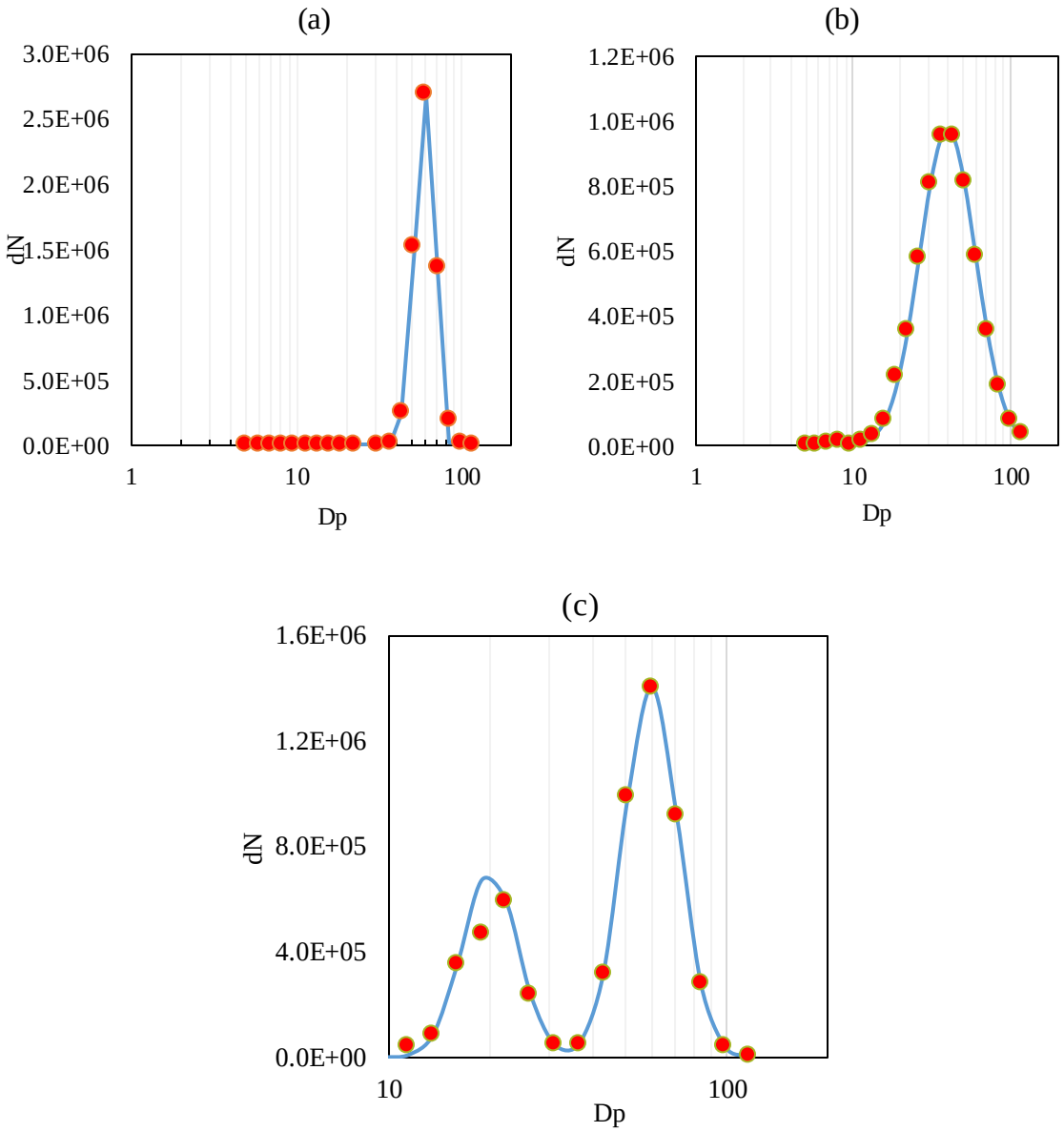

Figure 8.7: Comparison of inversed particle size distribution based on constrained least square method and reference ones for three different cases: (a) Dp,mean = 60 nm, σg =1.15; (b) Dp,mean = 40 nm, σg =1.5;; and (c) biomodal distribution with Dp,mean,1 = 20 nm and Dp,mean,2 = 60 nm

To applied constrained least square method to recover particle size distribution when using the prototype mini e-UPS to measure aerosol generated in the laboratory, a collision

atomizer was used and a SMPS was used to measure particle size distribution parallelly at the downstream. The comparative measurement results were shown in Figure 8.8, indicating a good agreement between mini e-UPS and SMPS. The peak sizes of two aerosol instruments were close to each other. The overall shape of two distributions are similar and overlap. It thus proved the prototype mini e-UPS's sizing ability for measuring unimodal particle size distribution.

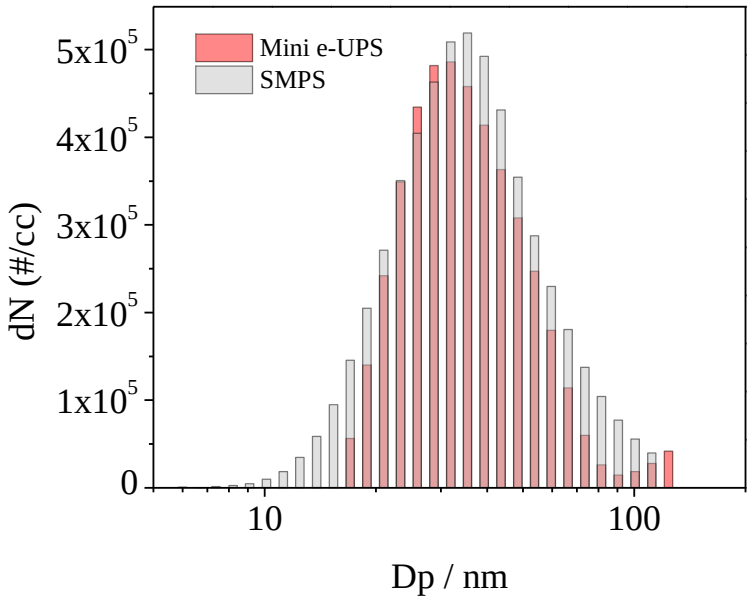

Figure 8.8: Comparison of particle size distribution measurement between mini e-UPS and SMPS.

8.6 Summary

A prototype mini e-UPS was developed by assembling the aerosol inlet, mini-plate charger, mini-plate DMA, mini Faraday cage, pumps, flow meters, filters, and some

electronic components together. The overall size is 6" in length, 5" in width, and 4" in height. It is smaller and lighter than any other aerosol sizers in the market. A software based on Visual Basic language was also developed to operate stepping mode on mini e-UPS. Based on the component calibration results reported in Chapter 6 and Chapter 7 for mini-plate charger and mini-plate DMA, respectively, a data inversion scheme was developed for deconvoluting particle size distribution form measured signals. To reduce calculation power, the constrained least square method was utilized by establishing a penetration matrix. Since it is a linear algebra calculation between the current data and outputting the size distribution profile, the inversion scheme enabled a fast measurement for the prototype. The raw data were recorded for further precise analysis as well.

Three different simulated particle size distributions and currents were applied to test the developed data inversion scheme. The excellent agreement between the inversed and reference size distribution indicated reliability of the data inversion scheme. For evaluating the measuring performance of the prototype unit, laboratory generated aerosol were used for test. The result verified the measurement capability of the prototype mini e-UPS. To further evaluate the mini e-UPS, more laboratory and field tests are recommended to conducted in near future.

CHAPTER 9 Dissertation Accomplishments and Recommendation for Future Work

9.1 Summary of Accomplishments

In this dissertation, ultrafine particle generation technique and measurement technique were studied. In ultrafine particle generation part, a single capillary ES with soft X-ray photoionzer as charge reduction scheme was developed and evaluated for producing monodisperse aerosol. To generate ultrafine particles in high mass concentration, a TSE twin-head ES was investigated and optimized. For ultrafine particle measurement part, two key components of a miniature electrical ultrafine particle sizer (i.e., mini-eUPS), mini-plate charger and mini-plate DMA were designed and constructed. Their performances were carefully evaluated. Finally, a prototype mini-eUPS with developed software was assembled and tested to perform aerosol measurement. The detailed accomplishments of each part of the study are summarized as follows:

9.1.1 Ultrafine Particle Generation via Two New Electrospray Systems

(a) Development of a Prototype ES Aerosol Generator with Photoionizer as Chage Reduction Scheme

A prototype single-capillary ES aerosol generator with a soft X-ray (photo-ionizer) for the charge reduction has been designed and experimentally investigated in this

dissertation. The prototype consists of two chambers: one for liquid spray and the other for charge reduction. A disk plate with an orifice at the center (having the thickness of 0.125″) was used to partition two chambers. With the prototype design, highly charged particles generated in the spray chamber were quickly carried by carrier flow through the orifice and entered the charge reduction chamber in which both the direct photo-charging and bipolar diffusion charging of particles took place at the same time. Bipolar ions were produced by photoemission of gas molecules when exposed to the soft X-ray. As a result, the charge level on ES-generated particles was reduced. The performance of the prototype was optimized by testing the X-ray radiation direction effect, orifice opening effect and carrier gas effect on the particle transmission efficiency. To evaluate the soft X-ray's effect on electrospray operation, the spray current as a function of applied voltage was recorded.

Our study found that, by testing four configurations, the operation of a soft X-ray photoionizer does not affect the electrospray in the setup having 90 ° X-ray irradiation and 0.25″ D orifice plate, and the applied voltage needed to operate the electrospray was shifted towards the higher voltage region for the other setups. The largest shift of I-V curve was observed in the case with 180 ° X-ray irradiation and the 1.25″ D orifice plate. For the cases using CO_2 as the carrier gas flow, the similar trend of voltage shifting was also observed. The reason for the observed voltage shift is because of the X-ray exposure in the spray chamber. The higher the X-ray exposure chance in the spray chamber, the larger the ES voltage shift for ES operation. However, the spray current at the cone-jet mode operation in all of the test cases using the same spray solutions remained at the same value.

Fluorescence-labeled sucrose particles with sizes ranging from 30 to 300 nm were generated in the studied ES aerosol generator to evaluate the particle transmission efficiency of the prototype. Our study also evidenced that the particle transmission efficiency of the prototype could be improved by increasing the carrier gas flow rate. Our evaluation indicated that the highest particle transmission efficiency, 46%, was achieved for the prototype having the 180 ° X-ray irradiation and 0.25″ D orifice plate, operated at the carrier gas flow rate of 8.0 lpm (regarded as the optimal configuration and operation for the prototype). It is further shown that the transmission efficiency remained at the same level for the test particle size ranging from 50 to 300 nm.

The charge fractions (i.e., both positively and negatively charged, and neutral fractions) of particles exiting the prototype were finally characterized in this study to investigate the charge status of produced particles. Using the above measurement at various particle sizes and comparing them with the calculated Fuchs bipolar charge distribution of test particles, it is concluded that the smaller the particles, the more effective the soft X-ray neutralization. For particles with the sizes less than 110 nm, the reasonable agreement between the measured fraction data and the calculated Fuchs data was obtained. The deviation from the Fuchs bipolar charge fraction was noted in the cases of particles with sizes larger than 110 nm. The reasons for the deviation could be attributed to (1) relatively insufficient ion concentration generated by the soft X-ray source; (2) spacial non-uniformity of ES generated aerosols and soft X-ray irradiation inside of generation chamber; (3) the potential of direct photoionization of particles under the X-ray irradiation.

(b) Evaluation of TSE Twin-head ES Aerosol Generation System

The concern of adverse health effects due to the exposure of nanoparticles has recently been increasing along with the fast development and wide application of nanotechnology. Tools are in demand to perform the toxicity studies of nanoparticles, particularly in its individual form (not in the agglomerate form). Unfortunately, such a tool for studying the toxicity of nanoparticles in their individual form has not been commercially available until now. With the capability of producing un-agglomerated droplets/particles with sizes ranging from nanometers to super-micrometers, a twin-head electrospray nanoparticle disperser was developed by TSE Systems Inc. With the presence of a DC electrical field for its operation, particles produced by electrospray are highly charged in the same polarity. Such charged particles are in general difficult to be kept airborne because of the electrostatic effects. The charge reduction is thus necessary for electrosprayed particles in order to minimize the loss during the particle transport. Without using radioactive materials or corona discharge as the bi-polar ion sources for reducing charges on electrosprayed particles, the twin-head electrospray technique was implemented in the studied disperser to achieve the same task. In the disperser, positive high voltage was applied to one spray head (i.e., capillary), producing positively charged particles, and negative high voltage applied to the other, generating negatively charged ones. The mixing and collision of particles in both polarities in general reduced the charge level on particles while increasing the mass concentration of particles exiting the studied disperser.

A systematic study has been performed on the studied electrospray disperser regarding to its mass throughput and quality of particle size distribution. The performance of the disperser was studied by varying the spray capillary tip distance, carrier-to-sheath flow rate ratio, total gas flow rate, liquid feeding rate, nanoparticle suspension concentration and particle material. In addition, the size distribution of dispersed nanoparticles and spatial uniformity of particles in the inhalation exposure chamber was also investigated. It was found that the maximal mass concentration of nanoparticles exiting from the studied disperser was achieved by having a capillary tip distance of 3.0 cm, and operating it at the total flow rate of 10.0 lpm with the carrier-to-sheath flow rate ratio of 4:3 and the suspension feeding flow rate of 20 μl/min. The applied voltages on both spray capillaries ranged from 7.5 to 8 kV. Under this setting, nanoparticles in high mass concentrations (i.e., > 10 mg/m^3) could be produced when spraying a suspension of nanomaterial concentrations higher than 8.0 g/L. The linear relationship between the mass throughput and the mass concentration of sprayed nanoparticle suspensions was also observed in this study. Further, the mass throughput of the studied THES disperser depended on the nanoparticle composition. As a result, a mass concentration monitor is thus recommended to be included in the system for measuring the actual mass concentration of particles exiting from the disperser.

9.1.2 Ultrafine Particle Measurement via A New Mini-eUPS

(a) Development of a Prototype Mini-plate Aerosol Charger

The performance of a prototype DC corona-based, unipolar aerosol charger has been experimentally investigated in this dissertation. The design of the prototype charger consists

of two similar brass blocks, where four identical corona channels (two in each) were designed inside. 50 μm Tungsten wires were used to provide corona ions when high electric field was established between wires and the grounded perforated plates. An aerosol charging channel was designed in the bottom block, surrounding by corona channels. Aerosol flow was injected into the charger through the top tube, passed through the charging zone and then exited from the bottom tube. The ion concentration in the charging zone depended on the strength of the high voltage applied to the wires, number of the wire used (or which corona channels were used). For simplifying the operation, no sheath air and ion driving voltage were designed to be used in this prototype.

The charger's performance was optimized by varying operational parameters (i.e., corona position, aerosol flowrate, corona current) for achieving as high extrinsic charging efficiency as possible. DMA classified monodisperse NaCl particles of 40 nm mobility diameter was used for test. Based on the experimental results (i.e. intrinsic and extrinsic charging efficiencies), it is concluded that one wire corona condition is better for particle charging than two wire corona. The corona occurring at the channel closest to the aerosol outlet provides highest extrinsic charging efficiency, resulting in less particle loss. By investigating the charging performance at different corona currents and aerosol flowrates, the corona current of 2 μA and 0.6 lpm aerosol flowrate was determined as optimal operation condition, because of the good charging efficiency, low energy consumption and high particle number counts.

Both intrinsic and extrinsic charging efficiencies of particles with mobility diameters ranging from 10 to 200 nm were measured at the optimal operation condition (i.e. 0.6 aerosol flowrate and 2 μA corona current occurring at the channel D). As expected, the intrinsic and extrinsic charging efficiencies increase with the increase of particle size. The highest extrinsic charging efficiency of the prototype was about 85%. The extrinsic charge distributions of monodisperse particles from 10 nm to 100 nm at the downstream of the prototype were measured by the tandem-DMA technique. Multiple charge effect was found for particle larger than 20 nm. The average charge was calculated based on the experimental charge distribution data. A Gaussian distribution function with particle size as variable was used to fit particle charge distribution. And a reasonable agreement was achieved when the fitted charge distribution of particles were compared with the extrinsic charge distributions measured, indicating the fitted Gaussian function could be used into the data inversion scheme for retrieving particle size distribution from the measured mobility distribution in a particle mobility analyzer.

(b) Development of Miniature Plate DMA for Ultrafine Particle Sizing

Miniature plate DMAs (i.e., mini-plate DMAs) have been developed for ultrafine particle measurement/monitoring. The tandem DMA technique was applied to evaluate the performance of mini-plate DMAs. Two prototype mini-plate DMAs (i.e., DMA-1 and DMA-2) were constructed. Mini-plate DMA-1 has the classification length of 52.4 mm, 75% aerosol slit opening in length (related to the width of the classification zone) and 2.11 mm in the plate-to-plate spacing, while mini-plate DMA-2 has 35.7 mm in length, 50% aerosol

slit opening and 3.2 mm in height. By design, the particle sizing range of DMA-2 is less than that of DMA-1 under the same sheath flowrate operation. Compared with cylindrical DMAs, mini-plate DMAs are cost effective and easy to make and maintain. They however require detail experimental calibration for their performance. The compact size of mini-plate DMAs make it suitable to incorporate in low-cost and compact ultrafine particle sizers.

For the sizing accuracy of mini-plate DMAs a correction factor (η) was proposed to modify the equation derived from the 2-D assumption in order to better determine the applied voltage for sizing particles with the selected electrical mobility. Because of the difference in the DMA dimensions, the correction factors for DMA-1 and DMA-2 are different. It is interesting to observe that the factor is a linear function of aerosol-to-sheath flowrate ratio (β). To investigate the performance of mini-plate DMAs a piecewise linear deconvolution scheme was applied in our study to recover the real transfer function of DMAs from the collected TDMA data. For both DMA-1 and DMA-2 the typical transfer functions are in the triangular shape for non-diffusive particles (i.e., particles in large sizes). The maximal height, area and FWHM of DMA transfer function indicate the maximal transmission efficiency of particles with the central electrical mobility, transmission efficiency of DMA at a fixed DMA voltage and the sizing resolution, respectively. More, the experimental transfer function of DMAs is required in the data reduction schemes used to better recover the size distribution of particles.

In three studied cases (i.e., aerosol flowrate of 0.3 lpm; sheath flowrates of 1.5, 3.0 and 6.0 lpm) the height of transfer function of mini-plate DMAs increases as the particle size

increases while the FWHM decreases. The better height of transfer function was found when DMAs were operated at a high aerosol-to-sheath flowrate ratio. The discrepancies between the FWHMs obtained in experiments and calculated by the 2-D modeling were obvious for all studied flow cases. It is possibly because the aerosol slits were not fully opened along the entire width of classification zone. The higher percentage of opening in length (i.e., DMA-1) has the FWHM values closer to those calculated by the 2-D model when compared to those with DMA-2. It shall be noted that part of sheath flow was applied to keep the aerosol flow away from the side walls of DMAs, not for sheathing it from the aerosol exit slit. The effective sheath flowrate should be less than the total sheath flowrate used under the studied mini-plate DMA design. For plate DMAs having such aerosol slit design, the sizing resolution (i.e., FWHM) and accuracy cannot be simply estimated by the equations derived based on the ideal 2-D assumption. The less the percentage of slit opening in length (relative to the width of classification zone) the worse the particle sizing resolution.

(c) Development of a Prototype Mini-eUPS

A prototype mini e-UPS was developed by assembling the aerosol inlet, mini-plate charger, mini-plate DMA, mini Faraday cage, pumps, flow meters, filters, and some electronic components together. The overall size is 6" in length, 5" in width, and 4" in height. It is smaller and lighter than any other aerosol sizers in the market. A software based on Visual Basic language was also developed to operate stepping mode on mini e-UPS. Based on the component calibration results reported in Chapter 6 and Chapter 7 for mini-plate charger and mini-plate DMA, respectively, a data inversion scheme was developed for

deconvoluting particle size distribution form measured signals. To reduce calculation power, the constrained least square method was utilized by establishing a penetration matrix. Since it is a linear algebra calculation between the current data and outputting the size distribution profile, the inversion scheme enabled a fast measurement for the prototype. The raw data were recorded for further precise analysis as well.

Three different simulated particle size distributions and currents were applied to test the developed data inversion scheme. The excellent agreement between the inversed and reference size distribution indicated reliability of the data inversion scheme. For evaluating the measuring performance of the prototype unit, laboratory generated aerosol were used for test. The result verified the measurement capability of the prototype mini e-UPS. To further evaluate the mini e-UPS, more laboratory and field tests are recommended to conducted in near future.

9.2 Recommendations for Future Research

The electrospray with soft X-ray developed in this study has the charge reduction chamber made of PVC. The maximum transmission efficiency we can get for ES generated particles is about 47%, lower than previous work (Fu et al., 2011). One reasons could be the lower ion concentration generated by soft X-ray compared to 4 fresh ^{210}Po of 5 mCi, which was illustrated in this dissertation. And it was also found the most of particles loss were on the orifice plate due to the strong electric force. However, it still has possibility to improve the transmission efficiency by using a metal (e.g. Aluminum) charge reduction chamber, which has the same material as the charge reduction chamber used in Fu's study. Since the

orifice plate is grounded when operating electrospray, the metal charge reduction chamber against to the plate will be grounded as well. The electric field inside the entire generator thus could be changed. Particles generated in the ES chamber may have more chance to travel into the charge reduction chamber by the electric force and carrier flow, instead of loss on the orifice plate. Once more particles could enter the charge reduction chamber, the charges on them could be reduced by soft X-ray irradiation. Their transmission efficiency is probably going to be improved.

Based on the evaluation of mini-plate charger, we found one wire corona discharge has better charging performance than two wires configuration. So, for the second generation of mini-plate charger, it is recommended to be designed with one wire corona channel. It shall be smaller in size. And to make aerosol flow outlet as close to the charging zone as possible may help eliminate particle loss inside the charger, leading to a higher extrinsic charging efficiency. It is also suggested to directly inject or draw the aerosol flow into/out of the charging zone, instead of the two 90° turns in current design, to improve charging efficiency. Once the mini-plate charger of 2nd generation is constructed, its operational condition is going to be determined by measuring the charging efficiency and charge distribution of particles. The modified mini-plate charger will be final particle charger version in the mini e-UPS.

As discussed in the mini-plate DMA study, the classic 2D model cannot well predict both the central voltage for particle sizing and the transfer function of mini-plate DMA (including the height and FWHM of transfer function). Because 3D effect (e.g. flow

expansion inside the classification zone) does occur in real cases. That is also why previous studies all showed a deviation between the experimental and theoretical DMA resolution. In order to better investigate DMA performance in plate design, a 3D modeling work is highly recommended to be studied in the future, which will be very helpful on illustrating some experiment results and creating a new equation to describe performance of plate DMA more accurately.

The prototype mini-eUPS has been assembled and preliminarily tested. A simple data inversion scheme was developed. The future effort on this mini-eUPS will be focused on its software development and overall performance evaluation. The constrained least square data reduction algorithm will be coded into the current mini-eUPS program. The overall performance evaluation of the mini-eUPS will primarily include the comparison of particle size distributions measured by the mini-eUPS and SMPSs. Both uni-modal and bimodal particles with different size distributions will be generated in the lab for this overall evaluation.

With the collaboration of the research group of Prof. Lu in Washington University in St. Louis, the wireless sensor network function for mini-eUPSs is currently under development. Upon the completion of wireless network function, the mini-eUPS (having the modified key components), integrated with the wireless network function, will be tested in the laboratory and validated in a field study of ambient aerosol measurement for a period of time.

Literature Cited

Adachi, M., Kousaka Y., and Okuyama, K. 1985. Unipolar and bipolar diffusion charging of ultrafine aerosol particles. J. Aerosol Sci., 16(2): 109-122.

Adachi, M., Okuyama, K., Kousaka, Y., Kozuru, H., & Pui, D.Y.H. (1989). Bipolar diffusion charging of aerosol particles under high particle/ion concentration ratios. Aerosol Science and Technology, 11, 144-156.Alguacil, F. J., & Alonso, M. 2006. Multiple charging of ultrafine particles in a corona charger. Journal of Aerosol Science, 37(2), 875–884.

Allen, M.D. and Raabe, O.G. 1982. Re-evaluation at Millikan's Oil Drop Data for the Motion of Small Particles in Air, J. Aerosol Sci. 13: 537-547.

Allmaier, Günter, Laschober, C., & Szymanski, W.W. (2008). Nano ES GEMMA and PDMA, New tools for the analysis of nanobioparticles - protein complexes, lipoparticles, and viruses. Journal of the American Society for Mass Spectometry, 19(8), 1062-1068.

Alonso, M. (2002). Reducing the diffusional spreading rate of a Brownian particle by an appropriate non-uniform external force field. Aerosol Sci. 33:439-450.

Alonso, M., and Endo, Y. (2001). Dispersion of aerosol particles undergoing Brownian motion. J. Phys. A: Math. Gen., 34(49):10745-10755.

Alonso, M., Martin, M.I. and Alguacil, F.J. 2006. The Measurement of Charging Efficiencies and Losses of Aerosol Nanoparticles in a Corona Charger. J. Electrostat. 64: 203–214.

Bacher, G., Szymanski, W.W., Kaufman, S.L., Zollner, P., Blass, D. & Allmaier, G. (2001). Charge-reduced nano electrospray ionization combined with differential mobility analysis of peptides, proteins, glycoproteins, noncovalent protein complexes and viruses. Journal of Mass Spectrometry, 36, 1038-1052.

Bailey, A.G. (1988). Electrostatic spraying of liquids. Wiley, NY.

Biskos, G. 2004. Theoretical and Experimental Investigation of the Differential Mobility Spectrometer, Ph.D. Thesis, University of Cambridge, U.K.

Borra, J.P., Camelot, D., Chou, K.-L., Kooyman, P.J., Marijnissen, J.C.M., & Scarlett B. (1999). Bipolar coagulation for power production: micro-mixing inside droplets. Journal of Aerosol Science, 30(7), 945-958.

Borra JP, Goldman A, Goldman M, Boulaud D. 1998. Electrical discharge regimes and aerosol production in point-to-plane dc high-pressure cold plasmas: aerosol production by electrical discharges. J Aerosol Sci 29:661–674

Bräuner, E.V., Forchhammer, L., Meller, P., Simonsen, J., Glasius, M., Wåhlin, P., Raaschou-Nielsen, O., and Loft, S. (2007). Exposure to ultrafine particles from ambient air and oxidative stress-induced DNA damage, Environ. Health Perspect., 115(8): 1177-1182

Brunner TJ, Wick P, Manser P, Spohn P, Grass RN, Limbach LK, Bruinink A, Stark WJ (2006) In vitro cytotoxicity of oxide nanoparticles: comparison to asbestos, silica, and the effect of particle solubility. Environ Sci Technol 40:4374-4381

Buscher, P., Schmidt-Ott, A. and Wiedensohler, A. 1980. Performance of a Unipolar "Square Wave" Diffusion Charger with Variable Nt-Product. J. Aerosol Sci. 25: 651–663

Buscher, P., Schmidt-Ott, A.,&Wiedensohler, A. 1994. Performance of a unipolar 'square wave' diffusion charger with variable nt-product. Journal of Aerosol Science, 25, 651–663.

Caldow, R., Kolb, J., Berkner, L., et al. (2004). Performance of an engine exhaust particle sizer spectrometer. AAAR Conference, Atlanta, GA.

Camelot D, Marijnissen JCM, Scarlett B (1999) Bipolar coagulation process for the production of powders. Ind Eng Chem Res 38:631-638

Chen, C.C., Huang, S.H., Lin, W.Y., Shih, T.S., and Jeng, F.T. (1999).The virtual cyclone as a personal respirable sampler. Aerosol Sciencea nd Technology, 31: 422-432.

Chen, C.H., Emond, M.H.J., Kelder, E.M., Meester, B. & Schoonman, J. (1999). Electrostatic sol-spray deposition of nanostructured ceramic thin films. Journal of Aerosol Science, 30, 959-965.

Chen, D.R., Li, W.L., and Cheng, M.D. (2007). Development of a multiple-stage differential mobility analyzer. (MDMA). Aerosol Science and Technology, 41: 217-230.

Chen, D.R. & Pui, D.Y.H. (1997). Experimental investigation of scaling laws for electrospraying: dielectric constant effect. Aerosol science and technology, 27(3), 367-380.

Chen, D.-R., and Pui, D.Y.H. A high efficiency, high throughput unipolar aerosol charger for nanoparticles. J. Nanoparticle Res., 1: 115-126. 1999.

Chen, D.R. & Pui, D.Y.H. (2000). Electrospraying apparatus and method for introducing material into cells. US Patent 6,093,557.

Chen, D.R., and Pui, D.Y.H. (2008). Nanoparticle and ultrafine aerosol measurement, monograph to be included in air sampling technologies: principle and applications, published by ACGIH (available online).

Chen, D.R., Pui, D.Y.H., Hummes, D., Fissan, H., Quant, F.R., and Sem, G.J. (1998). Design and evaluation of a nanometer aerosol differential mobility analyzer (Nano-DMA). J. Aerosol Sci., 29: 497-509.

Chen, D.R., Pui, D.Y.H., & Kaufman, S.L. (1995). Electrospraying of conducting liquids for monodisperse aerosol generation in the 4 nm to 1.8 μm diameter range. Journal of Aerosol Science, 26, 963-977.

Chen, D.R., Pui, D.Y.H., Mulholland, G.W., and Fernandez, M. 1999. Design and Testing of an Aerosol/Sheath Inlet for High Resolution Measurements with a DMA. J. Aerosol Sci., 30: 983-999

Chen, D.R., Wendt, C.H. & Pui, D.Y.H. (2000). A novel approach for introducing bio-material into cells. Journal of Nanoparticle Research, 2, 133-139.

Chen J, Davidson JH. 2002. Ozone production in the positive DC corona discharge: model and comparison to experiments. Plasma Chem Plasma Process 22:495–522

Choi, Y. and Kim, S. 2007. An Improved Method for Charging Submicron and Nano Particles with Uniform Charging Performance. Aerosol Sci. Technol. 41: 259– 265.

Cloupeau, M. & Prunet-Foch, B. (1989). Electrostatic spraying of liquids in cone-jet mode. Journal of Electrostatics, 22,135-159.

Cloupeau, M. & Prunet-Foch, B. (1990). Electrostatic spraying of liquids: main functioning modes. Journal of electrostatics, 25,165-184.
Cloupeau, M. & Prunet-Foch, B. (1994). Electrohydrodynamic spraying functioning modes: a critical review. Journal of Aerosol Science, 25,1021-1036.
Ciach, T. (2007). Application of electro-hydro-dynamic atomization in drug delivery. Journal of Drug Delivery Science and Technology, 17, 367-375.
Coffee, R.A. (1964). Electrostatic spraying of liquids and powders. Electron Power, 10, 349-352.
Cole, R.B. (1997). Electrospray ionisation mass spectrometry. Wiley, New York.
Dabisch PA, Kline J, Lewis C, Yeager J, Pitt MLM (2010) Characterization of a head-only aerosol exposure system for nonhuman primates. Inhal Toxicol 22(3):224-233
Delfino, R.J., Sioutas, C., and Malik, S. (2005). Potential role of ultrafine particles in associations between airborne particle mass and cardiovascular health. Environ Health Perspect, 113: 934-946.
de Juan, L., & Fernández de la Mora, J. (1997). Charge and size distributions of electrospray drops. Journal of Colloid and Interface Science, 186, 280-293.
de Juan, L., & Fernández de la Mora, J., 1998. High Resolution Size Analysis of Nanoparticles and Ions: Running a Vienna DMA of Near Optimal Length at Reynolds Numbers up to 5000. J. Aerosol Sci., 29(5–6): 617–626.
Dabisch PA, Kline J, Lewis C, Yeager J, Pitt MLM (2010) Characterization of a head-only aerosol exposure system for nonhuman primates. Inhal Toxicol 22(3):224-233
Deng, W., Klemic, J.F., Li, X., Reed, M.A. & Gomez, A. (2007). Liquid fuel microcombustor using microfabricated multiplexed electrospray sources. Proceedings of the Combustion Institute, 31, 2239-2246.
Dulcks, Th. & Juraschek, R. (1999). Electrospray as an ionization method for mass spectrometry. Journal of Aerosol Science, 30, 927-943.
Dunn, P.F., Grace, J.M., & Snarski, S.R. (1994). The mixing of electrically charged droplets between and within electrohydrodynamic fine sprays. Journal of Aerosol Science, 25,1213-1227.
Dunn, P.F. & Snarski, S.R. (1991). Velocity component and diameter distribution characteristics of droplets within two interacting electrohydrodynamic sprays. Physics of Fluids, 3, 492-494.
Ebeling, D.D.,Westphall, M.S., Scalf,M., & Smith, L.M. (2000). Corona discharge in charge reduction electrospray mass spectrometry. Analytical Chemistry, 72, 5158-5161.
Erikson, H. A. (1921). The Change of mobility of the positive ions in air with age, Phys. Rev. 18: l00-101.
Fan, M., Fu, H., and Chen, D.R. (2011). A cost-effective differential mobility analyzer (c-DMA) for multiple DMA column applications. J. Aerosol Sci., 42: 462-473.
Fernández de la Mora, J., and Kozlowski, J. (2013). Hand-held differential mobility analyzers of high resolution for 1–30 nm particles: design and fabrication considerations, J. Aerosol Sci., 57: 45–53.

Fernández de la Mora, J. & Loscertales, I. G. (1994). The current emitted by highly conducting taylor cones. Journal of Fluid Mechanics, 260, 155-184.

Fenn, J.B., Mann, M., Meng, C.K. & Wong, S.F. (1989). Electrospray ionization gor mass-spectrometry of large biomolecules. Science, 246(4926),64–71

Flagan, R.C. (1998). History of Electrical Aerosol Measurements, Aerosol Science and Technology, 28:4, 301-380

Fissan, H., Hummes, D., Stratmann, F., Buscher, P., Neumann, S., Pui, D.Y.H. and Chen, D. (1996). Experimental comparison of four differential mobility analyzers for nanometer aerosol measurements. Aerosol Science and Technology, 24, 1-13.

Fry, F.A. (1970). Charge distribution on polystyrene aerosols and deposition in the human nose. Aerosol Sei. 1, 135-146.

Fu, H. Liu, Q. & Chen, D.R. (2012). Performance study of a twin-head electrospray system. Journal of Aerosol Science, 52, 33-44.

Fu, H., Patel, A.C., Holtzman, M.J. & Chen, D.R. (2011). A new electrospray aerosol generator with high particle transmission efficiency. Aerosol Science and Technology, 45, 1176-1183.

Fuchs, N.A. (1963). On the stationary charge distribution on aerosol particles in a bipolar ionic atmosphere. Geofis. Pura Appl. 56,185-193.

Fukuda, T., Asaki, H., Asano, T., Takagi, K., Honda, Z., Kamata, N., Ju, J. & Yamagata, Y. (2011). Surface morphology of fluorene thin film facricated by electrospray deposition technique using two organic solvents: application for organic light-emitting diodes. Thin Solid Films, 520(1), 600-605.

Gold, D. R., Litonjua, A., Schwarz, J., Lovett, E., Larson, A., Nearing, B., Allen, G., Verrier, M., Cherry, R., and Verrier, R. (2000). Ambient Pollution and Heart Rate Variability, Circulation 101: 1267-1273.

Gomez, A. (2002). The electrospray and its application to targeted drug inhalation. Respiratory Care, 47:1419-1431; discussion 1431-1413.

Habib MA, Muslim M, Shahadat MT, Islam MN, Ismail IMI, Ismail TSA, Mahmood AJ (2013) Photocatalytic decolorization of crystal violet in acqueous nano-ZnO suspension under visible light irradiation. J Nanostructure Chem 3:70

Han, B., Shimada, M., Okuyama, K. & Choi, M. (2003). Classification of monodisperse aerosol particles using an adjustable soft X-ray charger. Powder technology. 39, 336-344.

Hautreux, M., Hue, N., Kerdaniel Alexis Du Fou de, Zahir, A., Malec, V. & Laprévote, O. (2004). Under non-denaturing solvent conditions, the mean charge state of a multiply charged protein ion formed by electrospray is linearly correlated with the macromolecular surface. International Journal of Mass Spectrometry, 231(2-3), 131-137.

Heinlaan M, Ivask A, Blinova I, Dobourguier HC, Kahru A (2008) Toxicity of nanosized and bulk ZnO, CuO and TiO2 to bacteria Vibrio fischeri and crustaceans Daphnia magna and Thamnocephalus platyurus. Chemosphere 71:1308-1316

Hernández N, Moreno R, Sánchez-Herencia AJ, Fierro JL (2005) Surface behavior of nickel powders in aqueous suspensions. J Phys Chem-B 109(10):4470-4474

Hernandez-Sierra, A., Alguacil, F.J. and Alonso, M. 2003. Unipolar Charging of Nanometer Aerosol Particle in a Corona Ionizer. J. Aerosol Sci. 34: 733–745.

Hewitt, G.W. 1957. The charging of small particles for electrostatic precipitation. Trans. Amer. Inst. Elect. Engr. 76: 300-306.

Huberman, M.N., Beynon, J.C., Cohen, E., Goldin, D.S., Kidd, P.W., & Zafran, S. (1968). Present status of colloid microthruster technology. Journal of Spacecraft, 5, 1319-1324

Hutchins, D.K. and Holm, J. 1989. Aerosol Charger using Sinusoidally Driven Ion Current from a Corona Discharge. Aerosol Sci. Technol. 11: 244–253.

Hinds, W.C. Aerosol Technology. John Wiley & Sons, New York, 1999.Hines, R.L. (1966). Electrostatic atomization and spraying painting. Journal of Applied Physics, 37, 2730-2736.

Hoek, G., Brunekreef, B., Goldbohm, S., Fischer, P., and van den Brandt, P.A. (2002). Association between mortality and indicators of traffic-related air pollution in the Netherlands: a cohort study. Lancet, 360: 1203-1209.

Holguin, F. (2008). Traffic, outdoor air pollution, and asthma. Immunol Allergy Clin North Am 28: 577-588, viii–ix.

Hontañón, E., and Kruis, F. 2008. Single charging of nanoparticles by UV photoionization at high flow rates. Aerosol Sci. Technol., 42(4): 310-323.

Hontañón, E., and Kruis, F. E., 2009. A Differential Mobility Analyzer (DMA) for Size Selection of Nanoparticles at High Flow Rates. Aerosol Sci.Technol., 43(1): 25–37.

Hontañón, E., Rouenhoff, M., Azabal, A., Ramiro, E., and Kruis, F. E. (2014). Assessment of a cylindrical and a rectangular plate differential mobility analyzer for size fractionation of nanoparticles at high-aerosol flow rates. Aerosol Sci. Technol., 48(3): 333–339.

Horie M, Fukui H, Endoh S, Maru J, Miyauchi A, Shichiri M, Fujita K, Niki E, Hagihara Y, Yoshida Y, Morimoto Y, Iwahashi H (2012) Comparison of acute oxidative stress on rat lung induced by nano and fine-scale, soluble and insoluble metal oxide particles: NiO and TiO2. Inhal Toxicol 24(7):391-400

Hosseinmardi, A., Shojaee, N., Keyanpour-Rad, M. & Ebadzadeh, T. (2012). A study on the photoluminescence properties of electrospray deposited amorphous and crystalline nanostructured ZnO thin films. Ceramics International, 38(3), 1975-1980.

Huang, L., and Chen, D.R. (2010). Development of a mini- aerosol Faraday cage for personal nanoparticle monitor. AAAR 29th Annual Conference. Portland, OR.

Hummes, D., Stratmann, F., Neumann, S. and Fissan, H. (1996). Experimental determination of the transfer function of a di¤erential mobility analyzer (DMA) in the nanometer size range. Part. Part. Syst. Charact. 5: 327-332.

Hurd, F. K., and Mullins, J. C. (1962). Aerosol size distributions from ion mobility, J. Colloid Integace Sci. 17: 91-100.

Ijsebaert, J.C., Geerse, K.B., Marijnissen, J.C.M., Lammers, J.J. & Zanen P. (2001) electro-hydrodynamic atomization of drug solutions for inhalation purposes. Journal of Applied Physiology, 91, 2735-2741.

Intra, P. and Tippayawong, N. 2011. An overview of unipolar charger developments for

nanoparticle charging. Aerosol and Air Quality Research, 11: 187-209.
Ito, T., Otani, Y. & Namiki, N. (2004). Electrostatic separation of carbon dioxide by ionization in bifurcation flow. Aerosol and Air Quality Research, 4(1), 91-104.
Jaworek, A. (2007). Electrospray droplet sources for thin film deposition. Journal of Material Science, 42, 266-297.
Jaworek, A. & Krupa, A. (1999). Classification of the modes of EHD spraying. Journal of Aerosol Science, 30(7), 873-893.
Jiang, J., Hogan, J.C., Chen, D.R. & Biswas P. (2007a). Aerosol charging and capture in the nanoparticle size range (6-15nm) by direct photoionization and diffusion mechanisms. Journal of Applied Physics, 102, 034904-034907.
Jiang, J., Lee, H.M. & Biswas, P. (2007b). Model for nanoparticle charging by diffusion, direct photoionization, and thermionization mechanisms. Journal of Electrostatics, 65, 209-220.
Jones, A.R. & Thong, K.C. (1971). The production of charged monodisperse fuel droplets by electrical dispersion. Journal of Physics D: Appled Physics, 4,1159-1166.
Kandlikar, M. & Ramachandran, G. 1999. Inverse methods for analysing aerosol spectrometer measurements: a critical review. Journal of Aerosol Science 30(4):413-437.
Kaufman, S.L. (1998). Analysis of biomecules using electrospray and nanoparticle methods: the gas-phase electrophoretic mobility molecular analyzer (GEMMA). Journal of Aerosol Science, 29, 537-552.
Kaufman, S.L., Skogen, J.W., Dorman, F.D., Zarrin, F. & Lewis, K.C. (1996). Macromolecule analysis based on electrophoretic mobility in air: globular proteins. Analytical Chemistry, 68, 1895-1904.
Kim, S.C., Chen, D.R., Qi, C., Gelein, R.M., Finkelstein, J.N., Elder, A., Bentley, K., Oberdörster, G. & Pui, D.Y. (2010). A nanoparticle dispersion method for in vitro and in vivo nanotoxicity study. Nanotoxicology, 4(1), 42-51.
Kim, D.S., Kim, Y.M., Kwon, Y.T., and Park, K. (2011). Evaluation of a soft X-ray unipolar charger for charging nanoparticles. J. Nanopart Res, 13: 579-585.
Koropchak, J.A., Sadain, S.Y., Magnusson, X., Heybroek, L-E., Anisimov, M. & Kaufman, S.L. (1999). Nanoparticle detection technology for chemical analysis. Analytical Chemistry, 71(11), 386-394.
Kousaka, Y., Okuyama, K., Adachi, M., and Mimura, T. 1986. Effect of Brownian Diffusion on Electrical Classification of Ultrafine Aerosol Particles in Diffcrential Mobility Analyzcr, J. Chem. Eng. Japan 19:401-407.
Kreyling WG, Semmler M, Erbe F, Mayer P, Takenaka S, Schulz H (2002) Translocation of ultrafine insoluble iridium particles from lung epithelium to extrapulmonary organs is size dependent but very low. J Toxicol Environ Health 166:998-1004
Kulkarni, P., Namiki, N., Otani, Y., & Biswas, P. (2002). Charging of particles in unipolar coronas irradiated by in-situ soft X-rays: enhancement of capture efficiency of ultrafine particles. Journal of Aerosol Science, 33, 1279-1296.
Kulkarni, P. and Wang, J. 2006. New fast integrated mobility spectrometer for real-time

measurement of aerosol size distribution – I: concept and theory. Aerosol Science, 37: 1303- 1325.
Kulmala, M., Vehkamaki, H., Petaja, T., Dal Maso, M., Lauri, A., Kerminen, V.-M., Birmili, W., and McMurry P. (2004). Formation and growth rates of ultrafine atmospheric particles: A review of observations, J. Aerosol Sci., 35: 143-176.
Knutson, E. O., and Whitby, K. T. (1975). Aerosol classification by electric mobility: apparatus, theory, and applications. J. Aerosol Sci. 6:443-451.
Kruis, F.E., and Fissan, H. 2001. Nanoparticle charging in a twin Hewitt charger. J. Nanoparticle Res., 3: 39-50.
Labowsky, M.,&Fernández de la Mora, J. 2006.Novel ion mobility analyzers and filters. Journal of Aerosol Science, 37, 340–362.
Langevin, P. 1902. Sur la inobilit6 des ions dans les gaz, Conzptes rendus 134:646-649.
Langevin, P. 1903. L'Ionization des gaz, Ann. Chim. Phys. 28:289-384.
Langer, G. & Yamate, G. (1969). Encapsulation of liquid and solid aerosol particles to form dry powders. Journal of Colloid Interface Science, 29, 450-455.
Lee, Y.H., Bai, M.Y., and Chen, D.R. (2011). Multidrug encapsulation by coaxial tri-capillary electrospray. Colloids and Surfaces B: Biointerfaces, 82,104-110.
Lee, H.M, Kim, C.S., Shimada, M. & Okuyama, K. (2005). Bipolar diffusion charging for aerosol nanoparticle measurement using a soft X-ray charger. Aerosol Science, 36, 831-829.
Lee YH, Mei F, Bai MY, Zhao S, Chen DR (2010) Release profile characteristics of biodegradable-polymer-coated drug particles fabricated by dual-capillary electrospray. J Controlled Release 145:58-65
Lee YH, Park HK, Lee YM, Kim K, Park SB (2007) A practical procedure for producing silver nanocoated fabric and its antibacterial evaluation for biomedical applications. Chem Commun 2959-2961
Lenggoro, I.W., Okuyama, K., Fernández de la Mora, J. & Tohge, N. (2000). Preparation of ZnS nanoparticles by electrospray pyrolysis. Journal of Aerosol Science, 31, 121-136.
Li, L. and Chen, D.R. 2011. Performance study of a DC-corona-based particle charger for charge conditioning. Journal of Aerosol Science, 42: 87-99.
Li, L., Chen, D. R., Qi, C., and Kulkarni, P. S. (2009). A miniature disk electrostatic aerosol classifier (Mini-disk EAC) for personal nanoparticle sizers. J. Aerosol Sci., 40(11): 982–992.
Li, N., Harkema, J.R., Lewandowski, R.P., Wang, M., Bramble, L.A., Gookin, G.R., Ning, Z., Kleinman, M.T., Sioutas, C., and Nel, A.E. (2010). Ambient Ultrafine Particles Provide a String adjuvant Effect in the secondary immune response: implication for traffic-related asthma flares, Am. J Physiol Lung Cell Mol. Physiol, 299: L374-383
Li S, Zhu R, Zhu H, Xue M, Sun X, Yao S, Wang S (2008) Nanotoxicity of TiO2 nanoparticles to erythrocyte in vitro. Food Chem Toxicol 46:3626-3631
Li, W., Li, L., and Chen, D.R. (2006). Technical Note: A new deconvolution scheme for the retrieval of true DMA transfer function from tandem DMA data, Aerosol Science and

Technology, 40: 1052 -1057.
Lin, H.C., Lee, M.H., Yeh, C.H., Chung, Y.C. & Lin, Y.C. (2010). Electrospraying microfluidic chip for emulsion generation and satellite droplet separation. 14th International Conference on Miniaturized Systems for Chemistry and Life Sciences 3-7 October 2010, Groningen, The Netherlands
Liu, B.Y.H, Pui, D.Y.H. and Lin, B.Y. 1986. Aerosol charge Neutralization by a radioactive alpha source. Part. Charact. 3: 111-116.
Liu, B.Y.H., & Pui, D.Y.H. (1974a). Equilibrium bipolar charge distribution of aerosols. Journal of Colloid and Interface Science, 49, 305-312.
Liu, B. Y. H., and Pui, D. Y. H., 1974b. A Submicron Aerosol Standard and the Primary, Absolute Calibration of the Condensation Nucleus Counter, J. Colloid Interface Sci., 47(1), pp. 155–171.
Liu, B.Y., and Pui, D.Y.H. (1975). On the performance of the electrocal aerosol analzyer. J. Aerosol. Science, 6: 249-264.
Liu, B., Pui, D. Y.H., & Lin, B. (1986). Aerosol charge neutralization by a radioactive alpha source. Particle & Particle Systems Characterization, 3, 111-116.
Liu, B. Y. H., Whitby, K. T., and Pui, D. Y. H. 1974. A Portable Electrical Analyzer for Size Distribution Measurement of Submicron Aerosols, APCAJ, 24(11), pp. 1067–1072.
Liu, B.Y.H., Whitby, K.T. and Yu, H.H.S. 1967. Diffusion Charging of Aerosol Particles at Low Pressures. J. Appl. Phys. 38: 1592–1597.
Lohmann, M., Beyer, H., & Schmidt-Ott, A. (1997). Size and charge distribution of liquid metal electrospray generated particles. Journal of Aerosol Science, 28, S349-S350.
Loo, J.A. (2000). Electrospray ionization mass spectrometry: a technology for studying noncovalent macromolecular complexes. International Journal of Mass Spectrometry, 200(1-3), 175-186.
Loscertales, I. G., Barrero, A., Guerrero, I., Cortijo, R., Marquez, M. & Ganan-Calvo, A. M. (2002). Micro/nano encapsulation via electrified coaxial liquid jets. Science, 295, 1695-1698.
Madani SY, Naderi N, Dissanayake O, Tan A, Seifalian AM (2011) A new era of cancer treatment: carbon nanotubes as drug delivery tools. Int J Nanomedicine:2963-2979
Maisels, A., Jordan, F. & Fissan, H. (2002). Dynamics of the aerosol particle photocharging process. Journal of Applied Physics, 97, 3377.
Marín, Á. G., Loscertales, I. G., Márquez, M. & Barrero1 A. (2007). Simple and double emulsions via coaxial jet electrosprays. Physical Review Letters, 98,014502(1-4)/
Marquard, A., Meyer, J. and Kasper, G. 2006. Characterization of Unipolar Electrical Aerosol Chargers—Part II: Application of Comparison Criteria to Various Types of Nanoaerosol Charging Devices. J. Aerosol Sci. 37: 1069–1080.
Matsumoto, H., Mizukoshi, T., Nitta, K., Minagawa, M., Tanoika, A. & Yamagata, Y. (2005). Organic/inorganic hybrid nano-microstructured coatings on insulated substrates by electrospray deposition. Journal of Colloid Interface Science, 286(1), 414-416.
McClelland, J. A. 1898. On the Conductivity of thc Hot Gases from Flames. Phil. Mag.

46:29-42.
McClelland, J.A, and Kennedy,H.(1912). The Large Ions in the Atmosphere, Proceedings of the Royal Irish Academy, 30: 72–91.
Medved, A., Dorman, F., Kaufman, S.L. and Pocher, A. 2000. A New Corona-Based Charger for Aerosol Particles. J. Aerosol Sci. 31: s616–s617.
Michelson, D. (1990). Electrostatic atomization. Adam Hilger, Bristol and New York.
Mirme, A. (1994): Electric Aerosol Spectrometry. Ph.D. Thesis, University of Tartu.
Misra, C., Singh, M., Shen, S., Sioutas, C., and Hall, P.M. (2002). Development and evaluation of a personal cascade impactor sampler (PCIS). Journal of Aerosol Science, 33: 1027–1047.
Nawab, M.A. & Mason, S.G. (1958). The preparation of uniform emulsions by electrical dispersion. Journal of Colloid Science, 13,179-187.
Martinez-Lozano, P., and Labowsky, M., 2009. An Experimental and Numerical Study of a Miniature High Resolution Isopotential DMA. J. Aerosol Sci., 40(5): 451–462.
Meesters, G.M.H., Vercoulen, P.H.W., Marijnissen, J.C.M. & Scarlett, B. (1992). Generation of micron-sized droplets from the taylor cone. Journal of Aerosol Science, 23, 37-49.
Mei, F., and Chen, D.R. (2007). Investigation of compound jet electrospray: particle encapsulation. Physics of Fluids, 19,1-10.
Modesto-Lopez, L. B., Kettleson, E.M. & Biswas, P. (2011). Soft X-ray charge (SXC) system for use with electrospray for mobility measurement of bioaerosols. Journal of Electrostatics, 69, 357-364.
Morozov, V.N., & Vsevolodov, N.N. (2007). Electrospray-neutralization method for manufacturing free and supported nanomats. Advanced Materials, 19, 4381-4386.
Nel A, Xia T, Madler L, Li N (2006) Toxic potential of materials at the nanolevel. Science, 311:622-627
Oh, H. & Kim, S. (2007). Synthesis of Ceria nanoparticles by flame electrospray pyrolysis. Journal of Aerosol Science, 38(12), 1185-1196.
Oldham MJ, Phalen RF, Budiman T (2009) Comparison of Predicted and Experimentally Measured Aerosol Deposition Efficiency in BALB/C Mice in a New Nose-Only Exposure System. Aerosol Sci. Technol 43:970-977.
O'Shaughnessy PT, Achutan C, O'Neill ME, Thorne PS (2003) A small whole-body exposure chamber for laboratory use. Inhal Toxicol 15:251-263
Oberdörster, G., Oberdörster, E., and Oberdörster, J. (2005). Nanotoxicology: an emerging discipline evolving from studies of ultrafine particles. Environ Health Perspect, 113: 823-839.
Oberdörster, G., Sharp. Z., Atudorei, V., Elder, A., Gelein, R., Kreyling, W., and Cox, C. (2004). Translocation of Inhaled Ultrafine Particles to the Brain. Inhal. Toxicol., 16(6-7): 437-45.
Park, D., An, M., and Hwang, J. 2007. Development and Performance Test of a Unipolar Diffusion Charger for Real-Time Measurements of Submicron Aerosol Particles Having a Log-Normal Size Distribution. J. Aerosol Sci. 38: 420–430.

Park, D., Kim, Y.H., Lee, S.G., Kim, C., Hwang, J. and Kim, Y.J. (2010). Development and Performance Test of a Micromachined Unipolar Charger for Measurements of Submicron Aerosol Particles having a Log-Normal Size Distribution. J. Aerosol Sci. 41: 490–500.

Park MV, Neigh AM, Vermeulen JP, de la Fonteyne LJ, Verharen HW, Briede JJ, van Loveren H, de Jong WH (2011) The effect of particle size on the cytotoxicity, inflammation, developmental toxicity and genotoxicity of silver nanoparticles. Biomaterials 32:9810-9817

Patel, M.M. and Miller, R.L. (2009). Air pollution and childhood asthma: recent advances and future directions. Curr. Opin. Pediatr., 21: 235-242.

Peters, A., von, K.S., Heier, M., Trentinaglia, I., Hormann, A., Wichmann, H.E., and Lowel, H. (2004). Exposure to traffic and the onset of myocardial infarction. N. Engl. J. Med., 351: 1721-1730.

Paul, S. (1985). Surface coating: science and technology, 1st edn (1985) and 2nd edn (1996), Wiley Baffins Lane, Chichester, West Sussex, England

Pauluhn J (1994) Validation of an improved nose-only exposure system for rodents. J Appl Toxicol 13: 55-62

Pauluhn J, Thiel A (2007) A simple approach to validation of directed-flow nose-only inhalation chambers. J Appl Toxicol 27:160-167

Paur H, Cassee FR, Teeguarden J, Fissan H, Diabate S, Aufderheide M, Kreyling WG, Hänninen O, Kasper G, Riediker M, Rothen-Rutishauser B, Schmid O (2011) J Aerosol Sci 42:668-692

Phillips, D. L. 1962. A technique for the numerical solution of certain integral equations of the Þrst kind. J. Ass. Comp. Mach. 9, 84Ð97.

Pui, D.Y.H. 1976. Experimental Study of Diffusion Charging of Aerosols, Ph.D. thesis, University of Minnesota, Minneapolis, U.S.A.

Qi, C., Chen, D.R., and Greenberg, P. (2008). Fundamental study of a miniaturized disk-type electrostatic aerosol precipitator for a personal nanoparticle sizer. Aerosol Science and Technology, 42: 505–512.

Qi, C., Chen, D.R., and Pui, D.Y.H. (2007). Experimental study of a new corona-based unipolar aerosol charger. Journal of Aerosol Science, 38:775–792.

Qi, C., and Kulkarni, P. 2012. Unipolar Charging Based, Hand-held Mobility Spectrometer for Aerosol Size Distribution Measurement. J. Aerosol Sci., 49:32–47

Rader, D.J. and McMurry, P.H. (1986). Application of the tandem differential mobility analyzer to studies of droplet growth or evaporation. Journal of Aerosol Science, 17, 771-787.

Ranjan, M., and Dhaniyala, S. (2007). Theory and design of a new miniature electrical-mobility aerosol spectrometer. Aerosol Science, 38: 950-963.

Reavell, K. (2002). Determination of Real-Time Particulate Size Spectra and Emission Parameters with a Differential Mobility Spectrometer. International ETH Conference on Nanoparticle Measurement.

Reischl, G. P., M€akel€a, J. M., and Necid, J., 1997. Performance of Vienna Type Differential Mobility Analyzer at 1.2–20 Nanometer," Aerosol Sci. Technol., 27(6): 651–672.

Rizzi, R., Guzzi, R., & Legnani, R. 1982. Aerosol size spectra from spectral extinction data: the use of a linear inversion method. Applied Optics 21(9):1578-1587.

Romay, F.J., Liu, B.Y.H., and Pui, D.Y.H. 1994.A sonic jet corona ionizer for electrostatic discharge and aerosol neutralization. Aerosol Sci. Technol., 20: 31-41.

Romay, F.J., and Pui, D.Y.H. 1992. On the combination coefficient of positive ions with ultrafine neutral particles in the transition and free-molecule regime. Aerosol Sci. Technol., 17: 134-147.

Rossell-Llompart, J., Loscertales, I. G., Bingham, D., and de la Mora, J. F. 1996. Sizing Nanoparticles and Ions with a Short Differential Mobility Analyzer, J. Aerosol Sci. 27:695-719.

Russell, L. M., Stolzenburg, M. R., Zhang, S. H., Caldow, R., Flagan, R. C., and Seinfeld, J. H. (1996). Radially Classified Aerosol Detector for Aircraft Based Submicron Aerosol Measurements, J. Atmos. Oceanic Technol. 13: 598-609.

Salam, M.T., Islam, T., and Gilliland, F.D. (2008). Recent evidence for adverse effects of residential proximity to traffic sources on asthma. Curr Opin Pulm Med, 14: 3-8.

Salata, O.V. (2005). Tools of nanotechnology: electrospray. Current Nanoscience, 1, 25-33.

Samet, J.M., Dominici, F., Curriero, F.C., Coursac, I., and Zeger, S.L. (2000). Fine particulate air pollution and mortality in 20 US cities, 1987–1994. N Engl J Med 343: 1742–1749.

Santos, J. P., Honta~n_on, E., Ramiro, E., and Alonso, M. (2009). Performance Evaluation of a High-Resolution Parallel-Plate Differential Mobility Analyzer.Atmos. Chem. Phys., 9: 2419–2429.

Scalf, M., Westphall, M.S., Krause, J., Kaufman, L.S. & Smith, L.M. (1999). Controlling charge states of large ions. Science, 283,194-197.

Schneider JM, Lindblad NR, Hendricks CD (1965) An apparatus to study the collision and coalescence of liquid aerosols. J colloid Sci 20:610-616.

Schmidt-Ott, A., and Siegmann, H.C. Photoelectron emission from small particles suspended in air. Appl. Phys. Lett., 32(11): 710-713, 1978.

Shimada, M., Han, B., Okuyama, K. & Otani, Y. (2002). Bipolar charging of aerosol nanoparticles by a soft X-ray photoionizer. Journal of Chemical Engineering of Japan. 35, 786-793.

Scheibel, H.G., and Porstendorfer, J. (1983). Generation of monodisperse Ag and NaCl aerosols with particle diamters between 2 and 300 nm. Journall of Aerosol Science, 14, 113-126.

Schemchel, D., Lindsley, W.G., Chen, T.B., Blachere, F.M., Green, B.J., Brundage, R.A. and Beezhold, D.H. (2007). A Two-stage Personal Cyclone Sampler for the Collection of Fungal Aerosols and Direct ELISA and PCR Sample Analysis. Journal of Allergy and Clinical Immunology, 119 (1): S188.

Shah, A.P., Pietropaoli, A.P., Frasier, L.M., Speers, D.M., Chalupa, D.C., Delehanty, J.M., Huang, L.S., Utell, M.J., and Frampton, M.W. (2008). Effect of inhaled carbon ultrafibe particles on reactive hyperemia in healthy huna subjects, Environ. Health Perspectives, 116(3): 375-380.

Shin Y, Liu W, Su Y (2012) Aggregation of stabilized TiO2 nanoparticle suspensions in the presence of inorganic ions. Environ Toxicol Chem 31(8):1693-1698

Si, B.Q., Byun, D. & Lee, S. (2007). Experimental and theoretical study of a cone-jet for an electrospray microthruster considering the interference effect in an array of nozzles. Journal of Aerosol Science, 38(9), 924-934.

Smith, R.D., Bruce, J.A., Wu, Q. & Lei, P. (1997). New mass spectrometric methods for the study of noncovalent associations of bipolymers. Chemical Society Reviews, 26,191-202.

Smijs TG, Pavel S. (2011). Titanium dioxide and zinc oxide nanoparticles in sunscreens: focus on their safety and effectiveness. Nanotechnol Sci Appl 4:95-112

Snarski, S.R. & Dunn, P.F. (1991). Experiments characterizing the interaction between two sprays of electrically charged liquid droplets. Experiments in Fluids, 11, 268-278.

Somasundaran P, Fang X, Ponnurangam S, Li B (2010) Nanoparticles: characteristics, mechanisms and modulation of biotoxicity. KONAPower Part J 28:38-48

Song, D.K., and Dhaniyala, S. (2007). Change in distributions of particle positions by Brownian diffusion in a non-uniform external field. Aerosol Science, 38: 444-454.

Steer, B., Gorbunov, B., Muir, R., Ghimire, A., and Rowles, J. (2014). Portable planar DMA: development and tests. Aerosol Science and Technology, 48: 250-259.

Sterling, H.J., Daly, M.P., Feld, G.K., Thoren, K.L. Kintzer, A.F., Krantz, B.A. & Williams, E.R. (2010). Effects of supercharging reagents on noncovalent complex structure in electrospray ionization from aqueous solutions.Journal of the American Society for Mass Spectrometry, 21(10), 1762-1774.

Stewart, J., Chalupa, D.C., Devlin, R., Frasier, L.M., Huang, L.S., Little, E.L., Lee, S.M., Phipps, R.P., Pietropaoli, A.P., Taubman, M.B., Utell, M.J., and Frampton, M.W. (2010). Vascular effects of ultrafine particles in persons with type 2 Diabetes, Environ. Health Perspectives 118: 1692-1698.

Stommel, Y.G., and Riebel, U. A corona-discharge-based aerosol neutralizer designed for use with the SMPS-system. J. Electrostatics, 63: 917-921, 2005.

Suh, J., Han, B., Okuyama, K. & Choi, M. (2005). Highly charging of nanoparticles through electrospray of nanoparticle suspension. Journal of Colloid and Interface Science, 287, 135-140.

Takenaka S, Karg E, Roth C, Schulz H, Ziesenis A, Heinzamann U (2001) Pulmonary and systemic distribution of inhaled ultrafine silver particles in rats. Environ Health Persp 109:547-551

Tang, K. & Gomez, A. (1994). Generation by electrospray of monodisperse water droplets for targeted drug delivery by inhalation. Journal of Aerosol Science, 25, 1237-1249.

Tomita, Y., Ishibashi, I., & Yokoyama, T. (1986). Fundamental studies on an electrostatic ink

jet printer. Bulletin of Japan Society of Mechanical Engineers, 29, 3737-3743.
Thompson, J.F., Warsi, Z.U.A. & Mastin, C.W. (1985). Numerical grid generation: foundations and applications. North-Holland, New York.
Trotta M, Cavalli R, Trotta C, Bussano R, Costa L (2010) Electrospray technique for solid lipid-based particle production. Drug Dev Ind Pharm 36:431-438
Twomey, S. 1965. The application of numerical filtering to the solution of integral equations encountered in indirect sensing measurements. Journal of the Franklin Institute 279(2):95-109.
Twomey, S. 1977. Introduction to the Mathematics of Inversion in Remote Sensing and Indirect Measurements. Elsevier, New York.
van Zomeren, A.A., Kelder, E.M., Marijnissen, J.C.M. & Schoonman, J. (1994). The production of thin films of limn2o4 by electrospraying. Journal of Aerosol Science, 25 (6), 1229-1236.
Vassiliou A, Bikiaris D, Chrissafis K, Paraskevopoulos KM, Stavrev SY, Docoslis A (2008) Nanocomposites of isotactic polypropylene with carbon nanoparticles exhibiting enhanced stiffness, thermal stablitiy and gas barrier properties. Compos Sci Technol, 68:933-943
Vivas, M.M., Hontañón, E., and Schmidt-Ott, A. 2008. Reducting multiple charging of submicron aerosols in a corona diffusion charger. Aerosol Sci. Technol. 42: 97-109.
Wang, S.C.; Flagan, R.C. (1990). Scanning electrical mobility spectrometer. Aerosol Sci. Technol. 13: 230.
Whitby, K.T. 1961. Generator for producing high concentrations of small ions. The Review of Scientific Instruments, 32(12): 1351-1355.
Whitby, K. T., and Clark, W. E. 1966. Electrical Aerosol Particle Counting and Sizc Distribution Measuring Systcm for the 0.015 to 1 μ Size Range, Tellus 18573-586.
Wiedensohler, A. (1988). Technical note an approximation of the bipolar charge distribution for particles in the submicron size range. Journal of Aerosol Science, 19 (3), 387-389.
William GS, Laura MM, Marcia LH, Ranjana U, John MG, Erin ES, Crystal S, Katharine MB, Lauren T, John V, Randall JB, Alan RS (2009) Flexible low-cost system for small animal aerosol inhalation exposure to drugs, proteins, inflammatory agents, and infectious agents. Biotechniques 46:Piii-Pviii.
Winklmayr, W., Reischl, G. P., Lindner, A. O., and Berner, A. (1991). A new electromobility spectrometer for the measurement of aerosol size distributions in the size range from 1 to 1000 nm, J. Aerosol Sci. 22: 289-296.
Wyslouzil BE, Wu Y, Yu B, Jackson A, Zha WB, Lee LJ (2009) Coaxial Electrohydrodynamic Spraying: a novel one-step technique to prepare oligodeoxynucleotide encapsulated lipoplex nanoparticles. Mol Pharm 6:1371-1379
Wong BA (2007) Inhalation exposure systems: Design, methods and operation. Toxicol pathol 35:3-14
Xie, J., Ng, W.J., Lee, L.Y. & Wang, C.H. (2008). Encapsulation of protein drugs in biodegradable microparticles by co-axial electrospray. Journal of Colloid and Interface

Science, 317(2), 469-476.
Yamashita, M. & Fenn, J.B. (1984). Electrospray ion source: another variation on the free-jet theme. Journal of Physical Chemistry, 88, 4451-4459.
Yi J, Chen BT, Schwegler-Berry D, Frazer D, Castranova V, McBride C, Knuckles TL, Stapleton PA, Minarchick VC, Nurkiewicz TR (2013) Whole-body nanoparticle aerosol inhalation exposures. J Vis Exp 75:e50263
Yli-Ojanperä, J. Mäkelä, J.M., Marjamäki, M., Rostedt, A., and Keskinen, J. 2010. Towards traceable particle number concentration standard: single charged aerosol reference (SCAR). Journal of Aerosol Science, 41: 719-728
Voutilainen, A., Kolehmainen, V., & Kaipio, J. P. 2000. Statistical inversion of aerosol size distribution data. Journal of Aerosol Science 31, Supplement 1(0):767-768.
Yuliati, L., Seo T. & Mikami, M. (2012). Liquid-fuel combustion in a narrow tube using an electrospray technique. Combustion and Flame, 159(1), 462-464.
Zeleny, J. 1898. On the Ratio of the Velocities of the Two Ions Produced in Gases by Rontgen Radiation; and on Some Related Phenomena, Phil. Mag. 46:120-154.
Zeleny, J.(1900). The velocity of the ions produced in gases by Rontgen rays. Philosophical Transactions A, 195:193–234.
Zeleny, J. (1914). The electrical discharge from liquid points, and a hydrostatic method of measuring the electric intensity at their surfaces. Physical Review, 3, 69-91.
Zeleny, J. (1915). On the condition of instability of electrified drops with applications to the electrical discharge from liquid points. Proceedings of Cambridge Philosophical Society, 18,71-83.
Zeles-Hahn, M.G., Lentz, Y.K., Anchordoquy, T.J. & Lengsfeld, C.S. (2011) Effect of electrostatic spray on human pulmonary epithelial cells. Journal of Electrostatics, 69(1), 67-77.
Zhang, J.J., and Chen, D.R. (2014). Differential mobility particle sizers for nanoparticle characterization. journal of nanotechnology in engineering and medicine, 5: 020801-1
Zhang, M. and Wexler, A. S. 2006. Cross flow ion mobility spectrometry: Theory and initial prototype testing, Int. J. Mass Spectrom., 258, 13–20.
Zhang, S. H., Akutsu, Y., Russell, L. M., and Flagan, R. C. (1995). Radial differential mobility analyzer, Aerosol Sci. Technol. 23:357-372.
Zimlich, W. C. J., Dvorsky, J. E., Busick, D. R. and Peters, R. D. (1999). Pulmonary aerosol delivery device and method, Battelle Pulmonary Therapeutics, Inc., USA.

Appendices

Design and Testing of a Programmable Aerosol Diluter for 10 nm to 1.0 μm particles

Qiaoling Liu[1], Da-Ren Chen[1*]

[1]Particle Lab, Department of Mechanical and Nuclear Engineering, Virginia Commonwealth University, 401 West Main Street, Richmond, VA, USA, 23294

Abstract

Real-world aerosols are often varied in time. A dynamic aerosol generation system is thus needed to evaluate the performance of aerosol sensors for characterizing time-dependent aerosol size distribution. However, all the laboratory aerosol generators are designed for the production of aerosols with stable concentration and steady size distribution. A simple way to produce reliable time-dependent aerosols is to combine a stable aerosol generator with a programmable aerosol diluter. Aerosol diluters are also needed for measuring aerosols in high concentration using existing aerosol instruments. In this study, we focused on the design and testing of a programmable aerosol diluter. The dilution flow rate of the aerosol diluter was controlled by a programmable mass flow controller having the maximal flow rate of 200 L/min. Steady and dynamic dilution processes in the diluter were programmed by a developed Visual Basic code. Experiments were carried out to characterize the steady and dynamic dilution performance of the aerosol diluter for particles with sizes ranging from 10 nm to 1.0 μm. The steady dilution result shows that the diluter has a non-size dependent dilution performance and a good linear relationship between aerosol dilution ratio and dilution flow rate ratio (with a calibrated line slope of 1.03, close to the ideal line slope of 1.0). Our experiments further indicate that efficient aerosol mixing in the diluter can be achieved when operated at the flow Reynolds number of 450. The evaluation of four dynamic dilution modes also evidences an excellent performance of the diluter with the capability of continuously producing well-defined dynamic aerosols. Finally, a simple empirical model was proposed to describe the steady and dynamic dilution performance of the diluter.

***Keywords*:** Diluter; Dilution ratio; Dynamic aerosol; Programmable control

* Corresponding author. Tel: 1-804- 828-2828; Fax: 1-804- 827-7030
E-*mail address*: dchen3@vcu.edu

INTRODUCTION

Real-world aerosols are often time-varied in their physical properties, such as particle concentration and size. Examples of such time-varied aerosols are the nucleation event of particles in the atmosphere (Weber et al., 1995, 1996; Mäkelä et al., 1997; Kulmala, 2003, 2004, 2013) and the aerosols produced by the combustion processes (Flagan, 1979; Leskinen, et al., 1998; Yu et al., 2005; Xu et al., 2011). The performance of aerosol instruments under the challenge of dynamic aerosols needs to be understood in order to properly characterize the behavior of aerosols. However, none of the aerosol generators are able to reliably produce well-defined dynamic aerosols for aerosol instrument calibration. All the existing instruments are currently evaluated by stable laboratory aerosols, lack of dynamic performance information for users to properly interpret measured data. Further, with the modern development of aerosol instruments, the investigation of the dynamic response of instruments becomes essential. It is thus desired to develop a dynamic aerosol generation system for evaluating the dynamic performance of aerosol sensors. A simple way to produce time-varied aerosols in the lab is to combine a stable aerosol generator with a programmable aerosol diluter.

Particles in high concentration are often encountered in the measurements of aerosols originating from various particle sources, e.g., combustion. Because of the limitations of aerosol instruments, such as portable Condensation Particle Counter (CPC, TSI Model 3007) having the measurement limit of particle concentration below 105 #/cm3, they are unsuitable for directly characterizing particles in high concentrations. Aerosol dilution is a common

technique to deal with this issue. Up to now, a number of different dilution approaches have been developed and commercialized for the study of particle emissions from diesel vehicles (Casati et al., 2007), cigarette smoke aerosols (McCusker et al., 1982) and laboratory-generated aerosols. In an ideal dilution, the dilution ratio of aerosols is directly determined by the ratio of these two flows (i.e., no particle loss during the dilution process). Fuchs and Sutugin (1965), Delattre and Friedlander (1978) and Mikkanen et al. (2001) used porous tube diluters for aerosol dilution, in which the dilution air entered through a tube with a porous wall and was mixed with the particle-free air. The similar design concept can also be found in a "leaky filter" type diluter, which consisted of a glass capillary tube placed in a HEPA Capsule filter (Collins, 2010). Also based on the similar principle, Guichard (1982) designed another new diluter by sending aerosol flow into a cone shape dilution channel which was perforated with rings of blowing holes. Venturi principle was very commonly applied in dilution approach, as well. Koch et al. (1988) developed a Venturi aerosol diluter with a fixed dilution factor of 10, and Abdul-Khalek et al. (1998) designed a Venturi based aerosol ejector. Both of them can achieve a quick dilution for the entire size range from nanometers up to several micrometers. Helsper et al. (1990) tested a cascade Venturi dilution system with dilution ratio up to 10,000 for particle sizes between 0.1 and 10 μm. Moreover, Koch and Ilgen (1992) developed a particle size selective dilution system based on virtual impaction theory for fine particles (<1μm). Differing from the dilution-ratio-fixed designs described above, Hueglin et al. (1997) designed a rotating disk type dilution system for particle sizes between 10 nm and 700 nm. In this diluter, the aerosol dilution ratio showed a

linear relationship with the control parameters (e.g. rotating frequency) and can be selected continuously between 10 and 10,000. But for larger particles, the impaction-caused loss in the diluter resulted in a deviation from the ideal condition. And the flow rate of diluted gas was restricted to a few liters per minute (Burtscher, 2005).

During the dilution, passing particles may alter their sizes through many mechanisms such as particle condensation, agglomeration and coagulation. A representative aerosol diluter thus requires a quick and stable dilution process for all particle sizes under consideration. Cheng et al. (2002) investigated the turbulent mixing effect on particle size distribution in an ejector diluter and found no apparent shift on aerosol peak value and distribution spread. Wong et al. (2003) also found an ejector diluter could provide reliable diesel exhaust particle number and size distribution because of negligible coagulation effects in a fast mixing process. Particle losses within the diluters however need to be considered to recover the size distribution of originally sampled aerosols. It is because a significant particle loss in ejector diluters may vary aerosol dilution ratio from the ideal volumetric flow rate ratio, resulting in a particle-size-dependent dilution. Yoon et al. (2005) reported their experimental result of 95% transmission efficiency for particle sizes between 3 nm and 20 nm in a modified Venturi diluter designed by Koch et al. (1988). Collins (2010) also studied the sub-100 nm particle loss within aerosol diluters (TSI 3302, MSP 1100, a laboratory "leaky filter" diluter and an orifice diluter). Particle loss was found to be primarily diffusion driven, and loss within the diluters increased with decreasing particle diameter. And aerosol charge may reduce particle penetration through diluters by as much as 40%.

In this study, we developed a new aerosol diluter and established a programmable aerosol generation system to deal with the two issues discussed in the first paragraph of this section: dilution of high concentration aerosol to meet detection limit of current aerosol instruments and time-varied aerosol generation for evaluating the dynamic response of aerosol sensors. Three design objectives of this new diluter are: (1) the aerosol diluter shall perform a controllable dynamic dilution and have a good repeatability; (2) the aerosol diluter shall have a size-independent dilution performance for particles with sizes less than 1.0 μm; (3) the particle loss in the diluter shall be kept as minimal as possible. To achieve these goals, we designed a new diluter enabling good turbulent flow mixing inside while minimizing the particle loss due to the turbulence flow effect. Experiments were further carried out to evaluate the steady and dynamic performance of the diluter for particles with sizes ranging from 10 nm to 1 μm. Finally we proposed a simple empirical model to describe the dynamic performance of the designed diluter.

STUDIED AEROSOL DILUTION SYSTEM AND EXPERIMENTAL METHOD

Design of aerosol diluter

In order to build up a size-independent aerosol dilution system, we designed and evaluated a new aerosol diluter which is shown in Figure 1. The aerosol diluter consists of three sections: fast premixing, full mixing/dilution and aerosol sampling sections. The aluminum-made fast premixing section is the most important part of the diluter. Three inlets are included in the section. The central inlet with the outer diameter (OD) of 1/4" (0.635 cm)

and inner diameter (ID) of 0.225" (0.5715 cm) is for undiluted aerosol and the other two identical side inlets with OD of 1/2" (1.27 cm) and ID of 0.41" (1.0414 cm) are for the injection of particle-free dilution gas flows. Each side inlet forms 45 º angles with the central aerosol inlet. In the pre-mixing section, two identical dilution gas flows at controllable flow rates are mixed with aerosol flow in a relatively small tubular space, whose diameter is 0.75" (1.905 cm), length is about 1.2" (30.48 mm) and volume is about 8.71 cm^3. Once mixed, the entire flow is then transported to the full mixing section, which is a cone shaped space with diameter increasing from 0.75" to 1.85" (4.699 cm), for complete mixing process. The full dilution section of the diluter is a 1-foot (30.48 cm) long aluminum tube with OD of 2" (5.08 cm) and ID of 1.85". The large space in the full dilution section weakens the flow turbulence effect. Particles continue their mixing with dilution air flow in the full dilution section, and a spatially uniform aerosol distribution across the cross section of the tube will be developed at the end of this section. The metal material was chosen to reduce potential particle loss resulted from the electrostatic effect. A "Y" shaped PVC connector at the downstream of diluted flow forms the sampling section of the diluter, in which only a portion of diluted aerosol flow is sampled via a stainless steel tubing of 0.375" (0.9525 cm) OD and 0.305" (0.7747 cm) ID for measurement while the majority of flow is exhausted from the side opening. For the operation, aerosol dilution is determined by the setting for the ratio of dilution flow rate to aerosol flow rate. When the undiluted aerosol flow rate is fixed, the concentration of diluted aerosol output from the diluter depends on the dilution gas flow rate.

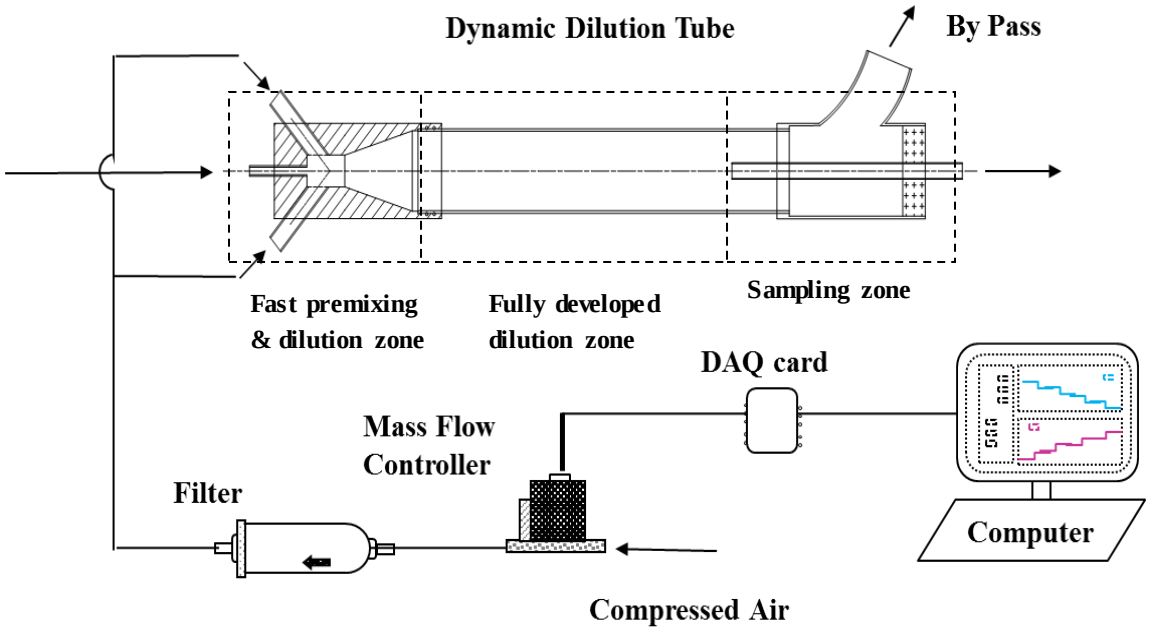

Figure 1 Schematic diagram of a newly developed aerosol diluter

Experimental setup

Figure 2 is the schematic of the experimental setup for testing the new aerosol diluter. As shown, a custom-made Collison atomizer and a diffusion dryer were used to generate dry solid polydisperse particles in a stable concentration and size distribution from liquids, which were prepared by dissolving sodium chloride in DI water for different concentrations (5%, 0.1% and 0.01%, in v/v). To test ultrafine particles, especially particles with diameter down to 10 nm, an aerosol generation system based on the evaporation and condensation technique (Scheibel and Porstendörfer 1983; Gurav et al. 1994; Li and Chen, 2005) was used in this study to produce particles in the same chemical compound as those generated by the Collison atomizer. This setup mainly consisted of a cylinder of nitrogen gas (Grade 4.8), a

Lingerberg tube furnace with a ceramic tube inside (Al_2O_3, Coors Ceramics Co), a combustion boat, and a compressed air source. NaCl powder was placed in the combustion boat located in the middle of the ceramic tube. To produce stable polydisperse nanoparticles of desired sizes, the tube furnace temperature was carefully controlled. Filtered N_2 gas was introduced into the ceramic tube to transport NaCl vapor, then mixed with a cold quenching stream of particle-free compressed air at the exit. Thus, the evaporation inside the furnace and condensation outside resulted in nanoparticle generation. In the experimental setup of aerosol generators, 4 laminar flow meters (LFMs) and 4 needle valves were used for flow rate monitoring and control, respectively.

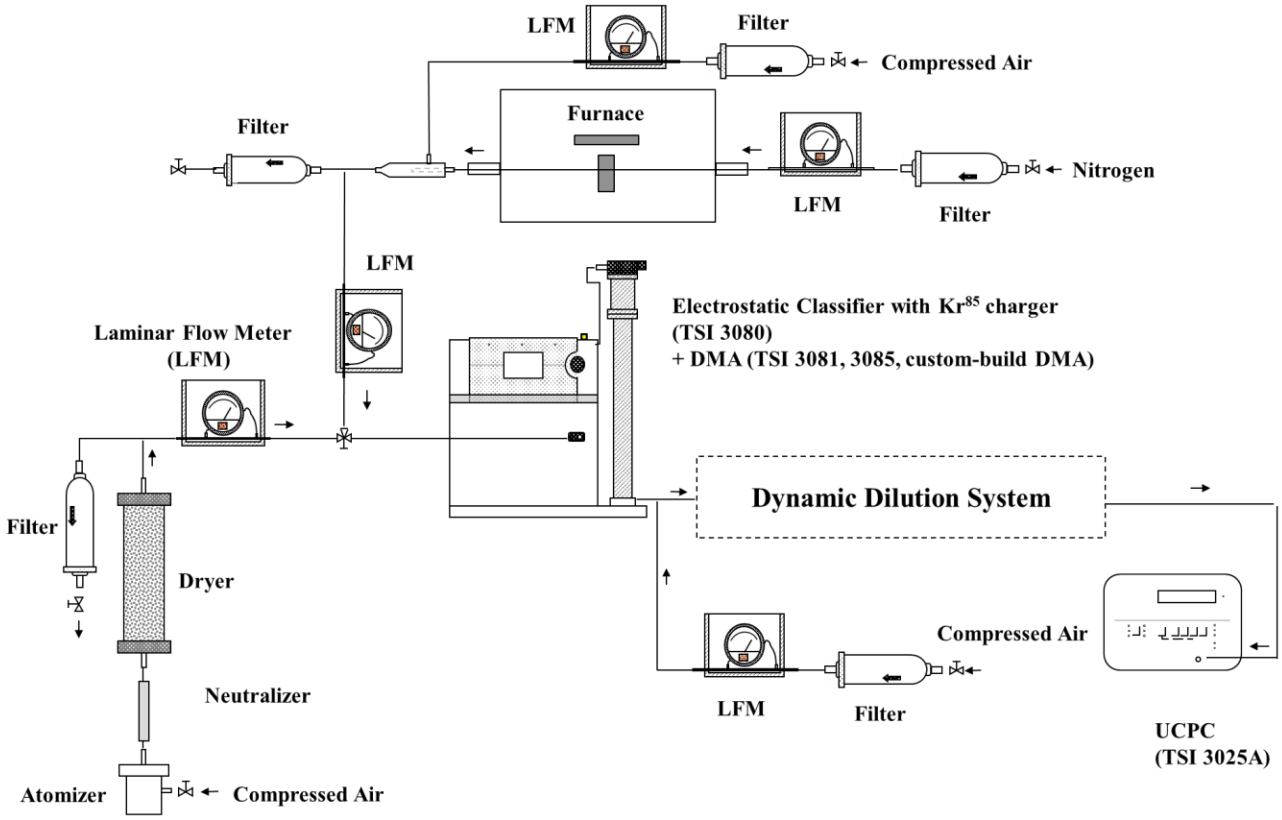

Figure 2 Schematic diagram of the experimental setup for the performance evaluation of proposed diluter

To obtained monodisperse particles with size up to 1.0 μm, TSI 3081 and 3085 differential mobility analyzers (DMAs) and custom-build DMA with the classification length of 66 cm, combined with TSI 3080 DMA platform, were used as the particle size selectors. The aerosol-to sheath flow rate ratios in all experiments were kept at 1:10 to guarantee the size quality of selected particles. Monodisperse particles with 16 different mobility sizes (which may not be geometric equivalent), covering the range from 10.0 nm to 1.0 μm, were chosen and delivered into the aerosol diluter for testing, individually. They were 10 nm, 30 nm, 50 nm, 100 nm, 150 nm, 200 nm, 250 nm, 300 nm, 350 nm, 400 nm, 500 nm, 600 nm, 700 nm, 800 nm, 900 nm and 1000 nm. Another LFM, filter and needle valve in front of the dilution system was used to inject a makeup flow in some cases. Undiluted monodisperse aerosol flow rates were thus controlled from 0.3 L/min to 5.0 L/min, according to the downstream flow rate of DMAs and required flow rate for dilution operation. Meanwhile, two particle-free dilution air flows controlled by a mass flow controller (MFC; MKS type 1559A), which receives control signals from a data acquisition (DAQ) card, were injected into the diluter to achieve the desired dilution effect (see in Figure 1). In this study, the flow rate of dilution air can be precisely adjusted from 0 to 200 L/min. The performance of MFC showed its quick response and flow rate adjustment within 2-3 seconds. The MFC can also send the flow rate signals back to the DAQ card for feedback control. A computer program developed on Visual Basic (VB) language communicated with

the DAQ card and TSI 3025A UCPC, and monitored the entire system by recording the data and operational parameters.

To evaluate aerosol dilution ratio for different sizes and dynamically control particle concentrations, six different dilution modes were developed in the VB program: constant dilution mode (in which the dilution flow rate remains unchanged during dilution), step dilution mode (in which the dilution flow rate changes step by step according to a user-defined step function), linear ramp dilution mode (in which the dilution flow rate is either increased or decreased linearly during the dilution), rectangular wave dilution mode (in which the variation of dilution flow rate is in a rectangular wave pattern), triangular wave dilution mode (in which the real dilution flow rate as a function of time follows a user-defined triangular wave pattern) and half-sine wave dilution mode (in which the real dilution flow rate curve as a function of time follows a user-defined half-sine wave function). The specific dilution process for these 6 modes all can be determined by setting dilution ratio or dilution flow rate, dilution step number and step dilution time or total dilution time. Both the real-time flow rate data of dilution air and the particle number concentration data were recorded and displayed with 1-second time resolution. To evaluate steady and transient dilution performance of aerosol diluter, constant dilution mode and step dilution mode were chosen. For each evaluation case of monodisperse aerosol (with size of 10 nm to 1.0 μm), at least 3 different flow rates were chosen to be tested to characterize the features of aerosol diluter, such as dilution ratio and delay time. To investigate dynamic performance of aerosol diluter, linear ramp dilution mode, rectangular wave dilution mode, triangular wave dilution

mode and half-sine wave dilution mode were conducted. Aerosol flows with particle size of 30nm, 300nm and 700nm and flow rate of 1.0 L/min or 0.5 L/min were used in this experiment. For each specific evaluation case, identical testing was done for at least 3 times, and the results proved an excellent repeatability of the studied dilution system.

RESULTS AND DISCUSSION

Steady Performance of Aerosol Dilution (Evaluation of aerosol dilution Ratio)

To evaluate the steady performance of the prototype aerosol diluter, particles of different sizes smaller than 1 μm were tested. For each monodisperse aerosol run, the same stepping dilution mode was chosen and operated to provide a series of dilution levels from the low flow rate ratio of 5 to the high flow rate ratio of 200. Here, we defined flow rate ratio (FR) and aerosol dilution ratio (AR) as:

$$FR_i = \frac{Q_{aero,i} + Q_{dilu,i}}{Q_{aero,i}} \quad (1)$$

and

$$AR_i = \frac{N_{non-dilu,i}}{\eta_i N_{dilu,i}} \quad (2)$$

where i indicates test particle size; $Q_{dilu,i}$ and $Q_{aero,i}$ are particle-free dilution flow rate and non-diluted aerosol flow rate, respectively; $N_{non-dilu,i}$ and $N_{dilu,i}$ are the aerosol concentrations of non-diluted aerosol and diluted aerosol measured at the downstream of aerosol diluter; η_i is the particle penetration efficiency through the diluter, defined as $N_{non-dilu,i} / N_{upstream,i}$. Particle penetration efficiency test was conducted before all programmable dilution experiments. The results showed that all particles (10 nm to 1 μm)

have more than 88% transmission efficiencies and 99% particles with size larger than 60 nm can pass through the diluter. Figure 3 shows the plot of experimentally obtained aerosol dilution ratio as a function of flow rate ratio. Also included in the above plot is the straight line assuming the ideal dilution (i.e., FR = DR) for the reference.

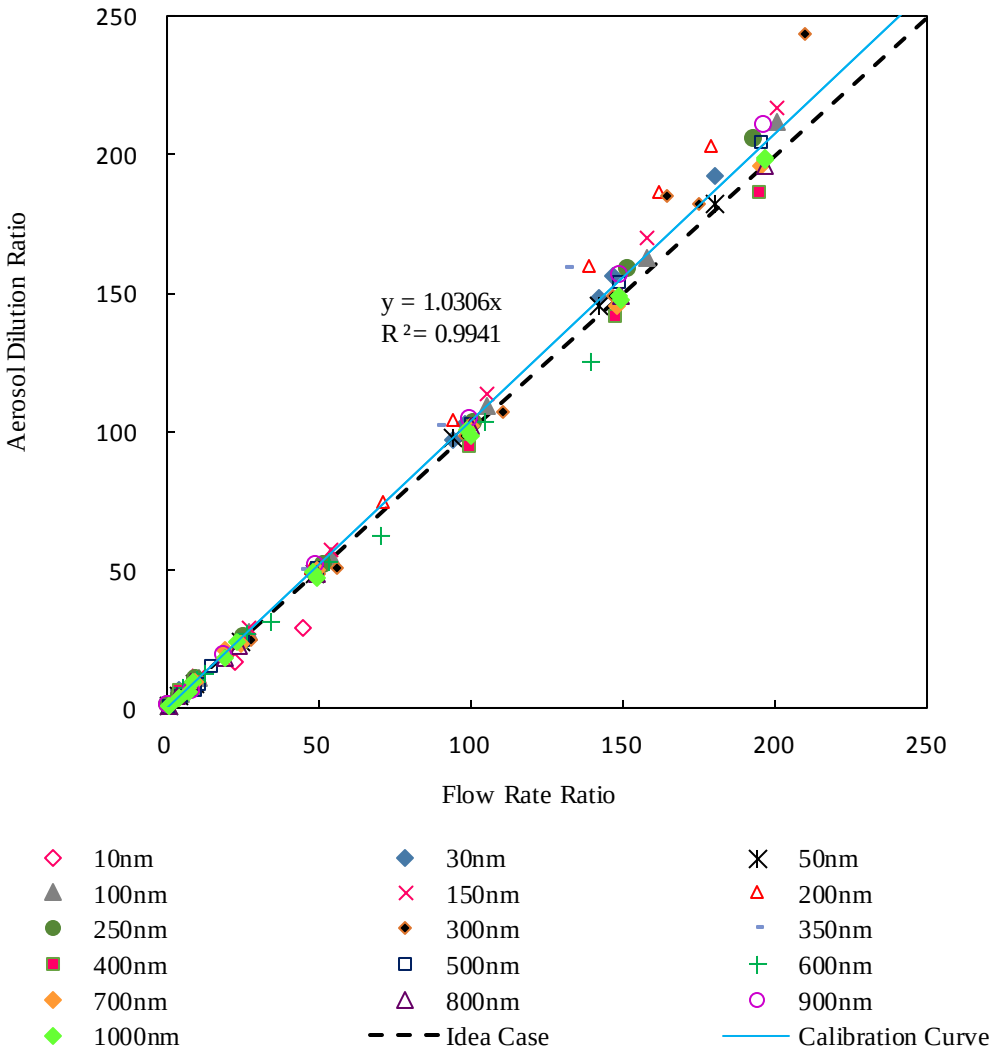

Figure 3 Steady state aerosol dilution result of studied aerosol diluter for monodisperse particles in various sizes

As evidenced in Figure 3, the dilution results for the tested aerosols with sizes from 10 nm to 1 μm in the studied aerosol diluter were all very close to the ideal case, indicating the performance of the studied diluter can follow its operational principle very well. In general, the characteristics of aerosol dynamics in an aerosol diluter are sensitive to the turbulent flow condition in the dilution tunnel/chamber. Gas flow introduced into the turbulent region of a diluter is transported and dispersed across it by the fluid eddy motion (from the largest eddies to the smallest ones). Such eddy motion of gas flow permits the flow mixing to proceed effectively (Dimotakis, 2005). At the same time, aerosol particles under such a turbulent mixing process are easily lost, resulting in that the real dilution data AR_i should be larger than flow rate ratio FR_i. Also, the more particles loss, the further real dilution data are away from their ideal results. The aerosol loss in the turbulent mixing should thus be minimized in order to achieve an ideal aerosol dilution state (i.e., no particle loss). Through curve fitting of all dilution ratio data in this experiment, the result of a straight line with slope of 1.03 demonstrates that particle loss inside the studied diluter is overall negligible. That is, the dilution strategy applied to the design of the studied aerosol diluter seems to work reasonably well in the particle size range of interest. In the studied aerosol diluter, the fast premixing was first achieved by impinging a highly concentrated aerosol stream with two particle-free dilution gas flows in a relatively small space, resulting in an effective mixing. Then, they were quickly transported to a large space to reach a stable mixing state with minimal loss. The curve-fitted line can then be used as the calibration curve of the studied aerosol diluter for particles with sizes smaller than 1.0 μm.

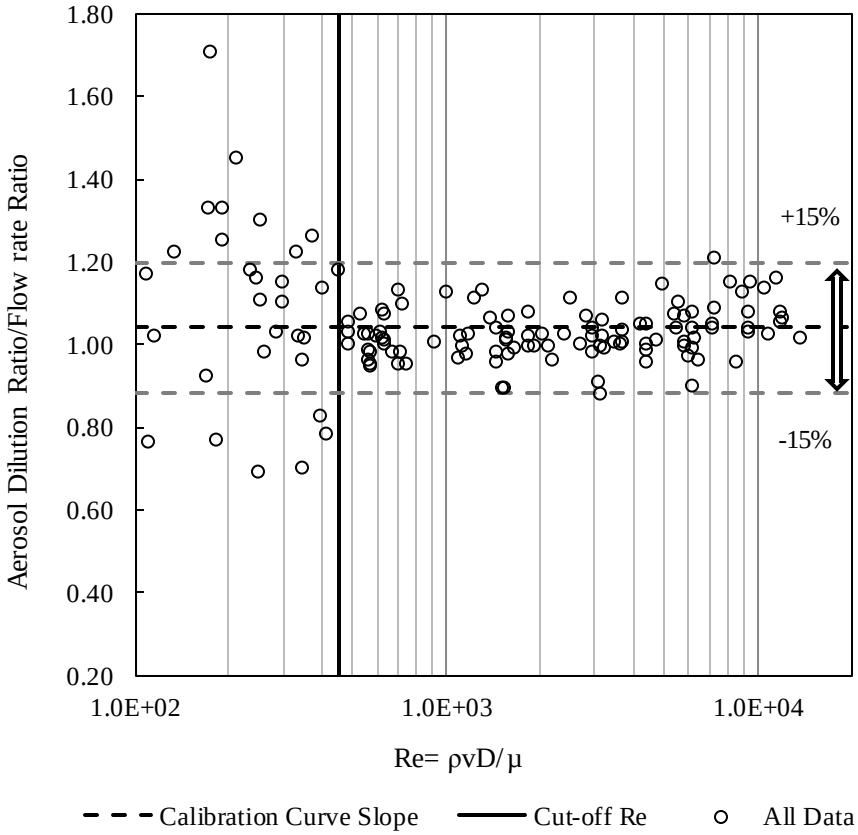

Figure 4 The ratio of aerosol dilution ratio (AR) to dilution flow rate ratio (FR) as a function of flow Reynolds number for the studied aerosol diluter

Detailed examination of the experimental data given in Figure 3 further reveals that for the studied prototype the aerosol dilution in some cases noticeably deviates from the ideal condition. To analyze those cases, the value of AR/FR for all the dilution cases (shown in Figure 3) is given in Figure 4 as the function of flow Reynolds number ($Re = \rho\ v\ D\ /\ \mu$, where ρ is the air density, v is flow velocity, D is the inner diameter of the fast premixing section of diluter and μ is the kinetic viscosity of the air). Two parallel dash lines are also included in Figure 4 as the ±15% deviation from the reference value (i.e., 1.03). As shown

in Figure 4, the scattering of dilution data was reduced as the flow Reynolds number increased and was within ±15% when the flow Reynolds number was higher than 450, and up to ~ 10^4 (maximum case in this study). The above observation is comparable with that reported by Dimotakis (1993) for fully developed turbulent flows. Dimotakis shows that the fully developed turbulent flow requires a minimum local Reynolds number of 10^4, or a Taylor Reynolds number ($Re_T = \rho\ u'\ \lambda_T\ /\ \mu$, where u' is the rms streamwise velocity fluctuation level, and λ_T is the Taylor microscale) of 10^2 to be sustained. Due to the flow impingement in the studied diluter, the critical Reynolds number for fully turbulent flows is expected to be less than that reported by Dimotakis (1993). The primary mixing of aerosol stream with particle-free flows in the studied diluter obviously resulted from the turbulent flow mixing. Note that the total flow rate for the Reynolds number of 450 in the studied diluter can be calculated as 6.0 L/min.

Transient Performance of Aerosol Diluter

As previously mentioned, particle-free gas flow in the studied dilution system can be quickly changed by the control program (usually less than 3 seconds). However, the additional time is required for the diluter to achieve its steady dilution state (i.e., delay time) once the dilution flow rate is changed. It is because of the finite dilution volume and mixing process in the studied diluter. The delay time is thus one of the primary parameters in describing the transient performance of an aerosol diluter. The determination of the delay time can be done by comparing the time-dependent dilution flow rate data with the time-

dependent CPC readouts for diluted aerosol concentration. The delay time in general depends on many parameters such as dilution flow rate, dilution volume, particle size, CPC residence time, etc.

To simplify the data analysis, the sampling tubing from the diluter exit to the UCPC inlet was reduced to the minimum, neglecting the time needed to transport the diluted aerosol to UCPC. The time resolution of UCPC data readout from its RS-232 communication protocol is 1.0 s, resulting in the same time resolution for the transient performance characterization of the studied aerosol diluter. Since the CPC response time for a change of aerosol concentration is estimated at 0.3 second when operated at the high flow rate mode, the delay time attributed by the CPC response can also be neglected (i.e., much less than 1.0 second). So, the factors contributing to the observed delay time in the studied aerosol dilution system are limited to the particle size (D_p), total flow rate ($Q_{tot} = Q_{aero} + Q_{dilu}$) and dilution volume (V) in the studied diluter.

The dilution delay time is expected to increase when the tested particle size increases. It is because small particles having less inertial effect in flows could easily follow the change of gas flows when compared with that for large particles, resulting in a quicker dilution response for small particles as compared with that of large particles. The particle inertial effect can be characterized by the particle relaxation time (τ), defined as the characteristic time for particles to change from one state to another state. Obviously, the time of particles residing in the diluter (t_r) will directly affect the response of the studied dilution system. Thus, the particle residence time in the diluter shall be included in the analysis of the delay

time for the studied diluter, as well. The values of t_r and τ can be calculated by the following equations:

$$t_r = \frac{V}{(Q_{aero} + Q_{dilu})} \quad (3)$$

and

$$\tau = mB = m\frac{v_t}{F_D} = \frac{\pi \rho_p D_p^3 v_t}{6\, F_D} \quad (4)$$

where the particle terminal velocity is $v_t = \frac{Q_{aero} + Q_{dilu}}{S}$, in which S is the cross section area of fully developed dilution zone; the drag force F_D is a function of the particle size, density and terminal velocity and can be calculated as $F_D = \frac{\pi\, D_p^2 \rho_p v_t^2 C_D}{8\, C_c(D_p, \lambda)}$; and ρ_p is the particle density. A set of 3D curve fitting functions were tested to find out the best-fitted curve of the dilution delay time t_{delay} as a function of particle resident time t_r and particle relaxation time τ. Because of its simple mathematic expression and unit uniformity between two sides of equation, we proposed to fit the experimental delay time $t_d\ (t_r, \tau)$ as

$$t_d = 0.379\ \times\ t_r + 9.516 \times 10^5 \times \tau + \ 7.4043 \quad (5)$$

Figure 5 shows the delay time deducted from the experiment runs and the curve for the proposed best-fitted equation. The delay time for particles of different sizes under various dilution conditions can thus be calculated by Eq. (5).

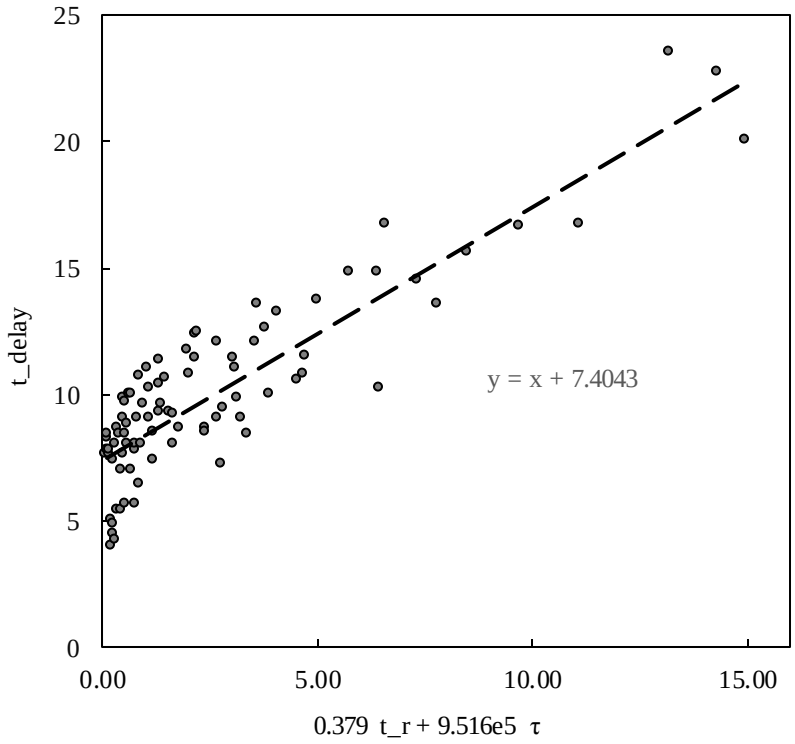

Figure 5 The dilution delay time as a function of particle residence time (V/Q_{total}) and particle relaxation time (τ)

Dynamic Performance of aerosol diluter at designated dilution modes

The unique feature of the studied aerosol dilution system is its capability of continuous variation of aerosol dilution according to commands signaled by the control program developed using Visual Basic. The program worked as the platform to carry out six dilution modes described in the diluter design section and to register the concentrations of diluted aerosol and operational parameters during the process. For this part of the experiment, undiluted aerosol flow rate was fixed at 1.0 L/min. Particles of 30, 300 and 700 nm were individually selected for the evaluation.

Figure 6 shows the dynamic dilution results of the prototype aerosol diluter operated at four dilution modes (i.e., linearly increased dilution mode (a); triangular wave mode (b); half-sine wave mode (c); and rectangular wave mode (d)) for the particles with the sizes of 30, 300 and 700 nm. For comparison, the changes of dilution flow rate ratio as the time proceeded in the process are also given in the corresponding figures. Note that, as mentioned previously, the real dilution flow rate in the studied diluter can be quickly changed after the change command is signaled by the control program, reaching its set flow rate in the duration of 2-3 s. The same observation was obtained in this part of the experiment for these four dilution modes.

Figure 6(a) shows the dilution result when the diluter was operated at the linearly increased dilution mode. In this case, the dilution flow rate ratio was kept at 10 for the initial 5 s and increased to 150 in the latter 290 s. During the same period of time, the measured aerosol dilution ratios for test particles initially increased to the corresponding dilution flow rate ratio and kept steady for a few seconds. The aerosol dilution ratio then linearly increased as the dilution flow rate ratio continuously increased. Eventually the aerosol dilution ratio matched the dilution flow rate ratio. Only slight time delay in aerosol dilution was observed in this operational mode.

The dilution results when the diluter was operated at the triangular and half-sine wave dilution modes are given in Figure6 (b, c), respectively. For both tested cases, the dilution process started from a dilution flow rate ratio of 50, and then gradually increased to 100 within 60s. After reaching the peak, dilution immediately went to decreasing mode and

finally got back to 50 within 60s. Such an operation formed a symmetric triangular wave and half-sine wave dilution function. The system can be controlled to repeat a series of the same waved dilution pattern until a stop command is send. In both modes, the testing results showed the aerosol dilution ratio had similar patterns as the corresponding dilution flow rate ratio. A constant time delay between the aerosol dilution and flow rate ratio was observed during these two dilution processes. The difference in the delay between the case (a) and the cases (b, c) is because of the finite response time needed for the airflow mixing in the diluter to achieve stability when the flow change was made. For the case of linearly increased dilution, the time rate of flow rate ratio change was estimated at 0.48, while for the cases of triangular and half-sine wave dilution, the time rate of flow rate dilution was 0.83. The quick time change in the dilution flow rate made it much harder for the aerosol dilution to catch up, resulting in a time delay between change of aerosol dilution and change of dilution flow rate. Particle size effect was not obvious in the above three dilution cases. It is because of the gradual change in the dilution flow rate.

Figure 6 (d) shows the dilution results when the prototype operated at continuous rectangular wave mode. 30 nm and 300 nm particles were chosen for testing. The first test had a 120s cycle time, with 60s for dilution flow rate ratio kept at 100 and 60s for non-dilution operation. The second test has the same 120s time period, but was controlled at two different dilution flow rate ratios (60s for dilution flow rate ratio of 10 and 60s for dilution flow rate ratio of 50). Different from the three continuous dilution modes discussed above, a bigger time delay in aerosol dilution was observed after the dilution flows were injected in

the diluter. Once the aerosol dilution started, the dilution ratio quickly ascended to reach the set maximal dilution flow rate ratio. However, the time rate of aerosol dilution increase was not as high as that of the dilution flow rate increase in this operation mode. Further, the larger the particle size, the slower the aerosol dilution ratio increased. However, once the dilution flow was turned off, the aerosol dilution ratio dropped at a much faster pace when compared with that in the dilution increase phase. No particle size effect in aerosol dilution was found during the dilution descending phase.

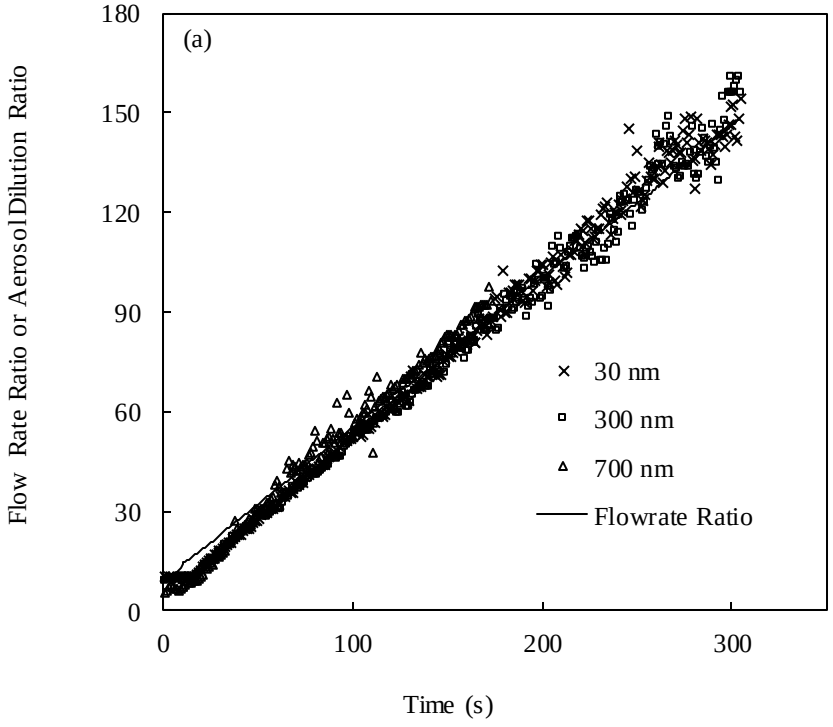

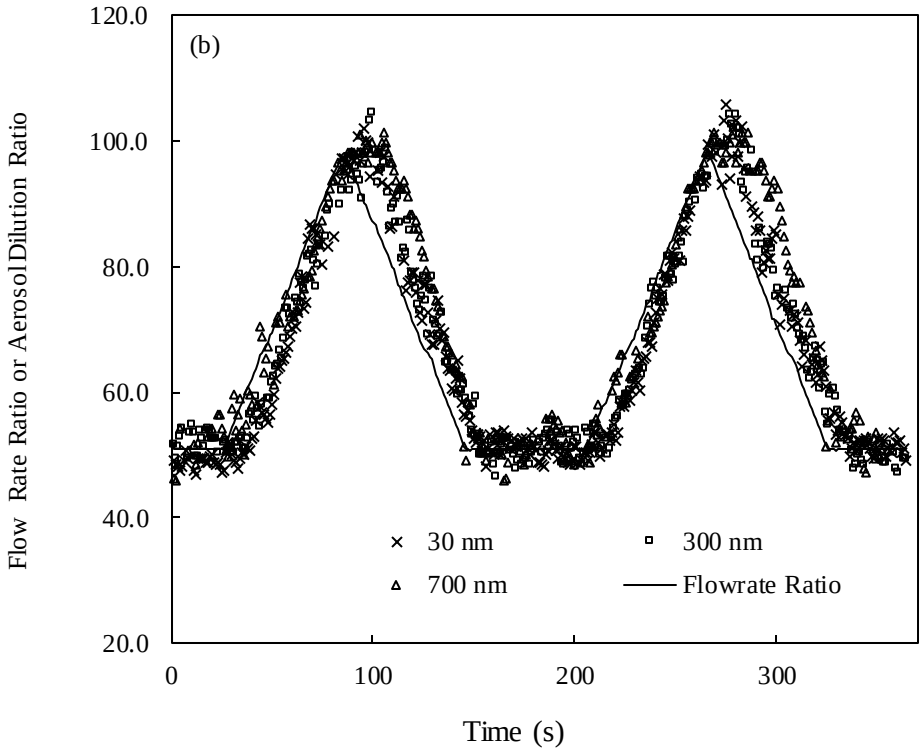
(b)
120.0
100.0
80.0
60.0
40.0
20.0
0
100
200
300
Flow Rate Ratio or Aerosol Dilution Ratio
Time (s)
30 nm
300 nm
700 nm
Flowrate Ratio

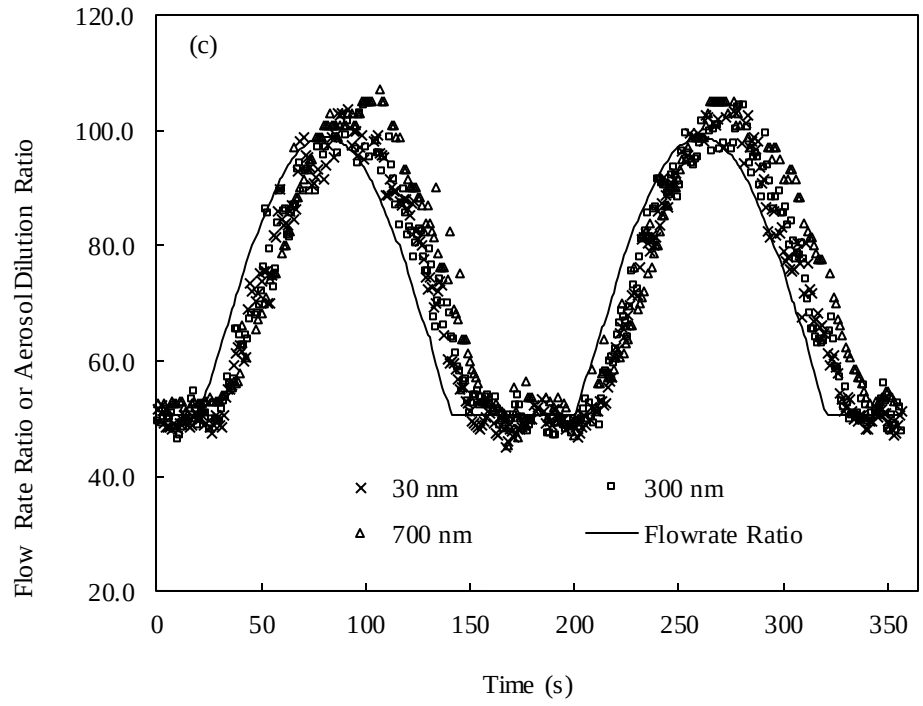
(c)
120.0
100.0
80.0
60.0
40.0
20.0
0
50
100
150
200
250
300
350
Flow Rate Ratio or Aerosol Dilution Ratio
Time (s)
30 nm
300 nm
700 nm
Flowrate Ratio

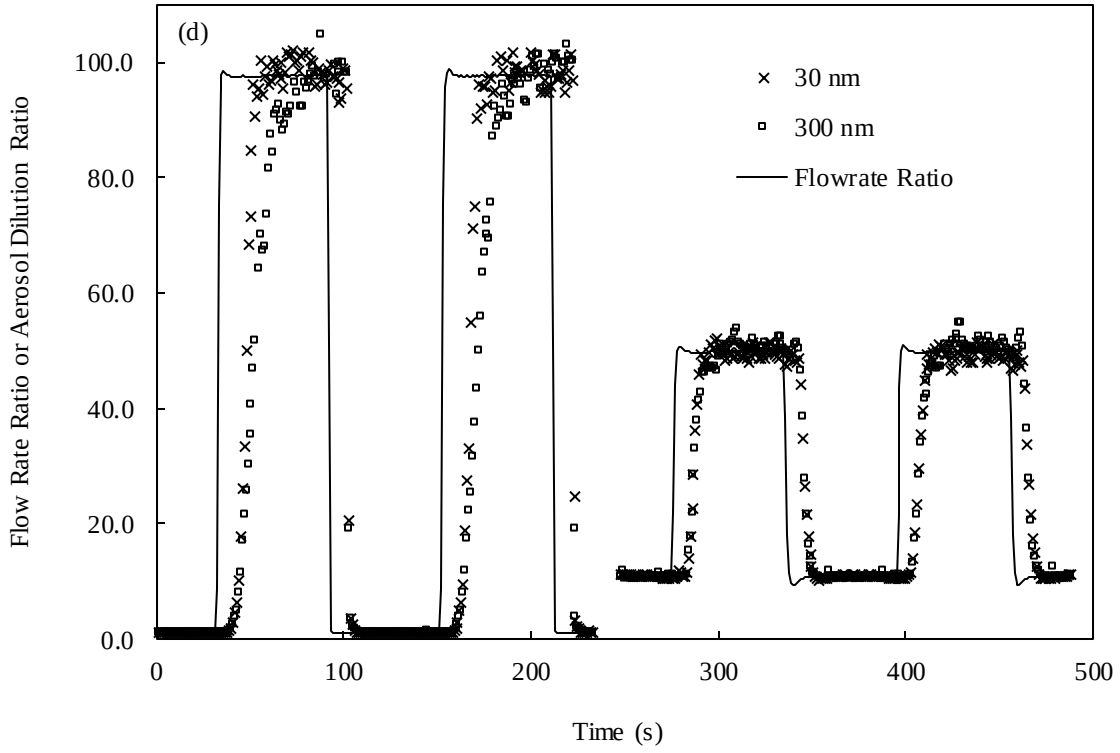

Figure 6 Dilution result of aerosol diluter when operated at four different dilution modes (a. linear increasing dilution; b. triangular wave patterned dilution; c. half-sine wave dilution; d. rectangular wave dilution)

MODEL TO PREDICT THE PERFORMANCE OF STUDIED AEROSOL DILUTER

In the steady state operation (i.e., fixed aerosol dilution), the dilution ratio for particles with sizes ranging from 10 nm to 1μm was measured as 1.0306 times the dilution flow rate ratio. A time delay between the onset flow rate ratio and output diluted aerosol ratio was also found in our study. In such cases one can simply apply the following equation to describe the time relationship between the aerosol dilution ratio and dilution flow rate ratio:

$$AR_i(t) = FR_i(t - t_d) * 1.0306 \qquad (6a)$$

where both aerosol dilution and dilution flow rate ratios are the functions of time t, and delay time t_d can be calculated by Eq. (5). The same equation can also be applied to the cases for continuous dilution modes of linear increase/decrease, triangular wave and half-sine wave modes.

For step and rectangular wave dilution modes, a different set of equations is proposed to describe the change of aerosol dilution ratio between two adjacent settings of dilution flow rate ratio:

$$\begin{cases} AR_i(t) = FR_i(t - t_d) * 1.0306\,, & t \le t_1 \\ AR_i(t) = exp\left(6.3 - \frac{t_d}{(t-t_1)^{0.5}}\right) + DR_i(t_1), & t_1 \le t \le t_1', \\ AR_i(t) = FR_i(t - t_d) * 1.0306, & t_1' \le t \le t_2 \end{cases} \quad \text{for the ascending case (6b)}$$

and

$$\begin{cases} AR_i(t) = FR_i(t - t_d) * 1.0306\,, & t \le t_1 \\ AR_i(t) = DR_i(t_1) - (2 * t_d) * ln(t - t_1), & t_1 \le t \le t_1', \\ AR_i(t) = FR_i(t - t_d) * 1.0306, & t_1' \le t \le t_2 \end{cases} \quad \text{for the descending case (6c)}$$

where the dilution flow rate ratio is assumed in the functional format of

$$\begin{cases} FR_i(t) = FR_1, & t \le t_1 \\ FR_i(t) = FR_2, & t_1 < t \le t_2 \end{cases},$$

One can easily use the Eq. (6) to predict the diluted aerosol concentration at any time t under the designated aerosol dilution modes developed in the studied aerosol dilution system, when un-diluted aerosol concentration, aerosol flow rate, particle-free dilution flow rate and the diluter geometry are known. The model can also assist in finding the resultant aerosol dilution under specific dilution flow rate curves defined by users.

To verify the above proposed model, the comparison of calculated aerosol dilution ratios and experimental results is shown in Figure 7. In this verification part of the experiment, four dilution modes were tested, and the particle size tested in each mode was randomly selected for each mode examination. For the case of linearly increased dilution mode (shown in Figure 7a), a 300 nm particle stream at the flow rate of 1.0 L/min was used. As expected, the trend of all experimental data for the aerosol dilution ratios varying from 10 to 150 in general follows the calculated line for aerosol dilution and falls in the domain bounded by the two predicted limited lines (± 10% deviation from the calculated line). The same verification was also done for the cases of triangular wave, half-sine wave and rectangular wave dilution modes (shown in Figure7b, c and d, respectively). A 30 nm particle stream of 1.0 L/min flow rate was selected in the verification of triangular wave dilution mode with the dilution flow rate ratio varying from 50 to 180. For the half-sine wave dilution mode, a 700 nm aerosol stream of 0.5 L/min flow rate was applied. A 30 nm particle flow at the rate of 1.0 L/min was used in the verification for the rectangular wave dilution mode. Two different operational settings were applied in this mode verification: one is for case of flow rate ratio setting from 0 to 100 and the other is for the case from 10 to 50. For all these cases, predicted results from the model can match the experimental data very well.

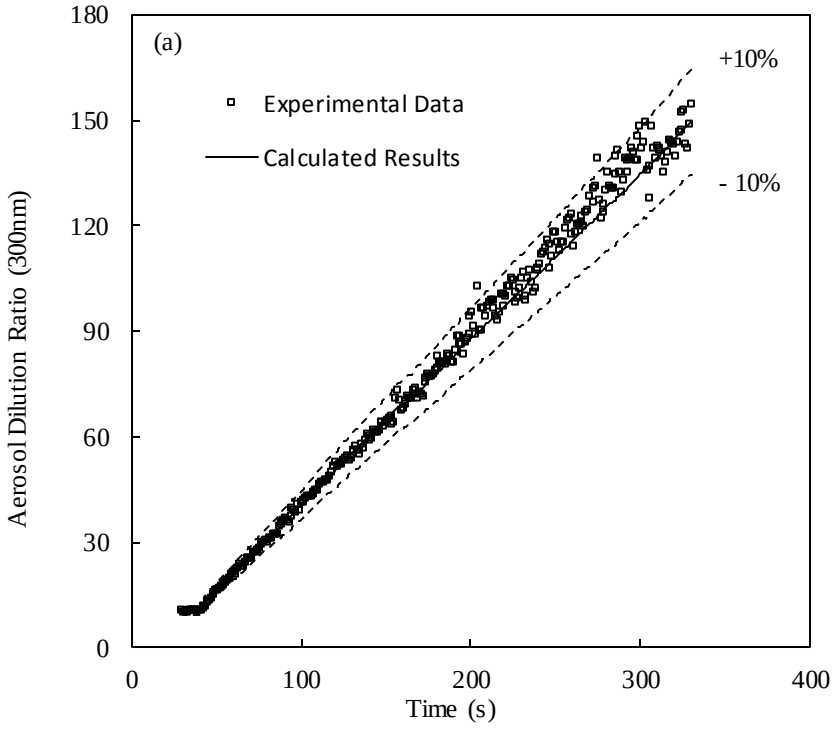
(a)
Experimental Data
Calculated Results
+10%
- 10%
Aerosol Dilution Ratio (300nm)
Time (s)
0
30
60
90
120
150
180
0
100
200
300
400

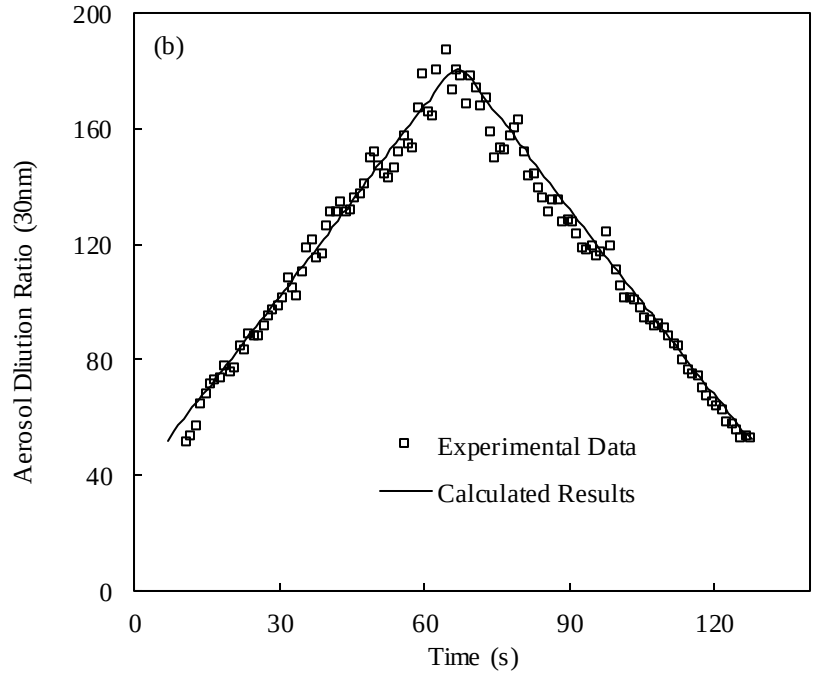
(b)
Experimental Data
Calculated Results
Aerosol Dliution Ratio (30nm)
Time (s)
0
40
80
120
160
200
0
30
60
90
120

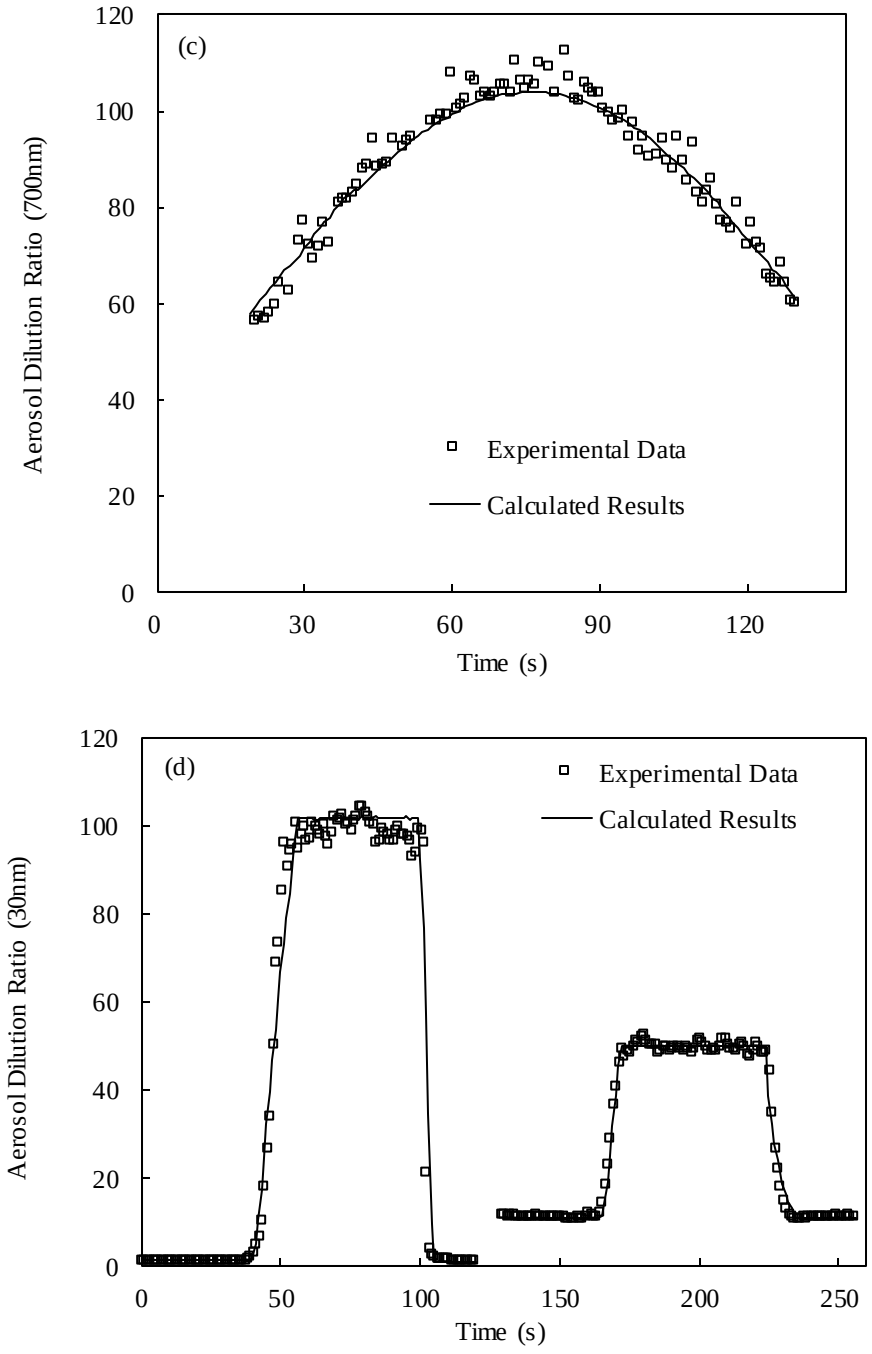

Figure 7 Comparison of calculated aerosol dilution ratio with experimental ratios for four continuous dilution modes in aerosol diluter (a. linearly increase dilution mode; b. triangular wave dilution mode; c. half-sine wave dilution mode; d. rectangular wave dilution mode)

CONCLUSION

A new aerosol diluter was designed and its performance was evaluated in this study in order to assemble a dynamic aerosol generation system. The designed diluter consists of three sections: pre-mixing, full mixing and aerosol sampling sections. In pre-mixing section, un-diluted aerosol flow meets with the programmable controlled dilution flows from two sides in a small volume to enhance the turbulent mixing. Then, the entire mixed particle laden flow is transported to the full-mixing section in a much larger volume, allowing completing dilution while minimizing the particle loss due to the turbulent flow effect. An aerosol sampling tubing closed to the diluter exit is used to sample the diluted aerosol stream for applications. The entire system works in six operational modes (constant dilution, step dilution, linear ramp dilution, rectangular wave dilution, triangular wave dilution, and half-sine wave dilution) via a Visual Basic based program.

Experiments were performed to evaluate the steady and dynamic dilution performance of the above-described diluter, by using monodisperse particles of various sizes in the sub-micrometer range. The experimental results for the steady aerosol dilution evidence that the aerosol diluter offers reliable performance in reducing the concentration of aerosols. The dilution of particles with sizes less than 1.0 μm followed the set curve of the dilution flow rate ratio (defined as the total flow rate divided by undiluted aerosol flow rate) very well. No apparent particle loss was detected in the studied aerosol diluter. The steady performance evaluation also identifies that efficient aerosol dilution can be achieved in the

prototype when operated at a high Reynolds number larger than 450. The time delay between the onset dilution flow rate ratio and diluted aerosol output, in general the function of particle size, total flow rate and the diluter's geometry, was also characterized. The evaluation of dynamic performance of the studied diluter shows that the aerosol dilution ratios under the continuous dilution modes (i.e., linear increase, triangular wave, half-sine wave and rectangular wave functional modes) are consistent with the onset functions for dilution flow rate ratio. A simple empirical model was then proposed to describe the variability of diluted aerosol concentration within the studied aerosol diluter and was further verified by experiments.

Finally, by combining the studied aerosol diluter with a stable aerosol generator, a dynamic aerosol generation system thus was constructed in the lab for the calibration of dynamic performance of aerosol sensors or instruments. The diluter can also be applied for diluting aerosols in high concentrations for use in existing aerosol instruments.

REFERENCES

Abdul-Khalek, I. S., Kittelson, D. B., Graskow, B. R., Wei, Q. and Brear, F. (1998). Diesel exhaust particle size: Measurement issues and trends. *SAE Technical Paper* 980525, doi:10.4271/980525.

Burtscher, H. (2005). Physical characterization of particle emissions from diesel engines: a review. *J. Aerosol Sci.* 36: 896-932.

Casati.R., Scheer, V., Vogt, R. and Benter, T. (2007). Measuremnt of nucleation and soot mode particle emission from diesel passenger car in real world and laboratory in situ dilution. *Atmos. Environ.* 41: 2125-2135.

Cheng, M. -D., Storey, J. M., Wainman, T. and Dam, T. (2002). Impact of venturi turbulent mixing on the size distributions ofsodium chloride and dioctyl-phthalate aerosols. *J. Aerosol Sci.* 33: 491-502.

Collins, A. M. (2010). Ultrafine particle loss in aerosol diluters. Master thesis, University of Minnesota, Minnesota.

Delattre, P. and Friedlander, S.K. (1978). Aerosol coagulation and diffusion in a turbulent jet. *Ind. Eng. Chem. Fundam.* 17:189-194.

Dimotakis, *P. E. (1993)* Some issues on turbulent mixing and turbulence. *GALCIT Report FM93-1a.*

Dimotakis, P. E. (2005) Turbulent mixing. *Annu. Rev. Fluid Mech.* 37: 329-356

Flagan, R.C. (1979). Submicron particles from coal combustion. *Proc. 17th combustion, combustion Inst.*: 97-104 (as cited in Damle et al., 1981).

Fuchs, N.A. and Sutugin, A.G. (1965). Coagulation rate of highly dispersed aerosols. *J. Colloid Sci.* 20: 492-500.

Guichard, J.C. (1982). Some uses of a diluter for aerosols. *Sci. Total Environ.* 23: 273-282.

Gurav, A. S., Kodas, T. T., Wang, L. M., Kauppinen, E. I., and Joutsensaari, J. (1994). Generation of nanometer size fullerene particles via vapor condensation. *Chem.l Phys. Lett.* 218: 304-308.

Helsper, C., Mölter,W. and Heller, P. (1990). Representative dilution of aerosols by a factor of 10,000. *J. Colloid Sci.* 21: S637-S640.

Hueglin, C., Scherrer, L. and Burtscher, H. (1997). An accurate, continuously adjustable dilution system (1:10 to 1:104) for submicron aerosols. *J. Colloid Sci.* 28: 1049-1055.

Koch, W., Lodding, H., Molter, W. and Munzinger, F. (1988). Dilution system for aerosol measurements with optical-particle counters at very high concentrations. *Staub Reinhalt Luft*, 48, 341-344.

Koch, W. and Ilgen, B. (1992). A particle size selective dilution system. *J. Colloid Sci.* 23: S281-S284.

Kulmala, M. (2003). How particles nucleate and grow? *Science* 302: 1000–1001.

Kulmala, M., Vehkamäki, H., Petäjä, T., Dal Maso, M., Lauri, A., Kerminen, V.-M., Birmili, W. and McMurry, P.H. (2004). Formation and growth rates of ultrafine atmospheric particles: a review of observations. *J. Aerosol Sci.* 35: 143-176.

Kulmala, M., Kontkanen J., Junninen, H., Lehtipalo, K., Manninen, H.E., Nieminen, T., Petäjä, T., Sipilä, M., Schobesberger, S., Rantala, P., Franchin, A., Jokinen, T., Järvinen, E., Äijälä, M., Kangasluoma, J., Hakala, J., Aalto, P.P., Paasonen, P., Mikkilä, J., Vanhanen, J., Aalto, J., Hakola, H., Makkonen, U., Ruuskanen, T., Mauldin III, R.L., Duplissy, J., Vehkamäki, H., Bäck, J., Kortelainen, A., Riipinen, I., Kurtén, T., Johnston, M.V., Smith, J.N., Ehn, M., Mentel, T.F., Lehtinen, K.E.J., Laaksonen, A., Kerminen, V.-M., Worsnop, D.R. (2013). Direct observations of atmospheric aerosol nucleation. *Science*. 339: 943-946.

Leskinen, A., Raunemaa, T., Ålander T., and Laitinen, L. (1998). Experimental studies on ozone and secondary aerosol formation in combustion. *J. Aerosol. Sci.* 29: S453-S454.

Li W. and Chen, D. (2005). Performance of Nano-DMA Operated with Different Gases for Sheath and Aerosol Carrier Flows. *Aerosol Science and Technology*, 39(10): 931-940.

Mäkelä, J.M., Aalto, P., Jokinen, V., Pohja, T., Nissinen, A., Palmroth, S., Markkanen, T., Seitsonen, K., Lihavainen, H. and Kulmala, M. (1997). Observations of ultrafine aerosol particle formation and growth in boreal forest. *Geophys. Res. Lett*. 24:1219-1222.

Mikkanen, P., Moisio, M., Keskinen, J., Ristimäi, J. and Marjamöi, M. (2001). Sampling method for particle measurements of vehicle exhaust. *SAE Technical Paper* 2001-01-0219, doi:10.4271/2001-01-0219.

McCusker, K., Hiller, F.C., Wilson, J.D., McLeod, P., Sims, R. and Bone, R.C. (1982). Dilution of cigarette smoke for real time aerodynamic sizing with a spart analyzer. *J. Colloid Sci.* 13: 103-110.

Scheibel, H. G., and Porstendörfer, J. (1983). Generation of monodisperse Ag- and NaCl-aerosols with particle diameters between 2 and 300 nm. *J. Aerosol Sci.* 14: 113-126.

Weber, R.J., McMurry, P.H., Eisele, F.L. and Tanner, J. (1995). Measurement of expected nucleation precursor species and 3–500 nm diameter particles at Mauna Loa observatory, Hawaii. *J. Atmos. Sci.* 52: 2242-2257.

Weber, R.J., Marti, J.J., McMurry, P.H., Eisele, F.L., Tanner, D.J. and Jefferson, A. (1996). Measured atmospheric new particle formation rates: implications for nucleation mechanisms. *Chem. Eng. Commun.* 151: 53-64.

Wong, C.P., Chan, T.L. and Leung, C.W. (2003). Characterisation of diesel exhaust particle number and size distributions using mini-dilution tunnel and ejector-diluter measurement techniques. *Atmos. Environ*. 37: 4435-4436.

Xu, M.H., Yu, D., Yao, H., Liu, X., and Qiao, Y. (2011). Coal combustion-generated aerosols: formation and properties. *Proc. Combust. Inst*. 33: 1681-1697.

Yoon, Y. J., Cheevers, S., Jennings, S.G. and O'Dowd, C.D. (2005). Performance of a venturi dilution chamber for sampling 2-30 nm particles. *J. Colloid Sci*. 36: 535-540.

Yu D., Xu, M.H., Liu X., Huang, J. and Li, G. (2005). Mechanisms of submicron and residual ash particle formation during pulverised coal combustion: a comprehensive review. *Asia-Pacific Journal of Chemical Engineering*, 13: 467-482.

VITA

Qiaoling Liu

EDUCATION

Ph.D. in Mechanical Engineering
Virginia Commonwealth University, Richmond, VA, USA 01/2013 – 08/2015

Ph.D program in Energy, Environmental & Chemical Engineering
Washington University in St. Louis, MO, USA *08/2010 – 12/2012*

Master of Science in Environmental Science
Peking University, Beijing, China *09/2007 – 06/2010*

Bachelor of Science in Environmental Science
Remin University, Beijing, China *09/2003 – 06/2007*

PUBLICATIONS

Accepted Journal Articles

1. **Liu Q.,** & Chen D.R. (**2014)**. Evaluation of win Head Electrospray Nanoparticle Disperser for Nanoparticle Study, Journal of Nanoparticle Research, 16, 2556-2567

2. **Liu Q.,** & Chen D.R. (**2014)**. An Electrospray Aerosol Generator with X-ray Photoionizer for particle charge reduction, Journal of Aerosol Science, 76, 148-162

3. **Liu Q.,** & Chen D.R. (**2014)**. A Programmable Diluter for Generating Time-Varied Sub-Micrometer Particles, Aerosol and Air Quality Research (in press)

4. Fu, H., **Liu Q.,** & Chen D.R. **(2012**). Performance Study of a Twin-head Electrospray System, Journal of Aerosol Science, 52: 33-44.

5. **Liu Q.,** Zhou Y., Chen L. & Zheng X. (**2010**). Application of MBR for Hospital Wastewater Treatment. Desalination, 250(2): 605-608.

6. Zheng X., & **Liu Q.** (**2008**). Analysis on the Application prospects of MBR in hospital wastewater treatment (in Chinese). Water & Wastewater Engineering, 34(10): 78-82.

Journal Articles in Preparation

7. **Liu Q.,** & Chen D.R. Design and Evaluation of a New Miniature Plate Electrostatic Aerosol Analyzer (Mini-Plate EAA).

8. **Liu Q.,** & Chen D.R. Experimental Evaluation of Miniature Plate DMAs (mini-plate DMAs) for Ultrafine particle Sizing and Classification.

9. **Liu Q.,** & Chen D.R. Experimental Study of Mini-Plate Differential Mobility Analyzers (mini-plate DMAs) with Expansion/Contraction Flow Channel.

10. Liu D., **Liu Q.,** & Chen D.R. Performance Comparison of Aerosol Corona-based Mini-chargers for Miniature Ultrafine Particle Sizers.

11. **Liu Q.,** & Chen D.R. Development of a New Miniature Ultrafine Particle Sizers.

PANTENTS

1. Zeng L., **Liu Q.,** Zhang, Y., A New on-line Carbonaceous Aerosol Analyzer, Chinese Patent, No. 201010249182.8.

2. Zeng L., **Liu Q.,** A New Dehumidifier for Airborne Aerosols, Chinese Patent, No. 200810224247.6.

CONFERENCES

1. **Liu Q.,** & Chen, D.R. Design and Evaluation of a New Miniature Plate Differential Mobility Analyzer (mini-Plate DMA). 2015 European Aerosol Conference (EAC), Sept. 6-11, 2015, Milan, Italy.

2. **Liu Q.,** & Chen, D.R. Development of a New Miniature Ultrafine Particle Sizers. The 9th Asian Aerosol Conference, June 24-27, 2015, Kanazawa, Tokyo.

3. Liu D., **Liu Q.,** & Chen, D.R. Performance Comparison of Aerosol Corona-based Mini-chargers for Miniature Ultrafine Particle Sizers.. American Association for Aerosol Research 34st Annual Conference, Oct. 12-16, 2015, Minneapolis, MN, USA.

4. **Liu Q.,** & Chen, D.R Experimental Study of Mini-Plate Differential Mobility Analyzers (mini-plate DMAs) with Expansion/Contraction Flow Channel. American Association for Aerosol Research 34st Annual Conference, Oct. 12-16, 2015, Minneapolis, MN, USA.

5. **Liu Q.,** & Chen, D.R. Design and Evaluation of a New Miniature Plate Differential Mobility Analyzer (Mini-plate DMA). American Association for Aerosol Research 33st Annual Conference, Oct. 20-Oct.24, 2014, Orlando, FL, USA.

6. **Liu Q.,** & Chen, D.R. Design and Evaluation of a New Miniature Plate Electrostatic Aerosol Classifier (mini-Plate EAC). 2014 International Aerosol Conference (IAC), Aug. 28-Sept. 2, 2014, Busan, Korea.

7. **Liu Q.,** & Chen, D.R. Evaluation of a TSE Twin-head Electrospray System for Nanoparticle Exposure Study. American Association for Aerosol Research 32st Annual Conference, Sept. 30-Oct.12, 2013, Portland, OR, USA.

8. **Liu Q.,** & Chen, D.R. Electrospray Aerosol Generator Using Photoionizer as Charge Reduction Scheme. American Association for Aerosol Research 31st Annual Conference, Oct. 8-12, 2012, Minneapolis, MN, USA.

9. **Liu Q.,** & Chen, D.R. A Dynamic Aerosol Generation System for Aerosol Sensor calibration, The 7th Asian Aerosol Conference, Aug. 17-20, 2011, Xi'an, China.